

**PRESSURE TRANSIENT TESTING AND PRODUCTIVITY ANALYSIS
FOR HORIZONTAL WELLS**

A Dissertation

by

YUEMING CHENG

Submitted to the Office of Graduate Studies of
Texas A&M University
in partial fulfillment of the requirements for the degree of

DOCTOR OF PHILOSOPHY

August 2003

Major Subject: Petroleum Engineering

**PRESSURE TRANSIENT TESTING AND PRODUCTIVITY ANALYSIS
FOR HORIZONTAL WELLS**

A Dissertation

by

YUEMING CHENG

Submitted to Texas A&M University
in partial fulfillment of the requirements
for the degree of

DOCTOR OF PHILOSOPHY

Approved as to style and content by:

W. John Lee
(Chair of Committee)

Thomas A. Blasingame
(Member)

Duane A. McVay
(Member)

Wayne M. Ahr
(Member)

Hans C. Juvkam-Wold
(Head of Department)

August 2003

Major Subject: Petroleum Engineering

ABSTRACT

Pressure Transient Testing and Productivity Analysis for Horizontal Wells. (August 2003)

Yueming Cheng, B.S., Southwestern Petroleum Institute, China;

M.S., Graduate School, Research Institute of Petroleum Exploration and
Development (RIPED), China

Chair of Advisory Committee: Dr. W. John Lee

This work studied the productivity evaluation and well test analysis of horizontal wells. The major components of this work consist of a 3D coupled reservoir/wellbore model, a productivity evaluation, a deconvolution technique, and a nonlinear regression technique improving horizontal well test interpretation.

A 3D coupled reservoir/wellbore model was developed using the boundary element method for realistic description of the performance behavior of horizontal wells. The model is able to flexibly handle multiple types of inner and outer boundary conditions, and can accurately simulate transient tests and long-term production of horizontal wells. Thus, it can serve as a powerful tool in productivity evaluation and analysis of well tests for horizontal wells.

Uncertainty of productivity prediction was preliminarily explored. It was demonstrated that the productivity estimates can be distributed in a broad range because of the uncertainties of reservoir/well parameters.

A new deconvolution method based on a fast-Fourier-transform algorithm is presented. This new technique can denoise “noisy” pressure and rate data, and can deconvolve pressure drawdown and buildup test data distorted by wellbore storage. For cases with no rate measurements, a “blind” deconvolution method was developed to restore the pressure response free of wellbore storage distortion, and to detect the afterflow/unloading rate function using Fourier analysis of the observed pressure data. This new deconvolution method can unveil the early time behavior of a reservoir system masked by variable-wellbore-storage distortion, and thus provides a powerful tool to improve pressure transient test interpretation. The applicability of the method is demonstrated with a variety of synthetic and actual field cases for both oil and gas wells.

A practical nonlinear regression technique for analysis of horizontal well testing is presented. This technique can provide accurate and reliable estimation of well-reservoir

parameters if the downhole flow rate data are available. In the situation without flow rate measurement, reasonably reliable parameter estimation can be achieved by using the detected flow rate from blind deconvolution. It has the advantages of eliminating the need for estimation of the wellbore storage coefficient and providing reasonable estimates of effective wellbore length. This technique provides a practical tool for enhancement of horizontal well test interpretation, and its practical significance is illustrated by synthetic and actual field cases.

DEDICATION

This dissertation is dedicated with all my heart to my beloved mother, to my lovely son, and to my understanding husband.

ACKNOWLEDGMENTS

I would like to express my hearty appreciation to my graduate advisor Dr. W. John Lee for serving as Committee Chairman. His invaluable supervision, support, and encouragement made this study possible.

I would like to thank Dr. Thomas A. Blasingame, Dr. Duane A. McVay, Dr. Wayne M. Ahr, and Dr. Raycho Lazarov for serving as committee members and Dr. John Gelderd for serving as the Graduate Council Representative. I acknowledge their helpful comments and suggestions.

My sincere appreciation goes to Dr. Jerry Jensen, Dr. Peter Valko, Dr. Robert A. Wattenbarger, Dr. Hans C. Juvkam-Wold and Dr. Marria A. Barrufet for their kindness and help during the years of my graduate study.

Finally, I would like to express my appreciation to the Department of Petroleum Engineering for providing excellent research facilities and environment for this study.

TABLE OF CONTENTS

CHAPTER	Page
I	INTRODUCTION 1
	1.1 Statement of the Problem 1
	1.2 Literature Review 3
	1.2.1 Application of Boundary Element Method 3
	1.2.2 Productivity of Horizontal Wells 5
	1.2.3 Horizontal Well Testing 8
	1.2.4 Deconvolution 10
	1.3 Research Objectives 13
	1.4 Dissertation Outline 14
II	HORIZONTAL WELL MODEL 15
	2.1 Introduction 15
	2.2 Reservoir Model 17
	2.3 Boundary Element Method (BEM) 20
	2.3.1 Solution of Reservoir Model 20
	2.3.2 Solution Expansion 22
	2.3.3 Numerical Implementation of the BEM 24
	2.4 Wellbore Model 28
	2.5 Procedure of Numerical Solution 30
	2.6 Model Validation and Application 31
	2.6.1 Validation 31
	2.6.2 Applications 37
	2.7 Chapter Summary 58
III	PRODUCTIVITY OF HORIZONTAL WELLS 59
	3.1 Introduction 59
	3.2 Transient Productivity Index 60
	3.3 Pseudo-Steady-State Productivity Index 63
	3.4 Steady-State Productivity Index 64
	3.5 Well Productivity Index Uncertainty 67
	3.6 Chapter Summary 73
IV	DECONVOLUTION 74
	4.1 Introduction 74
	4.2 FFT-Based Deconvolution Method 76
	4.2.1 Theoretical Background 76
	4.2.2 Validation 79
	4.3 Deconvolution of Noisy Pressure and Rate Measurements 86

CHAPTER	Page
4.3.1	Effect of Noise on Deconvolved Pressure 86
4.3.2	New Afterflow/Unloading Rate Model 87
4.3.3	Nonlinear Regression of Afterflow Rate Function 90
4.3.4	Denoising Technique 94
4.3.5	Applications 104
4.4	Blind Deconvolution 107
4.4.1	Methodology 107
4.4.2	Applications 116
4.5	Chapter Summary 126
V	HORIZONTAL WELL TESTING 127
5.1	Introduction 127
5.2	Methodology 129
5.3	Uncertainty of Parameter Estimates 134
5.4	Applications 137
5.5	Chapter Summary 166
VI	CONCLUSIONS AND RECOMMENDATIONS 167
	NOMENCLATURE 171
	REFERENCES 175
	APPENDIX A 182
	APPENDIX B 190
	APPENDIX C 194
	VITA 197

LIST OF TABLES

TABLE	Page
2-1 Reservoir and fluid properties for case 2-1	32
2-2 Reservoir and fluid properties for case 2-2	36
2-3 Reservoir and Fluid Properties for Case 2-4	52
2-4 Reservoir and fluid properties for Case 2-6	57
2-5 Grid System for Various Schemes.....	57
3-1 Reservoir and fluid properties for case 3-1	61
3-2 Mean and 95% confidence interval of reservoir and well parameters	68
3-3 Scenarios for ten random sets of reservoir and well parameters	69
4-1 Reservoir and fluid properties for horizontal well case	84
4-2 Reservoir and fluid properties for field case 1.....	119
4-3 Reservoir and fluid properties for field case 2.....	123
5-1 Estimates and true values of well-reservoir parameters for case 5-1	138
5-2 Covariance matrix for case 5-1.....	141
5-3 Cross correlation matrix for case 5-1	142
5-4 Estimates and true values of well-reservoir parameters for case 5-2.....	144
5-5 Covariance matrix for case 5-2.....	148
5-6 Cross correlation matrix for case 5-2.....	148
5-7 Estimates and true values of well-reservoir parameters for case 5-3	149
5-8 Covariance matrix for case 5-3.....	152
5-9 Cross correlation matrix for case 5-3	152
5-10 Estimates and true values of well-reservoir parameters for case 5-4.....	155
5-11 Covariance matrix for case 5-4.....	159

TABLE	Page
5-12 Cross Correlation matrix for case 5-4	159
5-13 Reservoir and fluid properties for Case 5-5	160
5-14 Initial guesses and estimates of well-reservoir parameters for case 5-5	161
5-15 Covariance matrix for case 5-5.....	165
5-16 Cross correlation matrix for case 5-5.....	166

LIST OF FIGURES

FIGURE	Page
2-1 Schematic diagram of well-reservoir system.....	23
2-2 Illustration of elements.....	27
2-3 Validation of BEM – pressure change and derivative for case 2-1.....	33
2-4 Validation of BEM – drawdown pressure for case 2-1.....	33
2-5 Eclipse's nonuniform grid system 51*51 in horizontal plane for case 2-1.....	34
2-6 Comparison with Eclipse – pressure change and derivative for case 2-1.....	34
2-7 Comparison with Eclipse – drawdown pressure for case 2-1.....	35
2-8 Comparison of BEM with Thompson's model for case 2-2.....	36
2-9 Pressure change and derivative at heel in log-log plot for case 2-3.....	38
2-10 Pressure change and derivative at heel in semi-log plot for case 2-3.....	39
2-11 Pressure change and derivative at heel in Cartesian plot for case 2-3.....	40
2-12 Pressure change and derivative at mid-point of wellbore (log-log) for case 2-3.....	41
2-13 Pressure change and derivative at mid-point of wellbore (semi-log) for case 2-3.....	41
2-14 Pressure profile at time 0.029 hr.....	43
2-15 Pressure profile at time 3.117 hr.....	43
2-16 Pressure profile at time 40 hr.....	43
2-17 Pressure profile at time 90 hr.....	43
2-18 Flux profile at time 0.029 hr.....	44
2-19 Flux profile at time 3.117 hr.....	44
2-20 Flux profile at time 40 hr.....	44
2-21 Flux profile at time 90 hr.....	44
2-22 Flux distribution along finite conductivity horizontal wellbore for case 2-3.....	45

FIGURE	Page
2-23 Flux distribution along infinite conductivity horizontal wellbore for case 2-3.	45
2-24 Pressure derivative from uniform flux solution at equivalent points for case 2-3.	47
2-25 Deviation of uniform flux solution at equivalent points from infinite conductivity solution for case 2-3 (semilog plot).	48
2-26 Deviation of uniform flux solution at equivalent points from infinite conductivity solution for case 2-3 (Cartesian plot).	48
2-27 Average pressure of uniform-flux solution at time 0.029 hr	50
2-28 Average pressure of uniform-flux solution at time 3.117 hr	50
2-29 Average pressure of uniform-flux solution at time 40 hr	50
2-30 Average pressure of uniform-flux solution at time 90 hr	50
2-31 Difference of averaged uniform-flux and infinite-conductivity solutions for case 2-3.	51
2-32 Pressure behavior of a horizontal well producing in reservoir with constant pressure boundary at bottom (case 2-4).	53
2-33 Pressure profile along horizontal wellbore for steady-state flow (case 2-4).	53
2-34 Flux profile along horizontal wellbore for steady-state flow (case 2-4).	54
2-35 Drawdown and buildup pressure responses from various models for case 2-5.	55
2-36 Drawdown and buildup pressure responses from various models for case 2-5.	55
2-37 Pressure responses to change of flow rate for case 2-6.	58
3-1 Diagnostic plot for case 3-1.	62
3-2 PI (productivity index) for transient flow period.	62
3-3 PI (productivity index) for pseudo-steady state flow period.	63
3-4 Diagnostic plot for case 3-1 with constant pressure at the bottom of reservoir.	65
3-5 PI (productivity index) with constant pressure at the bottom of reservoir.	66
3-6 Comparison of PI (productivity index) of pseudo-steady-state flow with steady- state flow (bottom constant pressure boundary).	66

FIGURE	Page
3-7 Comparison of PI (productivity index) of pseudo-steady-state flow with steady-state flow (lateral side constant pressure boundary).....	67
3-8 Sampling of reservoir and well parameters.....	70
3-9 Uncertainty of PI (productivity index) in transient period.....	71
3-10 Comparison of average PI with true PI for transient period.....	71
3-11 Uncertainty of PI (productivity index) in pseudo-steady-state period.....	72
3-12 PI (productivity index) in pseudo-steady-state period.....	72
4-1 Unloading rate differential.....	81
4-2 Deconvolution for the homogeneous reservoir.....	82
4-3 Deconvolution for dual-porosity reservoir (log-log plot).....	82
4-4 Deconvolution for dual-porosity reservoir (semilog plot).....	83
4-5 Deconvolution for horizontal well (log-log plot).....	85
4-6 Deconvolution for horizontal well (semilog plot).....	85
4-7 Unloading rate with different models.....	89
4-8 Measured vs. regressed afterflow rates.....	90
4-9 Semilog plot of unloading rate differential, Δq_D	92
4-10 Semilog plot of afterflow rate differential, Δq_D	92
4-11 Regressed and measured afterflow rates.....	94
4-12 Noisy unloading rate differential.....	95
4-13 Error range of noisy dimensionless pressure response.....	95
4-14 Regression of dimensionless unloading rate differential.....	96
4-15 Deconvolution of noisy rate and noise-free pressure.....	97
4-16 Deconvolution of denoised rate and noise-free pressure.....	97
4-17 Deconvolution of denoised rate and noisy pressure.....	98

FIGURE	Page
4-18 Deconvolved pressure in frequency domain.	99
4-19 Homogeneous reservoir solution in frequency domain.....	100
4-20 Dual-porosity reservoir solution in frequency domain.	100
4-21 Vertically fractured well solution in frequency domain.....	101
4-22 Horizontal well solution in frequency domain.	101
4-23 Regression of deconvolved pressure in frequency domain.	102
4-24 Deconvolution result using denoising technique (log-log plot).....	103
4-25 Deconvolution result using denoising technique (semi-log plot).	103
4-26 Regressed and measured afterflow rate.....	105
4-27 Deconvolution result using regressed afterflow rate.....	105
4-28 Denoising deconvolved pressure.	106
4-29 Denoised pressure derivative.....	106
4-30 Measured q_D and calculated q_D using classical model (shut-in time).	109
4-31 Measured q_D and calculated q_D using classical model (time index).	109
4-32 Magnitude of measured q_D and calculated q_D in frequency domain.	110
4-33 Phase of measured q_D and calculated q_D in frequency domain.....	111
4-34 Magnitude of q_D -integral in frequency domain.	112
4-35 Magnitude of q_D in frequency domain (Oil Well No. 1, Ref. 50).....	113
4-36 Magnitude of q_D -integral in frequency domain (Oil Well No 1, Ref. 50).....	113
4-37 Magnitude of q_D in frequency domain (field case, Ref. 47).....	114
4-38 Magnitude of q_D -integral in frequency domain (field case, Ref. 47).	114
4-39 Plausible set of q_D values.....	117
4-40 Plausible set of deconvolved pressures.	117
4-41 Restored pressures using detected afterflow q_D	118

FIGURE	Page
4-42 Pre-selected lines parallel to calculated q_D integral for field case 1.	119
4-43 Plausible set of afterflow rates, q_D for field case 1.	120
4-44 Plausible set of deconvolved pressures for field case 1.	120
4-45 Energy is minimum with step size of 0.12 for field case 1.	121
4-46 Detected afterflow rate for field case 1.	121
4-47 Restored pressure using detected q_D for deconvolution for field case 1.	122
4-48 Denoising restored pressure for field case 1.	122
4-49 Energy is minimum with step size of 0.10 for field case 2.	124
4-50 Detected dimensionless afterflow rate for field case 2.	124
4-51 Restored pressure using detected q_D for deconvolution for field case 2.	125
4-52 Restored pressure and derivative vs. equivalent time for field case 2.	125
5-1 Parameter estimates with iteration for case 5-1.	139
5-2 Root-mean-square error with iteration for case 5-1.	140
5-3 Observed pressure response matched with parameter estimates at the tenth iteration for case 5-1.	141
5-4 Energy is minimum with step size of 0.0 for case 5-2.	143
5-5 Detected unloading rate using blind deconvolution for case 5-2.	143
5-6 Error of detected unloading rate using blind deconvolution for case 5-2.	144
5-7 Parameter estimates with iteration for case 5-2.	146
5-8 Root-mean-square error with iteration for case 5-2.	147
5-9 Observed pressure response matched with parameter estimates at the fourth iteration for case 5-2.	147
5-10 Parameter estimates with iteration for case 5-3.	150
5-11 Root-mean-square error with iteration for case 5-3.	151

FIGURE	Page
5-12 Measured pressure response matched with parameter estimates at the 30 th iteration for case 5-3.	151
5-13 Energy is minimum with step size of 0.22 for case 5-4.	153
5-14 Detected unloading rate using blind deconvolution for case 5-4.....	154
5-15 Error of detected unloading rate using blind deconvolution for case 5-4.	154
5-16 Parameter estimates with iteration for case 5-4.....	157
5-17 Root-mean-square error with iteration for case 5-4.....	158
5-18 Measured pressure response matched with parameter estimates at the third iteration for case 5-4.....	158
5-19 Energy is minimum with step size of 0.06 for case 5-5.	160
5-20 Detected afterflow rate for case 5-5.....	161
5-21 Estimates of horizontal and vertical permeabilities with iteration for case 5-5.....	162
5-22 Estimates of well vertical position and skin factor with iteration for case 5-5.....	163
5-23 Estimates of effective well length with iteration for case 5-5.	163
5-24 Root-mean-square error with iteration for case 5-5.....	164
5-25 Measured pressure response matched with parameter estimates at the 30 th iteration for case 5-5.	164
5-26 Wellbore storage coefficient and detected afterflow rate for case 5-5.....	165

CHAPTER I

INTRODUCTION

Horizontal wells have been widely applied to increase well productivities. Reliable estimation of productivity is the key for design and management of horizontal wells. However, productivity evaluation in horizontal wells usually involves large uncertainties. It is a common practice to use transient well testing to determine reservoir/well parameters and estimate productivity. But, as well recognized, analysis of well tests in horizontal well is much more difficult than that in vertical wells. This chapter states the issues associated with productivity evaluation and well testing analysis in horizontal wells, reviews the historic development of related techniques, presents the objectives of this research, and outlines the structure of the dissertation.

1.1 Statement of the Problem

Today, horizontal wells have become a commonly applied completion technology in the petroleum industry. With a large reservoir contact area, horizontal wells can greatly improve well productivity and effectively handle problems with water and gas coning. It is most advantageous to drill horizontal wells in thin reservoirs and tight reservoirs with vertical fractures. However, it is more expensive to drill and complete a horizontal well than a vertical well. For optimal design and management of horizontal wells, it is essential to reliably estimate their productivities.

A horizontal well has quite different flow geometry (3D) from that of a vertical well (1D symmetrical radial flow). The performance of a horizontal well can be strongly influenced by the partial penetration and the anisotropy of horizontal to vertical permeability. Thus, modeling of a horizontal well is much more complex than modeling a vertical well. Available analytical models usually contain a number of simplifying assumptions. Although some theoretically rigorous semi-analytic models have been developed, they are often very complicated and lack flexibility in dealing with multiple types of boundary conditions. On the other hand, many factors, such as horizontal permeability, vertical permeability, effective well length etc., can

This dissertation follows the style and format of the *SPE Reservoir Evaluation and Engineering*.

affect the behavior of a horizontal well. These factors are the basic information needed to model a horizontal well. However, this information usually suffers from incompleteness and large errors. As a result, our estimation or evaluation of productivity in a horizontal well is more difficult, and subject to large uncertainties.

For horizontal wells, transient well testing is commonly used to determine reservoir parameters and to estimate well productivity. One of the challenges is the 3D nature of flow geometry in horizontal wells. The radial flow symmetry usually present in a vertical well no longer exists; instead, several flow regimes may occur in horizontal well tests. However, these flow regimes generally cannot be defined well based on the test data. Moreover, many factors, such as vertical permeability, effective well length etc., can affect the transient pressure behavior in a horizontal well test, but basically we have very little information about these factors. They have to be treated as unknowns in horizontal well test analysis. Consequently, conventional techniques, such as graphical and type-curve approaches are usually not effective for horizontal well test analysis.

Another big challenge for horizontal well test analysis is that wellbore storage effects are much more significant and last longer in horizontal wells than in vertical wells. Wellbore storage effects are so considerable in horizontal-well testing that the early-time radial flow and the following intermediate-time linear flow are often masked. Furthermore, unlike vertical well cases, horizontal-well transient analysis cannot restore the information destroyed by wellbore storage by relying on the pressure response data after wellbore storage effects disappear. To remove wellbore storage effects, we have developed deconvolution techniques to convert the measured pressure and rate data into the constant-rate pressure response of the reservoir, which is free of wellbore storage distortion. However, existing deconvolution techniques have had limited applications. One reason is that they suffer from instability problems because small errors in the data can cause large uncertainties in the deconvolved solution. Furthermore, they require simultaneous measurements of both pressure and downhole flow rate. Downhole flow rate measurements are not always available. Existing deconvolution techniques are, in general, not suitable for applications without rate measurement.

In horizontal well test analysis, we applied nonlinear regression techniques to estimate reservoir and well parameters. In cases without rate measurements, existing nonlinear regression techniques consider wellbore storage effects through the Laplace-domain solution, and the wellbore storage coefficient is viewed as a constant. However, this is often not the case in

horizontal-well transient testing. The phenomenon of changing wellbore storage is common and serious in horizontal well tests. Using a constant wellbore storage coefficient to represent the actual wellbore storage effects is often inadequate and results in erroneous estimation of parameters.

1.2 Literature Review

This section reviews the historic development of techniques related to productivity evaluation and well-test analysis for horizontal wells from four aspects: the boundary element method, productivity, pressure transient testing, and deconvolution.

1.2.1 Application of Boundary Element Method

Using source and Green's functions to solve unsteady-state flow problems in reservoir has become common since Gringarten and Ramey¹ introduced them into petroleum engineering in 1973. This method, called the source/Green's function method, can rigorously express the solution of the second order partial differential equation governing fluid flow in porous media, together with the prescribed boundary conditions. The basic principle of this method is to find the Green's function of the partial differential equation under the prescribed boundary conditions, and then the solution for such a boundary value problem can be easily expressed in terms of an integral equation based on the Green's function obtained. In reservoir engineering, this method is particularly convenient and widely applied. Under the initial condition of uniform pressure field and outer boundary conditions of constant pressure or no-flow, there is only one term (the integral term of the wellbore domain) involved in the expression of the solution if we evaluate pressure drop instead of pressure. Since no discretization in the reservoir domain is required, this method is favorable for solving problems with complex 3D-flow geometries. Therefore, for horizontal wells, this method has been extensively used to develop models for reservoir performance evaluation because of the complexity of horizontal well system resulting from the intensive interaction among reservoir anisotropy, boundary, well length and well location.

To handle 3D-flow problems of a horizontal well, the most common procedure in the petroleum literature is to use the Newman product of three 1D source functions that express the

instantaneous source solution of the partial differential equation with its boundary conditions. Then the pressure behavior at an arbitrary point in the reservoir and at an arbitrary time can be obtained by integrating the Newman product with respect to time. For example, Clonts and Ramey² used source functions with a slab source and a plane source in an infinite reservoir (in horizontal x and y directions) respectively, and with a plane source in the z -direction slab reservoir (closed boundary at top and bottom). That is, they obtained a linear-source solution in an infinite reservoir with no-flow boundaries at the top and bottom, and infinite-acting boundaries at the lateral sides. Babu and Odeh³⁻⁴ obtained a point source function using the same plane sources in all three directions (x , y and z), in a closed-boundary slab reservoir, and then integrated the point source function along the wellbore length to represent the instantaneous linear-source solution. This means that a linear-source solution is obtained in a rectangular parallelepiped reservoir with no-flow boundaries at all boundaries.

The source function method is not flexible enough to handle boundary conditions which are different from those of the source functions and it is not able to deal with arbitrary boundary-shaped reservoirs. Clonts and Ramey² obtained short- and long-time transient pressure approximations through simplification of the three individual source functions in different time periods, but these approximations are applicable only to the transient pressure analysis in reservoirs with impermeable top- and bottom-boundaries. Babu and Odeh³⁻⁴ developed closed expressions for transient pressure response, and a general model for pseudo-steady-state flow. The models presented by Babu and Odeh³⁻⁴ are suitable only for closed box-shaped reservoirs. The source functions have very complex forms, and contain infinite series. Even though we can immediately write down the solution of a boundary value problem with appropriate source functions, the calculation at a point and time of interest is fairly complicated and intensive. For example, the exact solution developed by Babu and Odeh³⁻⁴ contains single, double and triple infinite series, and the simplified general solution is still complex.

A significant breakthrough in the Green's function method involves the use of the Green's function in the free space and BEM to develop the solutions. The free-space Green's function is the fundamental solution which satisfies the governing partial differential equation at a point source without satisfying any of the prescribed boundary conditions.⁵ Therefore, the solution, developed by the BEM using the free space Green's function, is not restricted to specific boundary conditions. At the same time, the BEM can be used efficiently and accurately to solve various boundary value problems. This method can reduce the dimension of the problem by

unity, such as from a 3D-volume integral to 2D-surface integrals, and thus only the discretization on boundaries is required. Compared with finite difference and finite element methods (“domain type” methods), the BEM has a great advantage in handling problems with complex flow and boundary geometries since there is no interior of the domain under consideration. The BEM is also superior to the Green’s function method in that it features the flexibility of being applicable to any reservoir boundary condition and to arbitrary boundary shapes in a reservoir.

In the petroleum literature, there have been many papers on the applications of the BEM in 2D-flow problems.⁶⁻¹² With the BEM, arbitrarily shaped reservoir boundaries can be easily handled. Some of these papers, even considered reservoir heterogeneity.¹¹⁻¹² The BEM was also used to solve tracer flow problems in reservoirs containing distributed thin bodies¹³ and flow problems in complex fracture systems.¹⁴⁻¹⁵ Koh and Tiab¹⁶ presented a reservoir model using the BEM to deal with horizontal-well flow problems. Their solution was developed in the Laplace domain and the solution in the time domain is obtained by numerical inversion using Stehfest’s algorithm with 8 terms.¹⁷

1.2.2 Productivity of Horizontal Wells

There are basically two categories of methods for calculation of horizontal well productivity: analytical and semi-analytical models. In earlier studies of horizontal wells, fluid flow potential theory was the foundation for developing analytical models for prediction of well productivity. In these models, the 3D flow problem of a horizontal well is approximated by two 2D problems, that is, 2D horizontal flow to a vertical fracture and 2D vertical flow to a horizontal well. It is obvious that such methodology is not rigorous and that the resulting solutions are applicable only as an initial screen and for comparison with vertical well productivity. These models estimate the productivity under steady-state flow.

Borisov¹⁸ developed one of the earliest analytical models for calculating steady-state oil production from a horizontal well. The horizontal flow was assumed from an equivalent circular drainage area toward a vertical fracture with drainage radius much larger than the vertical fracture length. Giger, Reiss, and Jourdan¹⁹ proposed a model similar to Borisov’s, but assumed an ellipsoidal drainage area. Considering the case of a large wellbore length comparable to the drainage length (parallel to the axis of the horizontal well), Giger²⁰ later presented a model with a rectangular drainage area. Joshi²¹ developed a model with elliptical flow in the horizontal plane

and radial flow in the vertical plane. The model was modified to take into account the influence of the horizontal-well eccentricity from the vertical center of reservoir and the anisotropy of horizontal to vertical permeability. Karcher, Giger, and Combe²² summarized the existing productivity-prediction models, and addressed the limiting assumptions and applicability of each model. Renard and Dupuy²³ modified the steady-state equation to include the effect of formation skin effect around the wellbore.

Later, a number of models, both analytical and semi-analytical, were developed using the source function method. The well drainage area was assumed to be a parallelepiped or infinite with no-flow or constant pressure boundaries at top, bottom and the sides. In general, the analytical models are asymptotic solutions under some appropriate simplifications and specific conditions, while the semi-analytical models are rigorous solutions of the original boundary value problem but have to be solved numerically.

In source-function-based analytical models, the basic assumptions are that (1) a horizontal well is a line source; (2) the horizontal well produces with a uniform flux along the wellbore; (3) the sides of the well drainage area are aligned with the horizontal principal permeability directions; and (4) the horizontal well is parallel to one of the horizontal principal permeability directions.

Babu and Odeh³⁻⁴ constructed a pseudo-steady-state productivity model, which takes the same form as the well-known productivity equation for a vertical well. Expressions for shape factor and partial penetration skin were derived by suitably simplifying and reducing their original solution of the boundary value problem with no-flow boundaries at top, bottom and the sides. Goode and Kuchuk²⁴ presented both steady-state and pseudo-steady-state models for horizontal-well inflow performance. They first described horizontal-well flow as a two-dimensional problem, which actually represents a fully penetrating vertical fracture with infinite conductivity; then, a geometric skin was used to account for the partial penetration in the vertical direction. Economides, Brand and Fick²⁵ presented a pseudo-steady state model that can deal with single and multiple horizontal wellbores along an arbitrary direction in the horizontal plane, using an approximate shape factor. Helmy and Watenburger,²⁶ using the numerical simulation results, proposed productivity models for constant bottomhole pressure and constant rate in a bounded reservoir. Correlations for shape factors and partial penetration skins were developed using nonlinear regression, and their applicability is restricted to the ranges of reservoir dimensions and well penetration ratio simulated.

None of models above took into account the pressure loss in the horizontal wellbore. In fact, to reduce the computational cost and to obtain an easy-to-use solution, a horizontal well was often treated as an infinite-conductivity wellbore. Although not realistic, the assumption of an infinite-conductivity wellbore is closer to reality than is a uniform-flux wellbore. However, the infinite-conductivity inner boundary condition imposes a complicated boundary value problem, and it is not feasible to derive an analytical model. Therefore, a commonly used procedure is to derive the uniform-flux solution first and then correct this solution to approximate the infinite-conductivity solution. For example, the pressure responses with an infinite-conductivity wellbore are obtained through averaging along the wellbore length the pressure responses calculated from the model with a uniform flux wellbore or to use the pressure at an equivalent point on the uniform flux wellbore. Realizing the fact that the pressure drop in a horizontal wellbore is significant under certain conditions, Dikken²⁷ first included the wellbore pressure drop into his analytical reservoir/wellbore model by assuming steady-state flow in the reservoir, and laminar or turbulent flow in the wellbore.

In general, semi-analytical models can consider the influence of a finite conductivity wellbore on horizontal-well inflow performance. The semi-analytical model directly controls the numerical integration of an instantaneous point-source solution with respect to time and wellbore length. Therefore, it is feasible to take into account the pressure drop in the wellbore at any time, for the durations of both transient flow and pseudo-steady state/steady state flow. Simultaneously, it is also easier to deal with curved or irregular trajectories of horizontal wells. A major concern in the semi-analytical models is dealing with the infinite series in the source functions. Since there are two forms of infinite series solutions (Fourier series and exponential series from the method of images), which have different convergence rates for small- and large-time values, the computations switch between the two infinite series based on a time criteria.

Thompson, Manrique, and Jelmert²⁸ used a line source solution, while Besson²⁹ and Economides, Brand and Fick²⁵ used a point source solution to develop their semi-analytical models for performance evaluation, but these models did not include the pressure drop calculation in the wellbore. In these models, no-flow boundary conditions were assumed at all boundaries of a parallelepiped reservoir. Besson²⁹ proposed a spatial transformation of wellbore and reservoir geometries and of the partial differential equation from an anisotropic medium into an equivalent isotropic medium. Spivey and Lee³⁰ systematically presented an effective method for obtaining the new solution for pressure transient responses of a horizontal well at an arbitrary

azimuth in an anisotropic reservoir. This method transforms the relevant parameters (permeability, reservoir thickness, wellbore length and radius, and vertical position of wellbore) to an equivalent isotropic system. Ozkan, Sarica, and Marc³¹ developed a model coupling steady-state or pseudo-steady-state reservoir models with a wellbore model. Since the wellbore model is nonlinear, the Newton-Raphson approach was applied to solve the resulting nonlinear set of equations. Ouyang³² presented a coupled model of the reservoir inflow with wellbore hydraulics, which is solved with a sequential approach. For the reservoir models of Ozkan-Sarica-Marc³¹ and Ouyang³², a horizontal wellbore is taken as a line source. Ding³³ used the boundary integral equation method to obtain a coupled reservoir/wellbore model. Ding's model³³ not only considered wellbore hydraulics, but also considered the wellbore as a cylindrical surface source instead of a line source.

As mentioned earlier, the semi-analytical models described above are applicable only to reservoirs having the same geometrical shape and boundary conditions as those of the source functions used to develop the model. In reality, the boundary situation is problem-dependent; however, these models can not flexibly deal with changing conditions. Using the BEM, Koh and Tiab¹⁶ developed a reservoir model which can prescribe arbitrary boundary shapes and conditions. They discretized the reservoir boundaries and wellbore surface with triangular elements. Their solution was developed in the Laplace domain and the solution in the time-domain was numerically inverted using Stehfest's algorithm.¹⁷ The frictional pressure loss in a horizontal wellbore was not considered in their model.

1.2.3 Horizontal Well Testing

In theory, up to five flow regimes could appear during horizontal-well transient flow. However, the existence of these flow regimes is closely associated with the dimensions of the reservoir drainage volume, wellbore length, and permeability anisotropy, etc. Hence, it is common that some of flow regimes are not present. Horizontal-well transient test analysis mainly includes conventional analysis techniques relying on approximate analytical models, and nonlinear regression techniques relying on semi-analytical models.

In conventional analysis techniques, each flow regime is described by an analytical expression, which indicates certain kind of linear relationship between pressure or pressure derivative versus time, such as semi-log linear or square root linear relations. These expressions

are approximations of transient pressure responses, derived from the original solution of the boundary value problem. The time duration corresponding to each expression (or flow regime) is estimated to help identify the flow regimes.

Davlau *et al.*³⁴ proposed that there are two identifiable flow regimes during transient flow, early-time radial and late-time pseudo-radial flow. Davlau *et al.*³⁴ presented the analytical solutions for pressure during these two flow regimes and the corresponding durations of the regimes for transient-test analysis. They were the first to consider wellbore storage effects in horizontal wells by coupling their model with the Cinco-Ley and Samaniego³⁵ numerical model. Based on the relative magnitude of wellbore length and reservoir thickness, Clonts and Ramey² considered two types of transient pressure behavior in a infinite reservoir, an initial radial flow followed by a transition to a pseudo-radial flow for a short drainhole and a rapidly ending initial radial flow followed by the pressure behavior of a uniform flux vertical fracture for a long drainhole. Like Davlau *et al.*³⁴, they presented analytical equations for short-time radial and long-time pseudo-radial flow and time criteria. Their solution is a solution for the uniform-flux condition. Goode and Thambynayagam³⁶ used successive Laplace and Fourier transforms to develop the solution for the original boundary value problem (a semi-infinite reservoir with no-flow boundary condition at the sides). They presented the analytical solution of transient pressure responses for four flow periods (early-time radial, intermediate-time linear, late-intermediate-time radial, and late-time linear), for drawdown and buildup, respectively. A strip source was used and then corrected to an effective wellbore radius. The above three early studies on horizontal-well testing all assumed no-flow boundaries at top and bottom of the reservoir. With a similar method to that of Davlau *et al.*³⁴ and Clonts and Ramey², Ozkan, Raghavan and Joshi,³⁷ and Ozkan³⁸ presented short- and long-time approximations for pressure transient behavior. They addressed the use of a pressure normalized (by pressure derivative) procedure in transient well-test analysis. Kuchuk *et al.*³⁹ extended the work of Goode and Thambynayagam,³⁶ and included pressure transient behavior for the constant pressure boundary condition at top or bottom of reservoir with infinite lateral boundaries. The hemi-radial flow regime was proposed. They also developed the solution in Laplace domain to consider wellbore storage effects, and used the equivalent wellbore radius to account for permeability anisotropy. Odeh and Babu's⁴⁰ transient flow equations, for drawdown and buildup, were developed in a closed parallelepiped reservoir. Besides early-radial, early linear, and late-pseudo-radial flow periods, they also presented analytical equations for the late-linear flow regime.

In the above models, the horizontal wellbore is treated as an infinite-conductivity inner boundary. As mentioned in section 1.2.2, the pressure transient response of the infinite-conductivity wellbore is obtained through averaging along wellbore length the pressure calculated from the uniform flux solution or using the result at an equivalent pressure point on the horizontal wellbore. However, Rosa's study⁴¹ showed that it could be quite dangerous for evaluating wellbore pressure for the infinite-conductivity case with a uniform flux model. Rosa developed short-time and long-time approximations for uniform flux and infinite-conductivity inner boundary conditions, respectively. The comparison indicated that the equivalent pressure point is not fixed for different well eccentricity (in vertical direction) and reservoir thickness. With a fixed equivalent point of 0.732 of wellbore length as used in some cases, an error greater than 13% in dimensionless pressure can result.

The semi-analytical models, discussed in section 1.2.2, can conveniently evaluate pressure behavior during any flow period (including transient and steady-state/pseudo-steady-state flow periods) under a prior knowledge of reservoir and wellbore parameters (such as permeability, wellbore length, drainage size, etc.). In addition, a semi-analytical model can easily overcome the inherent limitations in an analytical approach, such as wellbore alignment and configuration, uniform-flux wellbore, etc. Hence, it is advantageous to use a semi-analytical model as a forward model to perform pressure transient analysis with a nonlinear least-squares technique. Kuchuk⁴² and Horne⁴³ have made efforts to apply the nonlinear least-squares technique to estimate parameters through matching measured pressure responses with model results. In their forward models, wellbore storage effects are included, and a constant wellbore storage coefficient is used in the cases without rate measurements. However, in horizontal-well testing, changing wellbore storage phenomena are common⁴². Least-squares regression with a constant wellbore storage coefficient can cause large errors in parameter estimation. On the other hand, the analysis of well test data after the wellbore storage effects disappear cannot recover the information destroyed by wellbore storage. Therefore, it is essential in horizontal-well test analysis to remove wellbore storage effects from measured data and to expose the underlying reservoir response using deconvolution techniques.⁴⁴⁻⁴⁵

1.2.4 Deconvolution

The foundation of variable-rate well testing analysis is Duhamel's principle, which was introduced by Van Everdingen and Hurst⁴⁶ in 1949. It states that a variable-rate pressure solution is a convolution of the variable-rate and a constant-rate pressure solution. Based on Duhamel's principle, development of well testing analysis techniques can be basically categorized into convolution and deconvolution procedures.

The convolution procedure requires prior knowledge of the reservoir model so that an appropriate pressure solution can be selected and used in the convolution integral. Superposition time is usually obtained by convolving the sandface rate with logarithmic time or other appropriate pressure solutions. Estimation of reservoir parameters is based on the derived linear relationship between normalized/corrected pressure and the superposition time function^{42,47-51}. Gladfelter⁴⁷ was perhaps the first to use direct measurement of rate in buildup test analysis. He developed a linear relationship of corrected pressure versus logarithmic time. As shown by Meunier *et al.*⁵¹, Gladfelter's method actually use a superposition time function under the assumption that afterflow can be approximated by a linear function of time. Meunier *et al.* applied the logarithmic convolution time to interpret pressure buildup tests with sandface afterflow rate measurements, while Kuchuck⁴² used generalized rate convolution. Well test analysis techniques applying the convolution procedure are limited since identification of the reservoir system is not based on well-testing analysis but on prior knowledge. Convolution itself does not produce constant-rate pressure behavior.

The deconvolution procedure is an inverse problem. With this procedure, the desired constant-rate pressure response can be obtained without making any assumptions about the reservoir model and properties. In the case of no measurement error, the problem can be easily solved by a direct algorithm⁵²⁻⁵⁵. However, the direct algorithm is subject to measurement noises and is thus highly unstable. Even with a small amount of error, the direct method fails to provide interpretable results.

To reduce solution oscillation, various forms of smoothness constraints have been imposed on the solution. However, the results obtained are still questionable, and the stability and interpretability are uncertain when the level of noise increases. Coats *et al.*⁵⁶ presented a linear programming method with sign constraints on pressure response and its derivatives. Kuchuk *et al.*⁵⁷ used the constraints similar to Coats' and developed a constrained linear least-square method. This method can give a reasonable pressure solution at a low level of measurement noise, but its derivative, used for identification of reservoir system, oscillates. Baygun *et al.*⁵⁸

proposed different smoothness constraints to combine with least-squares estimation. Baygun *et al.*⁵⁸ proposed an autocorrelation constraint on the logarithmic derivative and an energy constraint on change of pressure derivative.

Another method is to perform deconvolution in Laplace domain. The deconvolution is simplified considerably by taking advantage of the fact that deconvolution because division in the Laplace domain. Kuchuk *et al.*⁵³ developed a Laplace-transform-based method, using exponential and polynomial approximations to measured rate and pressure data, respectively. Methods presented by Rouboutsos and Stewart⁵⁹ and Fair and Simmons⁶⁰ used piecewise linear approximations to rate and pressure data. All these Laplace-transform-based methods used Stehfest's algorithm¹⁷ to invert the results in Laplace domain back to real time space. It is obvious that these types of methods were greatly limited because continuous functional approximations were used to replace rate and pressure measurements and because no apparent mechanisms were used to solve the instability problem.

The Fast Fourier Transform (FFT) technique has been widely used in many branches of science and engineering. It is easy and quick to perform deconvolution using the FFT because deconvolution in the frequency domain is simply a division. The FFT algorithm deals with a set of data with each point discretely and evenly spaced in the time domain, which is appropriate for solving many engineering problems. The deconvolution procedure is sensitive to measurement noise which may be greatly amplified in the deconvolved results, but the FFT is convenient and effective for dealing with noise in the frequency domain. Therefore, the FFT is a favorable technique to remove noise components from measured data through an appropriate filter function in the frequency domain.

In the cases with no rate measurements, the classical constant-wellbore-storage model (in which afterflow rate is proportional to the derivative of downhole pressure with respect to time) have often been used to derive the afterflow rate.⁴⁶ However, the assumption of constant wellbore storage cannot be justified in most practical situations. Fair's study⁶¹⁻⁶² indicated that the wellbore-storage coefficient is not constant due to various wellbore effects, such as fluid compressibility, phase redistribution and momentum effects. The classical model cannot provide a reliable description of afterflow rate. In this situation, conventional deconvolution cannot be applied and we need to use blind deconvolution.

Blind deconvolution is a technique to deconvolve the measured signal without knowing the convolved kernel. Although blind deconvolution has been a very active research area in many

fields, such as signal processing and imaging processing⁶³⁻⁶⁶ over the last two decades, it has remained relatively unexplored in well testing. In blind deconvolution, it is required to simultaneously identify the convolution kernel and reconstruct the convolved signal response.

Most blind deconvolution approaches have been iterative in nature.⁶³⁻⁶⁴ In image deblurring, the iterative processes deblur the image at the n th stage using the psf (point spread function) calculated at the preceding stage. This deblurred image is then used to calculate a new psf. One problem with iterative approaches is the unexpected transformation of noise amplification at any stage to the next stage. Iterative blind deconvolution is generally ill-behaved because of the unlimited space of admissible solutions. As a result, the iterative processes may develop stagnation points or diverge. For successful blind deconvolution, it is very important and necessary to restrict the class of admissible solutions.

1.3 Research Objectives

The main objectives of this study are as follows:

1. To develop a general 3D reservoir model for horizontal wells. This model is able to deal with arbitrary well configurations, such as curvilinear trajectories, and with any kind of reservoir boundary conditions, such as infinite reservoirs and bounded reservoirs with no-flow boundaries or constant pressure boundaries.
2. To develop a coupled reservoir/wellbore model for analysis of the productivity of horizontal wells, and thus effectively consider the pressure drop along the horizontal wellbore.
3. To develop an approach to quantify the uncertainties in productivity index due to the uncertainties in reservoir/well parameters, and to estimate the productivity index uncertainties from nonlinear regression of well test data.
4. To develop a stable FFT-based deconvolution technique to solve the problems in pressure transient well testing resulting from wellbore storage. This technique is able to efficiently suppress noise in measurements of pressure and afterflow/unloading rate.

5. To develop a blind deconvolution technique to deal with the problems of changing wellbore storage in the situation of no flow rate measurement. The technique can effectively detect the afterflow/unloading rate and restore the pressure response free of wellbore storage distortion.
6. To develop a nonlinear regression technique for horizontal-well test analysis. Combined with application of blind deconvolution, this technique will be able to improve parameter estimation based on the automatic match of a set of observed pressure data.

1.4 Dissertation Outline

Chapter II presents a coupled reservoir/wellbore model. The boundary element method, used for development of the 3D reservoir model, is discussed. The numerical implementation procedures of reservoir and wellbore models are included in this chapter. The applicability of the coupled reservoir/wellbore model is demonstrated by synthetic cases.

Chapter III focuses on applying the above model to perform the productivity analysis of horizontal wells for various flow regimes, such as transient flow, pseudo-steady state and steady state flow. The uncertainty of productivity is assessed based on the uncertainties of parameters.

Chapter IV presents a stable Fast Fourier Transform (FFT) based deconvolution technique. The major results include: a new afterflow/unloading model; an effective denoising technique for deconvolved pressure and rate data; and, for the case of no rate measurement, a blind deconvolution technique for effective detection of afterflow rate function and restoration of the reservoir pressure using Fourier analysis.

Chapter V presents a non-linear least-squares regression technique that is combined with blind deconvolution to improve horizontal well testing interpretations. From the regression results, the uncertainties of the estimates and correlations between them are also quantified.

Chapter VI summarizes this work, and presents the conclusions. Further research areas are also discussed.

CHAPTER II

HORIZONTAL WELL MODEL

Reliable productivity evaluation and reasonable well-test analysis depend on the model developed and applied. By model, we mean the solution of the governing partial differential equation prescribing the fluid flow in porous media, together with boundary and initial conditions. With the model solution, well productivity can be evaluated for various flow periods, but in general we focus mainly on the productivity during stabilized flow, such as pseudo-steady state and steady state flow. Transient well-test analysis uses the solution in the transient flow period for well-test interpretation and reservoir parameter estimation.

In this chapter, we first present the set of equations describing the initial- and boundary-value problem of fluid flow in porous media. Then, the boundary element method (BEM) for the governing partial differential equation and the exact solution of the integral equation are derived. The numerical implementation of the BEM is achieved through discretization of the boundaries with bilinear elements over space and constant elements over time. A wellbore hydraulics model is developed to consider the influence of frictional pressure loss in the horizontal wellbore on the bottomhole pressure behavior. It is coupled with the reservoir model and solved by a sequential method. Finally, this coupled reservoir/ wellbore model is validated by synthetic cases and its power is demonstrated by various applications.

2.1 Introduction

In this chapter, we will develop the BEM for the solution of unsteady-state fluid flow problem in a 3D domain. The set of governing partial differential equations, which describe the boundary- and initial-value problem of fluid flow in porous media, is same as the heat-conduction problem. Therefore, it is often convenient to introduce the necessary background starting with heat conduction theory.

The general form for a 3D unsteady-state heat-conduction problem is:

$$\frac{\partial u}{\partial t} - \alpha \nabla^2 u = f(R, t) \quad R \in \Omega, \quad t > 0 \quad (2-1)$$

where ∇^2 stands for the Laplace operator, u is temperature, $f(R, t)$ denotes a source term, R is the source point located at $R(x, y, z)$ in the 3D domain Ω , and α is the thermal diffusivity. Eq. 2-1 is the governing equation of heat conduction theory. The solution is found in the 3D domain Ω with boundaries S_i and is required to satisfy the following initial and boundary conditions. The initial condition is

$$u(R, t) = u_i(R) \quad R \in \Omega, \quad t = 0 \quad (2-2)$$

The potential boundary conditions on the S_i may be described generally in a single formulation as

$$a_i \frac{\partial u}{\partial n_i} + b_i u = f_i(R, t) \quad \text{on } S_i, \quad t > 0 \quad (2-3)$$

When $a_i = 0$, Eq. 2-3 becomes boundary condition of the first kind; when $b_i = 0$, Eq. 2-3 becomes boundary condition of the second kind. When both a_i and b_i are not zero, Eq. 2-3 is called a boundary condition of the third kind. The boundary conditions are described by the function u on S_i or its derivative in the direction normal to S_i .

For the initial- and boundary-value problem represented above, the boundary integral equation method is often used to develop the expression of solution through finding the Green's function of the equation with given boundary conditions. However, a significant advance is using the Green's function in free space to develop the solution. The Green's function in the free space is the fundamental solution which satisfies the governing equation with a point source without satisfying any prescribed boundary conditions. That is, the solution satisfying the following equation, Eq. 2-4,

$$\frac{\partial u}{\partial t} - \alpha \nabla^2 u = \delta(R - R') \delta(t) \quad (2-4)$$

where $\delta(R - R')$ is the 3D Dirac delta function of space variables, and $\delta(t)$ is Dirac delta function of the time variable. The right-hand side of Eq. 2-4 equals zero except at the time of zero and the point R' , and tends to be infinite at the time of zero and the point R' . The form of the fundamental solution is

$$U(R - R', t) = \frac{1}{8[\pi\alpha]^{3/2}} \exp\left[-\frac{|R - R'|^2}{4\alpha t}\right] \quad (2-5)$$

Eq. 2-5 represents the temperature distribution at any point due to an instantaneous point source of unit strength released at the point R' at time zero.

With the help of the fundamental solution or the free space Green's function, the solution of the original 3D boundary value problem can be expressed with an integral equation and a 3D problem can be reduced to a 2D problem. The BEM, based on the integral equation formulation of boundary value problems, requires discretization only on the boundaries. In the following section, we will use the BEM to develop a general 3D reservoir model in the time domain.

In this chapter, for the related fundamental knowledge in reservoir engineering, we refer to *Well Testing* by W. John Lee;⁶⁷ for the derivation of the solution of the diffusivity equation, we refer to *Heat Conduction* by M.Necati Ozisik⁶⁸ and *Conduction of Heat in Solids* by H.S. Carslaw and J.G. Jaeger⁵; while for the BEM, we refer to *Boundary Elements -- Theory and Application* by J.T. Katsikadelis⁶⁹ and *Boundary element methods* by Prem K. Kytbe.⁷⁰

2.2 Reservoir Model

The governing partial differential equation for the fluid flow problem in a reservoir is derived from the continuity equation, Darcy's law, and equations of state. The basic mathematical expression developed for the unsteady-state flow of a single-phase slightly compressible fluid in an anisotropic porous media can be written as

$$\eta_{x_a} \frac{\partial^2 p}{\partial x_a^2} + \eta_{y_a} \frac{\partial^2 p}{\partial y_a^2} + \eta_{z_a} \frac{\partial^2 p}{\partial z_a^2} = \frac{\partial p}{\partial t} \quad (2-6)$$

where p is the pressure, and η_{x_a} , η_{y_a} , η_{z_a} are the diffusivities along three principal permeability direction, defined as

$$\eta_i = \frac{k_i}{\phi \mu c_i} \quad i = x_a, y_a, z_a \quad (2-7)$$

Eq. 2-6 is usually called the diffusivity equation. The assumptions for yielding this equation are: small and constant total compressibility (c_t); constant permeabilities (k_{x_a} , k_{y_a} , k_{z_a}), porosity (ϕ), and viscosity (μ); negligible pressure gradient squared and gravity effect.⁶⁷

Using appropriate coordinate transformation, we can reduce the problem, Eq. 2-6, in an anisotropic reservoir system to a corresponding problem in an isotropic system; i.e.,

$$\frac{\partial^2 p}{\partial x^2} + \frac{\partial^2 p}{\partial y^2} + \frac{\partial^2 p}{\partial z^2} = \frac{1}{\eta} \frac{\partial p}{\partial t} \quad (2-8)$$

where

$$\eta = \frac{k}{\phi \mu c_i} \quad (2-9)$$

$$k = \sqrt[3]{k_{x_a} k_{y_a} k_{z_a}} \quad (2-10)$$

When there is a point source/sink $q_v(x, y, z, t)$ in the reservoir, Eq. 2-8 can be rewritten as

$$\frac{\partial^2 p}{\partial x^2} + \frac{\partial^2 p}{\partial y^2} + \frac{\partial^2 p}{\partial z^2} + \frac{\mu}{k} q_v(x, y, z, t) = \frac{1}{\eta} \frac{\partial p}{\partial t} \quad (2-11a)$$

Or, in the form of Laplace operator,

$$\nabla^2 p(R, t) + \frac{\mu}{k} q_v(R, t) = \frac{1}{\eta} \frac{\partial p(R, t)}{\partial t} \quad (2-11b)$$

where $q_v(R, t)$ is flow rate per unit volume at the point source/sink. R represents an arbitrary point in the domain and p is a function of the location and time.

In reservoir engineering, we generally assume that reservoir is at uniform pressure p_i before production. So, the initial condition is

$$p(R, t) = p_i \quad R \in \Omega, \quad t = 0 \quad (2-12)$$

The boundary conditions involved can be classified as follows:

For outer boundaries:

1. Constant pressure boundary condition (Dirichlet boundary)

$$p(R, t) = p_i \quad \text{on } S_i, \quad t > 0 \quad (2-13)$$

2. No-flow boundary condition (Neumann boundary)

$$\frac{\partial p}{\partial n_i} = 0 \quad \text{on } S_i, \quad t > 0 \quad (2-14)$$

3. Infinite reservoir

$$p(R, t) = p_i \quad R \rightarrow \infty \quad (2-15)$$

For practical problems, boundary conditions may be a combination of three types of boundary conditions discussed above.

For the inner boundary:

1. Constant pressure boundary condition

$$p(R,t) = p_c \quad R \text{ on wellbore, } t > 0 \quad (2-16)$$

where p_c is a specified pressure.

2. Constant flow rate boundary condition

$$q_t = \frac{k_a}{B\mu} \int \frac{\partial p}{\partial n_i} ds = \text{const} \quad R \text{ on wellbore, } t > 0 \quad (2-17)$$

where k_a is the geometric average permeability in the plane normal to the direction of wellbore, B is the formation volume factor, and q_t is the total flow rate from the well.

For convenience in solving the problem, we often express the equation system and solution in dimensionless form. Hence, the following dimensionless variables are introduced,

$$p_D = \frac{2\pi k L_w \Delta p}{q_t B \mu} \quad (2-18a)$$

or in field units,

$$p_D = \frac{0.00708 k L_w}{q_t B \mu} (p_i - p_{wf}) \quad (2-18b)$$

$$t_D = \frac{\eta}{x_e^2} t \quad (2-19a)$$

or in field units,

$$t_D = \frac{0.0002637 k}{\phi \mu c_t x_e^2} t \quad (2-19b)$$

$$r_{wD} = \frac{r_w}{x_e} \quad (2-20)$$

$$x_D = \frac{x}{x_e} \quad (2-21)$$

$$y_D = \frac{y}{x_e} \quad (2-22)$$

$$z_D = \frac{z}{x_e} \quad (2-23)$$

$$L_{wD} = \frac{L_w}{x_e} \quad (2-24)$$

$$q_{hD} = \frac{q_h}{q_t / L_w} \quad (2-25)$$

where L_w is the wellbore length, x_e is the length of drainage volume, q_h is the flux (flow rate per unit length of wellbore), r_w is wellbore radius, q_t is total flow rate, and (x, y, z) is the location coordinates of a point in the 3D domain.

2.3 Boundary Element Method (BEM)

In this section, the BEM for the initial- and boundary-value problem presented in section 2.2 is set up and the exact solution of the problem is derived. The expansion of the solution over all boundaries and the discretizations over boundary surfaces and time are implemented.

2.3.1 Solution of Reservoir Model

To derive the solution of Eq. 2-11, we consider an auxiliary problem with the Green's function $G(R-R', t-\tau)$ in free space⁶⁸,

$$\nabla^2 G + \frac{1}{\eta} \delta(R-R') \delta(t-\tau) = \frac{1}{\eta} \frac{\partial G}{\partial t} \quad (2-26)$$

From the reciprocity relation of the Green's function, Eq. 2-26 can be expressed in terms of $G(R'-R, t-\tau)$ as

$$\nabla^2 G + \frac{1}{\eta} \delta(R'-R) \delta(\tau-t) = -\frac{1}{\eta} \frac{\partial G}{\partial \tau} \quad (2-27)$$

Rewrite Eq. 2-11 with variables R' and τ

$$\nabla^2 p(R', \tau) + \frac{\mu}{k} q_v(R', \tau) = \frac{1}{\eta} \frac{\partial p(R', \tau)}{\partial \tau} \quad (2-11)$$

Multiply Eq. 2-11 by G and Eq. 2-27 by p , and then subtract

$$G \nabla^2 p - p \nabla^2 G + \frac{\mu}{k} q_v(R', \tau) G - \frac{1}{\eta} \delta(R'-R) \delta(\tau-t) p = \frac{1}{\eta} \left(G \frac{\partial p}{\partial \tau} + p \frac{\partial G}{\partial \tau} \right) \quad (2-28)$$

Integrate with respect to R' over space domain and τ over time domain

$$\int_0^{t^+} \int_{\Omega} (G \nabla^2 p - p \nabla^2 G) d\Omega' d\tau + \frac{\mu}{k} \int_0^{t^+} \int_{\Omega} q_v(R', \tau) G d\Omega' d\tau - \frac{1}{\eta} p(R, t^+) = \frac{1}{\eta} \int_{\Omega} [Gp]_{\tau=0}^{t^+} d\Omega' \quad (2-29)$$

where Ω is a 3D domain, $t^+ = t + \varepsilon$. As discussed in the section 2.2, we assume that reservoir is a uniform pressure system at the initial time. Replace p with pressure drop Δp ($\Delta p(R, t) = p_i - p(R, t)$), and p_i is initial reservoir pressure). The original governing equation (Eq. 2-6) and subsequent resulting equations are not changed. Therefore, the term in right-hand side of Eq. 2-29 can be reduced to Eq. 2-30,

$$\int_{\Omega} [G\Delta p]_{\tau=0}^{t^+} d\Omega' = 0 \quad (2-30)$$

From Green's second identity, we can reduce the first term in left-hand side of Eq. 2-29 to Eq. 2-31,

$$\int_{\Omega} (G\nabla^2 p - p\nabla^2 G) d\Omega' = \int_S (G\nabla p - p\nabla G) dS' \quad (2-31)$$

where S ($S = \sum_i S_i$) comprises the boundary surfaces of the domain Ω . When we substitute Eq.

2-30 and Eq. 2-31 into Eq. 2-29 and let $\varepsilon \rightarrow 0$, we obtain Eq. 2-32, which is the exact solution of Eq. 2-11. Note that the Green's function does not satisfy any of the prescribed boundary conditions. Rather, the boundary conditions appear in the boundary integral.

$$\Delta p(R, t) = \frac{1}{\phi c_t} \int_0^t \int_{\Omega_1} q_v(R', \tau) G d\Omega_1' d\tau + \eta \int_0^t \int_S [G\nabla(\Delta p) - (\Delta p)\nabla G] dS' d\tau \quad (2-32)$$

where Ω_1 is the source domain. The Green's function that satisfies Eq. 2-26 is the fundamental solution and, based on Eq. 2-5, is expressed as

$$G(R - R', t - \tau) = \frac{1}{8[\pi\eta(t - \tau)]^{\frac{3}{2}}} \exp\left[-\frac{|R - R'|^2}{4\eta(t - \tau)}\right] \quad (2-33)$$

where

$$|R - R'| = \sqrt{(x - x')^2 + (y - y')^2 + (z - z')^2} \quad (2-34)$$

in Cartesian coordinates. Eq. 2-32 is the solution of the differential equation (Eq. 2-11) at any point inside the domain Ω in terms of the boundary values of p and its normal derivatives. In the cylindrical coordinate system, Eq. 2-34 can be written as.

$$|R - R'| = \sqrt{r^2 + r'^2 - 2rr'\cos(\theta - \theta')^2 + (z - z')^2} \quad (2-35)$$

where r and r' are radii, and θ and θ' are polar angles.

2.3.2 Solution Expansion

Eq. 2-32 is the solution of the governing equation. As we can see in Eq. 2-32, the pressure change includes the contribution from two parts: a well-source term and an outer boundary term. We take Δp_s to represent the pressure drop resulting from the well-source term, and Δp_b to represent that from outer boundaries. Thus, Eq. 2-32 can be expressed as

$$\Delta p(R, t) = \Delta p_s(R, t) + \Delta p_b(R, t) \quad (2-36)$$

where

$$\Delta p_s(R, t) = \frac{1}{\phi c_t} \int_0^t \int_{\Omega_1} q_v(R', \tau) G(R - R', t - \tau) d\Omega_1' d\tau \quad (2-37)$$

$$\Delta p_b(R, t) = \int_0^t \int_S [G(R - R', t - \tau) \nabla p - (\Delta p) \nabla G(R - R', t - \tau)] dS' d\tau \quad (2-38)$$

where R' in Eq. 2-37 denotes a point on the well surface, while R' in Eq. 2-38 denotes a point on the outer boundary. Note $\nabla(\Delta p) = \nabla p$. We will use different coordinate systems, cylindrical and Cartesian, for the well-source term (Eq. 2-37) and for the outer boundary term (Eq. 2-38), respectively.

When a well is considered to be cylindrical surface source, Eq. 2-37 becomes

$$\Delta p_s(R, t) = \frac{1}{2\pi\phi c_t} \int_0^t d\tau \int_0^{2\pi} d\theta \int_0^{L_w} q_h(R', \tau) G(R - R', t - \tau) dl \quad (2-39)$$

where q_h stands for the flow rate per unit length of the wellbore.

Based on the definitions of dimensionless variables listed from Eq. 2-18 to Eq. 2-25, we express Eq. 2-38 and Eq. 2-39 in the dimensionless forms as follows:

$$p_{sD}(R_D, t_D) = \int_0^{2\pi} d\theta \int_0^{L_{wD}} dl_D \int_0^{t_D} q_{hD}(R_D', \tau_D) G_D(R_D - R_D', t_D - \tau_D) d\tau_D \quad (2-40)$$

$$p_{bD}(R_D, t_D) =$$

$$\int_0^{t_D} d\tau_D \int_S \left\{ G_D(R_D, R_D', t_D - \tau_D) \nabla p_D(R_D', \tau_D) - p_D(R_D', \tau_D) \nabla G_D(R_D, R_D', t_D - \tau_D) \right\} dS_D' \quad (2-41)$$

If we assume that the reservoir geometry is a parallelepiped (Fig. 2-1), Eq. 2-41 includes integral terms for the six boundaries of the parallelepiped reservoir.

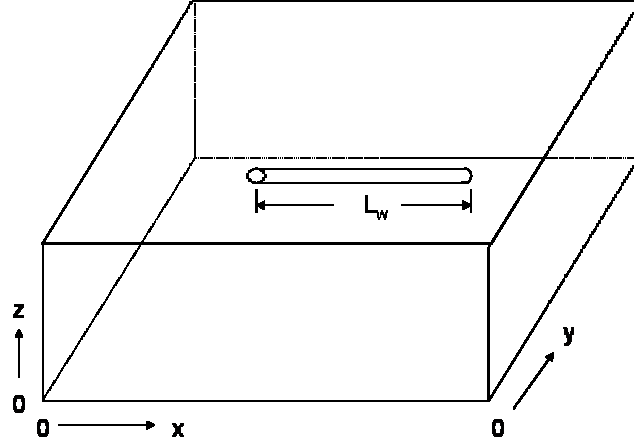


Fig. 2-1—Schematic diagram of well-reservoir system.

We denote positions of these six boundaries with $x = x_{b1}, x_{b2}$; $y = y_{b1}, y_{b2}$; $z = z_{b1}, z_{b2}$, respectively, and so the expansion of dimensionless pressure over outer boundaries can be expressed as

$$\begin{aligned}
 p_{bD}(R_D, t_D) = & \int_0^{t_D} d\tau_D \left\{ - \iint_{R \in x_{b1}} \left[G_D \frac{\partial p_D}{\partial x} - p_D \frac{\partial G_D}{\partial x} \right] dy'_D dz'_D + \iint_{R \in x_{b2}} \left[G_D \frac{\partial p_D}{\partial x} - p_D \frac{\partial G_D}{\partial x} \right] dy'_D dz'_D \right. \\
 & - \iint_{R \in y_{b1}} \left[G_D \frac{\partial p_D}{\partial y} - p_D \frac{\partial G_D}{\partial y} \right] dx'_D dz'_D + \iint_{R \in y_{b2}} \left[G_D \frac{\partial p_D}{\partial y} - p_D \frac{\partial G_D}{\partial y} \right] dx'_D dz'_D \\
 & \left. - \iint_{R \in z_{b1}} \left[G_D \frac{\partial p_D}{\partial z} - p_D \frac{\partial G_D}{\partial z} \right] dx'_D dy'_D + \iint_{R \in z_{b2}} \left[G_D \frac{\partial p_D}{\partial z} - p_D \frac{\partial G_D}{\partial z} \right] dx'_D dy'_D \right\} \quad (2-42)
 \end{aligned}$$

Therefore, dimensionless pressure at an arbitrary point in reservoir can be written as

$$p_D(R_D, t_D) = p_{sD}(R_D, t_D) + p_{bD}(R_D, t_D) \quad (2-43)$$

or

$$\begin{aligned}
\beta p_D(R_D, t_D) &= \int_0^{t_D} d\tau_D \int_0^{2\pi} d\theta \int_0^{L_{wD}} q_{hD} G_D dl_D \\
&+ \int_0^{t_D} d\tau_D \left\{ - \iint_{R \in x_{b1}} \left[G_D \frac{\partial p_D}{\partial x_D} - p_D \frac{\partial G_D}{\partial x_D} \right] dy'_D dz'_D + \iint_{R \in x_{b2}} \left[G_D \frac{\partial p_D}{\partial x_D} - p_D \frac{\partial G_D}{\partial x_D} \right] dy'_D dz'_D \right. \\
&\quad - \iint_{R \in y_{b1}} \left[G_D \frac{\partial p_D}{\partial y_D} - p_D \frac{\partial G_D}{\partial y_D} \right] dx'_D dz'_D + \iint_{R \in y_{b2}} \left[G_D \frac{\partial p_D}{\partial y_D} - p_D \frac{\partial G_D}{\partial y_D} \right] dx'_D dz'_D \\
&\quad \left. - \iint_{R \in z_{b1}} \left[G_D \frac{\partial p_D}{\partial z_D} - p_D \frac{\partial G_D}{\partial z_D} \right] dx'_D dy'_D + \iint_{R \in z_{b2}} \left[G_D \frac{\partial p_D}{\partial z_D} - p_D \frac{\partial G_D}{\partial z_D} \right] dx'_D dy'_D \right\}
\end{aligned} \tag{2-44}$$

where $\beta = 0.125$ for corner points; $\beta = 0.25$ for points on edges; $\beta = 0.5$ for points on outer boundary surfaces; and $\beta = 1$ for points inside the domain. The free-space Green's function in terms of dimensionless variables is

$$G_D(R_D - R'_D, t_D - \tau_D) = \frac{1}{8[\pi(t_D - \tau_D)]^{\frac{3}{2}}} \exp \left[- \frac{(x_D - x'_D)^2 + (y_D - y'_D)^2 + (z_D - z'_D)^2}{4(t_D - \tau_D)} \right]
\end{aligned} \tag{2-45}$$

in Cartesian coordinates, or

$$G(R_D - R'_D, t_D - \tau_D) = \frac{1}{8[\pi(t_D - \tau_D)]^{\frac{3}{2}}} \exp \left[- \frac{r_D^2 + r'_D{}^2 - 2r_D r'_D \cos(\theta - \theta') + (x_D - x'_D)^2}{4(t_D - \tau_D)} \right]
\end{aligned} \tag{2-46}$$

in cylindrical coordinates.

2.3.3 Numerical Implementation of the BEM

We use bilinear elements on the reservoir boundaries and linear elements on the horizontal well source surface for the space discretization. The pressures/pressure derivatives at nodes over the outer boundary, and the pressure and influx at nodes over the wellbore are the unknowns that we will determine numerically from the matrix system that will be formulated.

If we take C_1 to represent constant pressure boundaries ($p_D = C$), C_2 to represent impermeable boundaries ($\nabla p_D = 0$) in reservoir, then equation (2-44) in simple notation⁷⁰ can be expressed as

$$\begin{aligned} \beta p_D(R_D, t_D) &= \int_0^{t_D} d\tau_D \int_0^{2\pi} d\theta \int_0^{L_{wD}} q_{hD} G_D dl'_D \\ &+ \iint_{C_1} dS'_D \int_0^{t_D} (G_D \nabla p_D - p_D \nabla G_D) d\tau_D + \iint_{C_2} dS'_D \int_0^{t_D} (G_D \nabla p_D - p_D \nabla G_D) d\tau_D \end{aligned} \quad (2-47)$$

Let

$$Qq_D = \int_0^{t_D} d\tau_D \int_0^{2\pi} d\theta \int_0^{L_{wD}} q_{hD} G_D dl'_D \quad (2-48)$$

$$H\nabla p_D = \iint_{C_1} dS'_D \int_0^{t_D} G_D \nabla p_D d\tau_D \quad (2-49)$$

$$Ep_D = -\iint_{C_2} dS'_D \int_0^{t_D} p_D \nabla G_D d\tau_D \quad (2-50)$$

$$F = -C \iint_{C_1} dS'_D \int_0^{t_D} \nabla G_D d\tau_D \quad (2-51)$$

Note that

$$\iint_{C_2} dS'_D \int_0^{t_D} G_D \nabla p_D d\tau_D = 0$$

due to the no-flow boundary condition. Now, Eq. (2-47) may be written as

$$\beta p_D = Qq_D + H\nabla p_D + Ep_D + F \quad (2-52)$$

If $R_D \in C_1$, we have

$$Qq_D + H\nabla p_D + Ep_D = \beta p_D - F \quad (2-53)$$

where $p_D (= C)$ is constant. If $R_D \in C_2$, we have

$$-\beta p_D + Qq_D + H\nabla p_D + Ep_D = -F \quad (2-54)$$

If R_D is a point on wellbore, we have

$$-\beta p_{wD} + Qq_D + H\nabla p_D + Ep_D = -F \quad (2-55)$$

Eq. 2-53, Eq. 2-54 and Eq. 2-55 may be expressed with a single formulation as

$$Qq_D + H\nabla p_D + E^* p_D + T^* p_{wD} = F^* \quad (2-56)$$

E^* and F^* and T^* , respectively, are defined as

$$E^* p_D = Ep_D + d_1 \beta p_D \quad (2-57)$$

$$F^* = d_2 \beta p_D - F \quad (2-58)$$

$$T^* p_{wD} = d_3 \beta p_{wD} \quad (2-59)$$

where $d_1 = 0$, $d_2 = 1$ and $d_3 = 0$ for $R_D \in C_1$; $d_1 = -1$, $d_2 = 0$ and $d_3 = 0$ for $R_D \in C_2$; $d_1 = 0$, $d_2 = 0$ and $d_3 = -1$ for R_D on the wellbore.

Discretization of Eq. 2-56 over space and time gives

$$\sum_i \sum_k (Q\varphi_i \xi_k) q_{Di}^k + \sum_j \sum_k (H\psi_j \xi_k) \nabla p_{Dj}^k + \sum_j \sum_k (E^* \psi_j \xi_k) p_{Dj}^k + T^* p_{wD} = F^* \quad (2-60)$$

where φ_i denotes the basis function over the wellbore, ψ_j the basis function over the outer boundaries, and ξ_k the basis function over time. The resulting system of linear equations may be written in the form of vector as:

$$Q^{mn} q_D^n + H^{mn} \nabla p_D^n + E^{*mn} p_D^n + T^* p_{wD}^n = F^{*n} - \sum_{k=1}^{n-1} (Q^{nk} q_D^k + H^{nk} \nabla p_D^k + E^{*nk} p_D^k) \quad (2-61)$$

where the derivation of the coefficients (Q^{mn} , H^{mn} , E^{*mn} , Q^{nk} , H^{nk} , E^{*nk}) in Eq. 2-61 is provided in Appendix A. If we take N to denote the total number of nodes on outer boundaries and M to denote the number of nodes on inner boundary (i.e. wellbore), the above system of linear equations includes a total of $M+N$ equations.

Basis Function. A linear element and a bilinear rectangular element are shown in Fig. 2-2a and 2-2b, respectively.

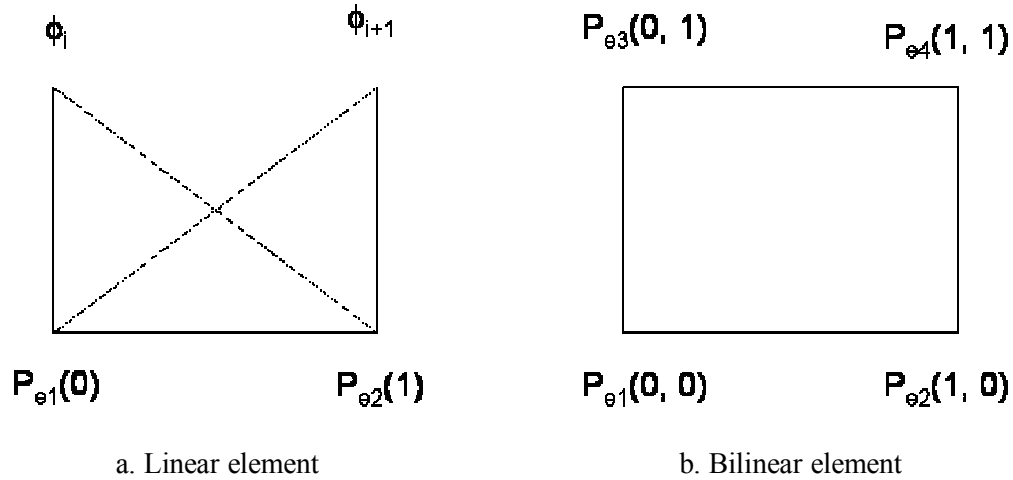


Fig. 2-2—Illustration of elements.

The basis function φ_e for a linear element on the rescaled interval $[0, 1]$ (local coordinate) is,

$$\begin{aligned}\varphi_{e1}(x) &= 1 - x \\ \varphi_{e2}(x) &= x\end{aligned}\quad (2-62)$$

Then q_D at an arbitrary point on this interval may be formulated through the two nodes of the element

$$q_D(x) = q_{D_i}\varphi_{e1}(x) + q_{D_{i+1}}\varphi_{e2}(x) \quad (2-63)$$

The base function ψ_e for a bilinear element on the rescaled area $[0, 1] \times [0, 1]$ is

$$\begin{aligned}\psi_{e1}(x, y) &= (1 - x)(1 - y) \\ \psi_{e2}(x, y) &= x(1 - y) \\ \psi_{e3}(x, y) &= y(1 - x) \\ \psi_{e4}(x, y) &= xy\end{aligned}\quad (2-64)$$

Then p_D or ∇p_D at an arbitrary point on this area may be formulated through the four nodes of the element

$$p_D(x, y) = \sum_{i=1}^4 p_{D_{ei}}\psi_{ei}(x, y) \quad (2-65)$$

For time discretization, we use constant elements. For example, for i -th time element from $t_{D_{i-1}}$ to t_{D_i} , we use the values at t_{D_i} to represent the changes within i -th time element. The basis function is defined as

$$\xi_{ei} = \begin{cases} 1 & \text{for } t_{i-1} < t \leq t_i \\ 0 & \text{otherwise} \end{cases} \quad (2-66)$$

Singular element. At end points of the horizontal wellbore, the flux solution is singular because the flux at the wellbore ends is discontinuous and unbounded, and the flux close to wellbore ends oscillates. The oscillation increases with an increase in the number of elements (i.e., finer elements). Therefore, for singular elements, the following basis functions should be used, which are obtained from the local singular solution developed by Motz⁷¹:

$$\zeta_1(x) = x^{\gamma-1} [1 - x^{2\gamma}] h_k^{\gamma-1} \quad (2-67)$$

$$\zeta_2(x) = x^{3\gamma-1} \quad (2-68)$$

Flux in singular element k may be expressed as

$$q^k(x) = K^k (k) \zeta_1(x) + q^k (k+1) \zeta_2(x) \quad (2-69)$$

When a wellbore is represented by a curved-line, corner points would appear. A corner node generally results in a singularity in the flux since the normals to two adjacent elements may be different. Similarly, cross points at the meeting edge of two boundaries can also cause singularity in the flux. The treatment of singular elements containing singular points is detailed in Appendix B using discontinuous element method.

2.4 Wellbore Model

To be able to accurately determine the productivity of horizontal wells, it is necessary to consider the pressure drop behavior in the horizontal-well wellbore and to develop a coupled reservoir/wellbore model.

The wellbore hydraulics model is based on the steady-state, single-phase flow formula.⁷²

$$\frac{dp_{wf}(l)}{dl} = C_w \frac{\rho f(l) q^2(l)}{r_w^5} \quad (2-70)$$

where $C_w = 9.236 \cdot 10^{-14}$, ρ is fluid density, $f(l)$ is the Fanning friction factor and $q(l)$ is the flow rate at l on wellbore. From Eq. 2-70, we can calculate the pressure loss per unit length of wellbore. Since the fluid enters from the reservoir along the well wall, $q(l)$ is a variable along the length of wellbore, and thus $f(l)$ is changing. For laminar flow, the definition of the friction factor, f , is

$$f = \frac{16}{N_{Re}} \quad (2-71)$$

for $N_{Re} < 2000$. For turbulent flow, we use the following explicit formulation by Zigrang and Sylvester,⁷²

$$\frac{1}{\sqrt{f}} = -4 \log \left[\frac{\varepsilon}{3.7 r_w} - \frac{5.02}{N_{Re}} \log \left(\frac{\varepsilon}{3.7 r_w} + \frac{13}{N_{Re}} \right) \right] \quad (2-72)$$

for $N_{Re} > 2000$. In Eq. 2-72, ε is the absolute roughness. N_{Re} , the Reynolds number, is defined by the following equation,

$$N_{Re} = \frac{0.0616 \rho q(l)}{\mu r_w} \quad (2-73)$$

The inflow flux from the reservoir can be included in the flow rate along the wellbore length using linear elements for the influx. The pressure drops between well segments are then calculated by Gauss Quadrature integration. For the i -th element, the frictional pressure loss is

$$\Delta p_{fi} = \frac{C_w \rho}{r_w^5} \int_{\tau_i}^{\tau_{i+1}} f(l) q^2(l) dl \quad (2-74)$$

where

$$q^i(l) = q_{i+1} + \frac{1}{2h_i} \left[(l_{i+1} - l)^2 q_{hi} + h_i^2 q_{hi+1} - (l - l_i)^2 q_{hi+1} \right] \quad (2-75)$$

where $\Delta p_{fi}(l)$ represents the frictional pressure loss over element i , $q^i(l)$ denotes the flow rate at an arbitrary point over i -th element, q_{i+1} the flow rate at the node $i+1$, q_{hi} and q_{hi+1} the inflow flux at the node i and $i+1$, respectively, and h_i is the length of i -th element.

In addition, from the continuity of flow rate, we can express the equation of total flow rate over the horizontal wellbore as follows,

$$q_t = \int_0^{L_w} q_h(l) dl = \sum_{i_e} \int_{i_e} q_h(l) dl \quad (2-76)$$

In dimensionless form,

$$L_{wD} = \sum_{i_e} \int_{i_e} q_{hD}(l_D) dl_D \quad (2-77)$$

We can obtain $M-1$ equations from Eq. 2-74 (the total number of nodes on the wellbore is M) and 1 equation from Eq. 2-77. Hence, the total number of the equations developed for the wellbore part is M .

2.5 Procedure of Numerical Solution

As mentioned before, we need to couple the reservoir model with the wellbore model to systematically investigate the effects of finite wellbore conductivity and different configurations of the well on the productivity of horizontal wells. From the results of previous sections, we develop a linear system including $N+2M$ equations, in which $N+M$ equations are from the reservoir model and M from the wellbore model. At the same time, we have $N+2M$ unknowns which include inflow flux and pressure at each of M nodes over wellbore, and pressures or influxes on N outer boundary nodes.

The reservoir model and wellbore model should be solved simultaneously to determine the unknown pressures and influxes. However, since the wellbore model is nonlinear (as shown in Eq. 2-74, the coefficients in the equation are functions of unknown influxes), the approach of Newton-Raphson is often used to solve this type of problem.^{31,33} In our study, we adopt a computationally efficient sequential approach presented by Ouyang.³² This sequential approach involves the following steps:

1. First assume infinite conductivity in the wellbore, and solve the reservoir model to obtain one wellbore pressure and the influxes at wellbore nodes, as well as the pressures/influx at reservoir boundary nodes.
2. Substitute the influx values (at wellbore nodes) from the reservoir model into the wellbore model, solve and calculate the pressures along the wellbore at the wellbore nodes.

3. Treat the calculated pressures at the wellbore nodes as knowns (except the pressure at the heel node) and substitute them back into the reservoir model. Solve the reservoir model, and obtain a new wellbore pressure at the heel node and a new set of influxes at all wellbore nodes.
4. Compare the new wellbore pressure and influx profiles with the previous ones. If the differences are greater than the specified tolerance, go back to step 2 and iterate. If the differences are below the specified tolerance, stop the iteration and go to the next time step.

In the following, we will validate the horizontal well- reservoir model developed above, and demonstrate its application.

2.6 Model Validation and Application

In previous sections, we presented the reservoir model, the wellbore model, and the numerical solution procedure. In this section, we validate the model system by comparing with analytical solutions, and we demonstrate its applicability under various reservoir and production conditions.

2.6.1 Validation

We first use the analytical cylindrical source solution for a vertical well to validate our model. Then through comparison with the commercial simulator *Eclipse* and the horizontal well model proposed by Thompson²⁸, we will further demonstrate the accuracy of our model.

Case 2-1 – Vertical Well. This case is a vertical well producing in a bounded reservoir with a no-flow boundary. The reservoir and fluid properties are given in Table 2-1.

We used the infinite conductivity wellbore to run our BEM model and compare with the analytical solution (cylindrical source solution in a bounded reservoir with a no-flow boundary). A uniform grid system of 10 by 10 by 4 was used with grid size 20 ft by 20 ft by 15 ft. The reservoir is isotropic and homogeneous. A vertical well is located at the center of the reservoir and fully penetrates the reservoir. Our model's pressure change and pressure derivative with respect to logarithmic time are shown in log-log plot (Fig. 2-3), which match with those of the

analytical solution very well. To clearly demonstrate the matching in more detail, pressure behavior over a small time interval is plotted in Fig. 2-4. The drawdown pressure is in excellent agreement with the analytical solution (Fig. 2-4).

At the same time, we also ran this case with *Eclipse*. With a uniform grid system, the simulated result from *Eclipse* is not consistent with the analytical solution. Thus, we used a refined non-uniform grid system of 51*51*1, which is shown in Fig. 2-5. With this refined grid system (an average grid size of 3.9ft*3.9 ft in horizontal plane and a minimum block size of 1.5ft *1.5 ft for the block in which the well is located), the pressure change seems to be consistent with the analytical solution in the log-log plot, but the pressure derivative is still questionable at the early times (Fig. 2-6). When we observe the detailed behavior over a small time interval, it is obvious that the drawdown pressures resulting from *Eclipse* have a noticeable deviation from the analytical solution (Fig. 2-7).

TABLE 2-1—RESERVOIR AND FLUID PROPERTIES FOR CASE 2-1

Reservoir geometry	= 200*200*60 ft ³
Porosity, ϕ	= 0.3
Viscosity, μ	= 0.69 cp
Compressibility, c_t	= 3.27×10^{-5} psi ⁻¹
Formation volume factor, B	= 1.355 RB/STB
Initial reservoir pressure, p_i	= 8171 psi
x -permeability, k_x	= 500 md
y -permeability, k_y	= 500 md
z -permeability, k_z	= 500 md
Wellbore radius, r_w	= 0.25 ft
Production rate, q	= 590 STB/D

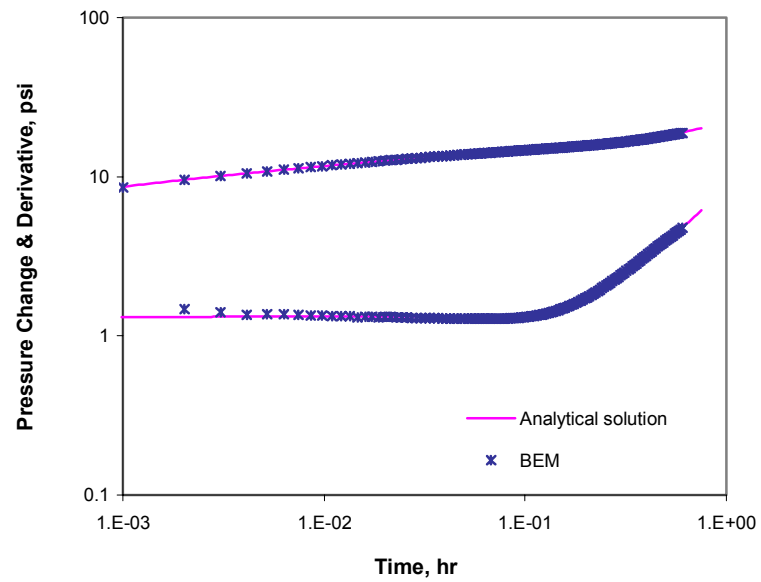


Fig. 2-3—Validation of BEM – pressure change and derivative for case 2-1.

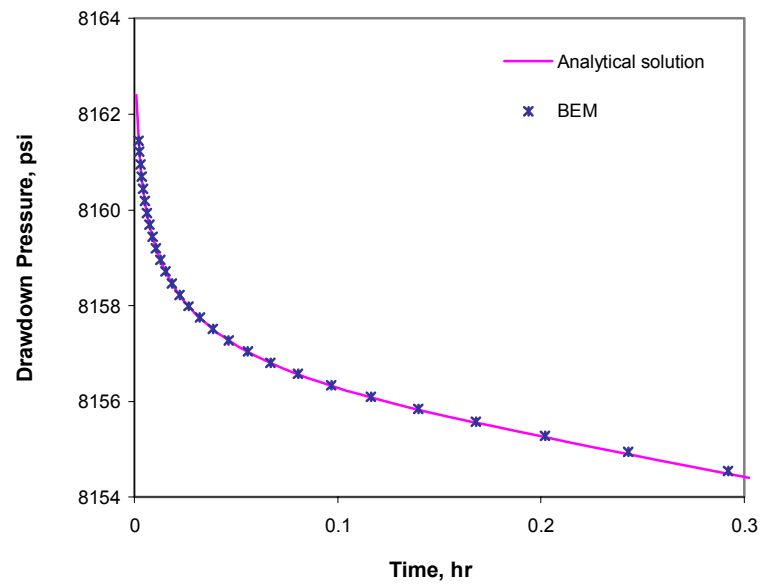


Fig. 2-4—Validation of BEM – drawdown pressure for case 2-1.

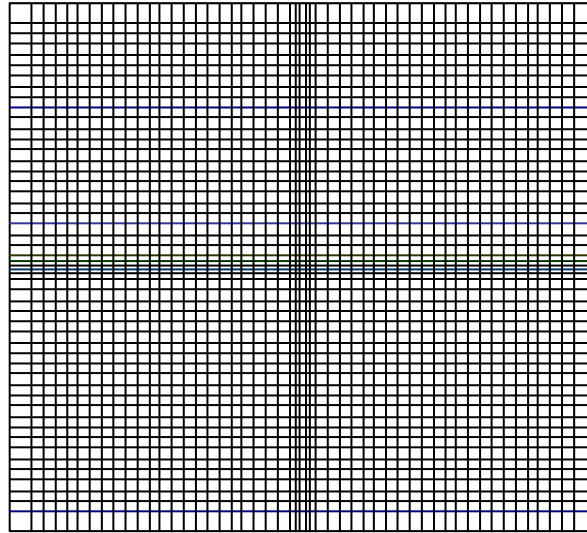


Fig. 2-5—Eclipse's nonuniform grid system 51*51 in horizontal plane for case 2-1.

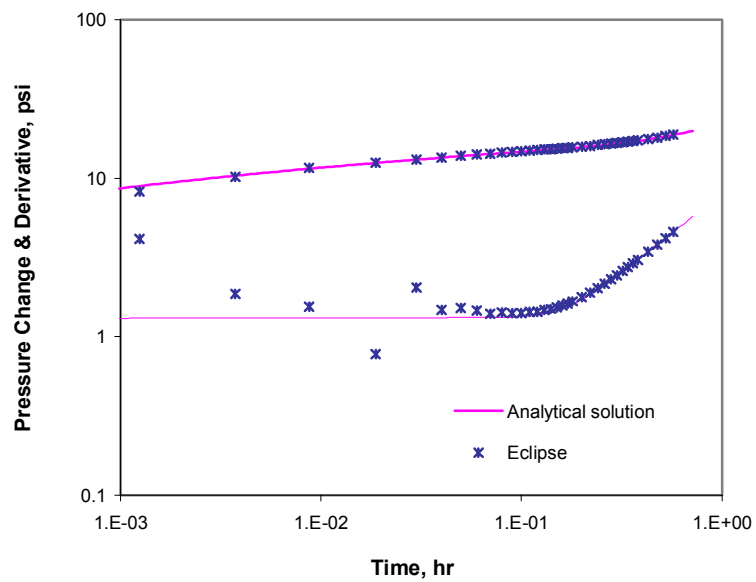


Fig. 2-6—Comparison with Eclipse – pressure change and derivative for case 2-1.

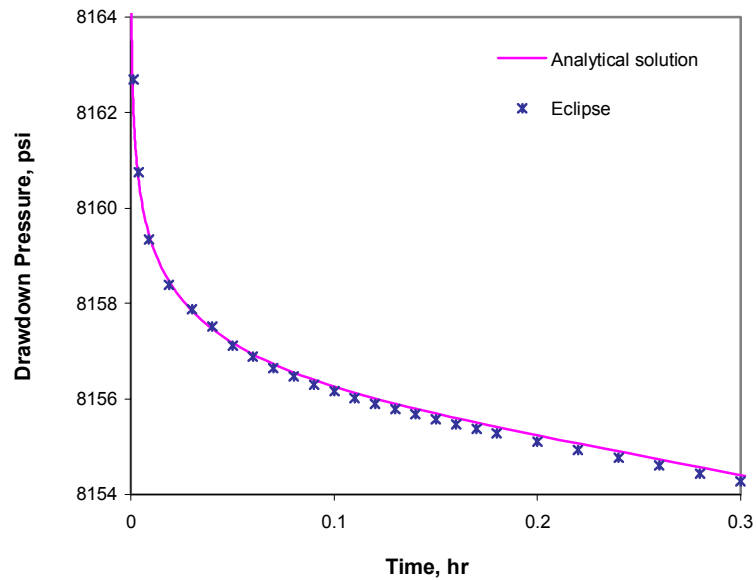


Fig. 2-7—Comparison with Eclipse – drawdown pressure for case 2-1.

Case 2-2 – Horizontal Well. This case is a horizontal well producing in a parallelepiped reservoir with no-flow boundaries. The reservoir and fluid properties are given in Table 2-2. In this case, we used the uniform flux source in our model to compare the result with the semi-analytical linear source solution from Thomson’s model with uniform flux.

A uniform grid system of 8 by 8 by 4 was used with grid size 500 ft by 500 ft by 25 ft. The reservoir is homogeneous but anisotropic. The horizontal well is centered in the box-shaped drainage area. The resulting pressure change and pressure derivative with respect to logarithmic time are shown in log-log plot (Fig. 2-8), along with the result calculated from Thomson’s model. The pressure data at the heel were used for comparison. Fig 2-8 indicates that the results from those two models agree quite well.

TABLE 2-2—RESERVOIR AND FLUID PROPERTIES FOR CASE 2-2

Reservoir geometry	= 4000*4000*100 ft ³
Porosity, ϕ	= 0.2
Viscosity, μ	= 1 cp
Compressibility, c_t	= 15×10^{-6} psi ⁻¹
Formation volume factor, B	= 1.25 RB/STB
x-permeability, k_x	= 400 md
y-permeability, k_y	= 400 md
z-permeability, k_z	= 20 md
Wellbore radius, r_w	= 0.25 ft
Effective wellbore length, L_w	= 2,500 ft, centered
Production rate, q	= 800 STB/D
Skin factor, s	= 0

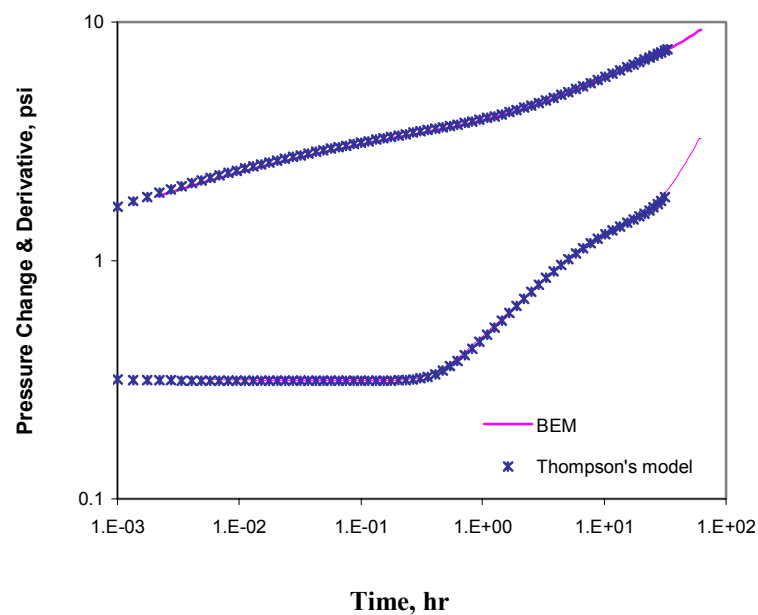


Fig. 2-8—Comparison of BEM with Thompson's model for case 2-2.

2.6.2 Applications

The reservoir-well system model developed in this study is applicable to various inner and outer boundary conditions, including no-flow boundaries and constant pressure boundaries; constant rate production, variable rate production and buildup tests; uniform flux or infinite conductivity wellbores, and finite conductivity wellbores.

Case 2-3 – Horizontal Well Behavior with Different Wellbore Conditions. Here, we consider a horizontal well with a finite conductivity wellbore. For this case, the reservoir and fluid data are same as those in Table 2-2 except for the production rate. To investigate the well performance behavior and reservoir responses in the presence of significant wellbore frictional pressure loss, we used a larger flow rate of 24,000 STB/D. The fluid density is 60 lbm/ft³ and the absolute roughness of the well wall is 2.5×10^{-5} ft. Wellbore storage effects and skin are not included. We compare the results from finite conductivity wellbore with those from uniform flux and infinite conductivity wellbore (under the same reservoir and wellbore conditions) so that the disparities under various inner boundary conditions can be clarified.

A uniform flux wellbore means that the flux is equal at every point over the entire wellbore, while an infinite conductivity wellbore means that the pressure response is equal at every point over the entire wellbore. A finite conductivity wellbore means that the frictional pressure loss over the wellbore is taken into account so that neither flux nor pressure are uniform over the wellbore. Due to the non-uniform distribution of pressure along the horizontal well length for finite conductivity and uniform flux wellbores, we selected pressure data at the heel and mid-point of the wellbore length, respectively, to investigate the features and differences in pressure responses.

Pressure Response at Heel. Fig. 2-9 is the log-log diagnostic plot of pressure change and pressure derivative with respect to logarithmic time, for the three types of wellbore conditions: finite conductivity, uniform flux and infinite conductivity. Since wellbore storage effects are not included, this diagnostic plot should be able to clearly display the flow regimes. From Fig. 2-9, there are three distinct flow regimes for each of the wellbore conditions considered. The early-time radial flow with a horizontal line and the pseudo-steady state with a unit-slope line can easily be identified from each of the three derivative curves (Fig. 2-9).

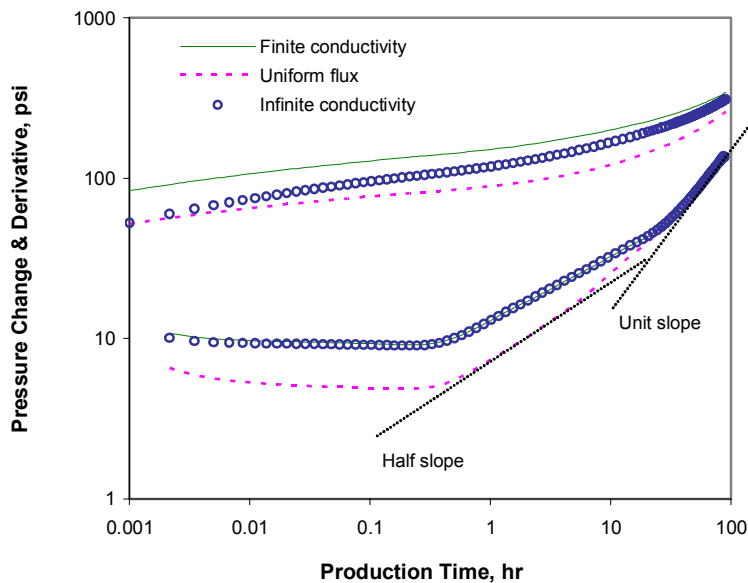


Fig. 2-9—Pressure change and derivative at heel in log-log plot for case 2-3.

However, for finite and infinite conductivity wellbores, the intermediate flow regime between early-time radial flow and pseudo-steady state is difficult to be identified because the slope of the corresponding straight line interval for the derivative is 0.4 instead of 0.5. A half-slope derivative line in conventional horizontal-well-test analysis is a signal of linear flow. In other words, early-time linear flow does not exist in the solutions for finite and infinite conductivity wellbores. This flow regime may be observed only in the uniform-flux solution (Fig. 2-9). For this case, we also note that, due to large wellbore length, the horizontal pseudo-radial flow did not appear. Early-time linear flow is followed directly by pseudo-steady state flow.

Comparing the derivative curves in Fig. 2-9, we can see that the derivative responses for finite and infinite conductivity wellbores are basically the same for this case. It seems that variation of the flux distribution profile with time did not cause significant changes in frictional pressure loss at the heel so that the pressure derivative curves are very close to each other for finite and infinite conductivity wellbores (Fig. 2-9). However, the pressure and pressure derivative curves for the uniform flux wellbore are very different from those for finite and

infinite conductivity wellbores before pseudo-steady state is reached (Figs. 2-9 and 2-10). After the flow becomes stabilized, the pressure response for the uniform wellbore flux seems to be parallel to those for finite and infinite conductivity wellbores (Fig. 2-11), and its derivatives appear to be consistent with the others (Fig. 2-9). This is because the flux distribution ceases to change for finite and infinite conductivity wellbores during the stabilized flow period. We will discuss the flux distribution further later.

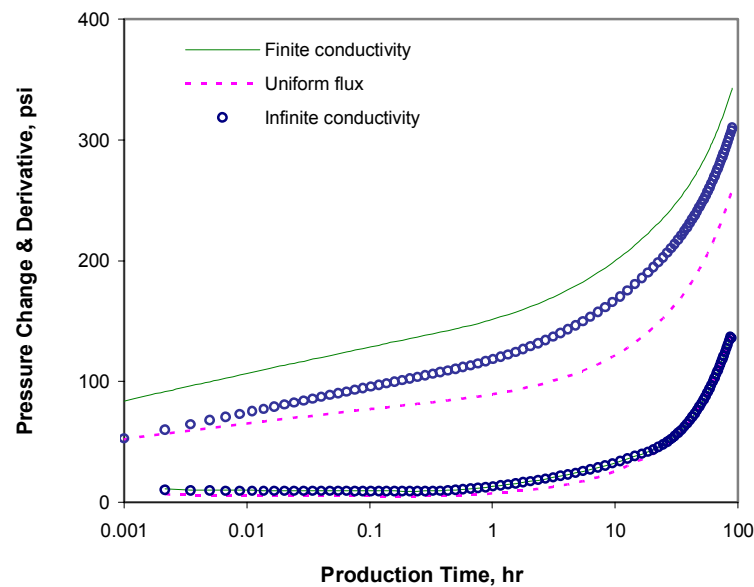


Fig. 2-10—Pressure change and derivative at heel in semi-log plot for case 2-3.

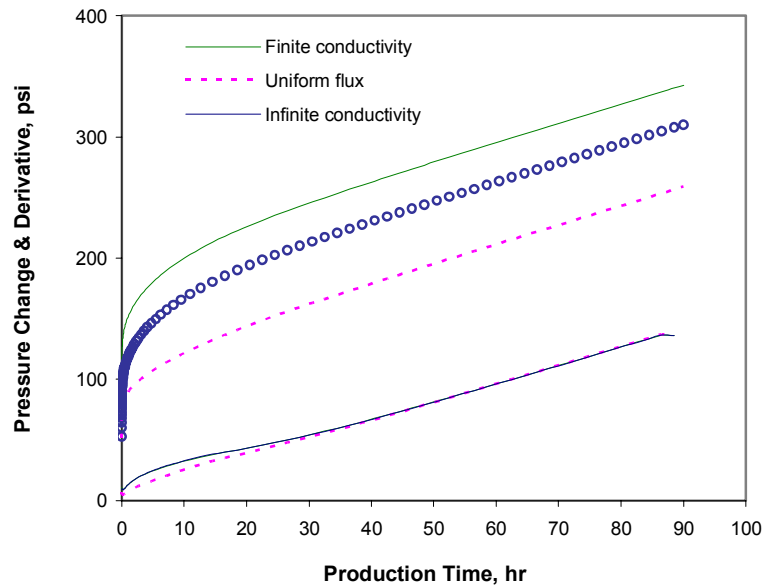


Fig. 2-11—Pressure change and derivative at heel in Cartesian plot for case 2-3.

Pressure Response at Mid-point of Horizontal Wellbore. Due to non-uniform distribution of pressure (for finite conductivity and uniform flux wellbores) along the horizontal wellbore length, we will further analyze the pressure response characteristics from a different perspective through using the pressure data at the mid-point of the horizontal wellbore.

Fig. 2-12 is the diagnostic plot of pressure and pressure derivative at the mid-point, and is different from that at the heel. The derivative curve for the uniform flux wellbore is similar to those for the finite and infinite conductivity wellbores, except for the intermediate flow period (i.e., early-time linear flow). The pressure responses at the mid-point for the three types of wellbore conditions (Fig. 2-13) are much more similar than those at the heel. Unlike the responses at the heel, pressure change and pressure derivative for uniform flux are larger than the others (Figs. 2-12 and 2-13). These differences in pressure and derivative behavior at the heel and at the mid-point are dominated by the flux distributions, and may be easily understood based on pressure and flux profiles shown later.

It is obvious that using pressure response at the mid-point is a better choice than that at the heel if one desires to use the uniform flux solution to approximate the infinite conductivity solution, such as the work by Buba and Odeh⁴ in horizontal well-test analysis. In existing literature, the approximation methods proposed by other authors are either the equivalent point

method (a fixed point where pressure from the uniform flux solution is equal to that from the infinite conductivity solution) or an averaging method (averaging pressure along wellbore). We will discuss these approximations in the following sections.

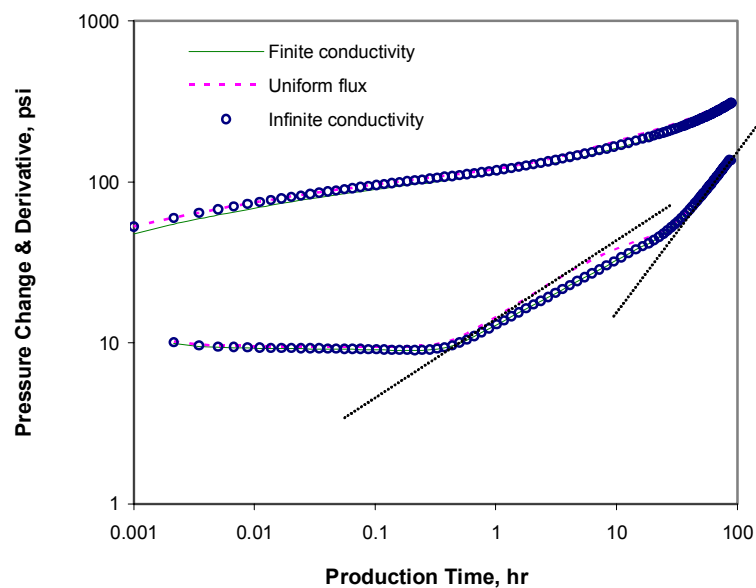


Fig. 2-12—Pressure change and derivative at mid-point of wellbore (log-log) for case 2-3.

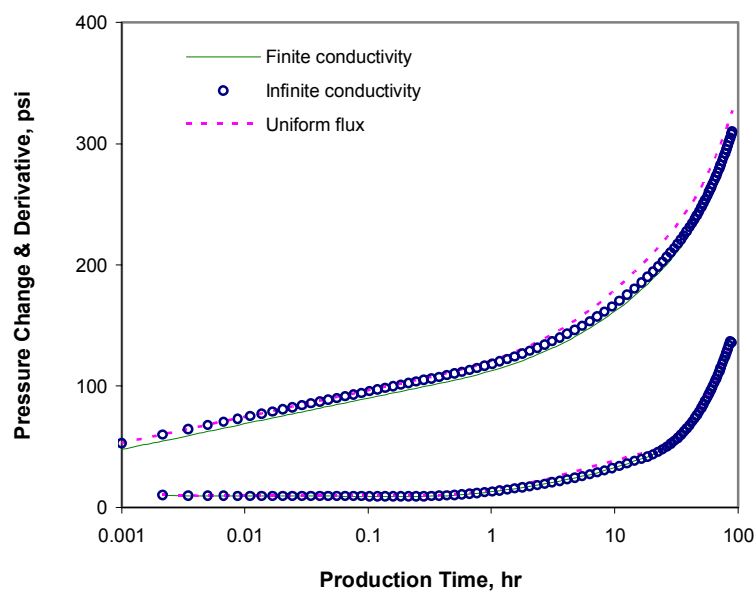


Fig. 2-13—Pressure change and derivative at mid-point of wellbore (semi-log) for case 2-3.

Pressure and Flux Distribution. Investigation of the distributions of pressure and flux along the wellbore length is important to reveal the flow mechanisms of a horizontal reservoir-well system. A uniform-flux wellbore has a pressure profile that is non-uniform and changes with time, while an infinite-conductivity wellbore has a non-uniform flux profile and a uniform pressure profile. For a finite-conductivity wellbore, both pressure and flux profiles are non-uniform and change with time.

Figs. 2-14 to 2-17 are pressure distribution profiles at different times. These figures give us a clear picture of the evolution of pressure profiles with time and differences among the three types of wellbore conditions. The pressure profiles at time 0.029 hr represent the distribution characteristics for early-time radial flow; at time 3.117 hr for intermediate (or linear) flow; and at time 40 and 90 hr for the pseudo-steady state flow. The pressure change along a finite conductivity wellbore is not always larger than that along an infinite conductivity wellbore. For example, the pressure change at the heel for a finite conductivity wellbore is larger than that for an infinite conductivity wellbore, while it is opposite at the toe. The pressure change profile for a uniform flux wellbore is symmetrical and has a maximum at the midpoint. Therefore, if the pressure change at the heel (as in Figs. 2-9 and 2-10) is taken and used for well-test analysis, the pressure response for the finite-conductivity wellbore is larger than the others; while if the pressure change at the mid-point (as in Figs. 2-12 and 2-13) is used, the pressure change for the uniform-flux wellbore is highest.

The pressure distribution is closely correlated with the distribution of flux along the wellbore. Figs. 2-18 to 2-21 display the evolution of flux profiles. For an infinite conductivity wellbore, we can see that the flux is uniform at very early times (Fig. 2-18). The shape of flux profile for the finite-conductivity wellbore is unsymmetrical and thus results in an unsymmetrical distribution in the pressure profile. The high flux values at the two ends of wellbore represent the convergence of the flowlines. The flux distributions for finite and infinite conductivity wellbores are continuously changing until a pseudo-steady state is reached. Flux distributions at different times displayed together are illustrative. Fig. 2-22 shows flux distributions at different times for a finite-conductivity wellbore and Fig. 2-23 is for an infinite-conductivity wellbore. These two figures clearly indicate that the flux distributions are almost identical after entering pseudo-steady state flow (for both finite- and infinite-conductivity wellbores); i.e., flux distribution profiles become stable after pseudo-steady state flow is reached.

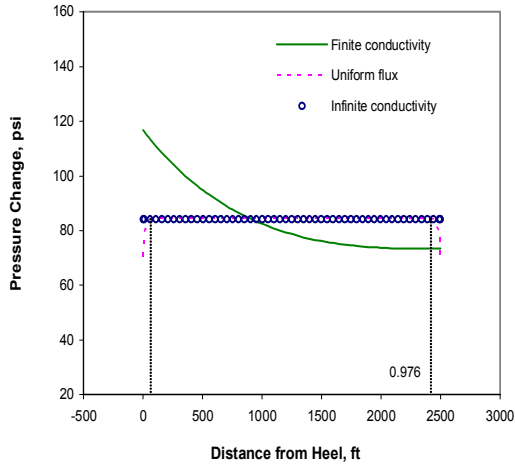


Fig. 2-14—Pressure profile at time 0.029 hr.

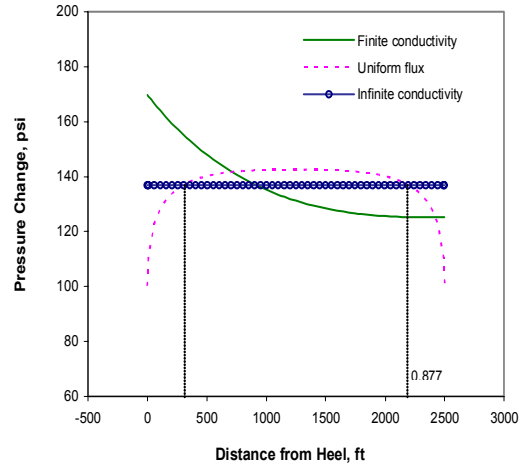


Fig. 2-15—Pressure profile at time 3.117 hr.

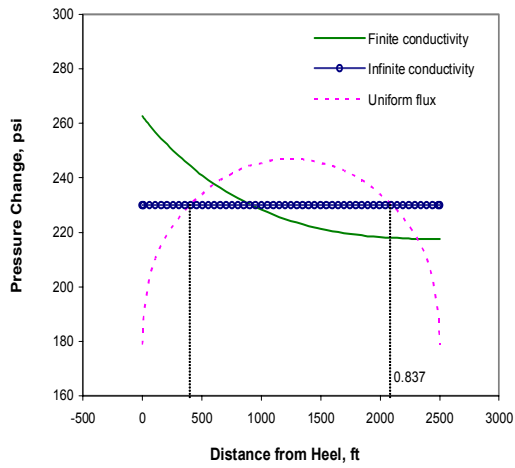


Fig. 2-16—Pressure profile at time 40 hr.

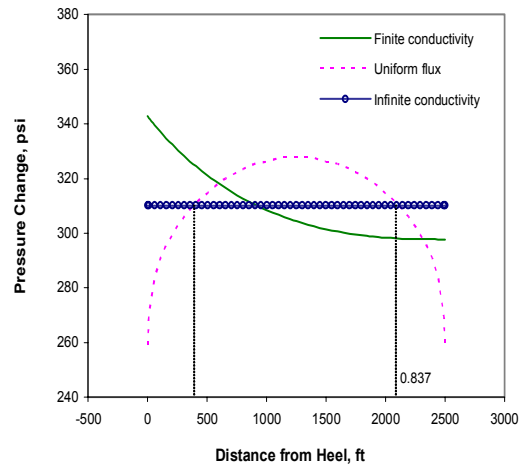


Fig. 2-17—Pressure profile at time 90 hr.

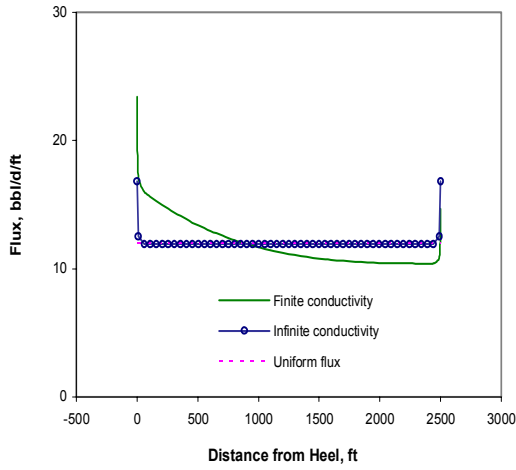


Fig. 2-18—Flux profile at time 0.029 hr.

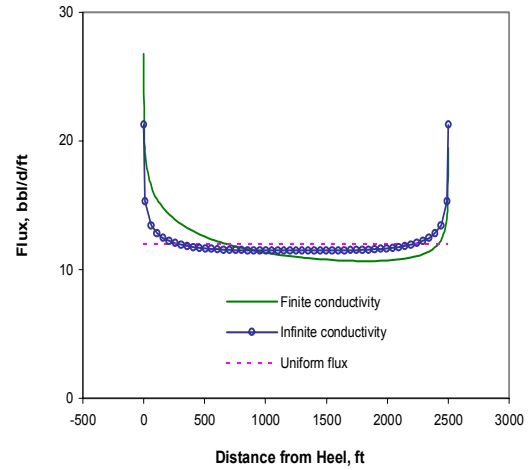


Fig. 2-19—Flux profile at time 3.117 hr.

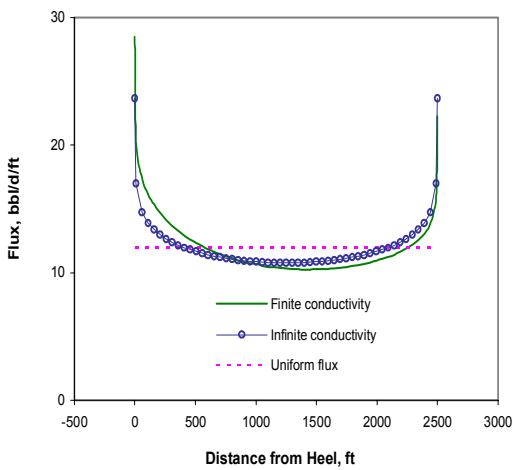


Figure 2-20—Flux profile at time 40 hr.

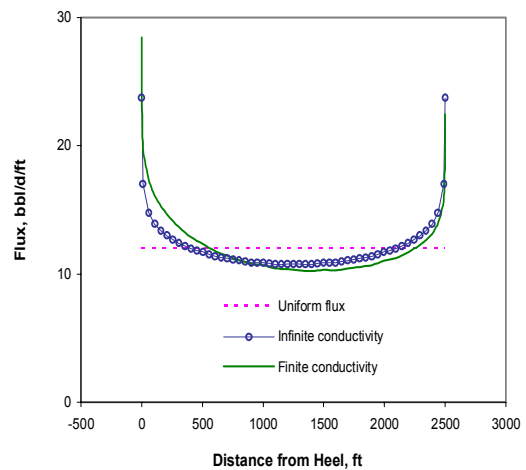


Fig. 2-21—Flux profile at time 90 hr.

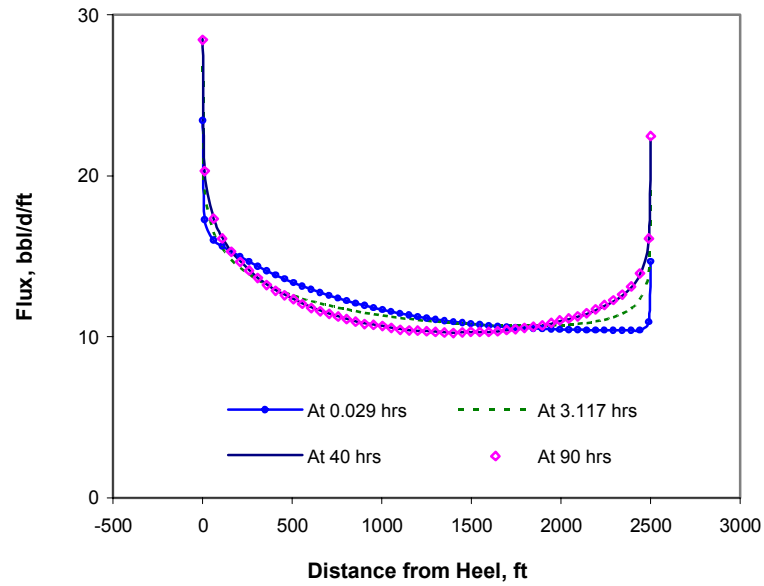


Fig. 2-22—Flux distribution along finite conductivity horizontal wellbore for case 2-3.

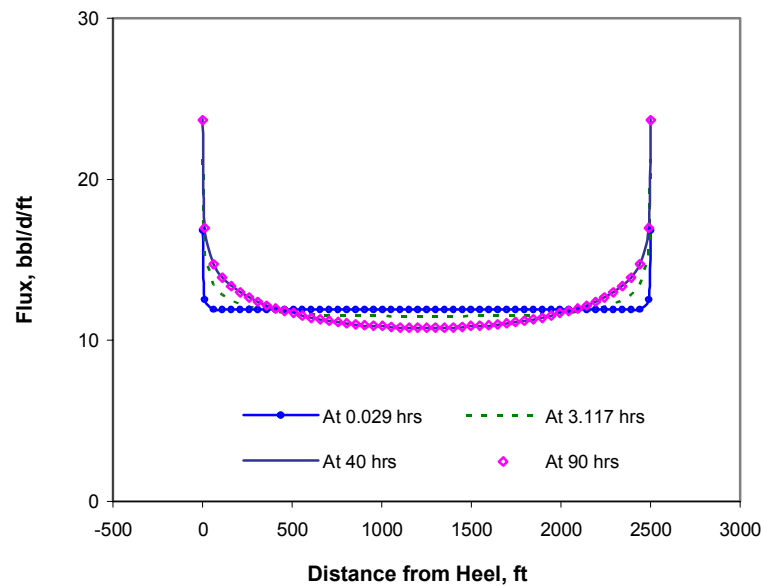


Fig. 2-23—Flux distribution along infinite conductivity horizontal wellbore for case 2-3.

Equivalent Point Method. An equivalent point is a point where pressure from the uniform-flux solution is equal to that from the infinite-conductivity solution. However, from Figs 2-14 to 2-17, we note that the equivalent point is not fixed but changes with time before stabilized flow (pseudo-steady state) is reached. The location of the equivalent point changes from 0.976 at 0.029 hr to 0.837 at 40 hrs. After flow enters the pseudo-steady state regime, the flux distributions become stable and pressure distributions display a stable change so that the relative position among the three curves (corresponding to the three types of wellbore condition) basically remains the same. Hence, the equivalent point is basically fixed at a location of 0.837 (or 0.163 due to the symmetric distribution of pressure profile) of a wellbore length. Gringarden *et al.*⁷³ proposed the equivalent pressure point at a location of 0.866 for a fully penetrated vertical fracture. By analogy with a vertically fractured well, Clonts and Ramey² suggested that evaluation of the uniform-flux solution for a horizontal well at 0.866 can also be used to represent the pressure for an infinite conductivity wellbore, while Daviau *et al.*³⁴ recommended a location of 0.85 for a horizontal well. On the other hand, Rosa⁴¹ showed that the location of the equivalent pressure point changes with the vertical position (eccentricity) of a horizontal wellbore and an improper use of the equivalent pressure point will result in an error as high as 13 % in the dimensionless pressure solution.

Fig. 2-24 illustrates logarithmic time derivatives of pressures at points 0.837, 0.85 and 0.866 of wellbore length for a uniform-flux wellbore, respectively. The infinite-conductivity pressure derivative is also plotted in this figure. As expected, behavior of derivatives at all three equivalent points are consistent with that of the infinite conductivity wellbore for early-time radial flow and stabilized flow regimes. For the intermediate flow regime, the derivative behavior at equivalent points deviates from that of the infinite conductivity wellbore. The deviations of pressures at equivalent points from those of the infinite conductivity wellbore are displayed in Figs. 2-25 and 2-26. Fig. 2-25 is a semi-log plot, which clearly shows that, for the early-time flow regime, the pressure deviations are the same at all three equivalent points and less than 2 psi. For the intermediate-time flow regime, the deviations are not monotonous but change from positive to negative at the equivalent points of 0.85 and 0.866. For the pseudo-steady state flow regime, the Cartesian plot gives a more clear demonstration (Fig. 2-26). The deviation at point of 0.837 gradually increases and the deviations at points of 0.85 and 0.866 have a trend from negative to positive. Generally speaking, the deviations are not large (absolute

value less than 4 psi) at all three equivalent points, and the result at point of 0.837 is better than the others.

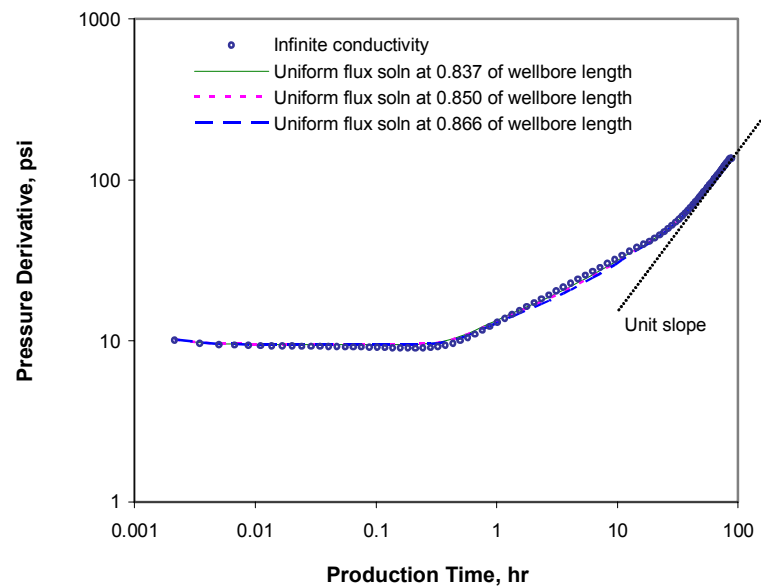


Fig. 2-24—Pressure derivative from uniform flux solution at equivalent points for case 2-3.

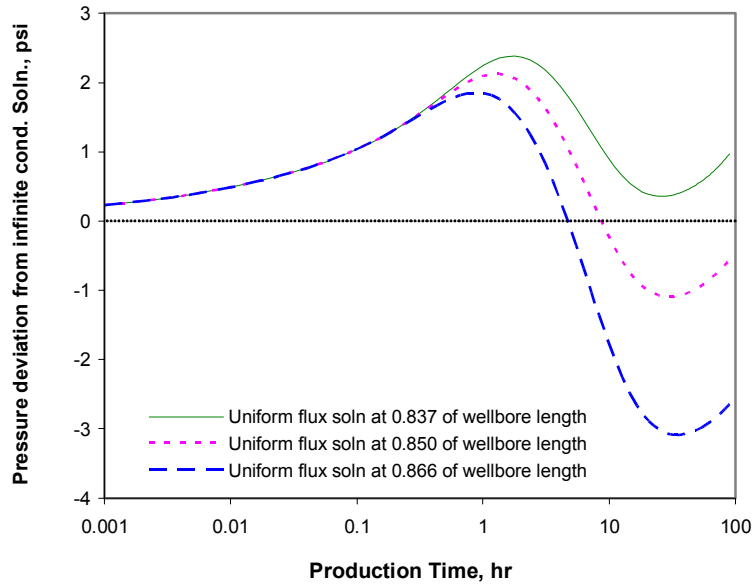


Fig. 2-25—Deviation of uniform flux solution at equivalent points from infinite conductivity solution for case 2-3 (semilog plot).

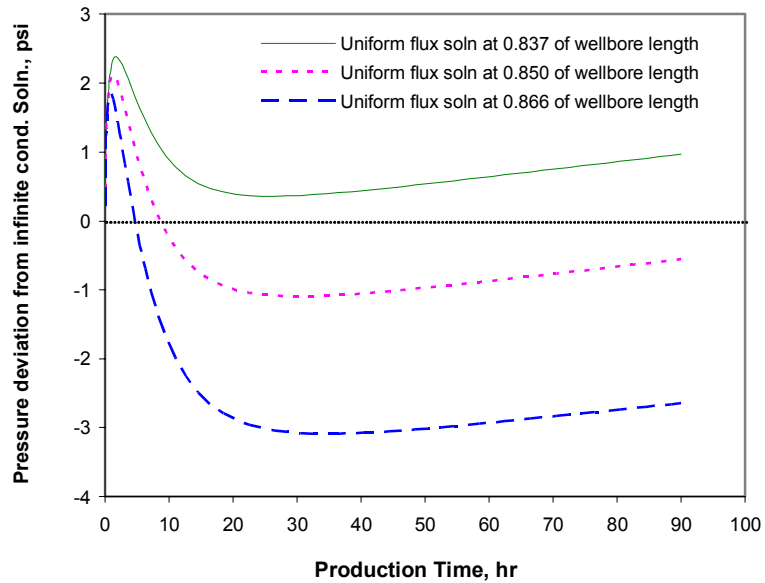


Fig. 2-26—Deviation of uniform flux solution at equivalent points from infinite conductivity solution for case 2-3 (Cartesian plot).

Pressure Averaging Method. The pressure averaging method means averaging the uniform flux pressure solution over the wellbore to represent the solution of an infinite conductivity wellbore. Figs. 2-27 to 2-30 shows the average pressures of the uniform flux solution at different times. The average pressure is very close to the infinite conductivity solution at the early times, but gradually deviates away from the infinite conductivity solution as time increases. From an engineering point of view, the difference between average pressures of the uniform-flux solution and the infinite-conductivity solution are not serious, less than 4 psi by a time of 90 hrs (Fig. 31).

Frictional Pressure Loss. At 90 hrs, the total pressure change is 342.8 psi at heel, and the frictional pressure loss (from the toe to the heel) accounts for 45.0 psi. This means that if we ignore the frictional pressure loss, an error of at least 13 % will be introduced. At early times, this error is even larger. For example, at 0.029 hr, the total pressure change is 116.7 psi at the heel and the frictional pressure loss is 43.4 psi, and the resulting error is as high as 37%. In addition, we also note that the frictional pressure loss is different at different times. This variation is caused by the changes in flux distribution, but because this variation is not large, there seems to be a constant difference between the finite-conductivity and infinite-conductivity solutions at a specific point resulting from the frictional pressure term. In this case, it is clear that the frictional pressure loss is significant.

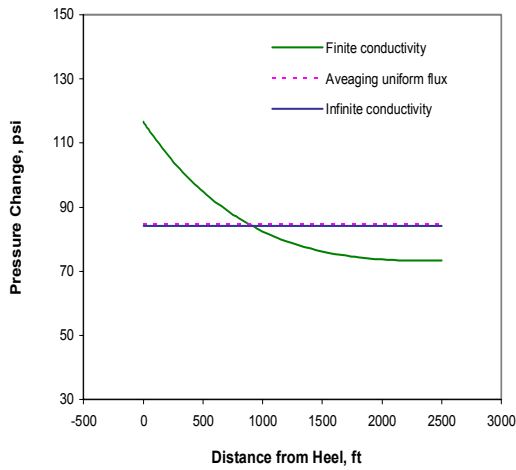


Fig. 2-27—Average pressure of uniform-flux solution at time 0.029 hr.

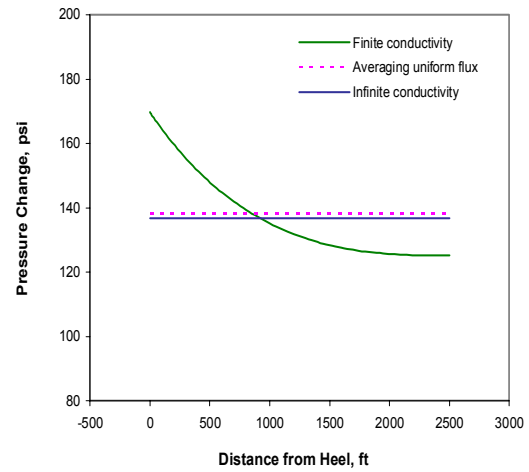


Fig. 2-28—Average pressure of uniform-flux solution at time 3.117 hr.

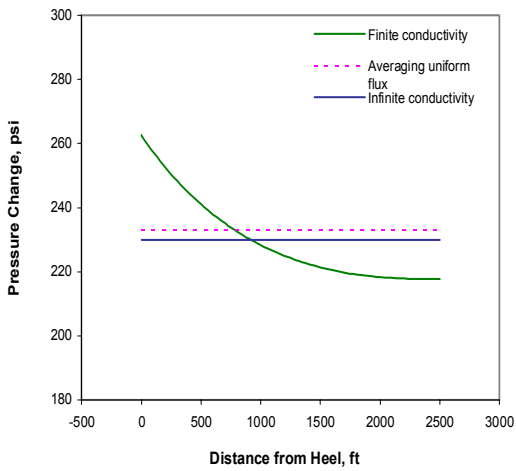


Fig. 2-29—Average pressure of uniform-flux solution at time 40 hr.

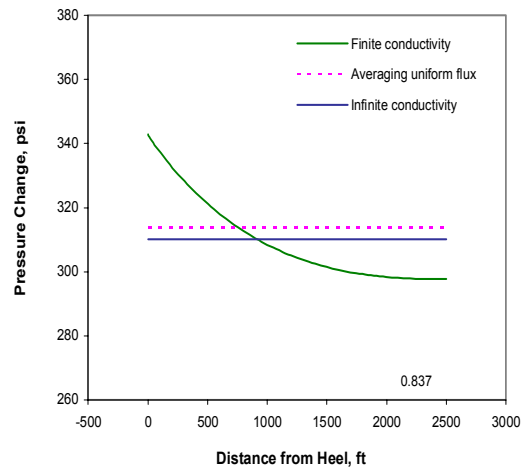


Fig. 2-30—Average pressure of uniform-flux solution at time 90 hr.

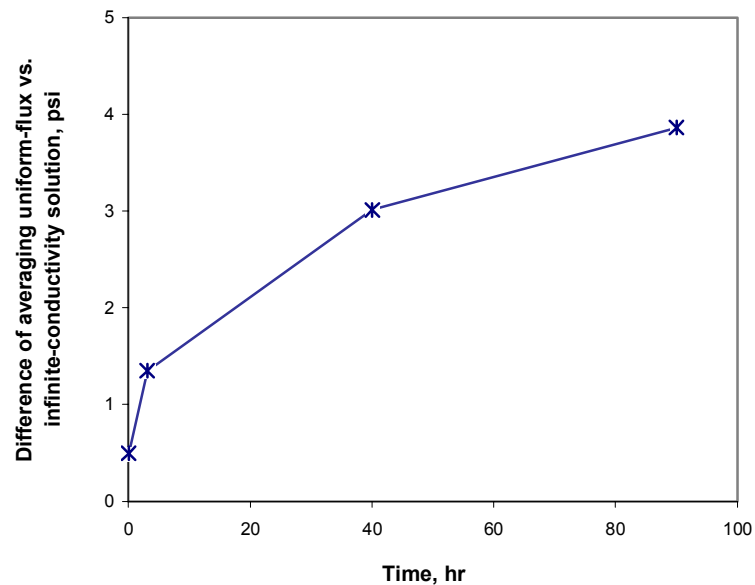


Fig. 2-31—Difference of averaged uniform-flux and infinite-conductivity solutions for case 2-3.

Case 2-4 – Horizontal Well in a Reservoir with Constant Pressure Boundary. This is an example of a horizontal well producing in a bounded reservoir with constant pressure condition at the bottom boundary and no-flow at all other boundaries. The reservoir and fluid properties are shown in Table 2-3.

Fig 2-32 displays pressure and logarithmic time derivative of pressure in a log-log plot. After a short early-time radial flow regime, flow enters a transition region which continues for a relatively long time before steady-state flow is reached. After this time, the distributions of pressure and flux do not change. Fig. 2-33 shows the profile of steady-state pressure along the wellbore length. Since the frictional pressure loss over the wellbore is considered, the pressure change profile is neither a horizontal line (for infinite conductivity) nor a symmetrical funnel (for uniform flux) but a concave curve upward, and pressure change decreases from heel to toe. However, with a rate of 2400 STB/D, wellbore conditions (radius of 0.25 ft and length of 160 ft) and with the fluid properties used, the influence of frictional pressure loss on pressure and flux behavior is not significant. The difference of pressure change along wellbore is very small, 793.90 psi (at the toe) to 793.92 psi (at the heel). Fig. 2-34 is the profile of steady-state flux. The

unsymmetrical distribution of flux along wellbore is not obvious because of the relatively small frictional pressure loss along the wellbore.

TABLE 2-3—RESERVOIR AND FLUID PROPERTIES FOR CASE 2-4
(constant pressure at the bottom boundary)

Reservoir geometry	= 800*800*40 ft ³
Porosity, ϕ	= 0.2
Viscosity, μ	= 2.0 cp
Compressibility, c_t	= 1.0×10^{-5} psi ⁻¹
Formation volume factor, B	= 1.25 RB/STB
x -permeability, k_x	= 100 md
y -permeability, k_y	= 100 md
z -permeability, k_z	= 10 md
Wellbore radius, r_w	= 0.25 ft
Effective wellbore length, L_w	= 160 ft, centered
Production rate, q	= 2400 STB/D

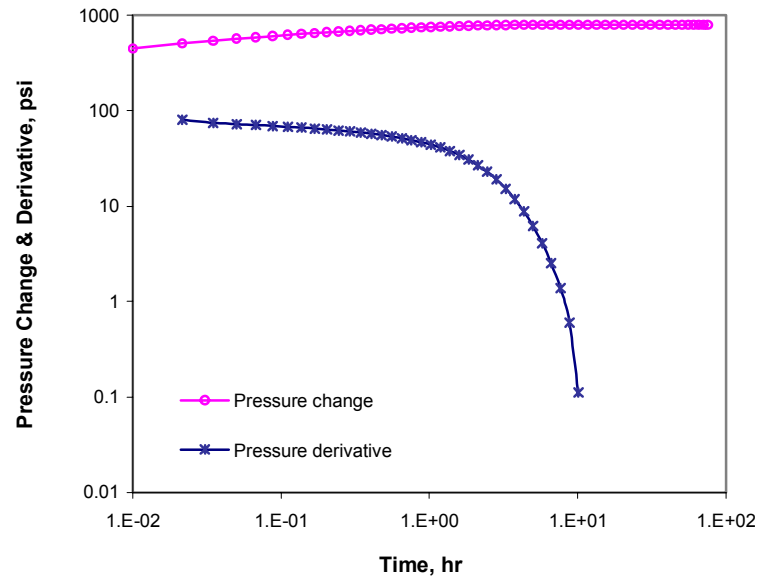


Fig. 2-32—Pressure behavior of a horizontal well producing in reservoir with constant pressure boundary at bottom (case 2-4).

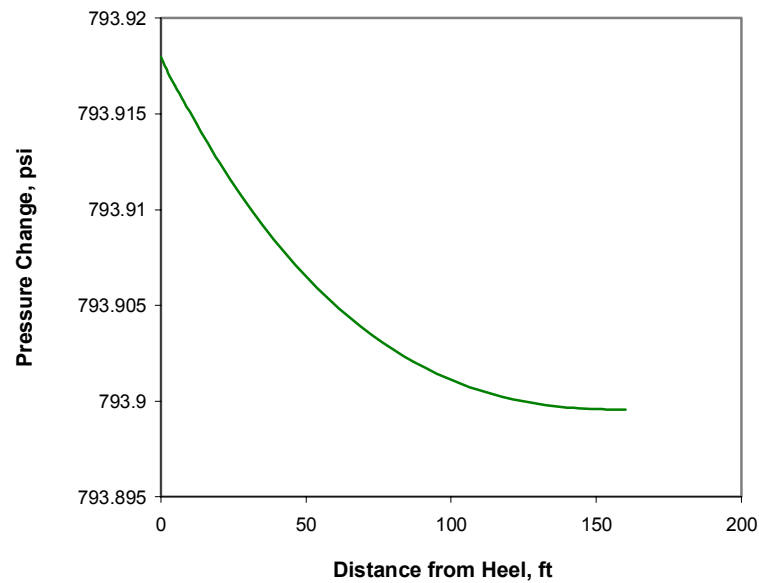


Fig. 2-33—Pressure profile along horizontal wellbore for steady-state flow (case 2-4).

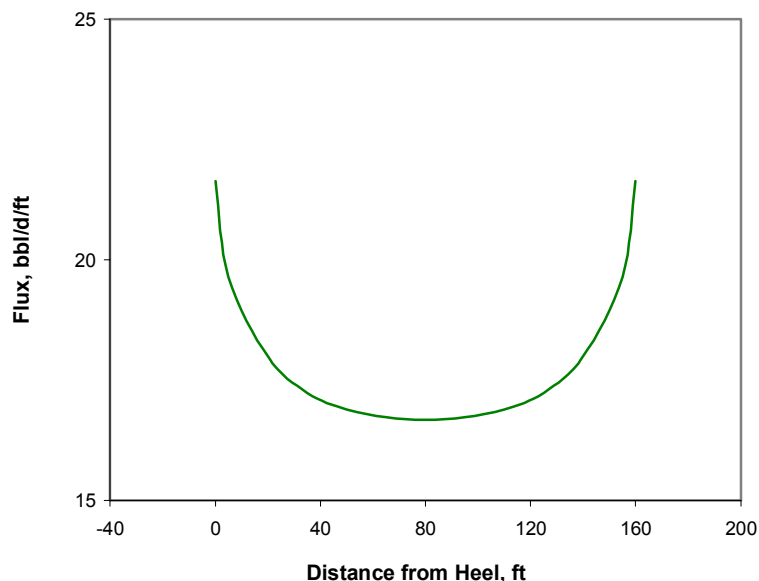


Fig. 2-34—Flux profile along horizontal wellbore for steady-state flow (case 2-4).

Case 2-5 – Vertical Well Pressure Buildup Behavior after Drawdown. Our model can be used to predict buildup pressure response after drawdown. We will use the data in Case 2-1 (Table 2-1) to simulate a process of drawdown plus buildup and validate the simulation results with the analytical solution (logarithmic solution). In this case, we produce this vertical oil well for 0.1 hr, and then shut it in for a buildup test of 0.11 hr. Here, we select a very short time interval for the drawdown and buildup tests to investigate the calculation accuracy when pressure response changes abruptly due to opening and shutting in the well.

Fig. 2-35 shows the result calculated using our model, the analytical solution and the simulation result using *Eclipse*. Again, we used a uniform grid system of 10 by 10 by 1 with a grid size 20 ft by 20 ft by 60 ft in our model, while a uniform grid system of 21 by 21 by 1 with a grid size 9.5 ft by 9.5 ft by 60 ft was used in *Eclipse*. Obviously, our model gives a result consistent with the analytical solution, but the result from *Eclipse* is not accurate. Then, we ran *Eclipse* again with a refined non-uniform grid system of 51*51*1, and result is shown in Fig. 2-36 along with the analytical solution and result from our model. With an average grid size of 3.9ft*3.9 ft in horizontal plane and a minimum block size of 1.5ft *1.5 ft for the block in which the well is located, *Eclipse* provides a result as accurate as our model. This indicates that, for a

short test or a sudden change in well production, our model can provide a reliable result and the result from *Eclipse* will be close to the analytical solution only if the grid size is refined small sufficiently.

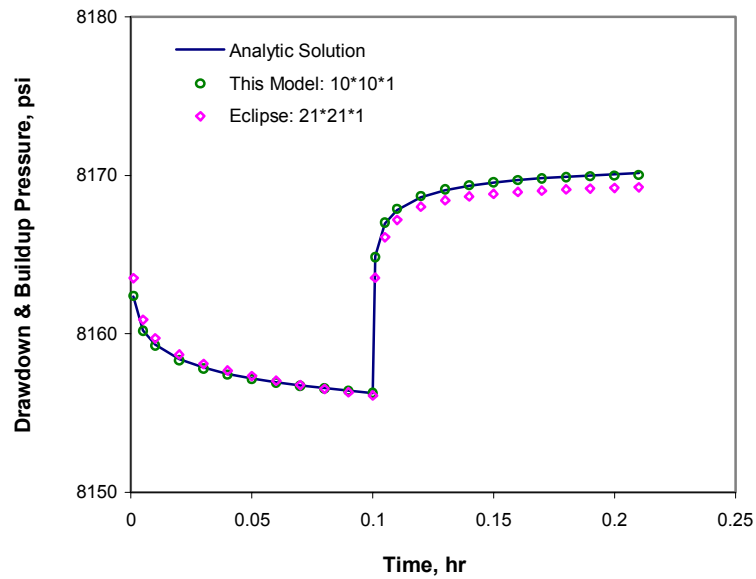


Fig. 2-35—Drawdown and buildup pressure responses from various models for case 2-5.

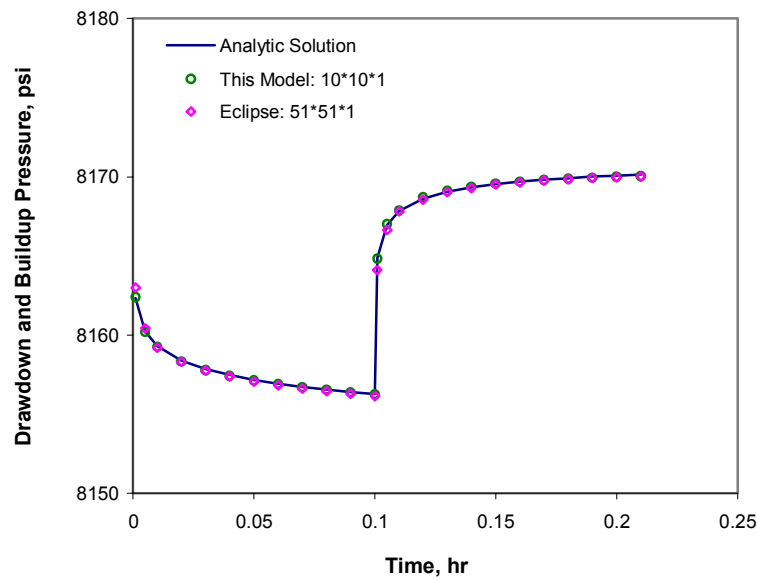


Fig. 2-36—Drawdown and buildup pressure responses from various models for case 2-5.

Case 2-6 – Horizontal Well Multiple Rate Test. We ran a multiple-rate test in a horizontal well using our model. This horizontal well is in a box-shaped reservoir bounded by no-flow boundaries. The horizontal wellbore is along the x-direction. Reservoir and fluid properties and drawdown history are shown in Table 2-4. For comparison, we also calculated the pressure responses using *Eclipse* with various refined grid systems.

Fig. 2-37 shows the production rates and pressure responses. We designed multiple grid systems in running *Eclipse*. Along the horizontal wellbore (x) direction, the grid size is uniform. In the y-z plane normal to wellbore, the grid size along both y and z directions are non-uniform. The grid systems are shown in Table 2-5. In Fig. 2-37, we see that, with the decrease in grid sizes, the pressure response curves calculated from *Eclipse* gradually move toward those from our model. However, there is still fairly large difference between the results from *Eclipse* and those from our model. A partial explanation is that the grid sizes are not refined enough. A more important reason may be the shortcomings inherent in the finite difference method, such as grid orientation and grid size effects etc. resulting in insufficient and inaccurate modeling of the complex 3D flow in the horizontal well-reservoir system. Therefore, caution must be used when a finite-difference simulator is used to model transient flow behavior in a horizontal well.

TABLE 2-4—RESERVOIR AND FLUID PROPERTIES FOR CASE 2-6

Reservoir bounded with no-flow boundaries

Reservoir geometry	= 2000*990*60 ft ³
Porosity, ϕ	= 0.25
Viscosity, μ	= 0.692 cp
Compressibility, c_t	= 1.4435×10^{-5} psi ⁻¹
Formation volume factor, B	= 1.444 RB/STB
x -permeability, k_x	= 100 md
y -permeability, k_y	= 100 md
z -permeability, k_z	= 20 md
Wellbore radius, r_w	= 0.51 ft
Effective wellbore length, L_w	= 1000 ft, centered
Initial reservoir pressure, p_i	= 4000 psi
Production history:	
Production rate, q (0~1 hr)	= 4155 STB/D
Production rate, q (1~3 hr)	= 3324 STB/D
Production rate, q (3~10 hr)	= 2077 STB/D

TABLE 2-5—GRID SYSTEM FOR VARIOUS SCHEMES

		Simulation grid size, ft			Wellbore	
		Dx	Dy	Dz	Grid number	Grid size, ft
Our model	Scheme 6*6*4	333	165	15	10	100
Eclipse	Scheme 20*9*9	100	10~300	2~10	10	100
	Scheme 20*51*9	100	4~33	2~10	10	100
	Scheme 20*81*9	100	4~18	2~10	10	100
	Scheme 40*81*9	50	4~18	2~10	20	50

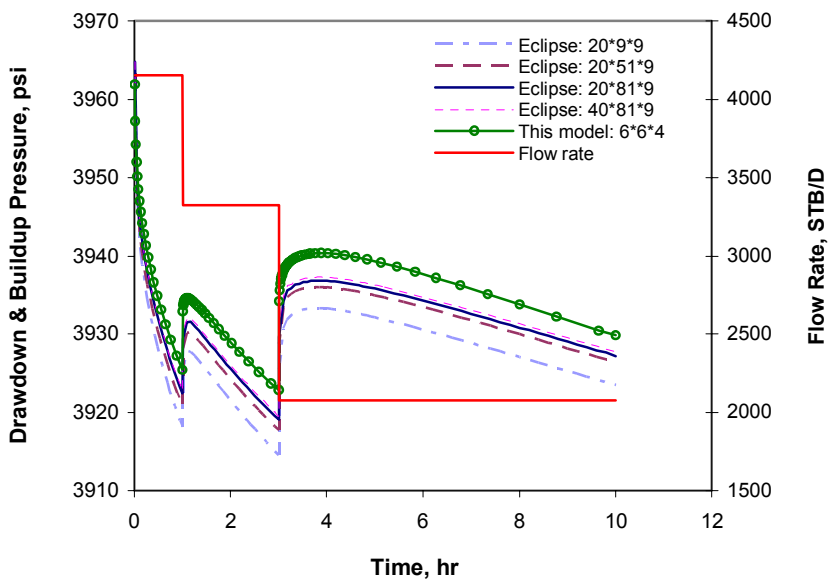


Fig. 2-37—Pressure responses to change of flow rate for case 2-6.

2.7 Chapter Summary

In this chapter, we developed a comprehensive model able to accurately predict the performance of horizontal wells. This model has been demonstrated to be applicable for various inner boundary conditions (uniform flux, infinite conductivity, and finite conductivity wellbores), various outer boundary conditions (no-flow, constant pressure, and mixed boundaries), and various well tests (pressure drawdown, pressure buildup, and multirate tests). It can be used to investigate the influences on well inflow performance of anisotropy (horizontal-to-vertical permeabilities and horizontal-to-horizontal permeabilities), well location (vertical eccentricity and horizontal orientation), and the relative dimensions of drainage area. The model provides a powerful tool to reliably evaluate well productivity and rigorously simulate pressure transient testing for horizontal wells.

CHAPTER III

PRODUCTIVITY OF HORIZONTAL WELLS

In the previous chapter, we developed a model capable of providing reliable evaluation of well productivity and rigorous simulation of pressure transient tests. In this chapter, we will focus on applying this model to analyze the productivity of horizontal wells for various flow regimes, such as transient flow, pseudo-steady-state flow and steady-state flow. Instead of investigating productivity sensitivity to a single individual parameter, we will study the comprehensive influences on productivity resulting from uncertainties of all parameters considered, i.e., we will quantify the uncertainty of productivity. The parameters considered include horizontal and vertical permeabilities, wellbore length, vertical eccentricity of the wellbore, and damage skin factor.

3.1 Introduction

Well productivity is one of primary concerns in field development and provides the basis for field development strategy. Well productivity is often evaluated using the productivity index, which is defined as the production rate per unit pressure drawdown. We often relate the productivity evaluation to the long-time performance behavior of a well, that is, the behavior during pseudo-steady-state or steady-state flow. However, as Economides, Brand, and Frick²⁵ pointed out, the transient productivity index is also important and may determine whether a well is economically attractive or not.

Maximizing well productivity at a minimum cost is our objective. Therefore, investigating the factors and parameters that influence or control the productivity index is our major interest. As reputed in the literature, a great deal of study has been made of effects of single parameters on well productivity. For example, Babu and Odeh³, using the assumption of a uniform-flux wellbore, studied the effects on productivity index of horizontal and vertical permeabilities, horizontal wellbore length and penetration degree, horizontal drainage dimensions, and well location; Economides, Brand, and Frick²⁵, using an infinite conductivity wellbore, studied the effect of horizontal wellbore orientation on the productivity index; while Ozkan, Sarica, and Haci³¹, using a finite-conductivity wellbore, studied the effects on productivity of horizontal

wellbore length and pressure loss within the horizontal wellbore. Many other authors also conducted studies with their models, but we will not list all this work here. The common feature of all these studies was separate treatment of the effect of each parameter on the well productivity. In practice, almost all parameters, either estimated or measured, contain uncertainties or errors, and are correlated with each other. Therefore, it is helpful to quantify the uncertainty in the estimated productivity index considering all parameters to vary, and such productivity evaluation is more realistic and practically significant.

3.2 Transient Productivity Index

The transient productivity index is calculated before the flow reaches the pseudo-steady-state or steady-state regime. During the transient flow period, the productivity index is defined as:

$$J = \frac{q_t}{p_i - p_{wf,h}} = \frac{0.00708kL_h}{B\mu(p_{Dr} + F_w + s_f)} \quad (3-1)$$

where p_i is the initial reservoir pressure, $p_{wf,h}$ is the flowing pressure at the heel, s_f represents total skin factor, including the damage skin and non-Darcy flow effect, etc. P_{Dr} is the dimensionless pressure, reflecting the pressure drawdown in reservoir, and can be written as:

$$P_{Dr} = \frac{0.00708kL_h}{q_t B\mu} (p_i - p_{wf,r}) \quad (3-2)$$

$p_{wf,r}$ is the pressure response not including the pressure loss in the wellbore. F_w represents additional pressure loss due to friction in the horizontal wellbore. Referring to Eq. 2-73, F_w can be formulated as

$$F_w = \frac{0.00708C_w \rho k L_h}{q_t B\mu_w^{.5}} \int_0^{L_h} f(x) q^2(x) dx \quad (3-3)$$

The summation of P_{Dr} and F_w can be obtained from the model developed in Chapter II.

Case 3-1. A synthetic case is used to illustrate the productivity index behavior during the transient flow period. Table 3-1 gives the relevant reservoir and fluid properties. We display the diagnostic plot (Fig. 3-1) so that the flow regimes and corresponding time ranges can be conveniently identified. Fig. 3-1 shows three flow regimes: early-time radial flow, late-time pseudo-radial flow, and pseudo-steady-state flow. The reservoir system is in the transient flow

regime for about 8 hrs after the start of production. The well productivity during the transient flow regime is illustrated in Figs. 3-2. The semi-log plot, Fig. 3-2, clearly indicates the productivity behavior for the earlier time range. Fig. 3-3 shows that the decline of the productivity index is fairly rapid within a short period of time.

TABLE 3-1—RESERVOIR AND FLUID PROPERTIES FOR CASE 3-1

Closed box-shaped reservoir	
Reservoir geometry	= 1000*1000*40 ft ³
Porosity, ϕ	= 0.2
Viscosity, μ	= 2 cp
Compressibility, c_t	= 2×10^{-5} psi ⁻¹
Formation volume factor, B	= 1.05 RB/STB
x -permeability, k_x	= 150 md
y -permeability, k_y	= 150 md
z -permeability, k_z	= 10 md
Wellbore radius, r_w	= 0.25 ft
Effective wellbore length, L_w	= 200 ft, centered
Initial reservoir pressure, p_i	= 4,000 psi
Production rate, q	= 1,905 STB/D

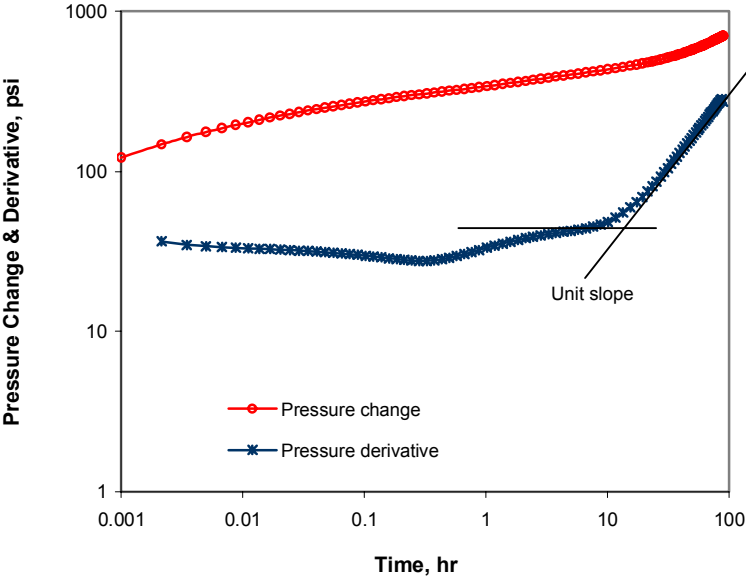


Fig. 3-1—Diagnostic plot for case 3-1.

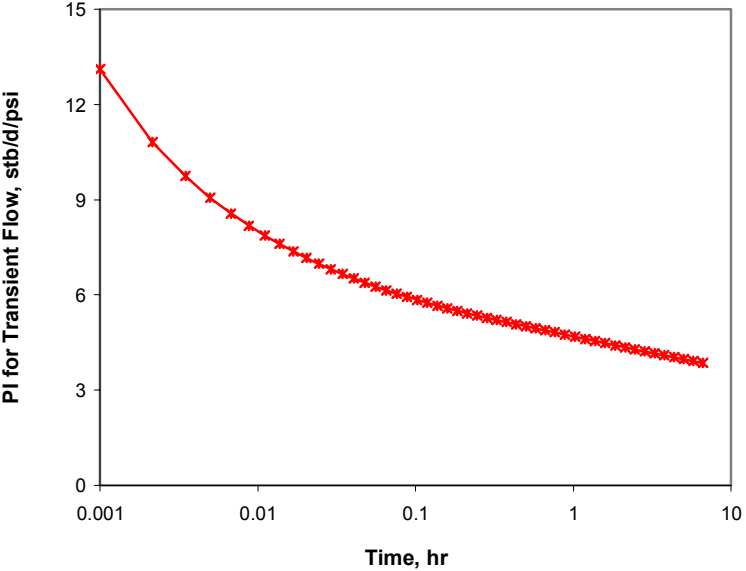


Fig. 3-2—PI (productivity index) for transient flow period.

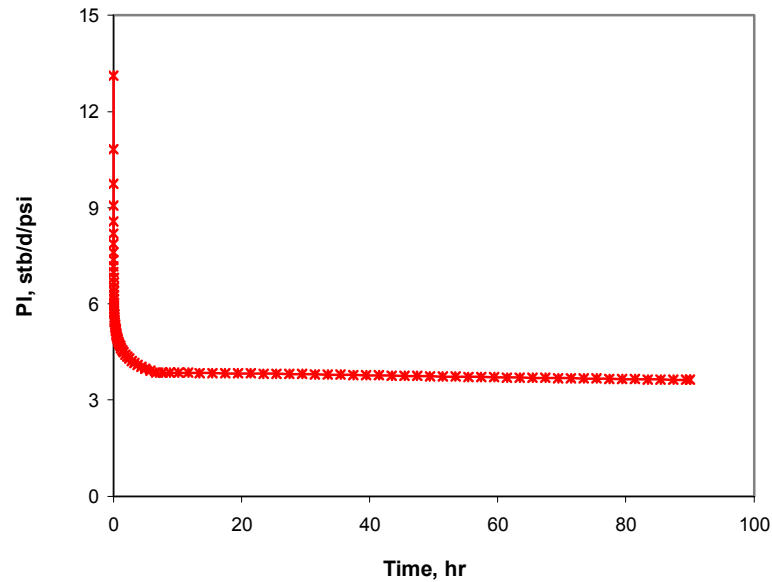


Fig. 3-3—PI (productivity index) for pseudo-steady state flow period.

3.3 Pseudo-Steady-State Productivity Index

For a bounded reservoir with no-flow boundaries, flow enters the pseudo-steady-state regime when the pressure transient reaches all boundaries after drawdown for a sufficiently long time. During this period, the rate of pressure decline is almost identical at all points in the reservoir and wellbore. Therefore, the difference between the average reservoir pressure and pressure in the wellbore approaches a constant (not changing with time). In the definition of pseudo-steady-state productivity index, the average reservoir pressure is used instead of the initial reservoir pressure and hence the productivity index is basically constant.

The pseudo-steady state productivity index is defined as:

$$J = \frac{q_t}{p_{av} - p_{wf,h}} \quad (3-4)$$

where $p_{wf,h}$ can be obtained by running the model developed in Chapter II of this dissertation. p_{av} is the average reservoir pressure, which can be obtained from a material balance for the reservoir; i.e.,

$$c_i V \phi (p_i - p_{av}) = 0.234 q_t B t \quad (3-5)$$

or

$$p_{av} = p_i - \frac{0.234 q_t B t}{c_i V \phi} \quad (3-6)$$

where V is the reservoir volume, and t is the production time.

We use the case from section 3.2 to illustrate well productivity behavior during pseudo-steady state flow. From the diagnostic plot (Fig. 3-1), pseudo-steady-state flow begins around 29 hrs. Fig. 3-3 shows that the well productivity index is basically constant after this time; i.e., in the pseudo-steady state flow regime, the horizontal well has a stabilized productivity index.

3.4 Steady-State Productivity Index

When a reservoir is bounded with a constant pressure boundary (such as a gas cap or an aquifer), flow reaches the steady-state regime after the pressure transient reaches the constant pressure boundary. Rate and pressure become constant with time at all points in the reservoir and wellbore once steady-state flow is established. Therefore, the productivity index during steady-state flow is a constant. The expression for the productivity index is

$$J = \frac{q_t}{P_e - P_{wf,h}} \quad (3-4)$$

where $p_{wf,h}$ is obtained by running the model developed in Chapter II, and p_e is the pressure at the constant pressure boundary.

We still use the same case as that in section 3.2, but with a constant pressure boundary at the bottom of the reservoir (like an aquifer), to illustrate well productivity behavior during the steady-state flow period. The diagnostic plot (Fig. 3-4) shows the pressure change and pressure derivative with respect to logarithmic time. From Fig. 3-4, the steady-state flow appears around 10 hrs, following early-time radial flow and a transition period. Fig. 3-5 displays the well productivity index for the entire drawdown period. The well productivity index for the steady-state flow period is constant, as indicated by the horizontal line.

To clarify the difference in the productivity behavior between the pseudo-steady-state flow and the steady-state flow (or the difference between assumptions of a no-flow boundary and a

constant-pressure boundary), we show both productivity indexes in a single semi-log plot, Fig. 3-6. Fig. 3-6 indicates that the well productivity index for steady-state flow is constant, while for pseudo-steady-state flow the productivity index varies slightly. We can see that with a constant pressure boundary at the top or bottom of the reservoir the productivity index for the steady-state regime is higher than that for the pseudo-steady-state regime (Fig. 3-6). If the constant pressure boundaries are at sides of the reservoir, the situation is reversed (Fig. 3-7).

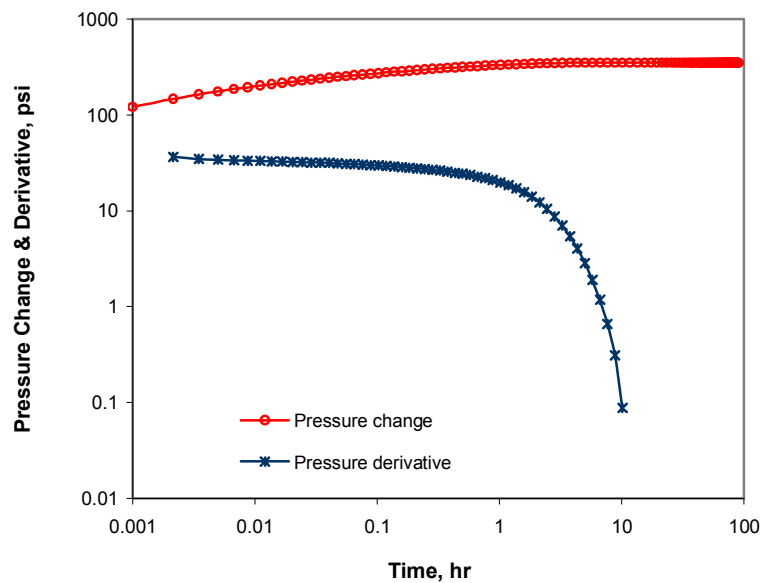


Fig. 3-4—Diagnostic plot for case 3-1 with constant pressure at the bottom of reservoir.

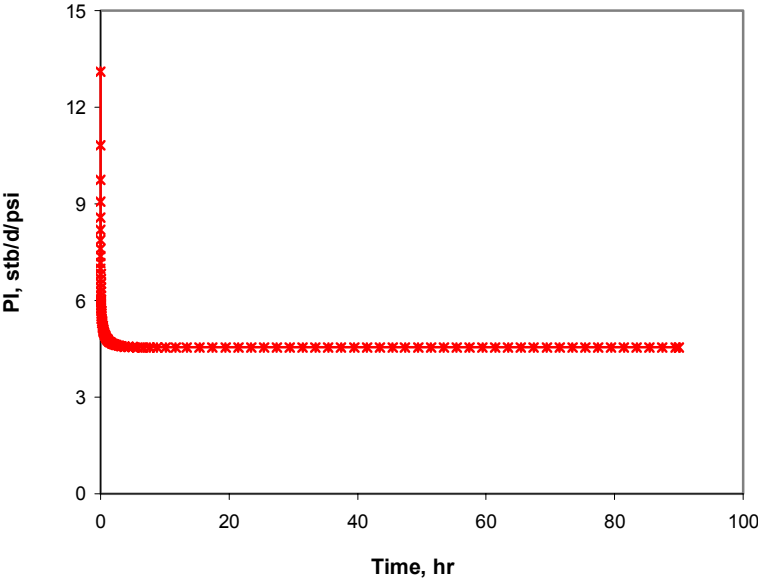


Fig. 3-5—PI (productivity index) with constant pressure at the bottom of reservoir.

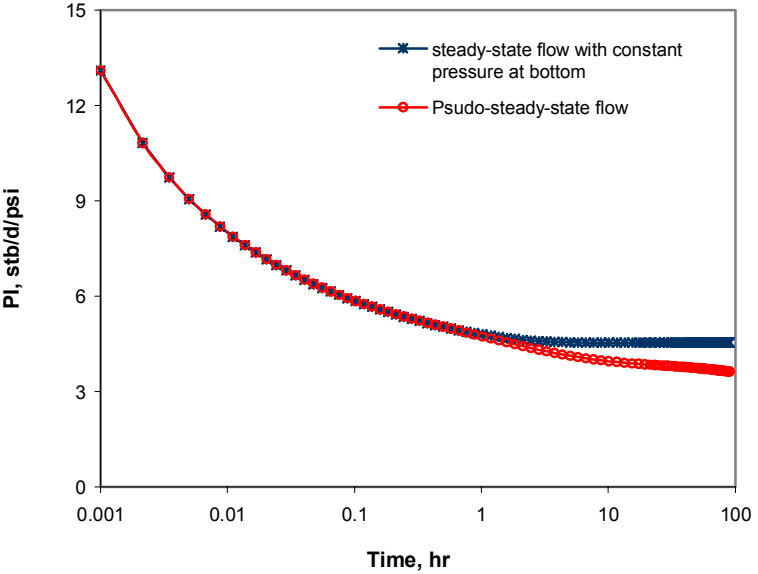


Fig. 3-6—Comparison of PI (productivity index) of pseudo-steady-state flow with steady-state flow (bottom constant pressure boundary).

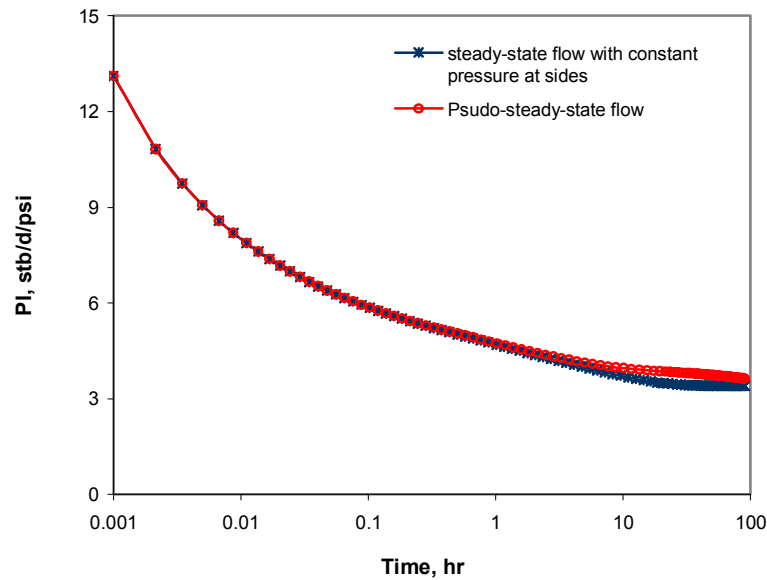


Fig. 3-7—Comparison of PI (productivity index) of pseudo-steady-state flow with steady-state flow (lateral side constant pressure boundary).

3.5 Well Productivity Index Uncertainty

In the previous three sections of this chapter, we depicted well productivity behavior for various flow regimes. Evaluation of well productivity or estimation of productivity index requires the knowledge of reservoir parameters and wellbore conditions, such as horizontal and vertical permeabilities, horizontal wellbore length, vertical location of wellbore, and formation damage, etc. However, all these parameters, either measured by well logging or estimated by well test analysis, usually contain errors or uncertainties. The uncertainties in parameters must cause uncertainty in the calculated productivity index. If the parameters are viewed as random variables because of uncertainties, the productivity index can be also viewed as a random variable subject to a certain kind of distribution. Therefore, it could be inappropriate in evaluation of well productivity using only a deterministic set of parameters to produce a single outcome. At least, the description of productivity behavior is insufficient. A sensitivity study on a specific parameter or factor, as commonly conducted, is helpful for understanding the trend of the productivity change under the influence of the specific parameter. However, such a sensitivity study is neither comprehensive nor complete for understanding productivity behavior

because the well productivity is affected by multiple parameters, all of which have uncertainties and which are correlated with each other.

Monte Carlo simulation can provide us the distribution of the dependent variable (productivity index) based on the distributions of independent variables (i.e., parameters used in the model). Quantification of the uncertainty of the estimated productivity index through examination of multiple scenarios enables us accomplish reasonable and realistic assessments of well productivity. In the following, we will use the information (estimates and uncertainties of parameters) provided by well test analysis (the nonlinear regression technique, which will be discussed in Chapter V) to find the estimate and uncertainty of productivity index by performing Monte Carlo simulation.

Case 3-2. This case uses the data from the Case 2-2 in Chapter II, but the parameters, horizontal and vertical permeabilities, horizontal wellbore length, and skin factor, are assumed unknown and can be obtained from well test analysis (discussed in Chapter V). Estimates of these parameters, together with the upper and lower limits of the 95% confidence interval, are from nonlinear regression and are listed in Table 3-2. We consider each of these parameters as a random variable and assume it subject to a normal distribution. Then, sampling can be performed based on the mean and variance (or standard deviation) of a parameter, and thus multiple scenarios are set up. Here, we establish just ten scenarios with ten random set of parameters (Table 3-3) to indicate the procedure. The sampling for each of parameters in ten scenarios is shown in Fig. 3-8.

TABLE 3-2— MEAN AND 95% CONFIDENCE INTERVAL OF RESERVOIR AND WELL PARAMETERS

(estimated from well test analysis)

Horizontal permeability, k_h	= 377.88±35 md
Vertical permeability, k_v	= 20.5±2 md
Effective wellbore length, L_w	= 2688±243.75 ft
Skin factor, s	= 0.31±0.041

TABLE 3-3—SCENARIOS FOR TEN RANDOM SETS OF RESERVOIR AND WELL PARAMETERS

<u>Scenario</u>	<u>K_h.md</u>	<u>K_v.md</u>	<u>L_w.ft</u>	<u>s</u>
1	346.3	22.8	2313	0.353
2	381.1	18.5	2720	0.259
3	413.5	22.7	2666	0.324
4	387.2	19.1	2802	0.279
5	436.6	20.3	2879	0.234
6	368.0	20.4	2917	0.288
7	359.0	15.8	2952	0.268
8	395.7	21.5	2642	0.300
9	333.6	23.9	2687	0.356
10	391.4	20.6	2314	0.363

We obtained ten sets of productivity-index data through running our model, which correspond to the ten scenarios. We put all productivity-index results obtained for the transient period on a semi-log plot, as shown in Fig. 3-9. We can see that the productivity index is uncertain and falls within a certain range. Although the range decreases with time, the differences between upper and lower limits are still obvious. Since we ran only limited scenarios, we simply describe the distribution of productivity index with an average value of productivity indexes from the ten scenarios and the range. That is, the average value is taken as the mean of the random variable (productivity index) and the range around the average value quantifies the uncertainties. We also plot the average value in Fig. 3-9, among uncertainties of productivity index. Fig. 3-10 compare the average value (or mean) with the true values obtained based on the true set of parameters (from Table 2-2, not from well test analysis). The average value of productivity index is close to the true value.

During the pseudo-steady-state flow period, the productivity indexes are not constant but change very slowly with time for all scenarios (Fig. 3-11). It is impressive that, based on parameter estimates from well test analysis, the uncertainty range of productivity index is quite wide (from 120 to 170 stb/d/psi, Fig. 3-12). Although we cannot determine the full distribution features of productivity index from ten scenarios, it is clear that evaluation of productivity index contains an uncertain range. The result reflects reality. The measured or estimated values of parameters, especially the permeability and effective wellbore length, often cannot be accurately

estimated in practice. Consequently, using uncertainty rather than a single value of productivity index to evaluate productivity is more reasonable.

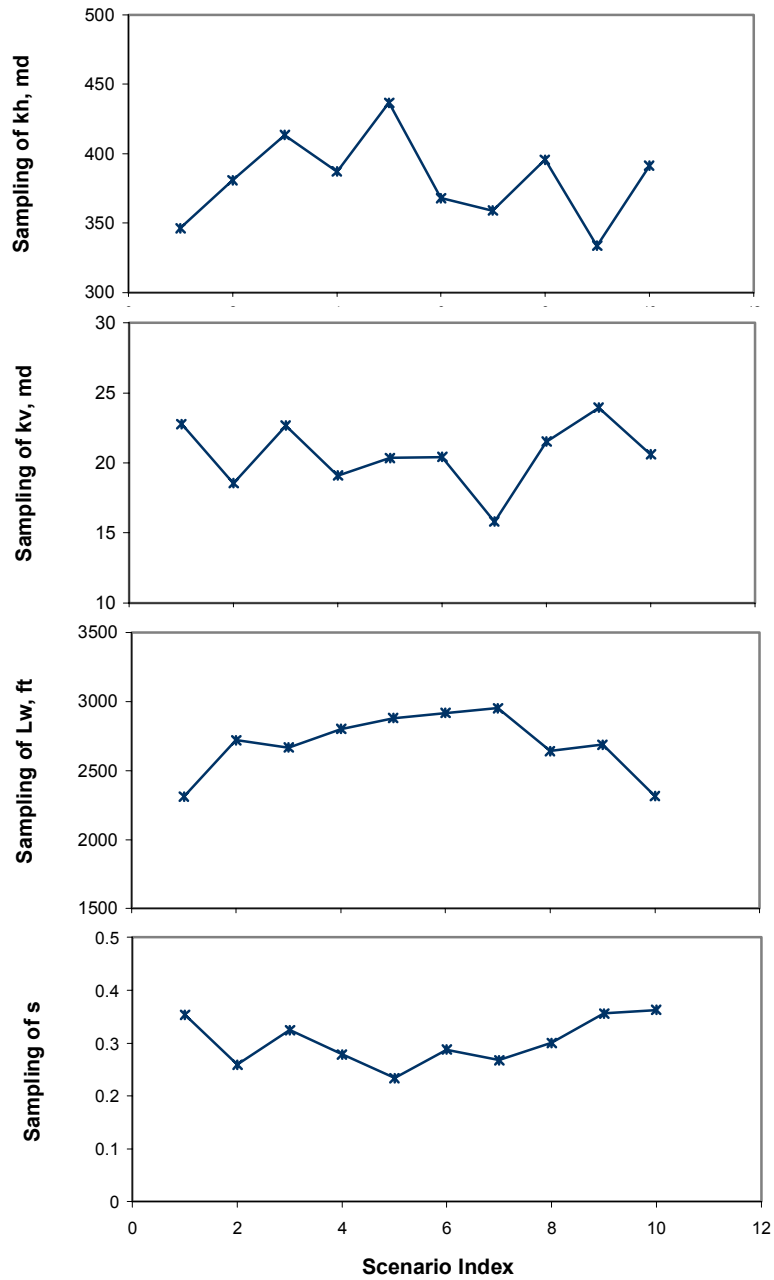


Fig. 3-8—Sampling of reservoir and well parameters.

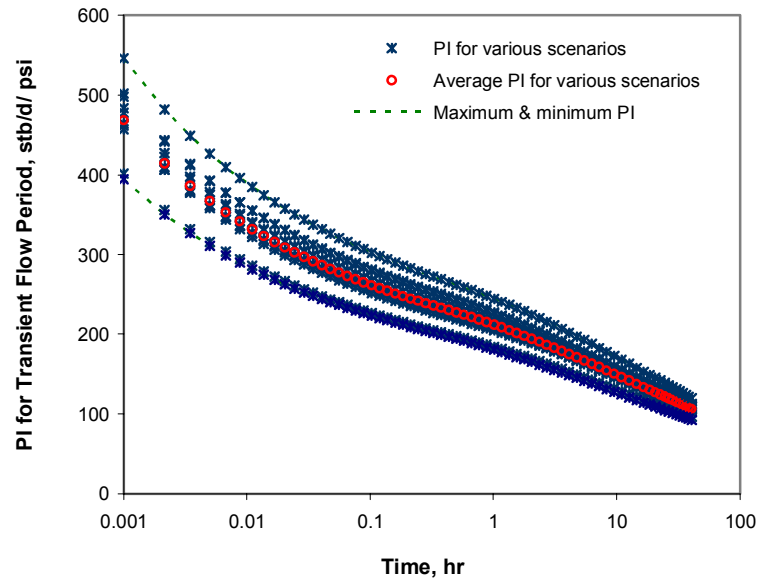


Fig. 3-9—Uncertainty of PI (productivity index) in transient period

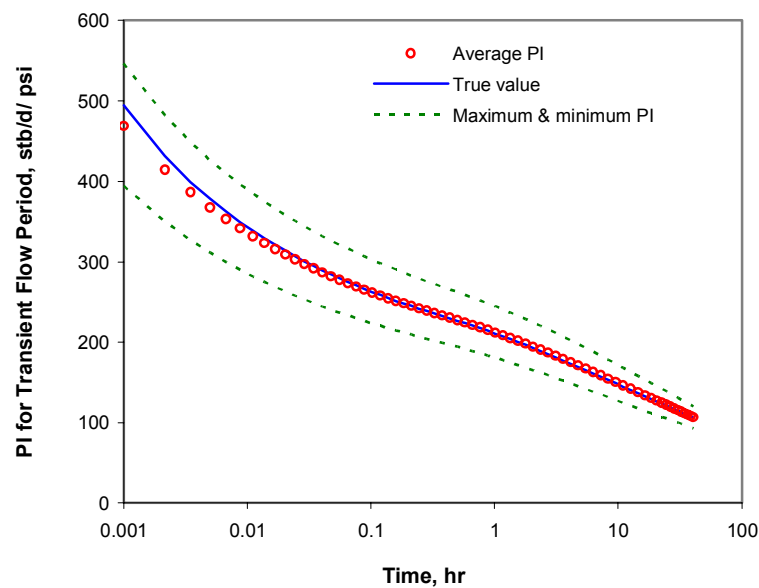


Fig. 3-10—Comparison of average PI with true PI for transient period.

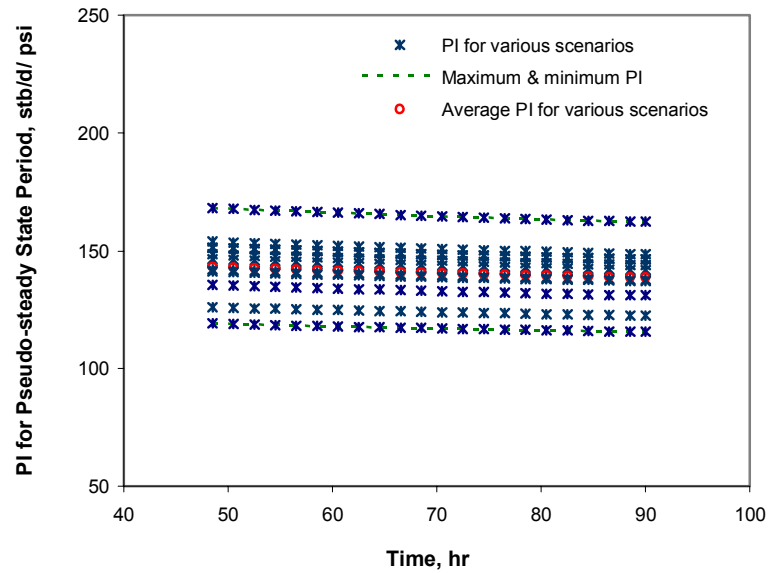


Fig. 3-11—Uncertainty of PI (productivity index) in pseudo-steady-state period.

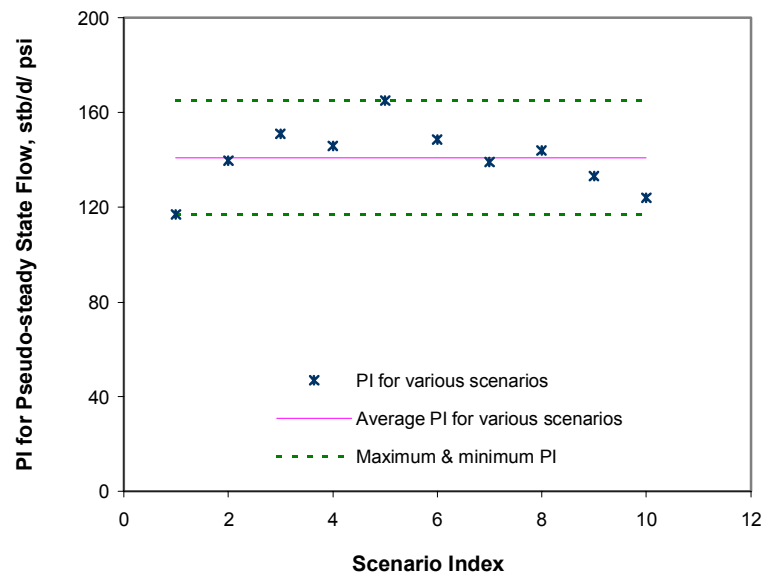


Fig. 3-12—PI (productivity index) in pseudo-steady-state period.

3.6 Chapter Summary

In this chapter, we address two major areas:

1. We can reliably evaluate transient, pseudo-steady state and steady state productivities using the performance prediction model developed in Chapter II. A number of examples demonstrate these evaluations.
2. Many parameters are required for evaluation of well productivity in horizontal wells. However, estimates of these parameters are not likely to be accurate, resulting in uncertainty in productivity. The uncertainty in productivity estimate can be quantified based on the uncertainties of the parameters.

CHAPTER IV

DECONVOLUTION

This chapter presents a deconvolution technique based on a fast-Fourier-transform algorithm. With this new technique, we can deconvolve “noisy” pressure drawdown and buildup test pressure-time data (distorted by wellbore storage) and “noisy” rate data. The wellbore storage coefficient can be variable in the general case. For cases with no rate measurements, we develop a “blind” deconvolution method to restore the pressure response free of wellbore storage distortion. Our technique detects the afterflow/unloading rate function using Fourier analysis of the observed pressure data.

The technique can unveil the early time behavior of a reservoir system masked by wellbore storage distortion and it thus provides a powerful tool to improve pressure transient test interpretation. It has the advantages of suppressing the noise in the measured data, handling the problem of variable wellbore storage, and deconvolving the pressure data without rate measurements.

We demonstrate the applicability of the method with a variety of synthetic and actual field cases for both oil and gas wells. Some of the actual cases include measured rates (which we use only for reference purposes) and others do not.

4.1 Introduction

In conventional well-test analysis, the pressure response to constant rate production is essential information that presents the distinct characteristics for a specific type of reservoir system. However, in many cases it is difficult to acquire sufficient constant-rate pressure response data. The recorded early-time pressure data are generally distorted by wellbore storage (variable rate). In some cases, outer boundary effects may appear before wellbore storage effects disappear. In horizontal well tests, the situation is more serious. Due to the additional horizontal wellbore volume and permeability anisotropy, wellbore storage is usually considerably larger and of longer duration. Therefore, it is often imperative to restore the early-time pressure response in absence of wellbore-storage distortion to provide confidence in our well-test interpretation.

Deconvolution is a technique used to convert measured pressure and rate data into the constant-rate pressure response of the reservoir. In other words, deconvolution provides the pressure response of a well-reservoir system free of wellbore storage distortion, as if the well were producing at a constant rate. Once the deconvolved pressure is obtained, conventional interpretation methods can be used for reservoir system identification and parameter estimation.

However, mathematically, deconvolution is a highly unstable inverse problem because small errors in the data can result in large uncertainties in the deconvolution solution. In the past 40 years, a variety of deconvolution techniques have been proposed in petroleum engineering, such as direct algorithms,⁵¹⁻⁵⁵ constrained deconvolution techniques,⁵⁶⁻⁵⁸ and Laplace-transform-based methods,^{53,59-60} but their application was largely limited because of instability problems. Direct deconvolution is known as a highly unstable procedure.⁵⁷ To reduce solution oscillation, various forms of smoothness constraints have been imposed on the solution. Coats *et al.*⁵⁶ presented a linear programming method with sign constraints on the pressure response and its derivatives. Kuchuk, Carter, and Ayestaran⁵⁷ used similar constraints and developed a constrained linear least-squares method. Baygun, Kuchuk, and Arikan⁵⁸ proposed different smoothness constraints to combine with least-squares estimation. The constraints were an autocorrelation constraint on the logarithmic derivative of pressure solution and an energy constraint on the change of logarithmic derivative.

Efforts were also made to perform deconvolution in the Laplace domain. Kuchuk and Ayestaran⁵³ developed a Laplace-transform-based method, using exponential and polynomial approximations to measured rate and pressure data, respectively. Methods presented by Roumboutsos and Stewart⁵⁹ and Fair and Simmons⁶⁰ used piecewise linear approximations to rate and pressure data. All the Laplace-transform-based methods used the Stehfest algorithm to invert the results in the Laplace domain back to the time domain.

Although the above methods may give a reasonable pressure solution at a low level of measurement noise, the deconvolution results can become unstable and uninterpretable when the level of noise increases. Furthermore, existing deconvolution techniques require simultaneous measurement of both wellbore pressure and sandface rate. However, it is not always possible to measure rate in actual well testing. Existing techniques are, in general, not suitable for applications without measured rates.

In this chapter, we develop a Fast-Fourier-Transform (FFT)-based deconvolution technique. Application of the FFT algorithm for deconvolution has not appeared previously in the

petroleum engineering literature to the best of our knowledge. FFT is a fast algorithm for evaluating the discrete Fourier transform (DFT), which can provide exact transformation of a discrete set of data from a digital point of view.⁷⁴⁻⁷⁵ The DFT or FFT is related to the Fourier integral transform, but is defined only for discrete values over a finite interval.

FFT-based deconvolution is very efficient computationally. More importantly, it deals with noise in the frequency domain effectively and conveniently. To increase the stability of deconvolution, we propose a new afterflow/unloading model and develop an effective denoising technique in the frequency domain. With our approach, noise in pressure and rate measurements can be effectively removed or suppressed so that a stable deconvolution can be achieved. In cases with no measured rates, we propose a blind deconvolution technique to effectively detect the afterflow rate function and restore the constant-rate pressure response through Fourier analysis of the observed pressure data. The new technique can unveil the early-time behavior of a reservoir system masked by wellbore storage and thus provides a useful tool to improve well-test interpretation.

4.2 FFT-Based Deconvolution Method

4.2.1 Theoretical Background

The Fourier transform is a broad technique of mathematical analysis. It is applicable in almost all areas of science and engineering. The FFT is a fast algorithm for computing the discrete Fourier transform (DFT), and can provide efficient and exact transformation of a discrete set of data. Here, we start with a brief review of the background of the Fourier transform, referring to Refs. 74 and 75.

Fourier Transform. The Fourier integral transform is used for investigating the frequency signatures of nonperiodic functions. A nonperiodic function subject to the Dirichlet conditions can be transformed from a time-domain function to a frequency-domain function by using

$$X(f) = \int_{-\infty}^{\infty} x(t)e^{-i2\pi ft} dt \quad (4-1)$$

where $X(f)$ is referred to as the Fourier transform of $x(t)$. Similarly, $X(f)$ can be inversely transformed back to time domain by using

$$x(t) = \int_{-\infty}^{\infty} X(f) e^{i2\pi ft} df \quad (4-2)$$

where $x(t)$ is referred to as the inverse Fourier transform of $X(f)$. In the above expressions, e is the base of natural logarithms, i is the imaginary unit of complex system, and f is the frequency. The Fourier integral exists only for a continuous function. If a set of data cannot be mathematically described as a continuous function, the above integral Fourier transform pair cannot be used.

The discrete Fourier transform (DFT) is a digital approach to Fourier transformation and is defined only for discrete data over a finite interval. We can obtain Fourier transform to observed discrete data through DFT, using the following expression:

$$X_d(k\Delta f) = \Delta t \sum_{n=0}^{N-1} x_d(n\Delta t) e^{-i2\pi k\Delta f n\Delta t} \quad (4-3)$$

Eq. 4-3 can transform a series of time-domain samples to a series of frequency-domain samples. The inverse DFT can be written as:

$$x_d(n\Delta t) = \Delta f \sum_{k=0}^{N-1} X_d(k\Delta f) e^{i2\pi k\Delta f n\Delta t} \quad (4-4)$$

With this equation, a series of frequency-domain samples can be transformed back to a series of time-domain samples.

In both Eqs. 4-3 and 4-4, N is number of samples, n is the time index ($n = 0, 1, 2, \dots, N-1$), and k is the frequency index ($k = 0, 1, 2, \dots, N-1$). Δt is the time interval between samples and Δf is the frequency interval $\Delta f = 1/N\Delta t$. $x_d(n\Delta t)$ is the set of time data and $X_d(k\Delta f)$ is the set of Fourier coefficients of $x_d(n\Delta t)$. The subscript d stands for “discrete”. The DFT and FFT operate on a finite set of data with each point discretely and evenly spaced in time.

Using the Euler identity ($e^{\pm i\theta} = \cos \theta \pm i \sin \theta$), and letting $\Delta t = 1$, thus $\Delta f = 1/N$, a more straightforward set of operations can be obtained to compute the discrete Fourier transform as follows:

$$X_d(k) = \frac{1}{N} \sum_{n=0}^{N-1} [x_d(n) \frac{\cos 2\pi kn}{N} - ix_d(n) \frac{\sin 2\pi kn}{N}] \quad (4-5)$$

and

$$x_d(n) = \sum_{k=0}^{N-1} [X_d(k) \frac{\cos 2\pi kn}{N} + iX_d(k) \frac{\sin 2\pi kn}{N}] \quad (4-6)$$

Convolution and Deconvolution. Fourier transforms move data to the frequency domain where many difficult problems in the time domain become greatly simplified. Performing convolution in the frequency domain is a representative example application of the FFT. Thus, we can also apply the FFT to solve the deconvolution problem in well testing.

In conventional well-test analysis, Duhamel's principle is used to derive the wellbore pressure solution for a system with continuously varying rates.⁴⁶ The solution can be written in terms of a convolution integral (for convenience of presentation, we use p to represent Δp in this chapter):

$$p_w(t) = \int_0^t r(\tau) p_\delta(t - \tau) d\tau \quad (4-7)$$

$$r(t) = q'_{sf}(t) / q_r = q'_D \quad (4-8)$$

where p_w is the variable-rate pressure response, r is the ratio of time derivative of the sandface flow rate to a reference rate (q_r), or the time derivative of a dimensionless sandface flow rate, and p_δ is the constant-rate pressure response of the reservoir corresponding to the reference rate (q_r). q_{sf} is the sandface flow rate, which contains cumulative wellbore effects such as wellbore storage, phase redistribution, and momentum effects. The deconvolution operation may be defined as obtaining the solution p_δ of Eq. 4-7, which we then can use to identify reservoir system and to estimate reservoir parameters.

Taking the Fourier transform of Eq. 4-7 and using the convolution theorem, we have

$$\tilde{p}_w(f) = \tilde{r}(f) \tilde{p}_\delta(f) \quad (4-9)$$

Where the head ' \sim ' stands for the Fourier transform. From Eq. 4-9, we can see that, in the frequency domain, the convolution becomes a multiplication and thus deconvolution becomes simply a division; i.e.,

$$\tilde{p}_\delta(f) = \tilde{p}_w(f) / \tilde{r}(f) \quad (4-10)$$

where \tilde{p}_δ is the constant-rate pressure solution in the frequency domain. Using the inverse Fourier transform of \tilde{p}_δ , we can obtain the constant-rate pressure solution p_δ in the time domain.

In well testing, acquired data are the discrete sets of pressure and rate measurements, so we need to develop the convolution and deconvolution expressions in discrete forms. The discrete convolution is written in the time domain as:

$$p_w(n\Delta t) = \sum_{j=1}^n \Delta q_D(j\Delta t) p_\delta(n\Delta t - j\Delta t) \quad (4-11)$$

and in the frequency domain as:

$$\tilde{p}_w(k\Delta f) = \tilde{\Delta q}_D(k\Delta f) \tilde{p}_\delta(k\Delta f) \quad (4-12)$$

Therefore, the discrete deconvolution can be written in the frequency domain as

$$\tilde{p}_\delta(k\Delta f) = \tilde{p}_w(k\Delta f) / \tilde{\Delta q}_D(k\Delta f) \quad (4-13)$$

Applying the inverse Fourier transform, we can obtain p_δ .

We use the following procedure to perform deconvolution:

- Afterflow/unloading rate normalization. The rate data are normalized with the stabilized rate before shut-in (for buildup) or during production (for drawdown).
- Data interpolation. Both the normalized rate and pressure data are interpolated (quadratically) into evenly spaced sets of data. The number of data points, for both normalized rate and pressure, is equal to 2 raised to an integer power. Then, normalized rate differential data are calculated by $\Delta q_{Dj} = |q_{Dj} - q_{Dj+1}|$.
- Fourier transformation of normalized rate differential and pressure data. The normalized rate differential and pressure data are transformed to the frequency domain by applying the FFT. The transformed components of normalized rate differential and pressure at each frequency are obtained. The FFT algorithm is discussed in the Appendix C.
- Deconvolution. The pressure components are divided by the corresponding rate differential components to obtain the components of deconvolved pressure at each frequency. We apply the inverse FFT to transform the deconvolved pressure in the frequency domain back to the time domain.

4.2.2 Validation

In this section, we use three synthetic cases for different reservoir-wellbore systems to validate the applicability of FFT-based deconvolution method.

We generate the synthetic wellbore pressures based on the following equation in the Laplace domain:

$$\bar{p}_{wD}(s) = \frac{\bar{p}_{\partial D}(s)}{1 + C_D s^2 \bar{p}_{\partial D}(s)} \quad (4-14)$$

where $\bar{p}_{wD}(s)$ is the Laplace transform of wellbore pressure, $\bar{p}_{\partial D}(s)$ is the Laplace transform of constant-rate pressure solution, s is the Laplace domain variable, and C_D is the dimensionless wellbore storage coefficient, which is treated as a constant in this application.

The wellbore pressure in Laplace space is first obtained by including the wellbore storage coefficient into the constant-rate solution using the above equation. It is then inverted back to real time space using Stehfest's inversion algorithm. Since a constant wellbore storage coefficient is used to generate the wellbore pressure response, the classical wellbore model is used to calculate the afterflow/unloading rate. The classical wellbore model will be discussed later.

Homogeneous Reservoir Case. This is an oil-well drawdown test in a homogeneous circular reservoir with a constant wellbore storage coefficient $C_D = 10^5$. The dimensionless pressure data were obtained from cylindrical source solution. The dimensionless unloading-rate was calculated from the derivative of dimensionless wellbore pressure with respect to dimensionless time. Fig. 4-1 shows the unloading-rate differential.

We used the FFT to deconvolve the dimensionless pressure and unloading-rate, and the results are presented in Fig. 4-2. Besides the deconvolved pressures and their logarithmic derivatives, pressure responses with and without wellbore storage are also plotted on Fig. 4-2 for comparison. It is easy to see that the deconvolved pressure and its logarithmic derivative overlay almost exactly the analytic solutions (without wellbore storage). Through deconvolution, we have successfully removed the wellbore storage effect so that radial flow can be identified at very early test times.

Dual-Porosity Reservoir Case. This is an oil-well drawdown test in a dual-porosity reservoir. The storativity ratio (ω) and transmissivity ratio (λ) are 0.1 and 10^{-6} , respectively. The wellbore storage coefficient is constant: $C_D = 10^5$. The dimensionless wellbore pressure data were obtained from the cylindrical source solution with pseudosteady state interporosity flow. It is not possible to identify the dual-porosity behavior characteristic of the reservoir from wellbore

pressure data since this behavior has been completely masked by wellbore storage, as indicated in Fig. 4-3.

We deconvolved the dimensionless pressure and unloading-rate, and present the results in Fig. 4-3. Fig. 4-3 shows that the deconvolution results are remarkably consistent with the analytical solution. After deconvolution, the dual-porosity behavior can be easily identified from the valley in the logarithmic derivative of pressure.

To further display the effectiveness of deconvolution, we also show the semilog plots, Fig. 4-4. The deconvolved pressure is almost identical with the analytical solution, which enables us to accurately estimate reservoir parameters.

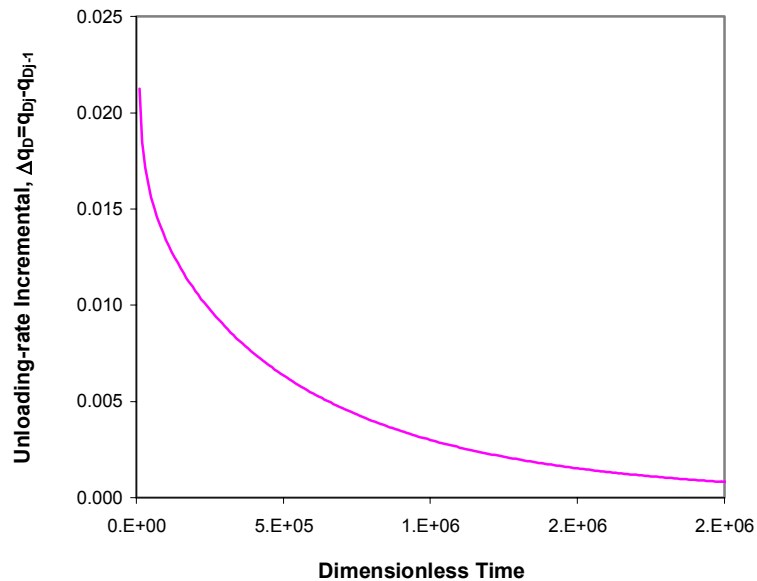


Fig. 4-1—Unloading rate differential.

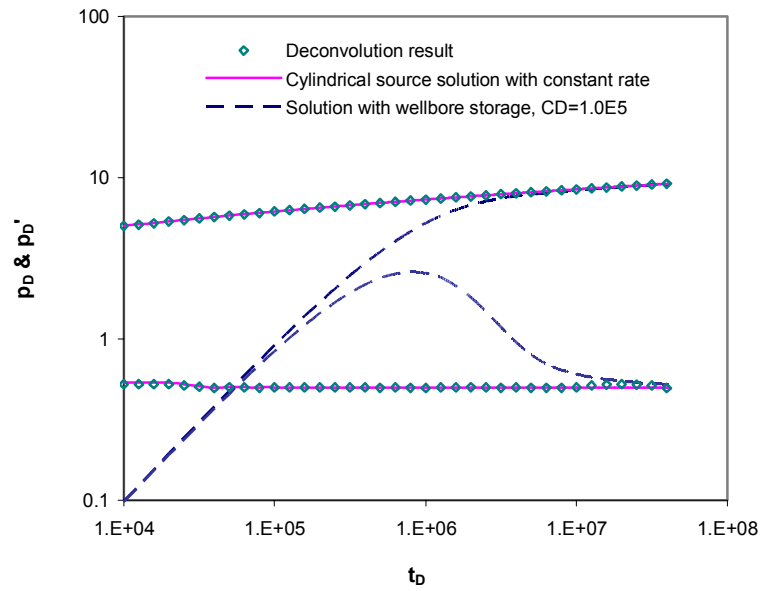


Fig. 4-2—Deconvolution for the homogeneous reservoir.

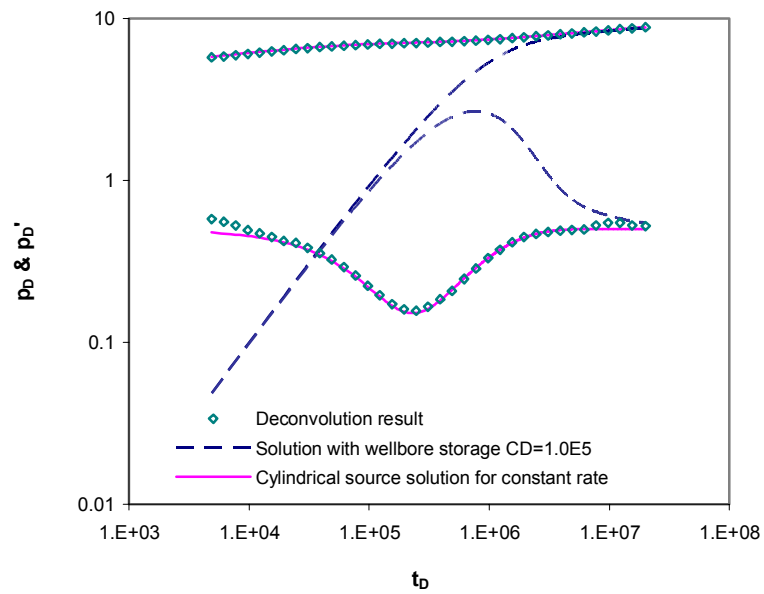


Fig. 4-3—Deconvolution for dual-porosity reservoir (log-log plot).

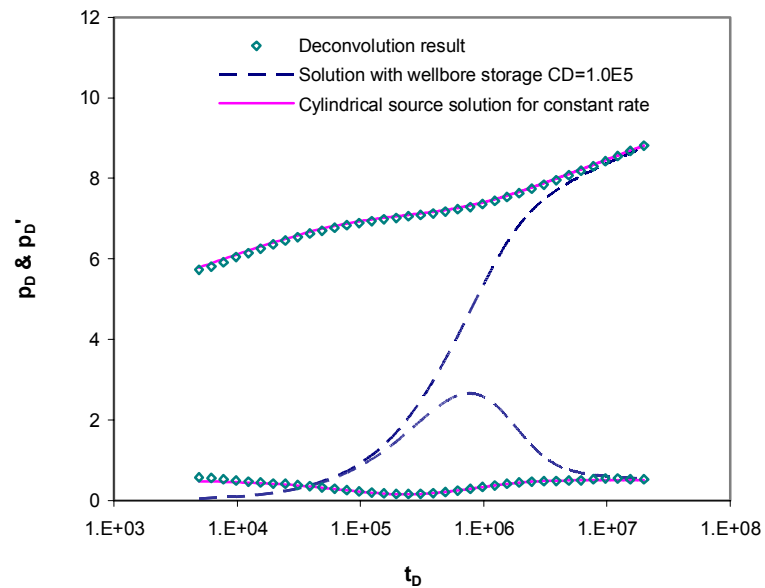


Fig. 4-4—Deconvolution for dual-porosity reservoir (semilog plot).

Horizontal Well Case. This case is the same as Case 2-2 in Chapter II. For convenience, the reservoir and fluid properties are listed again in Table 4-1. The horizontal-well has a drawdown test in a homogeneous reservoir, but with anisotropic permeability. We used our horizontal well model to generate the constant-rate pressure responses. Then the constant-rate pressure data were transformed into the Laplace domain using a quadratic interpolation between points to calculate the wellbore pressure with wellbore storage. The wellbore-storage coefficient we used was 1.63 bbl/psi.

TABLE 4-1—RESERVOIR AND FLUID PROPERTIES FOR HORIZONTAL WELL CASE

Reservoir geometry	= 4000*4000*100 ft ³
Porosity, ϕ	= 0.2
Viscosity, μ	= 1 cp
Compressibility, c_t	= 15x10 ⁻⁶ psi ⁻¹
Formation volume factor, B	= 1.25 RB/STB
x -permeability, k_x	= 400 md
y -permeability, k_y	= 400 md
z -permeability, k_z	= 20 md
Wellbore radius, r_w	= 0.25 ft
Effective wellbore length, L_w	= 2,500 ft, centered
Production rate, q	= 800 STB/D
Skin factor, s	= 0

In this case, the early-time radial flow has been completely masked by wellbore storage (Fig. 4-5). The deconvolution is based on the rate calculated from classical wellbore storage model, and the results are shown in Fig. 4-5. We performed the deconvolution with 2048 evenly spaced points. The time span is 20 hrs, and the length of the evenly spaced interval is 9.77×10^{-3} hrs. From Fig. 4-5, we can see that, except for the first few points, the derivatives of deconvolved pressure are basically consistent with the numerical solution. The small differences are perhaps due to the following factors: (1) the constant-rate pressure solution, used to generate the pressure response with wellbore storage, is a numerical solution; (2) quadratic interpolation was used for Laplace transformation of the constant-rate pressure solution; (3) the pressure response with wellbore storage was obtained by the numerical inversion. These factors bring errors into our wellbore pressure solution. From the deconvolved pressure, the early-time radial flow is now clearly demonstrated on the log-log plot.

The deconvolution results are also shown in a semi-log plot, Fig. 4-6. Again, we can hardly see the differences between the deconvolved pressure and the true constant-rate pressure solution.

The three synthetic cases above confirm the applicability of the FFT-based deconvolution method.

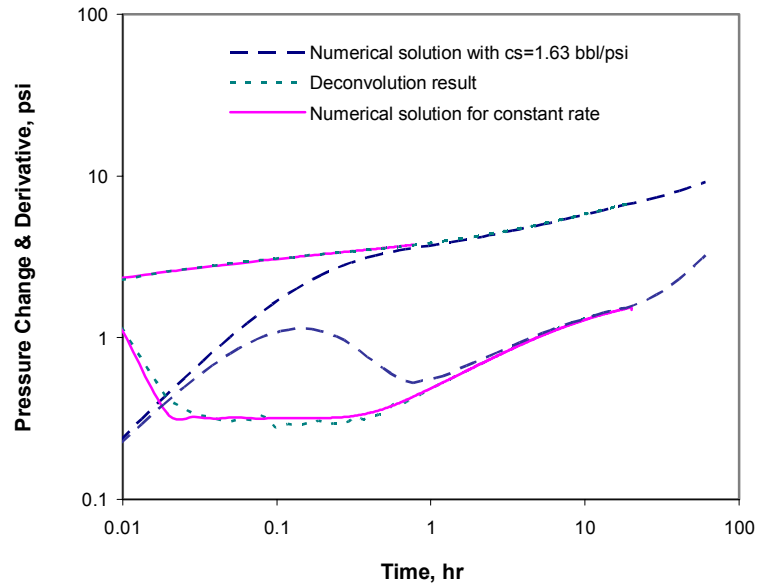


Fig. 4-5—Deconvolution for horizontal well (log-log plot).

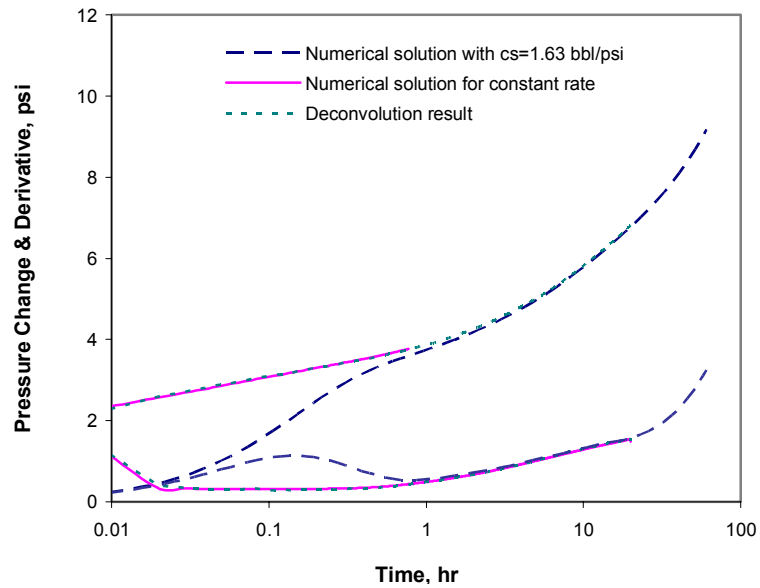


Fig. 4-6—Deconvolution for horizontal well (semilog plot).

4.3 Deconvolution of Noisy Pressure and Rate Measurements

In the previous section, we demonstrated the applicability of our FFT-based deconvolution method in synthetic cases with noise-free data. However, in reality, acquired data unavoidably contain measurement noise due to gauge resolution and disturbances from the environment surrounding the measurement point, and various other factors. Deconvolution may significantly amplify the noise so that the deconvolution result may be totally useless if we cannot implement an efficient denoising process. In this section, we will first analyze the effects of noise on deconvolved pressure, then propose a new afterflow/unloading rate model and a frequency-domain-based denoising technique.

The new rate model is able to accurately describe the behavior of afterflow/unloading rate. We use it to fit the rate measurement data by regression so that smoother rate data can be obtained. The high frequency noise in the measured rates can be removed in the process of rate smoothing. To further denoise the data, we use the Levy function to regress the mid/high frequency data of deconvolved pressures in the frequency domain. We prove in this section that Levy function can be a good representation of the constant-rate pressure solution for a variety of reservoir systems; therefore, the regression process actually functions as an effective way to further eliminate noise and to recover the true pressure response of the reservoir. We demonstrate the effectiveness of our denoising technique using synthetic and field examples.

4.3.1 Effect of Noise on Deconvolved Pressure

We represent the measured rate derivative $r_m(t)$ as a sum of true rate derivative and a systematic or random noise $\Delta r(t)$ in the rate derivative. Similarly, the measured wellbore pressure $p_w(t)$ is also represented as a sum of the noise-free wellbore pressure plus a systematic or random noise $\Delta p_w(t)$ in the pressure measurement. Then our convolution integral can be expressed as

$$p_w(t) - \Delta p_w(t) = \int_0^t (r_m(\tau) - \Delta r(\tau)) p_\delta(t - \tau) d\tau \quad (4-15)$$

At the same time, we can also write

$$p_w(t) = \int_0^t r_m(\tau) (p_\delta(t - \tau) + \Delta p_\delta(t - \tau)) d\tau \quad (4-16)$$

where Δp_δ is the uncertainty of deconvolved pressure. Combining these two equations, we have

$$\int_0^t r_m(\tau) \Delta p_\delta(t-\tau) d\tau = \Delta p_w(t) - \int_0^t \Delta r(\tau) p_\delta(t-\tau) d\tau \quad (4-17)$$

or

$$r_m * \Delta p_\delta = \Delta p_w - \Delta r * p_\delta \quad (4-18)$$

where * denotes a convolution.

In the frequency domain, the error or uncertainty of the deconvolution solution is

$$\Delta \tilde{p}_\delta(f) = \frac{\Delta \tilde{p}_w(f) - \Delta \tilde{r}(f) \tilde{p}_\delta(f)}{\tilde{r}_m(f)} \quad (4-19)$$

This relationship shows that the pressure and rate errors are transferred into deconvolved pressure errors by convolution and deconvolution, which indicates the non-local interconnection between the uncertainty in the deconvolved pressure and the rate and pressure noise. This means that the local errors in rate and pressure measurements will be spreading via convolution in the deconvolved pressure solution. To obtain a stable deconvolution, both rate and pressure noise must be effectively removed.

For random noise, because of its high frequency nature, we expect that, in the frequency domain, this noise should distort mainly the mid/high frequency information while the low frequency information will preserve the true signal's features. The noisy components superpose on the true signal to distort the mid/high frequency behavior. If we can filter out the noisy components in the mid/high frequency band, we can denoise the test data.

The impact of systematic noise will be much more complicated. Since its frequencies are generally low, systematic noise may contaminate the low frequency information of the signal. In the frequency domain, systematic noise is usually displayed as an integrated part of the signal and can hardly be distinguished from the true signal. A more accurate model to estimate afterflow/unloading rate can help us solve this problem.

4.3.2 New Afterflow/Unloading Rate Model

The constant wellbore-storage model⁴⁶ is commonly used to relate the afterflow/unloading rate to the measured wellbore pressure, and is expressed as:

$$q_{sf} = q + \frac{24C_s}{B} \frac{dp_w}{dt} \quad (4-20)$$

where q_{sf} is the sandface rate, q is the surface rate, C_s is the wellbore storage coefficient, B is the formation volume factor, and p_w is the wellbore pressure. Assuming a constant wellbore storage coefficient, the sandface flow rate is computed from Eq. (4-20). In fact, the constant wellbore storage concept implies three assumptions: (1) surface pressure is constant during the test period, so its time derivative can be neglected; (2) fluid in the wellbore has constant compressibility; (3) the surface rate remains constant during the test period. In general, conditions (1) and (2) cannot be strictly met in actual cases. Only condition (3) is obtained perfectly for the buildup test. Therefore, the wellbore-storage cannot be constant in general. In fact, in most cases of pressure buildup, the wellbore storage will decrease continuously because of rapid change of wellbore pressure. As reputed by many authors,^{54,61-62,76} the wellbore storage coefficient varies because of the combined effects of fluid compressibility, phase-redistribution, and momentum changes.

Many efforts have been made to use a functional formula to approximate the sandface flow rate. An exponential function or its polynomial is most often used to characterize afterflow rate in the literature,⁵³ i.e.,

$$q_D = \exp(-ct) \quad (4-21)$$

where c is a positive constant, which is determined by well and reservoir parameters. However, this common exponential approximation for afterflow rate is not sufficient for accurate deconvolution. We will demonstrate its inaccuracy later.

In this study, we propose a new afterflow rate model:

$$q_{D,\text{mod}} = \exp(-c_1(c_2 t)^{\frac{c_3}{(1+c_4 \ln(c_2 t+1))}}) \quad (4-22)$$

Where $c_1 \sim c_4$ are non-negative constants to be determined by nonlinear regression in both time and frequency domains. For drawdown, $1-q_D$ can be modeled by Eq. 4-22. We will show that this new rate model can accurately describe the afterflow/unloading rate in the following examples.

We used the new afterflow/unloading rate model, Eq. 4-22, to fit the constant wellbore-storage unloading rates calculated from the classical wellbore model (Eq. 4-20) for the homogeneous reservoir case discussed earlier. Fig. 4-7 shows the result. For comparison purposes, we also used Eq. 4-21 to fit the rate data, and we show the result in Fig. 4-7 also. We cannot distinguish the regressed values calculated with the new model from the true (analytical)

unloading rate, but we observe obvious deviation of rates calculated using the exponential model (Eq. 4-21) from the true rates.

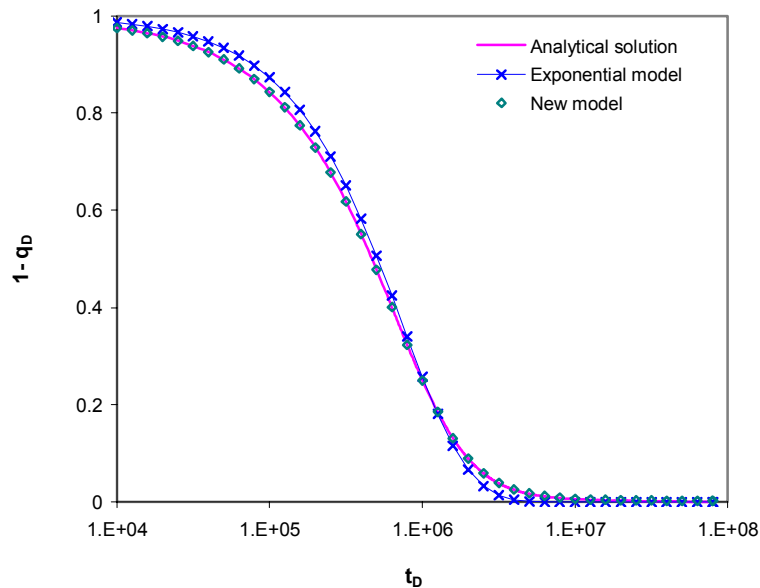


Fig. 4-7—Unloading rate with different models.

We also verified our new model with actual afterflow measurements, presented by Meunier, Wittmann, and Stewart,⁵¹ and also presented in Table 3-5 of *Well Test Analysis* by Sabet.⁷⁷ The afterflow rate in this case included significant effects of changing wellbore storage coefficient, as shown in Fig.1 of Ref. 51 and Fig. 4-5 of Ref. 77. When we used our new model to fit the measured data, we performed the regression not only in the time domain, but also in the frequency domain, because some information is represented better in the time domain and other information is better represented in the frequency domain. The details will be discussed in the following section.

The regressed afterflow rate for this case is shown in Fig. 4-8, along with the measured data. q_D in the figure is the dimensionless ratio of afterflow rates after shut-in to the rate at shut-in time, i.e. $q_{Dj} = q(\Delta t_j)/q(0)$. The regressed rate with the new model is quite consistent with the measured rates as shown in Fig. 4-8, which indicates that the new model can provide a more reasonable and reliable description of afterflow/unloading with changing wellbore storage and

thus lay a good foundation for the deconvolution process. Fig. 4-8 also shows the fit with the exponential model. Again, we observe obvious deviation of rates calculated using the exponential model from the measured rates.

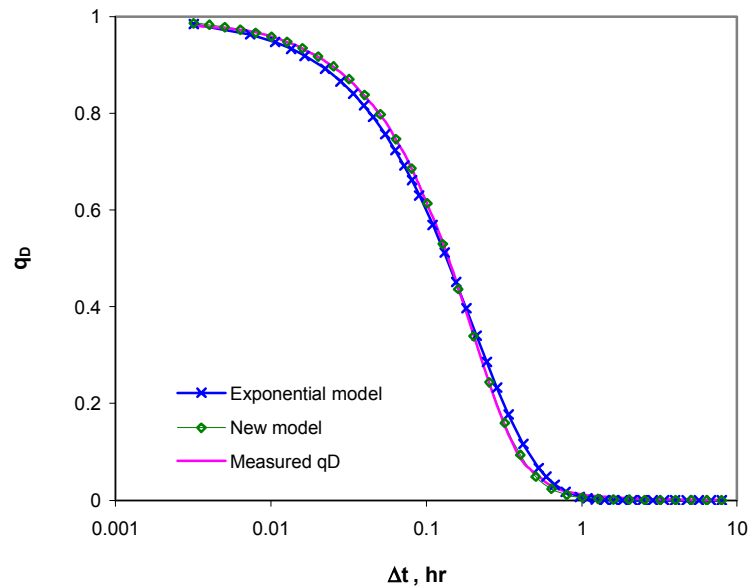


Fig. 4-8—Measured vs. regressed afterflow rates.

4.3.3 Nonlinear Regression of Afterflow Rate Function

Measured afterflow rates contain noise, and we need to smooth the afterflow rates and remove the measurement noise. In the previous section, we proposed an improved afterflow rate model, which can help us smooth observed rate data. In this section we will discuss a regression analysis procedure using this function to match the afterflow measurement. Since a reservoir can be considered to be a large capacitor, it will naturally damp fluctuations of afterflow rate. Therefore, true afterflow rates should be smooth. Regression of rate measurements can serve as an effective way to remove the noise in the measured rates.

We use normalized afterflow rate ($q_{Dj} = q(\Delta t_j)/q(0)$, normalized to the range of 0 to 1) to study the behavior of afterflow, as shown in Figs. 4-7 and 4-8. We are also particularly

concerned with the differential in afterflow rate, $\Delta q_{Dj} = q_{Dj} - q_{Dj+1}$. Recall our basic formula – the convolution integral equation (Eq. 4-7).

$$\Delta p_w(t) = \int_0^t r(\tau) \Delta p_\delta(t - \tau) d\tau \quad (4-7)$$

In this equation, r represents the time derivative of dimensionless afterflow rate. In the discrete form, this equation becomes Eq. 4-11.

$$p_w(n\Delta t) = \sum_{j=1}^n \Delta q_D(j\Delta t) p_\delta(n\Delta t - j\Delta t) \quad (4-11)$$

It can be seen that the dimensionless afterflow rate differential (Δq_D) is actually involved in the convolution operation. In fact, the dimensionless afterflow rate differential is required for our deconvolution operation, and its behavior greatly affects the accuracy of deconvolution. Because of its equivalence to differentiation, Δq_D is much more sensitive to noise than q_D . Fig. 4-9 demonstrates the semi-log plot of dimensionless afterflow rate differential for a noise-free synthetic case. It shows smooth behavior. However, for actual measurement data, Δq_D may oscillate and may be distorted. Fig. 4-10 is the semilog plot of Δq_D for an actual rate measurement. Even though the measured q_D can look smooth (Fig. 4-8), the noise in Δq_D is quite apparent (Fig. 4-10).

Thus, we perform regression not only on the dimensionless afterflow rate but also on the dimensionless afterflow rate differential. The objective function for regression is formulated as:

$$MIN \quad J_t = \sum [q_{D,mod}(t) - q_{D,meas}(t)]^2 + \sum \left\{ \frac{\Delta q_{D,mod}(t)}{\max[\Delta q_{D,mod}(t)]} - \frac{\Delta q_{D,meas}(t)}{\max[\Delta q_{D,meas}(t)]} \right\}^2 \quad (4-23)$$

where $q_{D,mod}$ is the dimensionless afterflow rate from Eq. 4-22, and $q_{D,meas}$ is from afterflow rate measurement. The dimensionless afterflow rate differential in the second sum term is normalized to interval [0, 1] so that both q_D and Δq_D can account for the same weight in minimization.

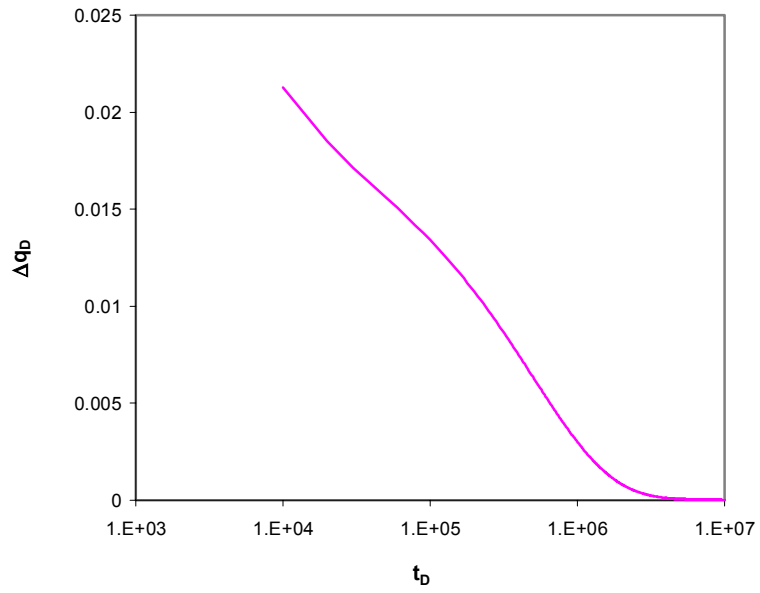


Fig. 4-9—Semilog plot of unloading rate differential, Δq_D .

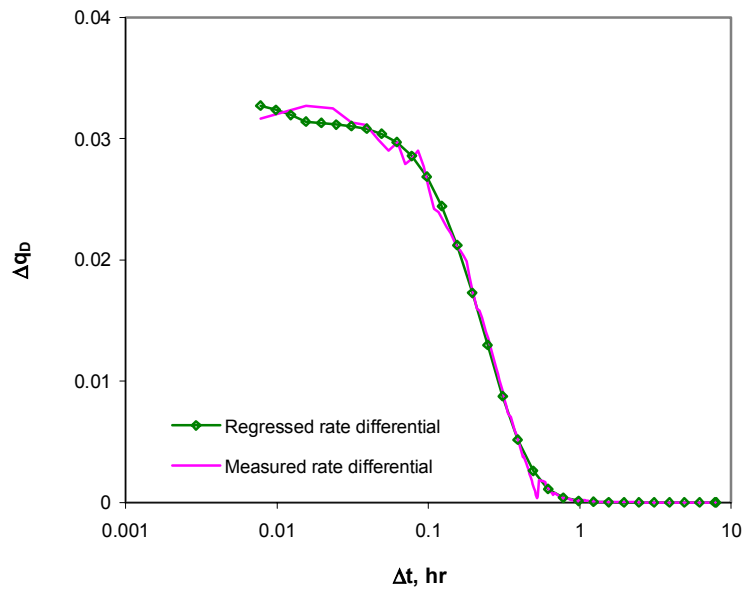


Fig. 4-10—Semilog plot of afterflow rate differential, Δq_D .
(1024 interpolated points)

Another important step in our regression procedure is also to regress the dimensionless afterflow rate and its differential in the frequency domain. So, regression is performed in both the time and frequency domains simultaneously. As can be seen from Eq. 4-5, the Fourier transform at each frequency involves information on all data points in the time domain. In other words, all the information in the time domain, at both large and small times, has been integrated into the spectral component in the frequency domain. Therefore, regression in the frequency domain can improve the match of small values of q_D that occur at large times in the time domain. The objective function in the frequency domain is formulated as:

$$MIN \ J_f = \sum [\Delta \tilde{q}_{D,mod}(f) - \Delta \tilde{q}_{D,meas}(f)]^2 + \sum \left\{ \frac{\tilde{q}_{D,mod}(f)}{\max[\tilde{q}_{D,mod}(f)]} - \frac{\tilde{q}_{D,meas}(f)}{\max[\tilde{q}_{D,meas}(f)]} \right\}^2 \quad (4-24)$$

where the head ' \sim ' stands for the Fourier transform. For an actual rate measurement, Fig. 4-11 shows the obvious improvement in fitting the measured q_D for values below 0.2 with regression in both time and frequency domains.

Another advantage of regression in the frequency domain is reduction of the influence of the noise component in the process of matching afterflow rate data. Noise components located in the high-frequency range have much smaller amplitudes (several orders of magnitude less) than signal components at low frequencies. So, in the objective function to be minimized, the signal components completely dominate, which is favorable to obtain an afterflow rate function representing a noise-free signal.

The final combined objective function is

$$MIN \ J = MIN \ (J_t + J_f) \quad (4-25)$$

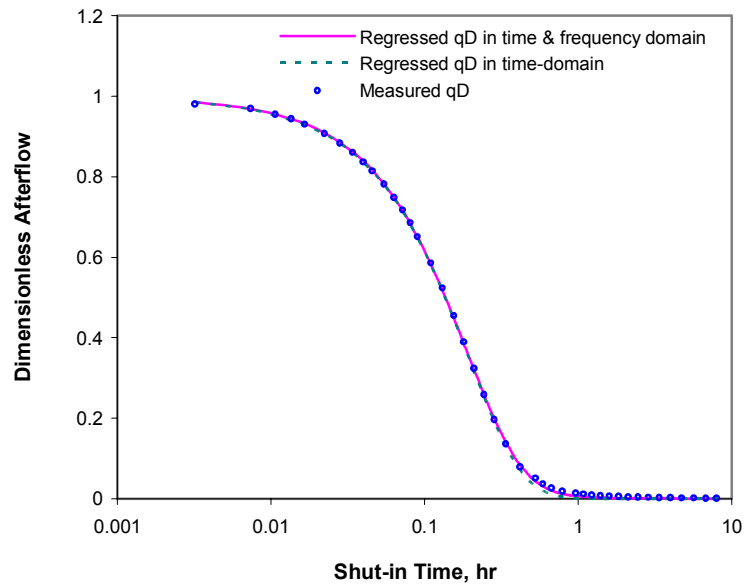


Fig. 4-11—Regressed and measured afterflow rates.

4.3.4 Denoising Technique

Our denoising technique consists of two major components. The first component involves using the new rate model with the regression procedure to obtain a denoised afterflow differential (Δq_D). As mentioned before, Δq_D is the quantity to be used in our deconvolution operation. With this smoothed afterflow rate differential, we can expect a much better deconvolution result. The second component is to regress on mid/high frequency data of the deconvolved pressure solution using the Levy probability density function to further remove noise in the deconvolved pressure. We will illustrate the denoising procedure with a synthetic case.

The synthetic case is the previous dual-porosity reservoir case. We add noise to the rate and pressure data. A noisy set of rate data with RMSE (root-mean-squared-error) of 17.3% for Δq_D were generated, as shown in Fig. 4-12. In the dimensionless pressure data range of 0.04–8.76, we added noise (random error) to the set of dimensionless pressure data with an error range of 0.01 (Fig. 4-13).

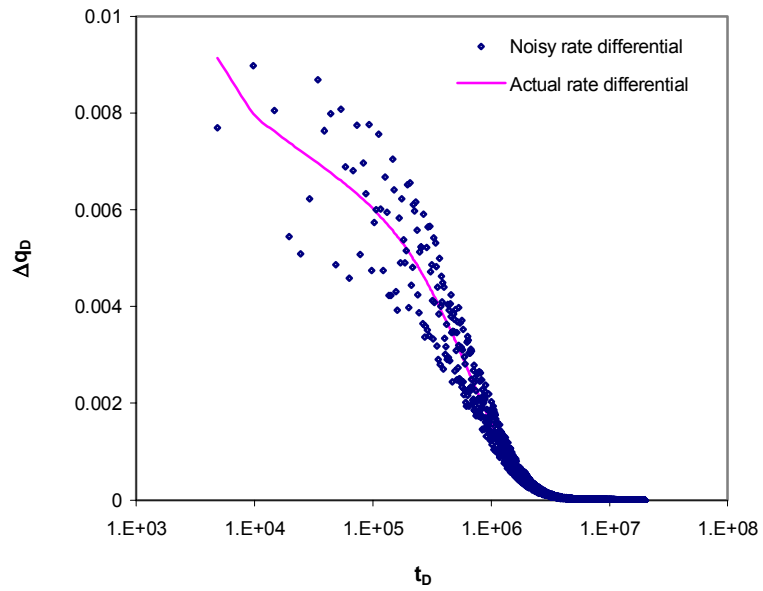


Fig. 4-12—Noisy unloading rate differential.

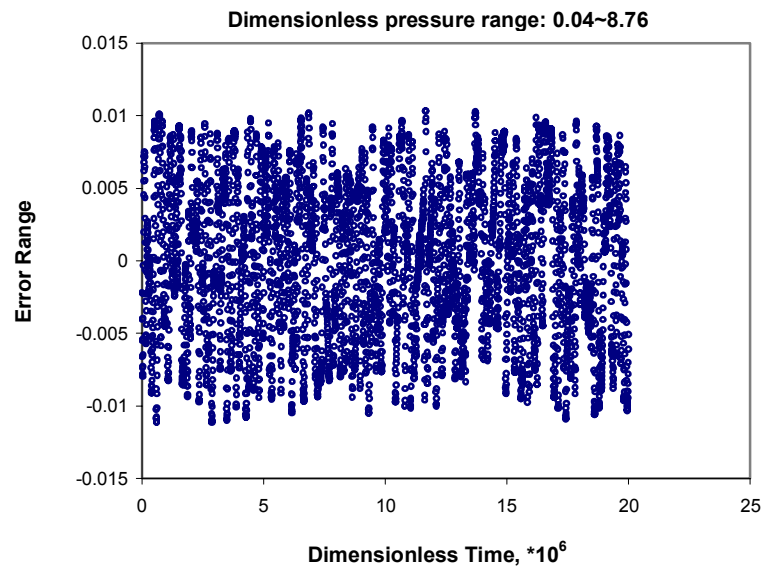


Fig. 4-13—Error range of noisy dimensionless pressure response.

Denoising Afterflow/Unloading Rate. Using the new model (Eq. 4-22) and our regression procedure discussed in Section 4.3.3, we obtain a denoised rate differential, as shown in Fig 4-14. The regressed rate differential has recovered the behavior of actual rate change almost exactly.

We deconvolved the noise-free dimensionless pressure with the noisy rates (Fig. 4-12) and the denoised rates from our afterflow rate model (Fig. 4-14). Fig. 4-15 displays the deconvolution result based on the noisy rates, and Fig. 4-16 shows the deconvolution result based on the denoised rates. Comparison of these two figures indicates that the noise in rate has significant detrimental effects on deconvolution and results in large oscillations in the deconvolution solution. As shown in Fig. 4-16, the deconvolved pressure based on the denoised rates is very close to the analytical solution, which validates the effectiveness of the regressed rates for removing the noises in rate data.

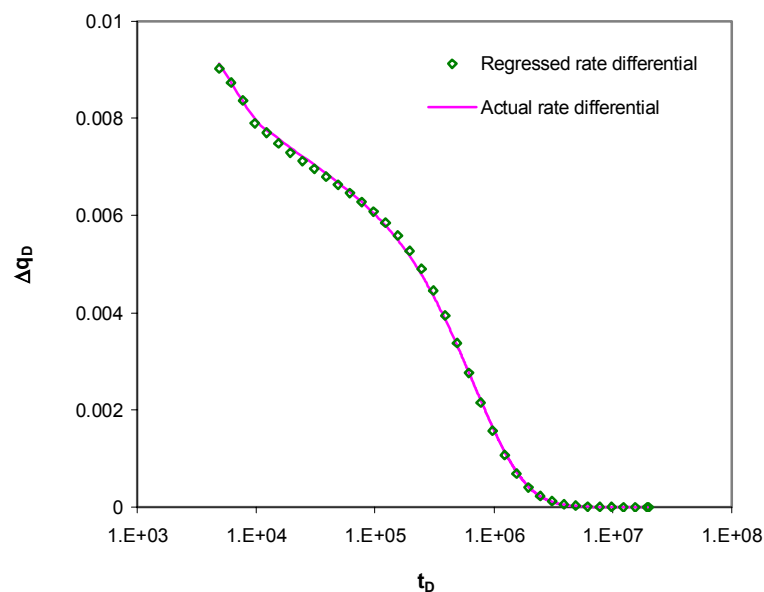


Fig. 4-14—Regression of dimensionless unloading rate differential.

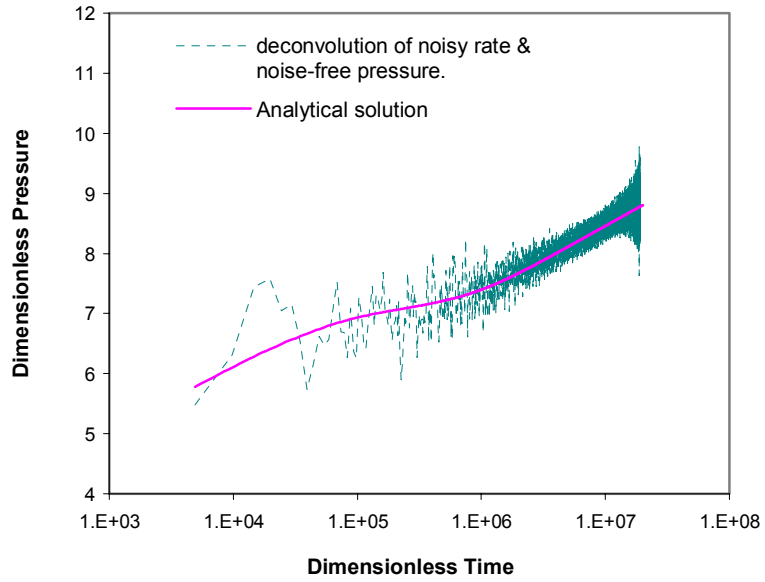


Figure 4-15—Deconvolution of noisy rate and noise-free pressure.

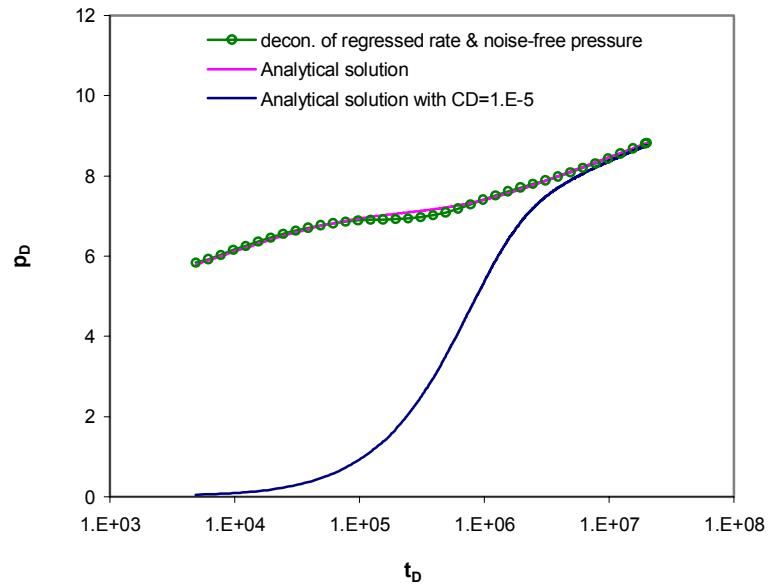


Fig. 4-16—Deconvolution of denoised rate and noise-free pressure.

Deconvolution of the Denoised Rate and the Noisy Pressure. From Eq. 4-19, we can see that noise in pressure data also causes uncertainty in the deconvolution result. Fig. 4-17 shows the deconvolution result using the denoised set of rate data and the noisy set of dimensionless pressure data. Obviously, noise in pressure also causes serious oscillation of the deconvolved pressure. Therefore, we need to further denoise the deconvolved pressure.

Examining the spectrum of the deconvolved pressure in the frequency domain (Fig. 4-18), we observe that the information at mid/high frequency has been heavily contaminated by noise. Fortunately, the noise was not completely destroyed the mid/high frequency information. The noise tends to mask the mid/high frequency information of the true signal by imposing serious additive oscillations upon the signal.

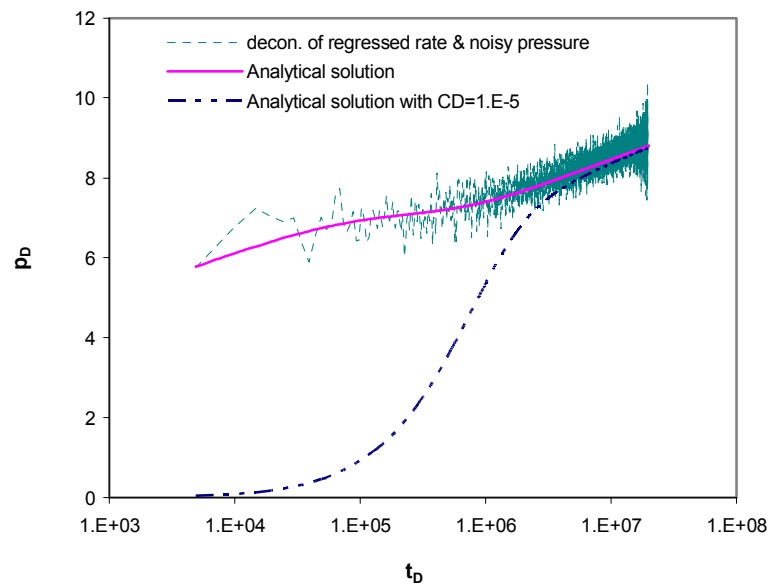


Fig. 4-17—Deconvolution of denoised rate and noisy pressure.

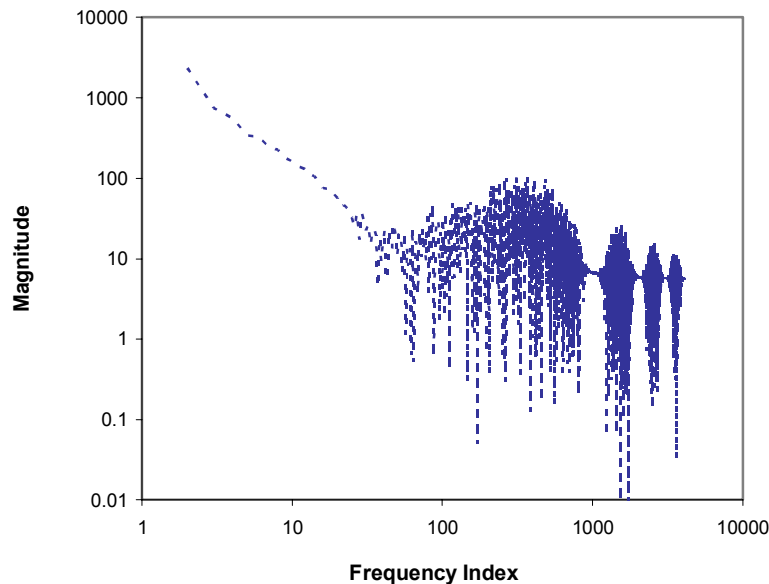


Fig. 4-18—Deconvolved pressure in frequency domain.

Further Denoising the Deconvolved Pressure. Our study found that the frequency-domain characteristics of the constant-rate pressure solution for different types of reservoir/well systems can be represented well by the Levy probability density function at some frequency ranges such as mid-frequency and high-frequency bands. The Levy function is expressed as:

$$L(f) = e^{-\alpha f^{2\beta}} \quad (4-26)$$

where α and β are two non-negative constants to be determined by regression. We investigated four types of reservoir/well systems: homogeneous reservoir, dual-porosity reservoir, vertically-fractured well, and horizontal well. We proved that a single function – the Levy function – is capable of describing the constant-rate pressure behavior of various reservoir systems in the frequency domain. We transformed the constant-rate pressure solutions for the above reservoirs into the frequency domain, then used Levy function to match them. Regression results are shown in Fig. 4-19 ~ Fig. 4-22. The regressed representations are remarkably consistent with the solutions of various reservoir systems in the frequency domain. From this observation, we can conclude that it is possible to further denoise the deconvolved pressure in the frequency domain with the aid of the Levy function.

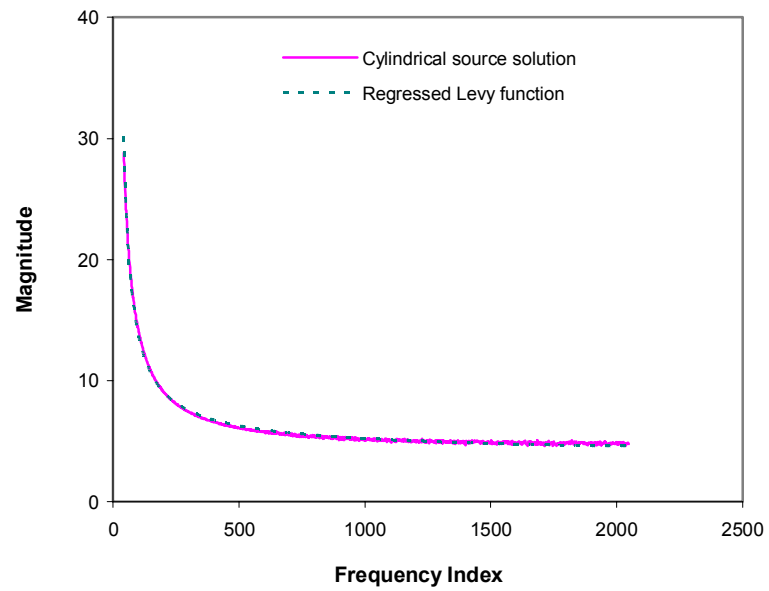


Fig. 4-19—Homogeneous reservoir solution in frequency domain.

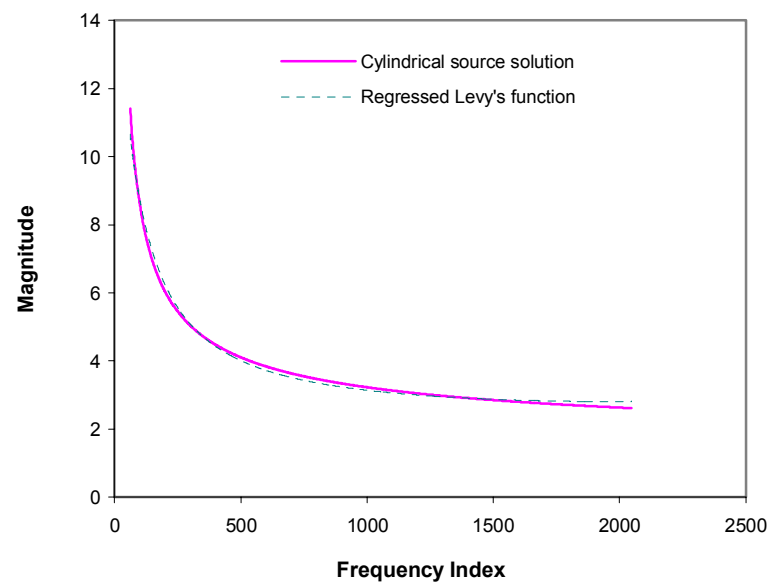


Fig. 4-20—Dual-porosity reservoir solution in frequency domain.

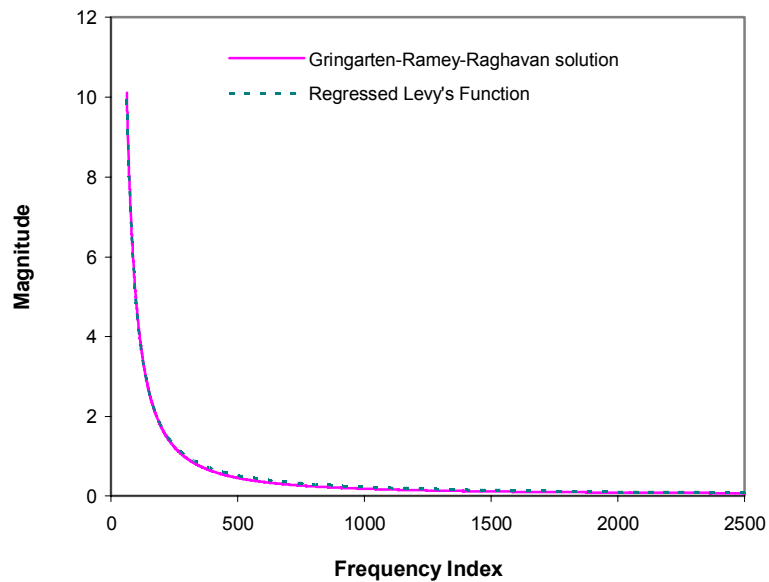


Fig. 4-21—Vertically fractured well solution in frequency domain.

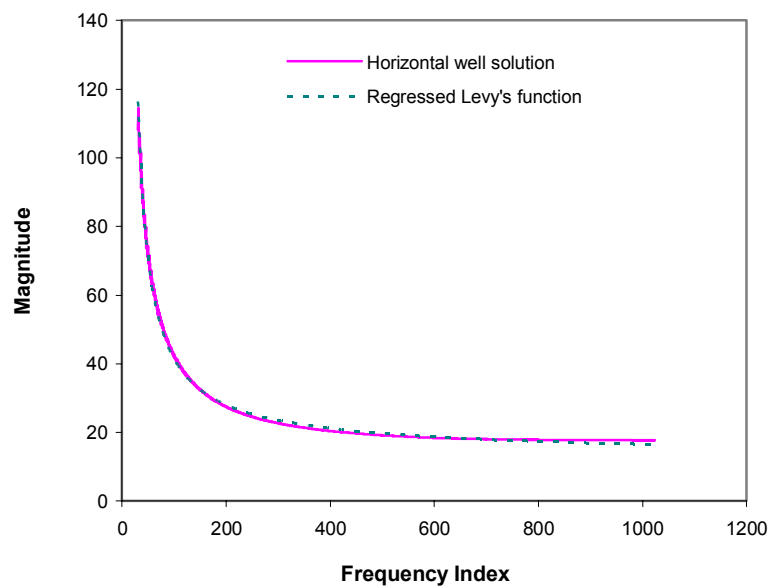


Fig. 4-22—Horizontal well solution in frequency domain.

It has been shown in Fig. 4-18 that the deconvolved pressure is seriously contaminated by noise at mid/high frequency bands. So we perform regression at mid/high frequency with the Levy function while retaining the low-frequency information. We compare the analytical solution and the regressed deconvolved pressure in the frequency domain (Fig. 4-23), and observe excellent consistency between them. When we inverted the regressed deconvolved pressure in the frequency domain back to the time domain, we obtained the final denoised constant-rate pressure, shown in Fig. 4-24 (log-log plot) and Fig. 4-25 (semi-log plot). Although there is some deviation from the analytical solution, the deconvolved pressure derivative in the log-log plot (Fig. 4-24) provides sufficient information for identifying the reservoir system. It displays very clearly the dual-porosity reservoir characteristics. Compared with the analytical solution, the final deconvolved pressure in the semi-log plot (Fig. 4-25) is recovered quite effectively, which provides a sound basis for accurate parameter estimation.

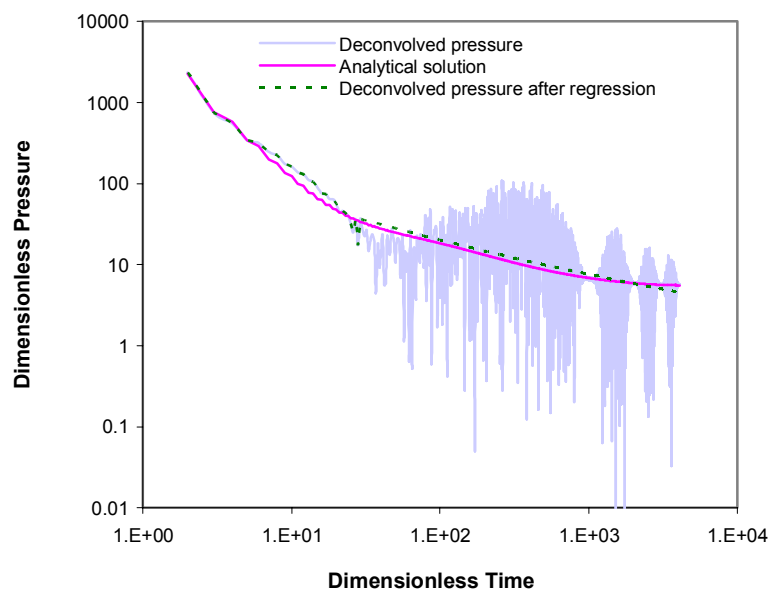


Fig. 4-23—Regression of deconvolved pressure in frequency domain.

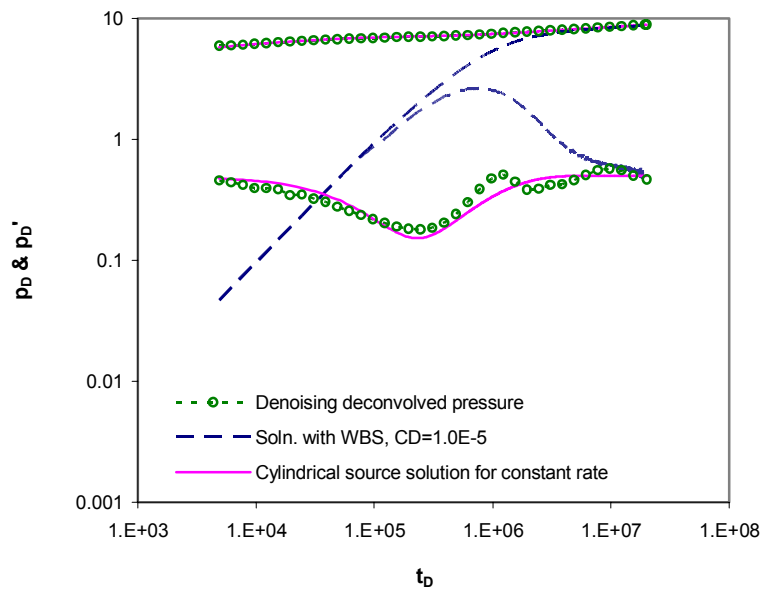


Fig. 4-24—Deconvolution result using denoising technique (log-log plot).

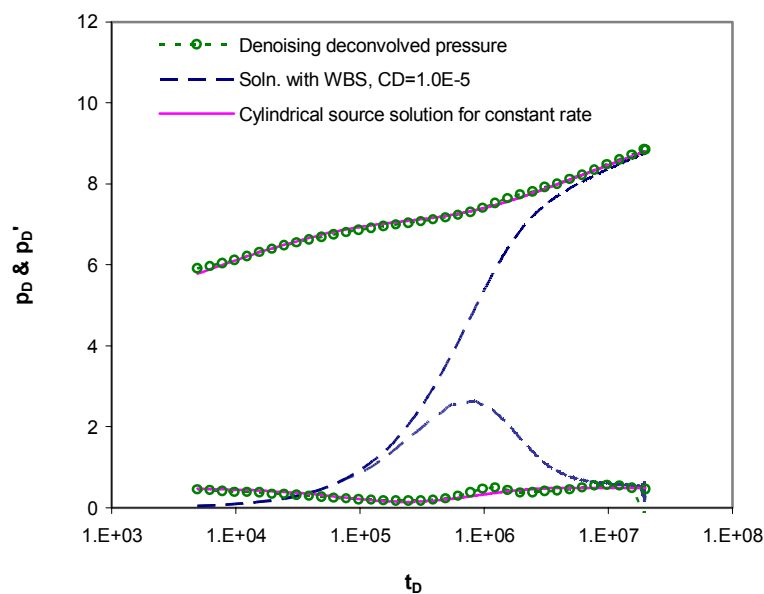


Fig. 4-25—Deconvolution result using denoising technique (semi-log plot).

4.3.5 Applications

In section 4.3.4, we presented the procedures of denoising technique and proved the applicability of this technique with a synthetic case. Here, we will apply this technique to a field case. This is an oil well reported by Meunier, Wittmann, and Stewart,⁵¹ which includes simultaneously measured bottomhole pressure and rate data during a buildup test.

Oil-well Case. Fig 4-26 illustrates the measured and regressed afterflow rate data. The regressed afterflow rates closely fit the measured data and capture the major characteristics of the afterflow rate. Fig. 4-27 is a semi-log plot of the measured and deconvolved pressures. The deconvolved pressures include those from direct deconvolution of the measured pressure and measured rate, and from deconvolution of the measured pressure and regressed rate. The latter is obviously much smoother than the direct deconvolution result, but the pressure derivative is not useful for system identification since there are still some oscillations in the pressure solution, which prevents us from obtaining smooth pressure derivatives. Fig 4-28 illustrates the final result obtained by denoising the deconvolved pressure. The pressure derivative plot in Fig 4-29 now becomes smooth and indicates dual-porosity reservoir features. This observation is consistent with evidence from production logging. Production logging during the shut-in indicated persistent crossflow between two layers of the reservoir,⁴⁹ which may cause pressure buildup test behavior similar to a dual-porosity reservoir.

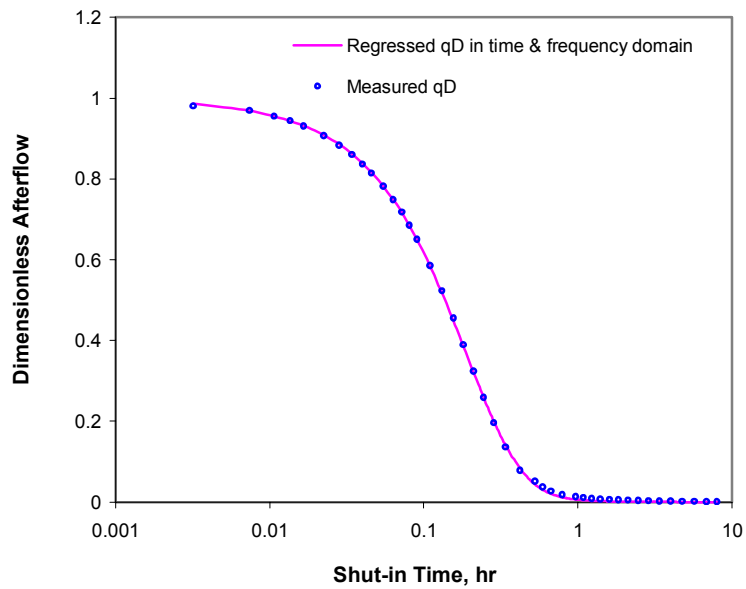


Fig. 4-26—Regressed and measured afterflow rate.

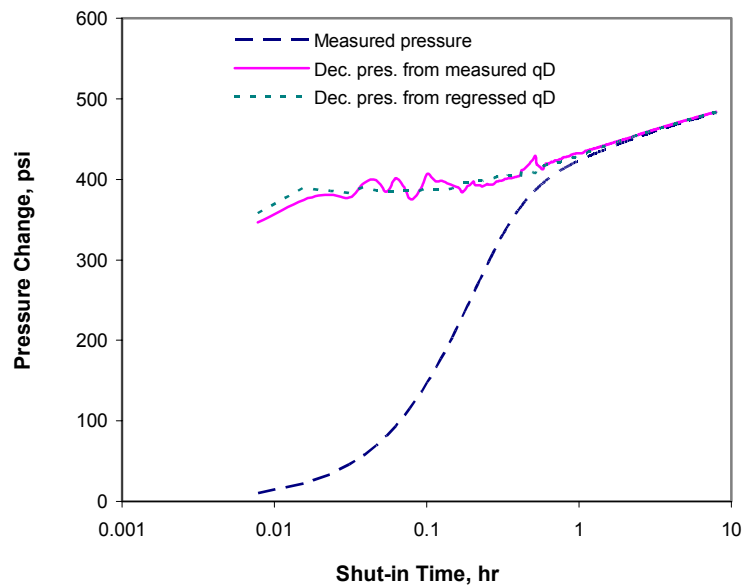


Fig. 4-27—Deconvolution result using regressed afterflow rate.

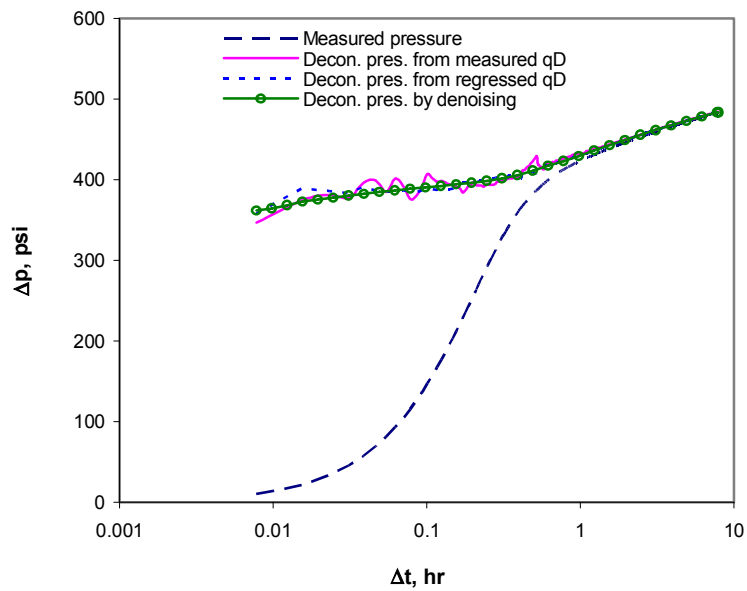


Fig. 4-28—Denoising deconvolved pressure.

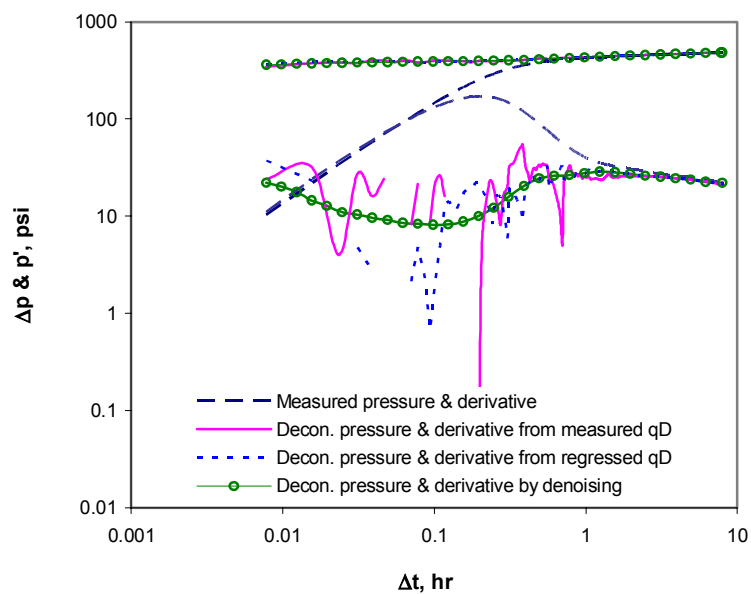


Fig. 4-29—Denoised pressure derivative.

4.4 Blind Deconvolution

In section 4.3, we discussed the deconvolution problem using measured rates. However, we do not always have afterflow rate measurements in actual well tests. When there are no rate measurements to deconvolve with the observed pressures, we need a technique to detect afterflow rate and unveil the undistorted pressure simultaneously; this process is called blind deconvolution.

Although blind deconvolution has been a very active research area in many fields over the last two decades, such as signal processing and imaging processing,⁶³⁻⁶⁶ it has been remained relatively unexplored in well testing. In blind deconvolution, we are required to simultaneously identify the unknown rate and reconstruct the constant-rate pressure response.

Blind deconvolution is a difficult problem. It is critical to restrict the space of plausible solutions for successful blind deconvolution. Most blind deconvolution approaches are iterative in nature. Iterative blind deconvolution usually treats all the data points in the deconvolution solution and the convolution kernel (the rate derivative) as the parameters to be estimated. With no restrictions on the plausible solutions, convergence is always a problem for iterative blind deconvolution.

In our study, we use Fourier analysis to limit the space of plausible solutions of our blind deconvolution to a series of parallel lines of the integral rate functions in the frequency domain. In this way, the parameters to be estimated have been collapsed into a single parameter, that is, the distance of a parallel line from the base line (illustrated in the following section). As a result, our blind deconvolution has been transformed into a single parameter estimation problem. We use a minimum energy criterion to estimate the best distance. This proves to be very efficient.

4.4.1 Methodology

With the observed pressure response only, how can we estimate the afterflow rates? As we know, the constant wellbore storage coefficient model (Eq. 4-20) is inadequate in most situations. Fig. 4-30, based on the Meunier *et al.*⁵¹ data, shows that the calculated afterflow rates using Eq. 4-20 differ significantly from the measured rates. The main reasons behind this include the amplification of measurement error in the pressure response with the process of differentiation and the influence of variable wellbore storage caused by various wellbore effects,

such as wellbore storage, phase redistribution and momentum.^{51,77} However, when we transformed the calculated rates (using the classical model, Eq. 20) into the frequency domain, we observed two useful signatures which provided us the possibility of using only the observed pressures to estimate afterflow rates and recover the constant-rate pressure responses. One feature is that the magnitudes of two rates at the mid-frequency band basically remain consistent with each other. Another feature is that the integral function of the calculated afterflow rate is parallel to that of the measured afterflow rate in the frequency domain. These two features provide us with incomplete yet quite valuable information. We will discuss the details of these two features based on the Fourier analysis of the observed pressure data in the following sections.

Signature of Dimensionless Afterflow Rate in Frequency Domain. Before transforming the measured pressures or calculated afterflow rates into the frequency domain, we need to interpolate to get evenly spaced points, as required by the FFT algorithm. As a result, we can conveniently use the time index as the abscissa instead of time to plot the data. In this way, the afterflow behavior near time zero can be more clearly displayed on a semi-log plot (the time index begins at one, when time is zero). Redrawing Fig. 4-30, we obtain Fig. 4-31 with the time index as abscissa, in which the dimensionless afterflow (q_D) rate behavior is now indicated more clearly on the whole time interval. Therefore, in the following, we will consider the dimensionless afterflow rate (q_D) as a function of the time index for better demonstration.

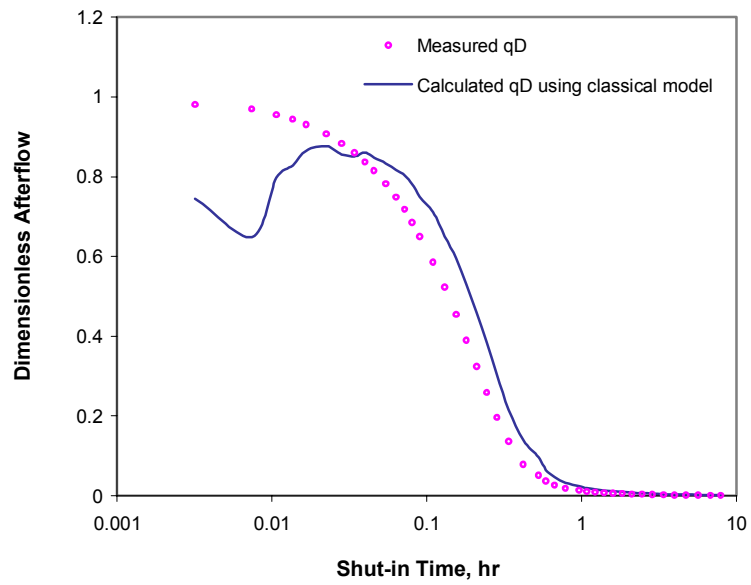


Fig. 4-30—Measured q_D and calculated q_D using classical model (shut-in time).

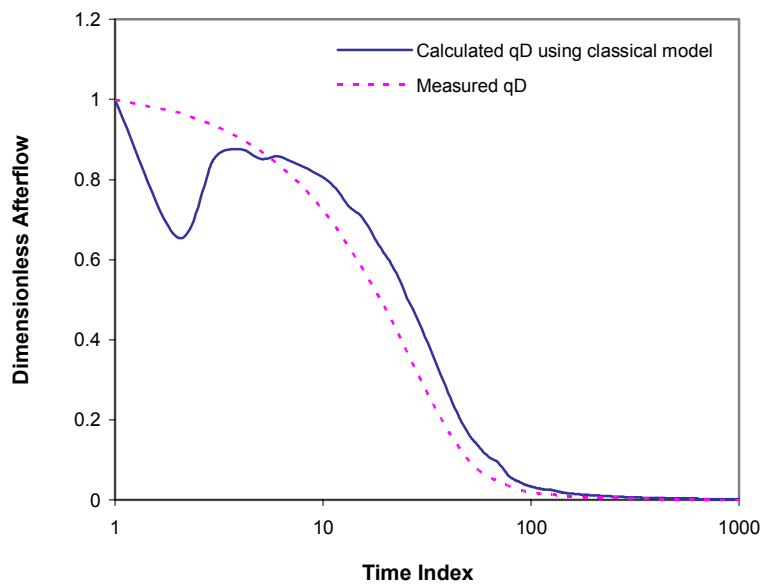


Fig. 4-31—Measured q_D and calculated q_D using classical model (time index).

Fig. 4-32 illustrates the frequency-domain signature of the dimensionless afterflow rate (q_D). As mentioned before, the magnitude of the calculated q_D (in the following, calculated q_D means the q_D calculated from wellbore pressure using the classical wellbore model) in the mid-frequency band is close to that of the measured q_D . Therefore, we can restrict the plausible solutions of q_D as those matching the mid-frequency band information of calculated q_D . We use the new rate model (Eq. 4-22) to describe the plausible rate solutions. We set up an objective function, Eq. 4-27 and require the plausible rate solution to minimize this objective function.

$$\text{MIN } J_{f,m} = \sum_{j=js}^{\frac{N}{2}-je} [\tilde{q}_{D,\text{mod}}(f_j) - \tilde{q}_{D,\text{cal}}(f_j)]^2 \quad (4-27)$$

where $q_{D,\text{mod}}$ is the dimensionless afterflow obtained from the new model (Eq. 4-22) and $q_{D,\text{cal}}$ is from the classical wellbore model (Eq. 4-20). N is the total number of frequency indices, and $N/2$ corresponds to the Nyquist (highest) frequency. js represents the starting point for the regressed mid-frequency band. je represents the distance of the endpoint from $N/2$ and may be roughly estimated as tenth of N . As for the starting point (js), we will refer to the inflection point in the phase plot (Fig. 4-33) of the calculated q_D .

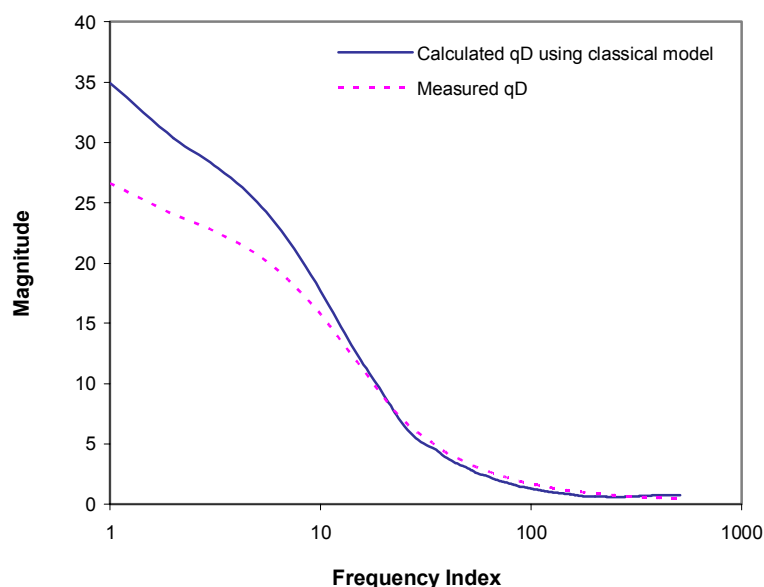


Fig. 4-32—Magnitude of measured q_D and calculated q_D in frequency domain.

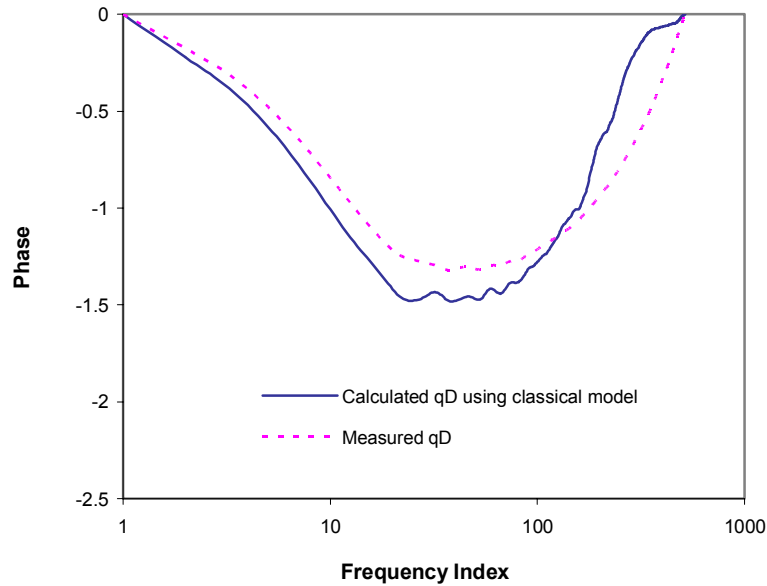


Fig. 4-33—Phase of measured q_D and calculated q_D in frequency domain.

Signature of Dimensionless Afterflow Rate-Integral in Frequency Domain. We numerically integrate the dimensionless afterflow rates (q_D) on each time interval and obtain a q_D integral at each time point. When we transform the q_D integral to the frequency domain, we find that the magnitudes of the calculated q_D integrals are basically parallel to those of the measured q_D integrals on the log-log plot except for the first few points (Fig. 4-34). Also the integral of the measured rate is below the integral of the calculated rate. Therefore, in the situation with no measured q_D , we can assume that a close approximation to the true rate lies in one of the lines parallel to calculated q_D integral. Therefore, we can restrict the plausible rate solutions to those matching these parallel lines of the rate integral in the frequency domain. Similarly, we set up an objective function, and require the plausible rate solutions to minimize this objective function.

$$\text{MIN } J_{f,l} = \sum [\tilde{q}_{D-\text{integ,mod}}(f) - \tilde{q}_{D-\text{integ},l}(f)]^2 \quad (4-28)$$

where l is the index of the pre-selected parallel line. By combining the previous two objective functions, we have our combined objective function written as:

$$\text{MIN } J = \text{MIN } (J_{f,m} + J_{f,l}) \quad (4-29)$$

This requires the plausible solutions of q_D to simultaneously match both the mid-frequency band information of q_D and the parallel lines of the q_D integral. The minimization will allow us to determine a set of coefficients (c_1-c_4) for each of the plausible solutions of q_D .

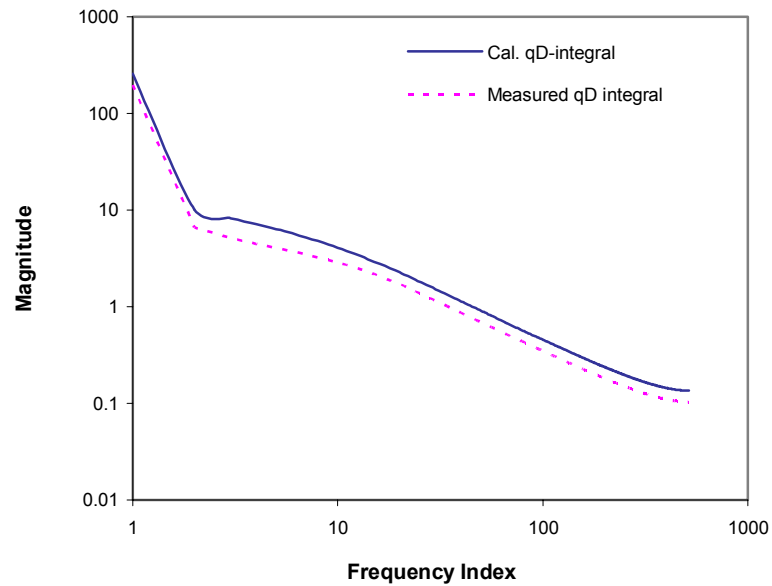


Fig. 4-34—Magnitude of q_D -integral in frequency domain.

We also studied other field cases. Figs. 4-35 and 4-36 show the case of Oil Well No. 1 in Ref. 50. Figs. 4-37 and 4-38 show the field case reported in the Ref. 47. We can see that these signatures are common.

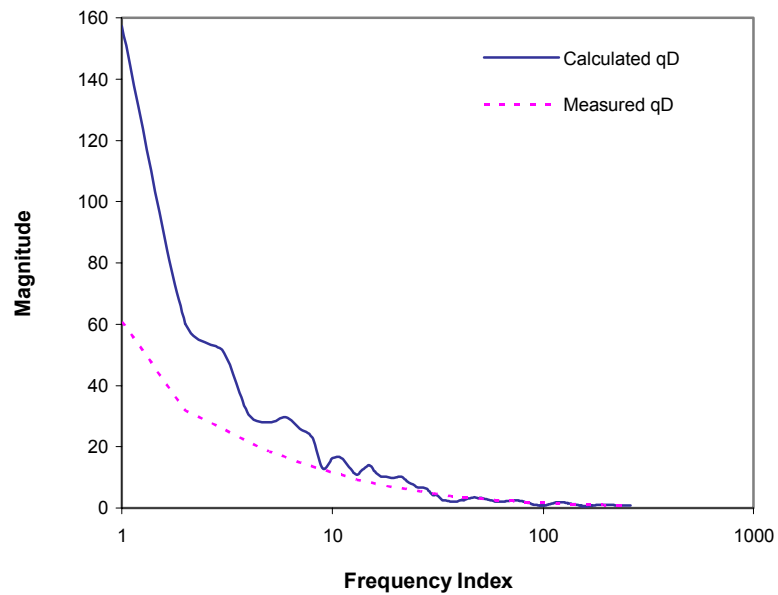


Fig. 4-35—Magnitude of q_D in frequency domain (Oil Well No. 1, Ref. 50).

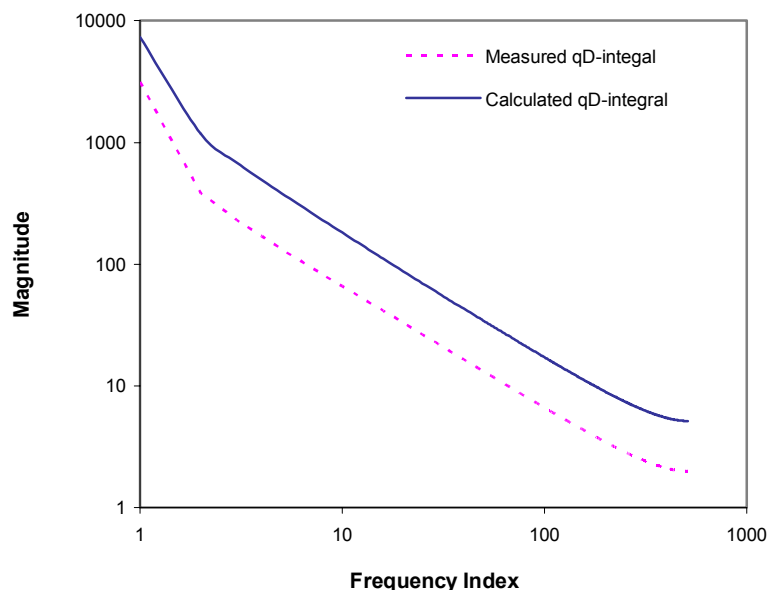


Fig. 4-36—Magnitude of q_D -integral in frequency domain (Oil Well No 1, Ref. 50).

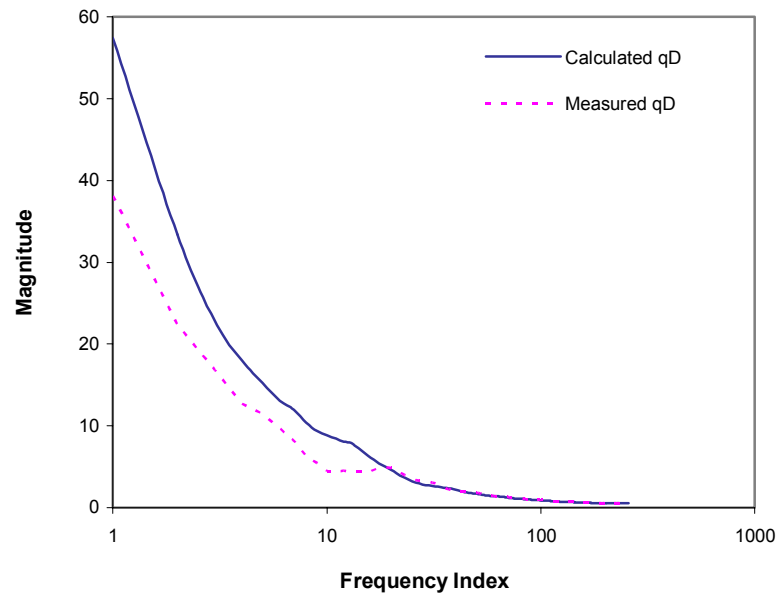


Fig. 4-37—Magnitude of q_D in frequency domain (field case, Ref. 47).

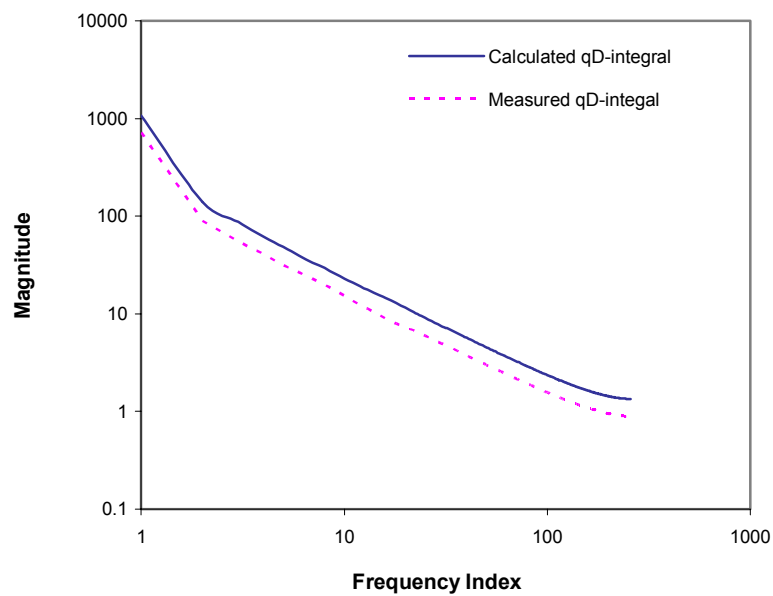


Fig. 4-38—Magnitude of q_D -integral in frequency domain (field case, Ref. 47).

Detection of Afterflow and Recovery of Constant-Rate Pressure. The regressions described above will generate a series of plausible rate functions. The next question is “which one should be picked as the best approximation to the true rate function?” Applying each of the plausible q_D values, we can obtain the corresponding deconvolved pressure solution. Baygun, Kuchuk, and Arikian⁵⁸ used an energy constraint in least-square deconvolution efforts. In our study, we use a similar energy criterion to determine the best distance or step size (the single parameter discussed earlier). Our energy criterion consists of two terms. One term is the sum of squared time derivatives of the deconvolved pressures. The other term is the sum of squared time derivatives of the dimensionless rate functions. Because of the limited energy of the reservoir/well system, we select the parallel line that gives the minimum energy as our optimal solution.

Here, we give a brief summary of our blind deconvolution procedure:

1. Calculate dimensionless afterflow ($q_{D,cal}$) using the classical model (Eq. 4-20). Then transform $q_{D,cal}$ into the frequency domain and select the mid-frequency band for regression.
2. Calculate $q_{D,cal}$ -integral and transform it into the frequency domain. Then design a set of parallel lines, which are parallel to and located below the $q_{D,cal}$ -integral line on the log-log plot of the magnitude of the q_D -integral.
3. Simultaneously minimize the objective functions, Eq. 4-27 for $q_{D,cal}$ and Eq. 4-28 for $q_{D,cal}$ -integral (i.e., minimize the combined objective function, Eq. 4-29), to obtain a regressed q_D corresponding to each parallel line until all pre-designed parallel lines are used. This will produce a series of plausible q_D solutions corresponding to the parallel lines.
4. Perform deconvolution using the plausible q_D solutions to obtain the deconvolved pressure solutions corresponding each q_D solutions. Screen q_D using the energy criteria, and find the one that produces the minimum energy. This final q_D represents the detected rate and the corresponding deconvolved pressure is the recovered constant-rate pressure solutions.

4.4.2 Applications

We have presented the procedures of blind deconvolution method in the previous section. In this section, we demonstrate its applicability using one synthetic case and two field cases.

Synthetic Case. This is a gas-well case, based on Example 6.4 in the book, *Gas Reservoir Engineering* by W. John Lee and Robert A. Wattenbarger.⁷⁸ The data are listed in Table 6.9 in the reference. As Lee and Holditch⁷⁹ pointed out, a gas-well flow problem can be conveniently solved using the slightly-compressible fluid methodology if pseudo-pressure and pseudo-time are used to replace pressure and time. We use normalized pseudopressure and pseudotime, which we call adjusted pressure and adjusted time, based on Table 6.9 of Ref. 78.

We pre-select a set of parallel lines with step sizes of 0.0, 0.01, 0.05, and 0.1, respectively. The step size stands for the distance between magnitudes of the pre-selected line and that of the calculated q_D . Fig. 4-39 illustrates the plausible set of afterflow rates, and Fig. 4-40 the corresponding set of deconvolved pressures. Based on the minimum energy criteria, the detected afterflow rates and restored pressures correspond to a step size of 0.0 (the quantities of energy are 268.08, 268.74, 269.22, and 288.64, respectively, for the parallel lines in the set). This result is exactly what we expect because the synthetic case assumes a constant wellbore storage coefficient. Since we use the constant wellbore-storage model to obtain the calculated q_D , among the set of parallel lines the line without deviation (zero step size) from the calculated q_D is the expected solution. In this case, although we only used a part of the data (from shut-in time to 16 hrs) to perform deconvolution, the restored pressures successfully recover the semi-log straight line (Fig. 4-41). This not only demonstrates that the blind deconvolution method is effective in successful detection of afterflow rate and recovery of pressure response, but also indicates that this method is applicable for a short test. With the deconvolved pressures, estimation of the reservoir parameters can proceed and the results, shown in Fig. 4-41, agree well with those of Example 6.4.⁷⁸

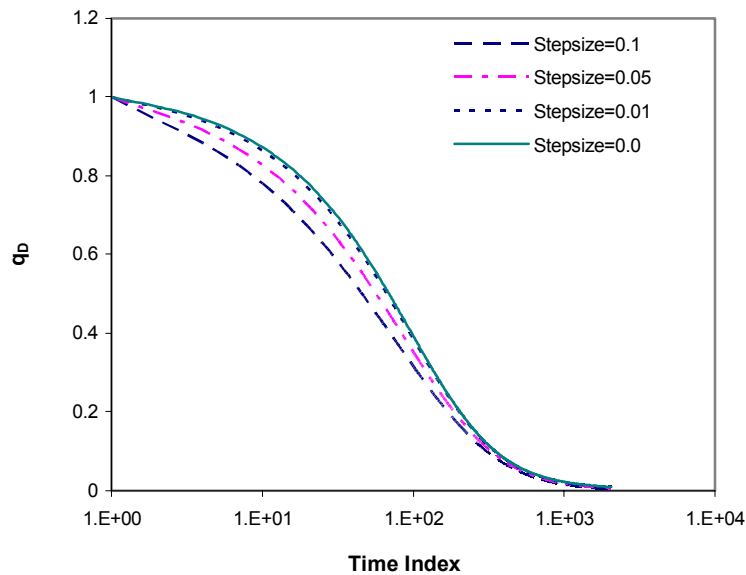


Fig. 4-39—Plausible set of q_D values.

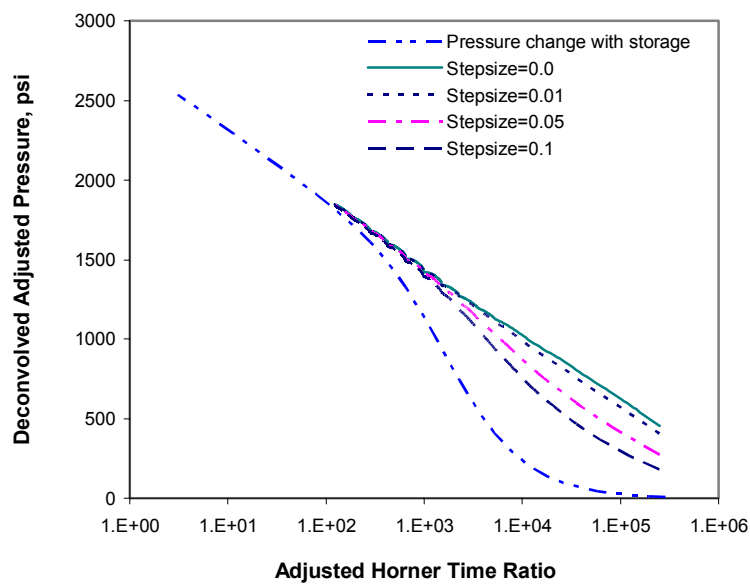


Fig. 4-40—Plausible set of deconvolved pressures.

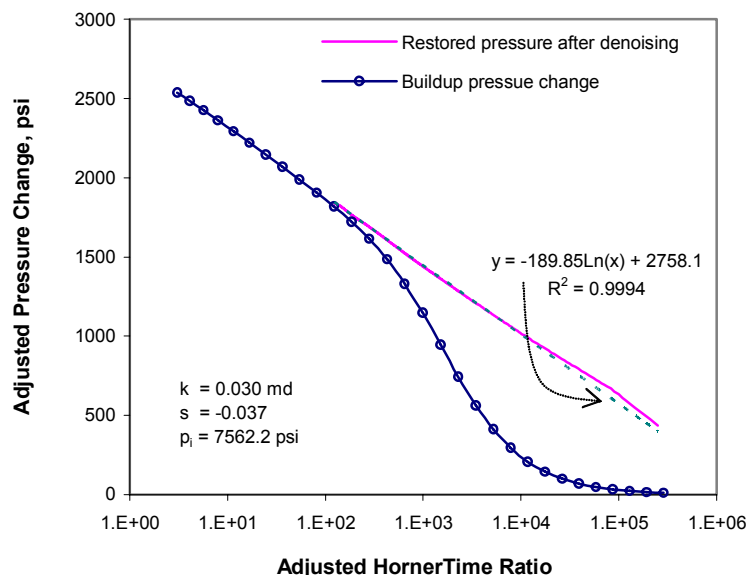
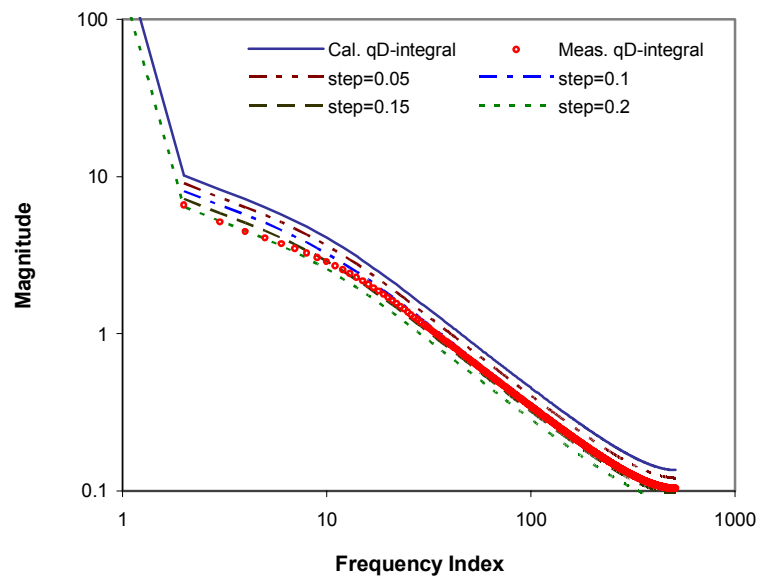


Fig. 4-41—Restored pressures using detected afterflow q_D .

Field Case 1. We again use the oil-well case reported by Meunier, Wittmann, and Stewart.⁵¹ The basic reservoir and fluid properties are shown in Table 4-2. A set of parallel lines are designed with stepsizes of 0.05, 0.1, 0.12, 0.15, and 0.2, respectively (Fig. 4-42). Fig 4-43 illustrates the plausible set of afterflow rates, and Fig 4-44 the corresponding set of deconvolved pressures. The detected afterflow and restored pressure solutions are determined based on the minimum energy criterion, which corresponds to a step size of 0.12 (Fig. 4-45). Fig. 4-46 shows that the detected afterflow rate is close to the measured q_D , especially for early-time data. The pressure deconvolved with the calculated q_D from the classical wellbore model oscillates badly, but can be greatly improved when we deconvolve with the detected q_D values (Fig. 4-47). Since the restored pressure still has some small oscillations, we further apply our denoising techniques. Fig. 4-48 illustrates the restored pressure and the pressure derivative after denoising. For the purpose of comparison, the restored pressure and the pressure derivative before denoising are also shown in Fig. 4-48. From the pressure derivative after denoising, the dual-porosity feature is identifiable.

TABLE 4-2—RESERVOIR AND FLUID PROPERTIES FOR FIELD CASE 1

Porosity, ϕ	= 0.27
Viscosity, μ	= 1.24 cp
Compressibility, c_t	= $2.5 \cdot 10^{-5}$ 1/psi
Formation volume factor, B	= 1.24 RB/STB
Wellbore radius, r_w	= 0.25 ft
Formation thickness, h	= 100 ft
Production rate, q	= 9200 STB/D

Fig. 4-42—Pre-selected lines parallel to calculated q_D integral for field case 1.

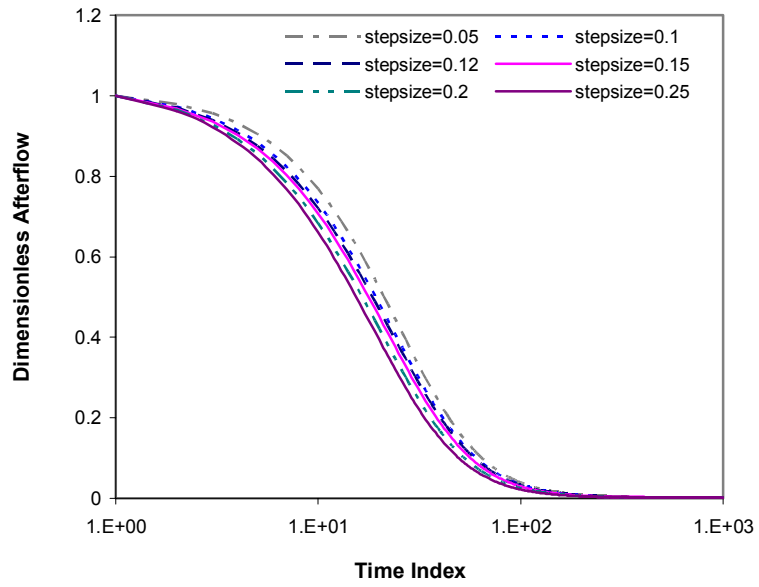


Fig. 4-43—Plausible set of afterflow rates, q_D for field case 1.

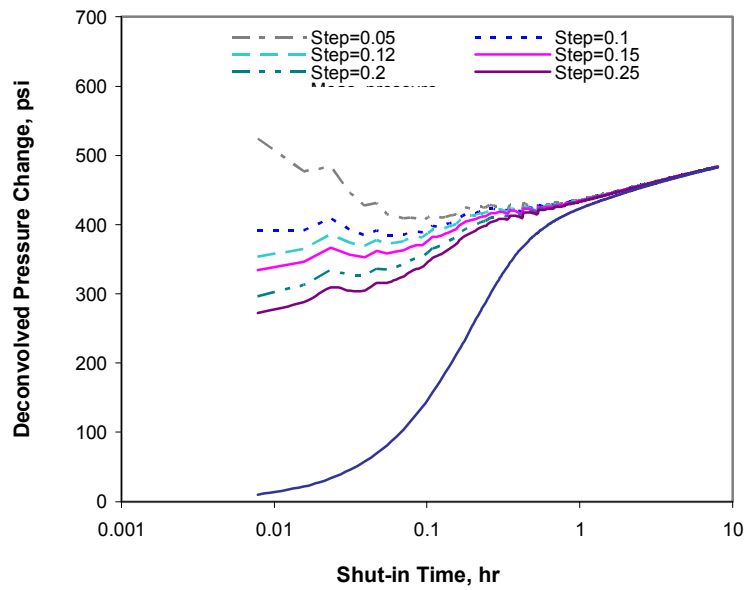


Fig. 4-44—Plausible set of deconvolved pressures for field case 1.

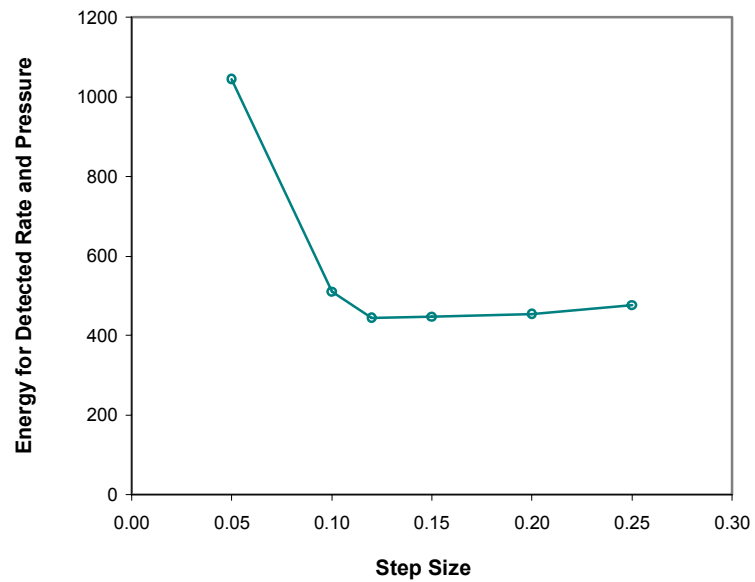


Fig. 4-45—Energy is minimum with step size of 0.12 for field case 1.

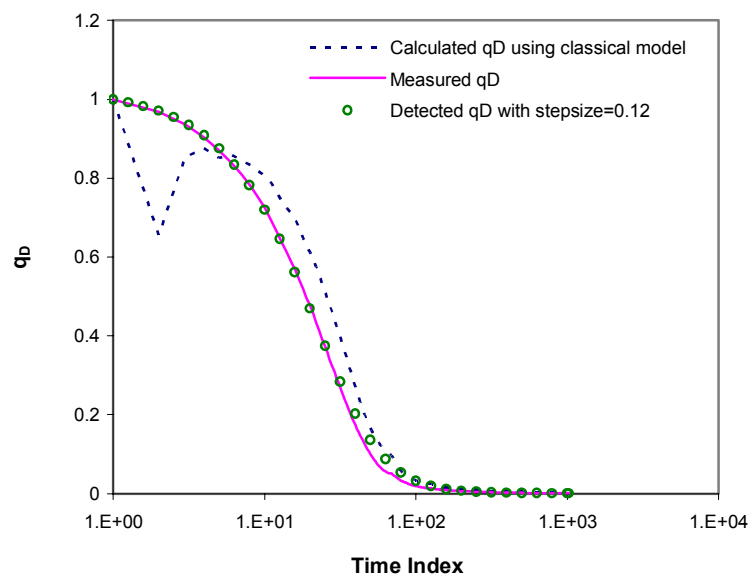


Fig. 4-46—Detected afterflow rate for field case 1.

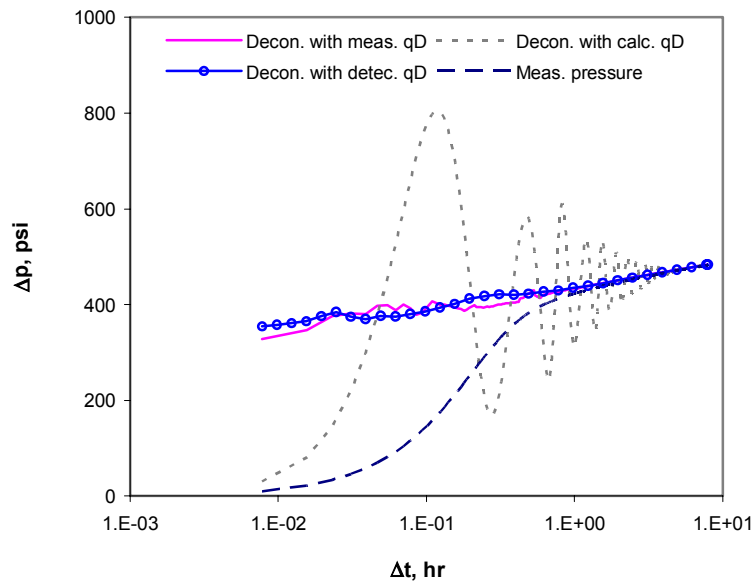


Fig. 4-47—Restored pressure using detected q_D for deconvolution for field case 1.

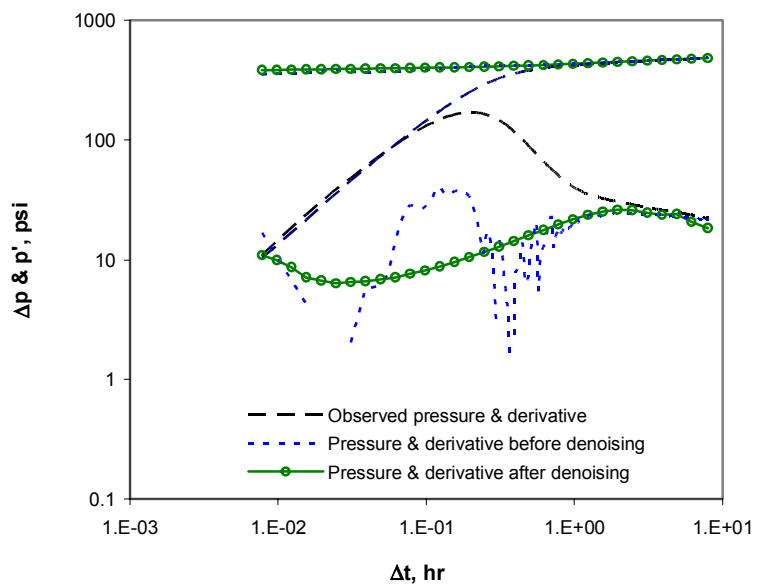


Fig. 4-48—Denoising restored pressure for field case 1.

Field Case 2. This case was reported by Boudet *et al.*⁸⁰ The basic reservoir and fluid properties are shown in Table 4-3. From the works of Sabet⁷⁷ and Horne,⁴³ we can see that this buildup test was run on a damaged oil well (skin factor from 7.4 to 8.5). Because of low permeability and considerable wellbore storage, the semilog-straight line is not well defined in the pressure data. With the same procedure as above, we discovered that the line with stepsize of 0.1 corresponds to the minimum energy (Fig. 4-49). The detected afterflow rate is illustrated in Fig. 4-50, which is very different from that of the q_D calculated with the constant wellbore storage model. After deconvolution with the detected q_D , the restored pressure presents a clear semi-log straight line interval starting as early as 1.5 hr, in contrast with the vague line from the measured pressure response (Fig. 4-51). The clear demonstration and extension of the semi-log straight line after blind deconvolution greatly increases our confidence in identifying the correct straight line with slope and intercept to estimate reservoir parameters accurately.

Since this well produced only 15 hrs before the buildup test, we use the equivalent time to plot the pressure derivatives⁴³ (Fig. 4-52). The range of the semi-log straight line is obviously extended, and the hump representing the wellbore storage effects is greatly reduced. However, the hump does not disappear. As Kuchuk⁸¹ pointed out, it is possible that additional wellbore storage effects may remain within the deconvolution pressures when the measurement point is not at the location of sandface and is some distance from the sandface. The wellbore volume between the measurement point and the location of sandface can introduce additional wellbore storage effects that can not be removed from the deconvolution.

TABLE 4-3—RESERVOIR AND FLUID PROPERTIES FOR FIELD CASE 2

Porosity, ϕ	= 0.25
Viscosity, μ	= 2.5 cp
Compressibility, c_t	= $1.053 \cdot 10^{-5}$ 1/psi
Formation volume factor, B	= 1.06 RB/STB
Wellbore radius, r_w	= 0.29 ft
Formation thickness, h	= 107 ft
Production rate, q	= 174 STB/D

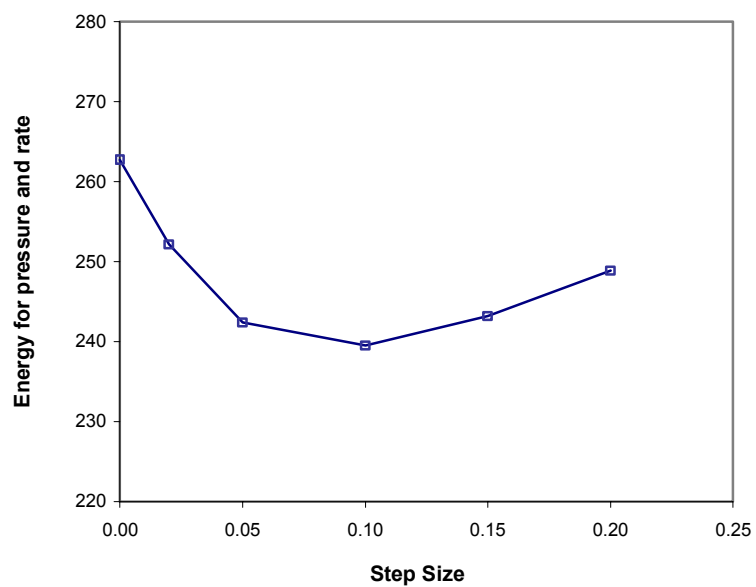


Fig. 4-49—Energy is minimum with step size of 0.10 for field case 2.

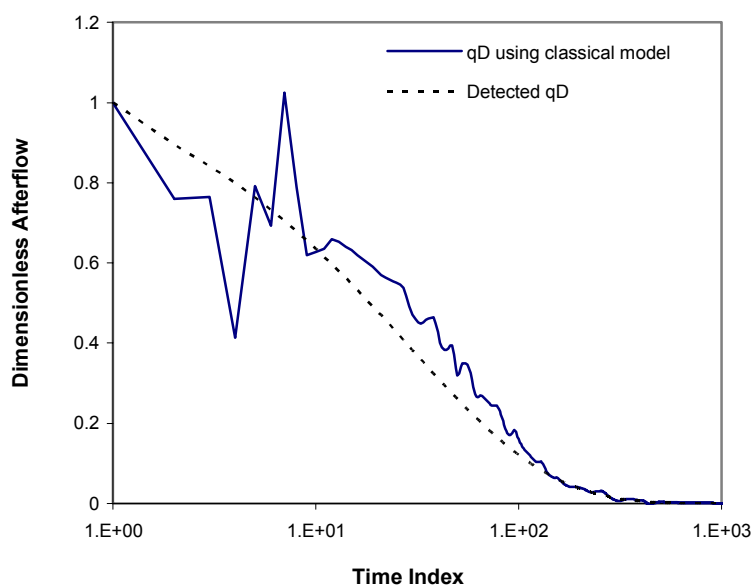


Fig. 4-50—Detected dimensionless afterflow rate for field case 2.

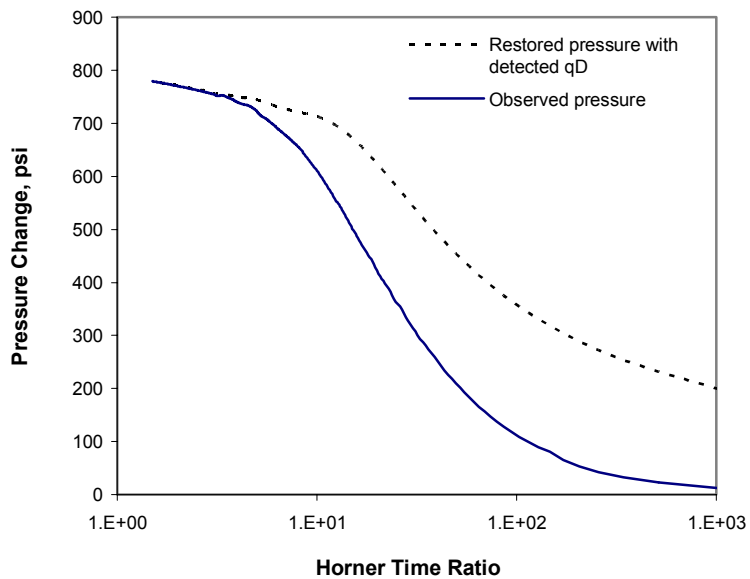


Fig. 4-51—Restored pressure using detected q_D for deconvolution for field case 2.

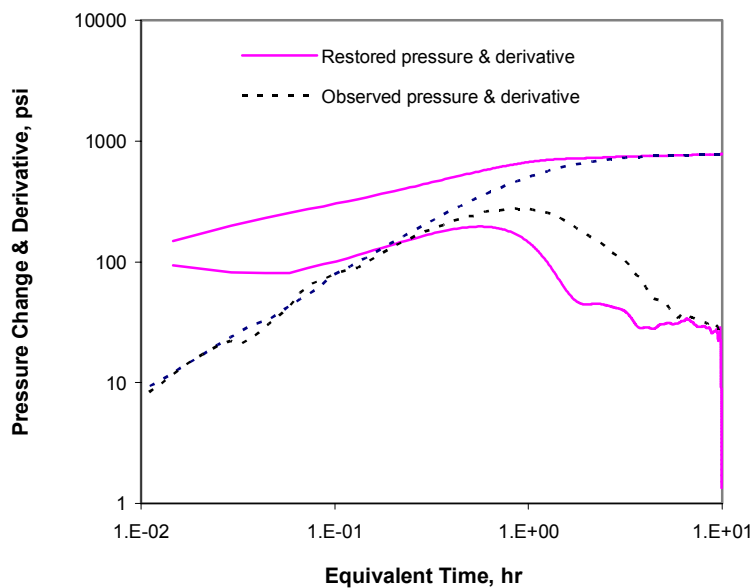


Fig. 4-52—Restored pressure and derivative vs. equivalent time for field case 2.

4.5 Chapter Summary

In this chapter, we developed a fast-Fourier-transform-based deconvolution method for restoring the constant-rate pressure response from measured pressure data with or without downhole rate measurements. A new afterflow/unloading rate model and a frequency domain-based denoising technique were proposed to effectively remove or suppress the noise in the measured pressure and rate data. Therefore, stable deconvolution results can be obtained even when the level of noise is quite high. For cases without downhole rate measurements, we developed a blind deconvolution technique. This technique simultaneously detects the rate function and restores the constant-rate pressure response, and greatly enhances the application of the deconvolution technique. With the new deconvolution approach, the early time behavior of a reservoir system masked by wellbore storage distortion can be effectively recovered. The wellbore storage coefficient can be variable in the general case. The new method thus provides a powerful tool to improve pressure transient test interpretation.

CHAPTER V

HORIZONTAL WELL TESTING

In Chapter IV, we developed a new deconvolution approach, which can effectively remove an obstacle in well testing analysis – the wellbore storage effect – and thus prepare us for horizontal well test interpretation. In this chapter, we develop a non-linear least squares regression technique, coupled with the new deconvolution approach, to improve parameter estimation in horizontal well testing interpretation. The uncertainties of the estimates and correlations between the estimates are also quantified.

5.1 Introduction

Based on analytical approximations, the diagnostic plot technique (log-log, semi-log, *etc.*) is commonly used in interpretation of vertical well testing. However, it is often not applicable in horizontal well testing although analytical approximations for horizontal wells are available. Missing one or two flow regimes is a common phenomenon in horizontal well testing, depending on relative dimensions of the reservoir and the wellbore and on permeability anisotropy. Due to the complex 3D flow geometry, well-defined flow periods are not as apparent as those in a vertical well. In horizontal wells, the additional volume of horizontal interval aggravates the wellbore storage effect even with downhole shut-in or downhole rate measurement. Anisotropy between horizontal and vertical permeability extends the time of wellbore storage effects.⁸² As Kuchuk⁸² and Ozkan⁴⁴ pointed out, the wellbore storage effect even distorts the mid-time pressure responses. The bad thing is once we lose the useful information at the early-time, we cannot recover it from the subsequent response data. For example, if the wellbore storage effect contaminates the early-time pressure response, we will lose the possibility to acquire information about vertical permeability. On the other hand, in a bounded reservoir, the presence of boundary effects can destroy the features of the late-time pseudo-radial and late-time linear flows. All the above effects make the interpretation of horizontal well testing extremely difficult using conventional interpretation techniques.

The use of type curves for well testing analysis is another common technique. Type curves are derived from analytical solutions and usually include a constant wellbore storage coefficient

in the solutions. Although the type curve technique is very useful to analyze pressure data containing the wellbore storage, it is usually very difficult to apply it to the problems of multiple parameter estimation if the number of parameters is more than three. Unfortunately, this is just the case for horizontal well testing analysis. In horizontal wells, not only are horizontal permeability, vertical permeability and skin factor unknown, but the effective wellbore length as well.

Subsequently, the nonlinear regression technique was developed and has become an important tool in analysis of horizontal well testing.^{42-43,82} The nonlinear regression technique can determine an optimal set of model parameters such that the model responses can “best” fit the measured responses (the relationship between model responses and model parameters are usually nonlinear). The most common method of ensuring a “best” fit between the measured and model data is to minimize the sum of the squares of the residuals, which are the difference between model responses and measured data. This technique can deal with multiple parameter estimation problems. The nonlinear regression technique is a powerful analysis tool in interpreting advanced and complicated well tests, like horizontal well tests. As Horne⁴³ mentioned, the nonlinear regression technique fully uses all the information contained in the measured responses and avoids inconsistent interpretation of separate portions of the responses. One of its advantages is that it can provide confidence evaluation of parameter estimates and interpret “uninterpretable” tests, i.e., provide information when well-defined flow regimes are not present and when only that of transition regions is acquired.

In the literature, authors repute use of nonlinear regression techniques with the convolved responses of measured rates and constant-rate pressure responses from a reservoir model to match the measured pressure responses if the downhole rate measurement is available. In the absence of downhole rate measurement, a constant wellbore storage coefficient is usually included in the model solution in the Laplace domain,⁸²

$$\bar{p}_{wD,cal}(s) = \frac{\bar{p}_{sD}(s)}{1 + C_D s^2 \bar{p}_{sD}(s)} \quad (5-1)$$

where head “ $\bar{\quad}$ ” denotes the Laplace transform, s represents the Laplace domain variable, and C_D is the dimensionless wellbore storage constant. In p_{sD} , the skin factor (s_d) is included; i.e.,

$$p_{sD} = p_{\delta D} + s_d \quad (5-2)$$

The Laplace domain solution is inverted back to the time domain to match the measured pressure data. The wellbore storage coefficient is treated as a parameter to be estimated. However, using a

constant wellbore storage coefficient to describe wellbore storage effects is often inadequate because in most cases the wellbore storage coefficient is changing, both in vertical wells and in horizontal wells. As Kuchuk⁸² pointed out, simulating the downhole pressure is difficult with a constant wellbore storage model, particularly at the early times. Kuchuk's work showed that if the actual wellbore storage is not constant, the estimation of reservoir parameters from the nonlinear regression is subject to significant errors, particularly the vertical permeability, since it is strongly correlated with the wellbore storage.

In this work, we use the blind deconvolution technique developed in the previous chapter to detect afterflow/unloading rate in the absence of rate measurement. This can overcome the problem brought on by the assumption of a constant wellbore storage coefficient in the application of the nonlinear regression technique. We then can obtain the model responses by convolving the detected rates with constant-rate pressure responses calculated from our reservoir model and subsequently fit them with the measured pressure responses. The optimal estimates of the parameters are determined by finding the "best" fit between the model and measured data.. The parameters considered in our nonlinear regression include horizontal permeability, vertical permeability, effective wellbore length of the horizontal well, vertical standoff of the wellbore, and skin factor. Considering the non-uniqueness problem in nonlinear regression, we further quantify the uncertainties of the parameter estimates and cross correlation between parameters.

5.2 Methodology

There are three major components in nonlinear regression: the model, the objective function, and the minimization procedure. The model predicts the reservoir/well system responses given a set of model parameters; the objective function measures the differences between the measured and model responses; and the minimization procedure seeks to find the optimal set of parameters by reducing the objective function to a minimum value.

As we know, the pressure data acquired from well tests correspond to variable-rate pressure responses resulting from the wellbore storage effect. To apply nonlinear regression, we first need to predict variable-rate pressure responses based on constant-rate pressure responses from the reservoir model in order to match the measured pressure responses. Based on the Duhamel's principle, the variable-rate pressure response can be obtained through the convolution of a constant-rate pressure solution with the variable rate.

$$\Delta p_{w,cal}(t) = \int_0^t q_D'(\tau) \Delta p_\delta(t - \tau) d\tau \quad (5-3)$$

$$q_D(t) = q_{sf}(t) / q_r \quad (5-4)$$

where $p_{w,cal}$ represents the calculated variable-rate pressure response, and p_δ is the constant-rate pressure response obtained from the reservoir model. Δp means the pressure change, i.e. $\Delta p = p_i - p_{wf}$ for a drawdown test and $\Delta p = p_{ws} - p_{ws}(\Delta t = 0)$ for a buildup test. To calculate variable-rate pressure responses ($p_{w,cal}$) from Eq. 5-3, afterflow/unloading rates must be convolved with the constant-rate pressure response (p_δ) from a appropriate reservoir model. In a numerical integration form, Eq. 5-3 can be written as:

$$\Delta p_{w,cal}(t_n) = \sum_{j=1}^n \Delta q_D(t_j) \Delta p_\delta(t_n - t_j) \quad (5-5)$$

where $\Delta q_D(t_j) = |q_D(t_{j+1}) - q_D(t_j)|$. The additional pressure drop caused by the damage skin is included in Δp_δ as

$$\Delta p_s = \frac{141.2 q_t B \mu}{k_{av} L_w} s_d \quad (5-6)$$

where s_d is the damage skin factor, q_t the flow rate, B the formation volume factor, μ the fluid viscosity and L_w the effective wellbore length. k_{av} is defined as:

$$k_{av} = \sqrt{k_h k_v} \quad (5-7)$$

To overcome the problem associated with the assumption of constant wellbore storage, we use the blind deconvolution technique developed in Chapter IV to detect the afterflow/unloading rates. This technique provides a close approximation of the measured rate data. In a brief, the procedure is to preselect a plausible set of afterflow rates (q_D) by capturing the signatures of afterflow rate in the mid-frequency band and afterflow-rate-integral in the frequency domain. Then, we perform deconvolution using this pre-determined set of q_D solutions with the measured pressure response and obtain a plausible set of deconvolved pressure solutions. An energy criterion is used to screen q_D and the corresponding constant-rate pressure responses. The detected rate is the one corresponding to the minimum energy.

The detected rate behavior carries the information of pressure responses to downhole environment effects and thus can represent the changing wellbore storage effects. Furthermore,

with the detected rates, the number of parameters required to be estimated can be reduced by one (i.e., there is no need to estimate the wellbore storage coefficient) because the afterflow/unloading rates containing the wellbore storage effects are directly used in the convolution. Consequently, the reliability of parameter estimation from the nonlinear regression can be enhanced.

With the measured wellbore pressure responses and calculated model pressure responses, we define an objective function as

$$J = \sum_{j=1}^n (p_{wj,mea} - p_{wj,cal})^2 \quad (5-8)$$

This equation represents the discrepancy between the measured and calculated pressure responses in a least squares sense. $p_{wj,cal}$ is obtained by the procedures discussed earlier. In our nonlinear regression, the set of parameters to be estimated can include any or all of the following: horizontal and vertical permeabilities, effective wellbore length, well vertical location and skin factor. If any one among these parameters can be acquired reliably by other methods, such as effective wellbore length and well vertical location determined by production logging, the number of parameter estimates can be reduced. We define the basic upper and lower limits for each of above parameters. These limits are:

$$0 < k_h, k_v < \text{arbitrary guess}$$

$$0 < L_w \leq \text{drilled length}$$

$$0 < z_w/h \leq 1$$

$$\text{arbitrary guess} < s \leq \text{arbitrary guess}$$

where z_w is the well vertical position and h is the reservoir thickness.

The effective wellbore length, in general, is not equal to the drilled length and is hard to determine due to the non-uniform skin distribution over long horizontal interval. Production logging is usually required to determine the effective wellbore length. In this study, we take the effective wellbore length as one of unknowns to be estimated. As we will show later, with accurate rate data, the nonlinear regression can provide an accurate estimate of effective wellbore length. Even with the detected approximate rates, we can provide a reasonable estimate of effective wellbore length.

To decrease the misfit between computed and measured pressures, the given set of parameters needs to be modified. We use a gradient-based minimization algorithm to find the necessary modifications of the parameters. Once the set of changes of the given guesses are obtained, the parameters can be updated and the next iteration proceeds with pressure responses recomputed using the updated parameters. The numerical perturbation method is used to compute the sensitivities of pressure responses to the parameters. These sensitivities are required by the minimization algorithm.

$$\frac{\partial p_{wj,cal}}{\partial \beta_k} = \frac{\Delta p_{wj,cal}}{\Delta \beta_k} \quad (5-9)$$

$$j = 1, 2, \dots, N \text{ and } k = 1, 2, \dots, M$$

where N is the number of the calculated pressure response points and M is the number of the parameters. The sensitivity matrix, \mathbf{A} , is given as:

$$\mathbf{A} = \begin{bmatrix} \frac{\partial p_1}{\partial \beta_1} & \frac{\partial p_1}{\partial \beta_2} & \dots & \dots & \frac{\partial p_1}{\partial \beta_M} \\ \frac{\partial p_2}{\partial \beta_1} & \frac{\partial p_2}{\partial \beta_2} & \dots & \dots & \frac{\partial p_2}{\partial \beta_M} \\ \dots & \dots & \dots & \dots & \dots \\ \dots & \dots & \dots & \dots & \dots \\ \frac{\partial p_N}{\partial \beta_1} & \frac{\partial p_N}{\partial \beta_2} & \dots & \dots & \frac{\partial p_N}{\partial \beta_M} \end{bmatrix} \quad (5-10)$$

For convenience, we use p_j in Eq. 5-10 instead of $p_{wj,cal}$ to represent the calculated pressure at time t_j from the reservoir model.

Using a locally linearized approximation of model responses around the current estimates, the objective function becomes

$$J = \sum_{j=1}^n [p_{wj,mea} - (p_{wj,cal}(\boldsymbol{\beta}^*) + \mathbf{A}\Delta\boldsymbol{\beta})]^2 \quad (5-11)$$

Then, the parameter changes can be determined by solving the following equation system in a least squares sense:

$$\mathbf{A}\Delta\boldsymbol{\beta} = \mathbf{p}_{mas} - \mathbf{p}_{cal} \quad (5-12)$$

where $\boldsymbol{\beta}^*$, \mathbf{p}_{mea} and \mathbf{p}_{cal} are all vectors. $\Delta\boldsymbol{\beta}$ is the parameter changes.

$$\Delta\boldsymbol{\beta} = (\Delta\beta_1, \Delta\beta_2, \dots, \Delta\beta_M)$$

$$\boldsymbol{p}_{mea} = (p_{w1,mea}, p_{w2,mea}, \dots, p_{wN,mea})$$

$$\boldsymbol{p}_{cal} = (p_{w1,cal}, p_{w2,cal}, \dots, p_{wN,cal})$$

In a matrix form, Eq. 5-12 may be expressed as:

$$\begin{bmatrix} \frac{\partial p_1}{\partial \beta_1} & \frac{\partial p_1}{\partial \beta_2} & \dots & \dots & \frac{\partial p_1}{\partial \beta_M} \\ \frac{\partial p_2}{\partial \beta_1} & \frac{\partial p_2}{\partial \beta_2} & \dots & \dots & \frac{\partial p_2}{\partial \beta_M} \\ \dots & \dots & \dots & \dots & \dots \\ \frac{\partial p_N}{\partial \beta_1} & \frac{\partial p_N}{\partial \beta_2} & \dots & \dots & \frac{\partial p_N}{\partial \beta_M} \end{bmatrix} \begin{bmatrix} \Delta\beta_1 \\ \Delta\beta_2 \\ \dots \\ \dots \\ \Delta\beta_M \end{bmatrix} = \begin{bmatrix} p_{mea1} - p_{cal1} \\ p_{mea2} - p_{cal2} \\ \dots \\ \dots \\ p_{meaN} - p_{calN} \end{bmatrix} \quad (5-13)$$

Parameters used in the model for the next iteration are renewed as

$$\beta_j^{n+1} = \beta_j^n + \Delta\beta_j \quad j = 1, 2, \dots, M \quad (5-14)$$

where n is the n -th iteration.

Another equally important component of nonlinear regression is uncertainty analysis. Parameter estimates obtained from nonlinear regression involve uncertainties, and are also correlated each other. In our work, the sensitivity information from the estimates is used to approximate the Hessian matrix, which is the second-order partial derivative of the objective function with respect to the parameters. From the Hessian matrix, we can calculate the covariance matrix and the cross-correlation matrix of parameter estimates. The covariance matrix quantifies the uncertainty of parameter estimates, and the cross-correlation matrix indicates the correlation between the parameters.

In summary, our nonlinear regression technique for interpretation of well tests from horizontal wells involves the following procedure:

1. Perform blind deconvolution to detect the afterflow rates using measured pressure data.
2. Calculate the constant-rate pressure response using the reservoir model and an initial guess of parameters to be estimated. The estimated parameters include horizontal and vertical permeabilities, effective wellbore length, well vertical position and skin factor.

3. Convolve the detected afterflow rates with the constant-rate pressure response to obtain the wellbore pressure which has included the wellbore storage effects.
4. Perform the least-squares minimization on the misfit between the measured wellbore pressure and calculated pressure to find necessary parameter changes.
5. Update the parameters and iterate the steps 2 to 4 until finding a best fit.
6. Evaluate the uncertainty of parameter estimates and correlation between the estimates by calculating covariance matrix, 95% confidence interval and cross-correlation matrix.

5.3 Uncertainty of Parameter Estimates

The quality of parameter estimates can be evaluated based on the nonlinear regression results. For example, we can use the 95% confidence interval to quantify the uncertainty of the estimate of a parameter, which is a function of the noise in data, the number of data points and the degree of correlation between unknowns.⁴³

We use a linearized approximation:

$$\mathbf{p}_{\text{cal}}(\boldsymbol{\beta}) = \mathbf{p}_{\text{cal}}(\boldsymbol{\beta}_t) + \mathbf{A}(\boldsymbol{\beta} - \boldsymbol{\beta}_t) \quad (5-15)$$

where the $\boldsymbol{\beta}_t$ are the true, but unknown, parameter values. Thus,

$$J = [\mathbf{p}_{\text{mea}} - \mathbf{p}_{\text{cal}}(\boldsymbol{\beta}_t) - \mathbf{A}\Delta\boldsymbol{\beta}]^T [\mathbf{p}_{\text{mea}} - \mathbf{p}_{\text{cal}}(\boldsymbol{\beta}_t) - \mathbf{A}\Delta\boldsymbol{\beta}] \quad (5-16)$$

where $\mathbf{p}_{\text{mea}} - \mathbf{p}_{\text{cal}}(\boldsymbol{\beta}_t)$ can be viewed as the pressure measurement errors, and $\Delta\boldsymbol{\beta} = \boldsymbol{\beta} - \boldsymbol{\beta}_t$, represents the uncertainties of the estimates.

$$\boldsymbol{\varepsilon} = \mathbf{p}_{\text{mea}} - \mathbf{p}_{\text{cal}}(\boldsymbol{\beta}_t) \quad (5-17)$$

A necessary condition for a minimum of the objective function is

$$\nabla J = 0 \quad (5-18)$$

or

$$\nabla J = 2\mathbf{A}^T (\mathbf{p}_{\text{mea}} - \mathbf{p}_{\text{cal}}(\boldsymbol{\beta}_t) - \mathbf{A}\Delta\boldsymbol{\beta}) = 0 \quad (5-19)$$

So, we have

$$\mathbf{A}\Delta\boldsymbol{\beta} = \boldsymbol{\varepsilon} \quad (5-20)$$

or

$$\Delta\boldsymbol{\beta} = (\mathbf{A}^T \mathbf{A})^{-1} \mathbf{A}^T \boldsymbol{\varepsilon} \quad (5-21)$$

We use our estimates of parameters, $\boldsymbol{\beta}^*$, for $\boldsymbol{\beta}_t$. We would like to know the errors in the estimates. If we assume that each component of measurement error ($\boldsymbol{\varepsilon}$) is a random variable and independently follows a normal distribution $N(0, \sigma^2)$, with a mean of zero and a variance of σ^2 , the joint distribution of $\boldsymbol{\varepsilon}$ is a normal distribution, $\boldsymbol{\varepsilon} \sim N(0, \sigma^2 I)$, with uncorrelated components. I is the unit matrix. The joint variance may be written as

$$\sigma^2 I = \begin{bmatrix} \sigma^2 & 0 & \dots & \dots & 0 \\ 0 & \sigma^2 & \dots & \dots & 0 \\ \dots & \dots & \dots & \dots & \dots \\ \dots & \dots & \dots & \dots & \dots \\ 0 & 0 & \dots & \dots & \sigma^2 \end{bmatrix} \quad (5-22)$$

An optimal estimation of σ^2 can be obtained as:

$$\sigma^2 \approx \frac{J}{N - M} = \frac{\sum_{j=1}^N (p_{mea,j} - p_{cal,j}(\boldsymbol{\beta}^*))^2}{N - M} \quad (5-23)$$

As a result, $\Delta\boldsymbol{\beta}$ follows a normal distribution, $\Delta\boldsymbol{\beta} \sim N(0, \sigma^2 (\mathbf{A}^T \mathbf{A})^{-1})$. $\mathbf{A}^T \mathbf{A}$ can be viewed as the Hessian matrix approximately. Hence, the covariance matrix of $\Delta\boldsymbol{\beta}$ is equal to the product of σ^2 and the inverse of the Hessian matrix. If we express the inverse of the Hessian matrix as:

$$Hessian^{-1} = (\mathbf{A}^T \mathbf{A})^{-1} = \begin{bmatrix} a_{11} & a_{12} & \dots & \dots & a_{1M} \\ a_{21} & a_{22} & \dots & \dots & a_{2M} \\ \dots & \dots & \dots & \dots & \dots \\ \dots & \dots & \dots & \dots & \dots \\ a_{M1} & a_{M2} & \dots & \dots & a_{MM} \end{bmatrix} \quad (5-24)$$

then, the covariance of $\Delta\boldsymbol{\beta}$ can be written as

$$Cov(\Delta\boldsymbol{\beta}) = \sigma^2 (\mathbf{A}^T \mathbf{A})^{-1} = \begin{bmatrix} \sigma^2 a_{11} & \sigma^2 a_{12} & \dots & \dots & \sigma^2 a_{1M} \\ \sigma^2 a_{21} & \sigma^2 a_{22} & \dots & \dots & \sigma^2 a_{2M} \\ \dots & \dots & \dots & \dots & \dots \\ \dots & \dots & \dots & \dots & \dots \\ \sigma^2 a_{M1} & \sigma^2 a_{M2} & \dots & \dots & \sigma^2 a_{MM} \end{bmatrix} \quad (5-25)$$

or simply expressed as

$$Cov(\Delta\boldsymbol{\beta}) = \sigma^2 (\mathbf{A}^T \mathbf{A})^{-1} = \begin{bmatrix} \sigma_1^2 & \sigma_{12} & \dots & \dots & \sigma_{1M} \\ \sigma_{21} & \sigma_2^2 & \dots & \dots & \sigma_{2M} \\ \dots & \dots & \dots & \dots & \dots \\ \dots & \dots & \dots & \dots & \dots \\ \sigma_{M1} & \sigma_{M2} & \dots & \dots & \sigma_M^2 \end{bmatrix} \quad (5-26)$$

where σ_{jk} represents covariance between β_j and β_k , defined as

$$\sigma_{jk} = \frac{\sum_{i=1}^n (\beta_{ji} - \bar{\beta}_j)(\beta_{ki} - \bar{\beta}_k)}{n} \quad i = 1, 2, \dots, n \quad (5-27)$$

$$j, k = 1, 2, \dots, M$$

where n is sample number of a specific parameter and M is the number of the parameters. With the variances of the estimated parameters, the 95% confidence interval on the estimates ($\boldsymbol{\beta}^*$) can be determined as

$$\beta_j \approx \beta_j^* \pm 2\sigma_j \quad (5-28)$$

From the covariance matrix, Eq. 5-26, the cross correlation matrix can be obtained:

$$Cor(\Delta\boldsymbol{\beta}) = \begin{bmatrix} \rho_{11} & \rho_{12} & \dots & \dots & \rho_{1M} \\ \rho_{21} & \rho_{22} & \dots & \dots & \rho_{2M} \\ \dots & \dots & \dots & \dots & \dots \\ \dots & \dots & \dots & \dots & \dots \\ \rho_{M1} & \rho_{M2} & \dots & \dots & \rho_{MM} \end{bmatrix} \quad (5-29)$$

where the correlation coefficient, ρ_{jk} , is defined as

$$\rho_{jk} = \frac{\sigma_{jk}}{\sigma_j \sigma_k} \quad (5-30)$$

$$\rho_{jj} = 1$$

From the correlation matrix, we can acquire information on the degree of correlation between the parameters. The autocorrelation coefficient is equal to 1, while the cross-correlation coefficient lies between -1 and 1, i.e. $-1 \leq \rho_{jk} \leq 1$.

5.4 Applications

In previous sections, we have presented the procedures of our nonlinear regression technique. In this section, we use synthetic, pseudo-synthetic and field cases to demonstrate the applicability of this technique.

Case 5-1. This is a synthetic case. The reservoir and fluid properties are the same as those shown in Table 4-1. The pressure response with wellbore storage was obtained by using the Laplace-domain solution with the constant wellbore storage model (classical model). This pressure response is equivalent to the measured pressure in practice, and we will call it the observed pressure response. In this case, the early-time radial flow has been completely masked by the wellbore storage effect (Fig. 5-3). The wellbore storage coefficient used was 1.63 bbl/psi.

Nonlinear regression is performed through matching the convolved pressure with the observed pressure response. The convolved pressure means the pressure obtained by convolution of the constant-rate pressure response from the reservoir model with the rate calculated from the classical wellbore model (Eq. 4-20).

Table 5-1 gives the initial guesses of the parameters, together with the estimates at the 1st and 10th iterations, and the true values of the parameters. The initial guesses of the parameters are selected far away from the true values, except for the well's vertical position and skin factor. In our model, the input well position is normalized on reservoir thickness, i.e. the ratio of the z-coordinator of the well to the reservoir thickness. We assume that we have good prior knowledge of the vertical position of the well and of the skin factor, so we use their true values as initial guesses. On the other hand, we want to examine the behavior of the estimation to see if the

nonlinear regression can preserve the good prior knowledge of these parameters. The well's vertical location returns to a value close to its true value after it deviated in the first iteration, while the skin factor basically remain close to its true value (Fig. 5-1). At the 10th iteration, all parameter estimates are very close to the true values (Table 5-1). The 95% confidence intervals of these estimates are also shown in Table 5-1 and presented in terms of the percentage values of the estimates, except for the skin factor, which is presented in terms of its absolute value. The parameter estimates all have very small confidence intervals, which indicate reliable parameter estimation.

TABLE 5-1—ESTIMATES AND TRUE VALUES OF WELL-RESERVOIR PARAMETERS FOR CASE 5-1

<u>Iteration No.</u>	<u>kh, md</u>	<u>kv, md</u>	<u>Lw, ft</u>	<u>zw, ft</u>	<u>s</u>
0	1000	100	3000	50	0
1	500.5	50.05	3000	70	0.018
10	400.13	19.95	2499.06	49.81	-0.007
95% confidence interval	± 0.16%	± 0.23%	± 0.14%	± 1.37%	± 0.005
True value	400	20	2500	50	0

Fig. 5-1 indicates the progress of parameter estimates during the iterations in the nonlinear regression. The horizontal and vertical permeabilities and effective well length are all close to their true values after the third iteration. As discussed above, the estimate of well position deviates away at first and then gradually moves back toward the true value after other parameters reach values close to their true values. The skin factor is basically stabilized around its true value. Fig. 5-2 shows that the root-mean-square error of the pressure misfit rapidly decreases in the first several iterations and reaches the order of 10^{-4} at the tenth iteration.

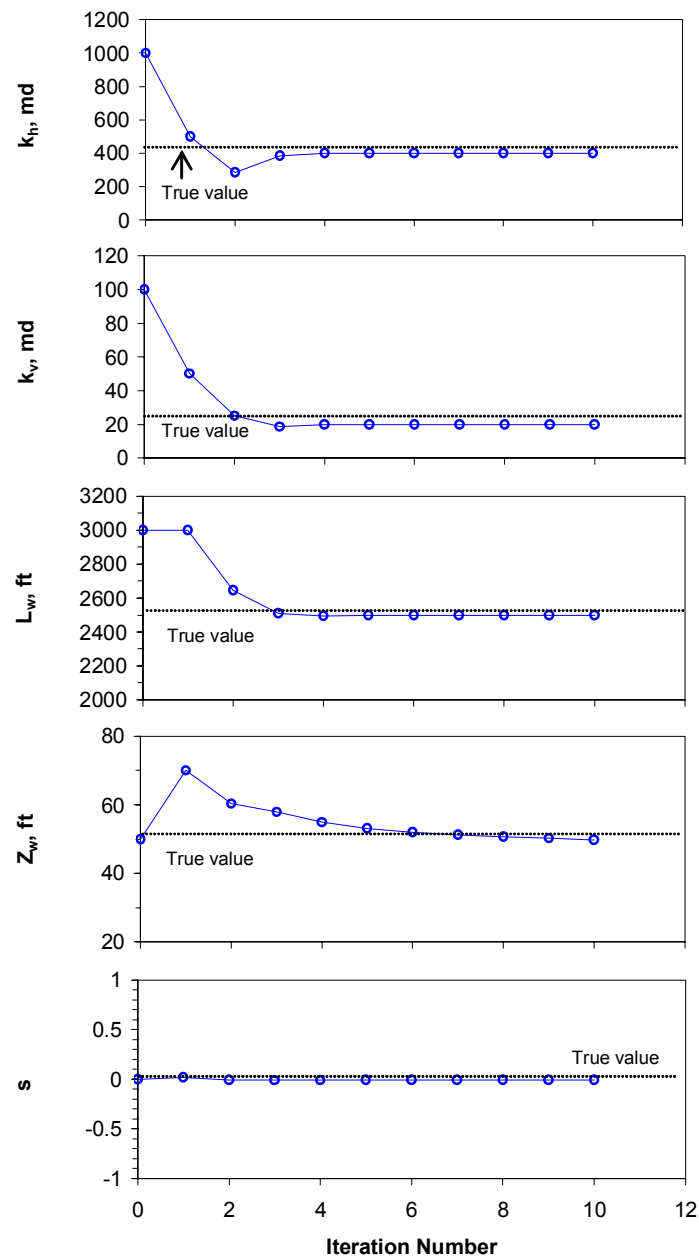


Fig. 5-1—Parameter estimates with iteration for case 5-1.

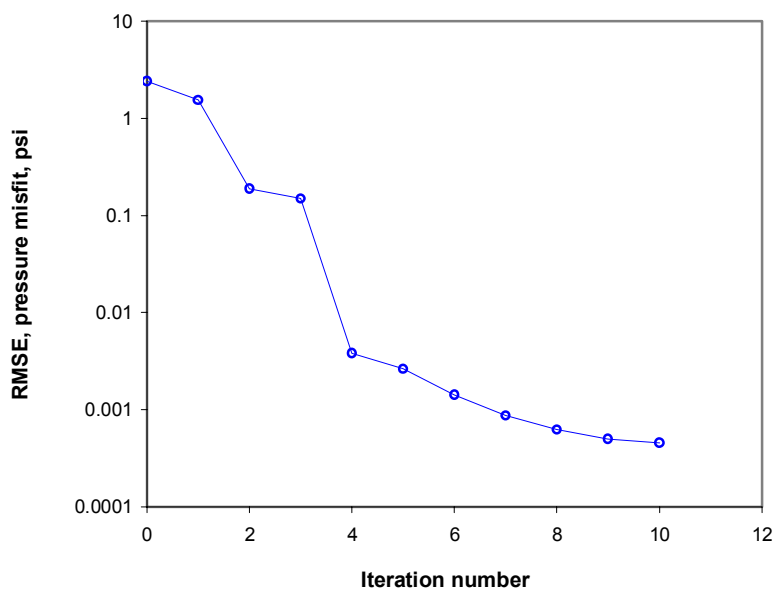


Fig. 5-2—Root-mean-square error with iteration for case 5-1.

Fig. 5-3 is a log-log plot of the pressure change and pressure derivative with respect to logarithmic time. The pressure responses at the initial guesses of the parameters are also presented in this figure; these responses differ greatly from the observed pressures. However, using the nonlinear regression technique, we can successfully match the observed pressure responses from these significantly different initial pressure responses and at the same time estimate parameters accurately (Table 5-1).

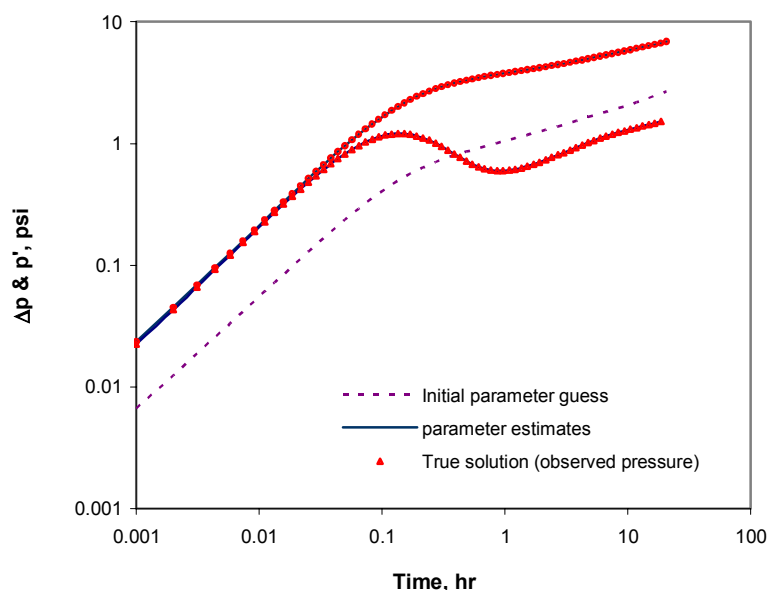


Fig. 5-3—Observed pressure response matched with parameter estimates at the tenth iteration for case 5-1.

Table 5-2 shows the covariance of parameter estimates. The cross correlations between estimates are displayed in Table 5-3. From Table 5-3, we can see that effective well length is strongly correlated with horizontal permeability, and vertical permeability is strongly correlated with skin factor.

TABLE 5-2 —COVARIANCE MATRIX FOR CASE 5-1

	<u>kh</u>	<u>kv</u>	<u>Lw</u>	<u>zw</u>	<u>s</u>
<u>kh</u>	1.06E-01	2.09E-03	-5.74E-01	-6.51E-02	-1.96E-04
<u>kv</u>	2.09E-03	5.35E-04	-1.14E-02	1.85E-03	5.03E-05
<u>Lw</u>	-5.74E-01	-1.14E-02	3.28E+00	4.36E-01	1.34E-03
<u>zw</u>	-6.51E-02	1.85E-03	4.36E-01	1.16E-01	5.86E-04
<u>s</u>	-1.96E-04	5.03E-05	1.34E-03	5.86E-04	6.85E-06

TABLE 5-3 —CROSS CORRELATION MATRIX FOR CASE 5-1

	<u>kh</u>	<u>kv</u>	<u>Lw</u>	<u>zw</u>	<u>s</u>
<u>kh</u>	1.000	0.277	-0.974	-0.588	-0.230
<u>kv</u>	0.277	1.000	-0.273	0.235	0.831
<u>Lw</u>	-0.974	-0.273	1.000	0.708	0.283
<u>zw</u>	-0.588	0.235	0.708	1.000	0.658
<u>s</u>	-0.230	0.831	0.283	0.658	1.000

Case 5-2. This case is the same as Case 5-1, but we assume that we have only the observed pressure data and that no rate data are available. Therefore, we use the detected rates, obtained by applying the blind deconvolution technique, instead of the true rate data, in the nonlinear regression. From the minimum energy criterion, the detected rates correspond to a step size of zero (Fig. 5-4), which means that the unloading rate resulting from a constant wellbore storage coefficient was detected. This result is just what we expect because the observed pressure responses in this synthetic case were generated using a constant wellbore storage. The detected rates are shown in Fig. 5-5, and are quite consistent with the true rates. Fig. 5-6 indicates the errors in the detected rates. We can see that the errors are quite small.

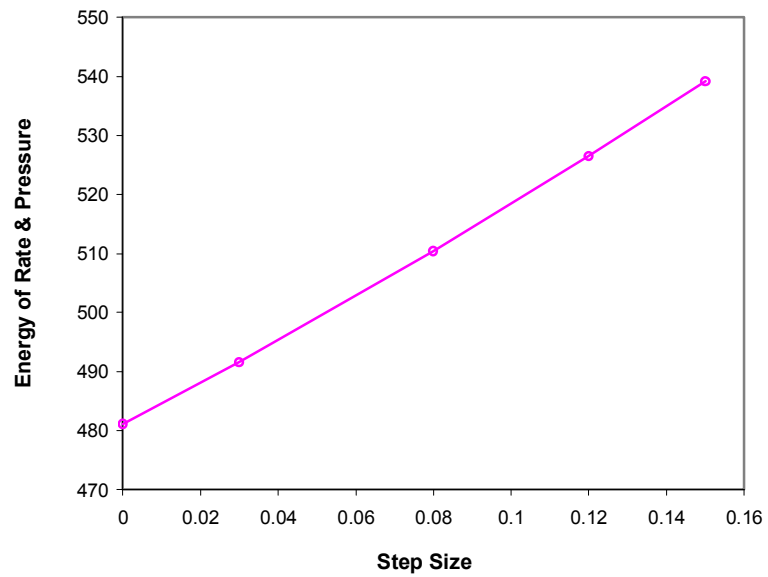


Fig. 5-4—Energy is minimum with step size of 0.0 for case 5-2.

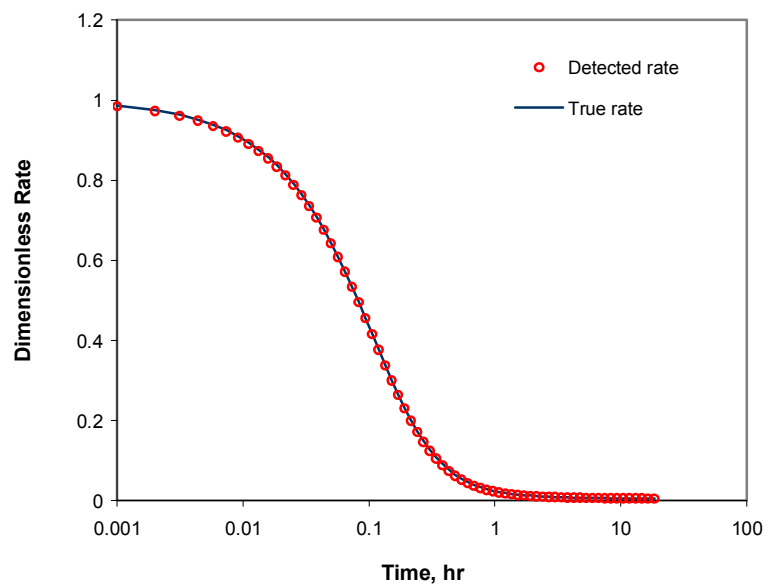


Fig. 5-5—Detected unloading rate using blind deconvolution for case 5-2.

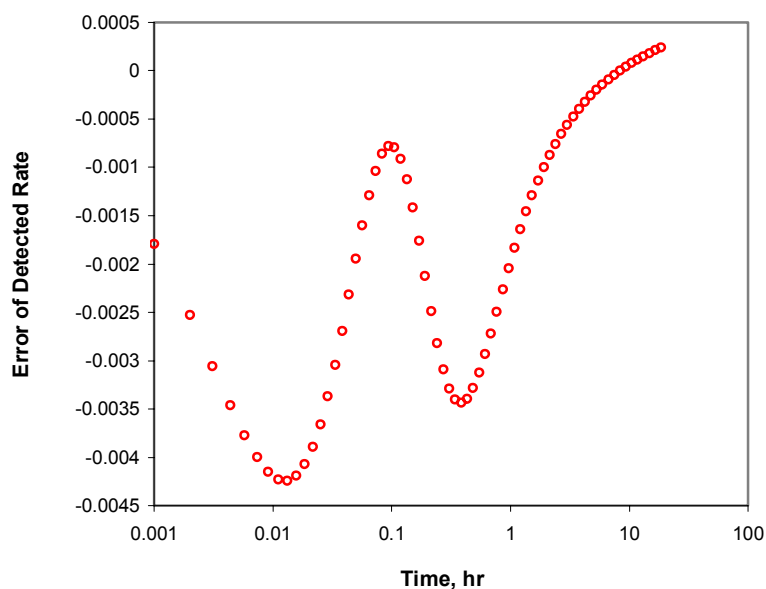


Fig. 5-6—Error of detected unloading rate using blind deconvolution for case 5-2.

Table 5-4 gives the initial guess of the parameters, together with the estimates at the fourth iteration, and the true values of parameters. At the fourth iteration, all parameter estimates are close to the true values (Table 5-4). The 95% confidence intervals of these estimates are also shown in Table 5-4. The parameter estimates have small confidence intervals, especially the estimates of permeabilities and effective well length, which indicate the parameter estimation is quite reliable from an engineering perspective.

TABLE 5-4—ESTIMATES AND TRUE VALUES OF WELL-RESERVOIR PARAMETERS FOR CASE 5-2

<u>Iteration No.</u>	<u>kh, md</u>	<u>kv, md</u>	<u>Lw, ft</u>	<u>zw, ft</u>	<u>s</u>
0	1000	100	3000	50	0
4	404.37	19.66	2465.82	52.23	-0.101
95% confidence interval	± 2.23%	± 3.19%	± 2.02%	± 8.76%	± 0.070
True value	400	20	2500	50	0

Fig. 5-7 indicates the changes of estimates with the iterations in the process of nonlinear regression. The horizontal and vertical permeabilities and effective well length are all close to their true values after the fourth iteration and basically become stable afterwards. The estimates of well position and skin factor are close to their true values. Fig. 5-8 shows that the root-mean-square error of pressure misfit decreases rapidly in the first several iterations and reaches a minimum of the order of 10^{-3} at the fourth iteration.

Fig. 5-9 is a log-log plot of pressure change and pressure derivative with respect to logarithmic time. The pressure response behavior obtained from the true values of the parameters and the estimates at the fourth iteration are presented, together with that at the initial guesses of the parameters. Fig. 5-9 shows that the observed pressure response can be matched very well by using the nonlinear regression technique.

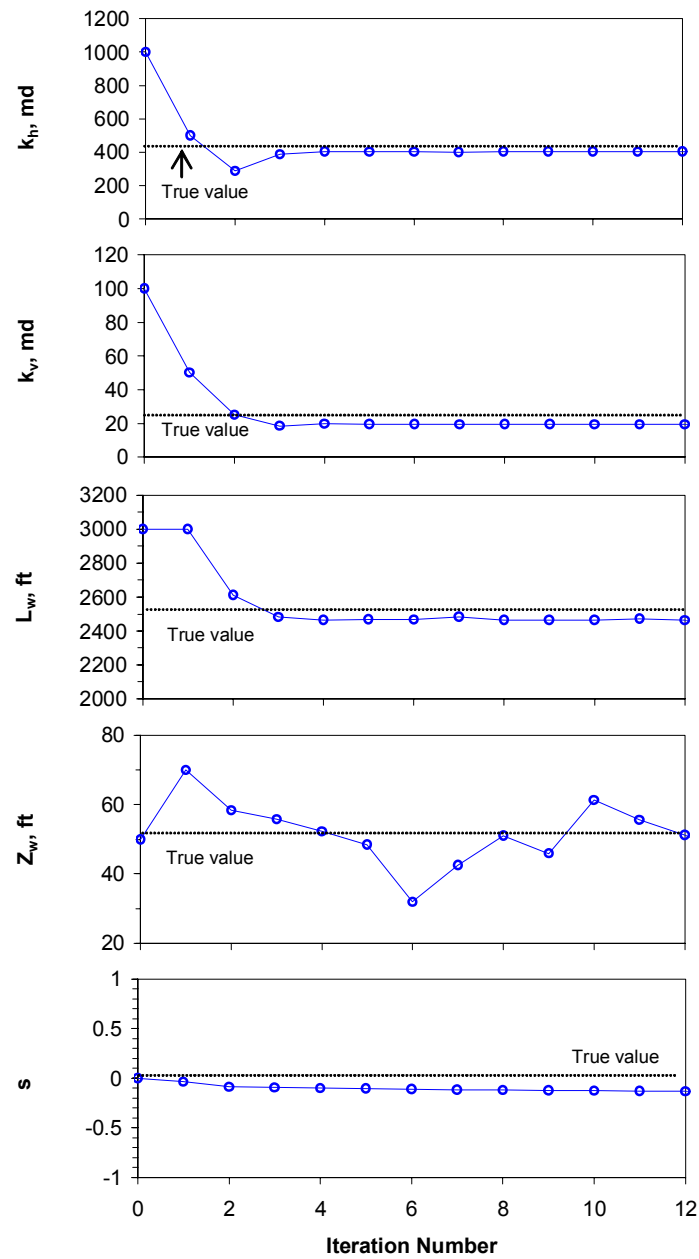


Fig. 5-7—Parameter estimates with iteration for case 5-2.

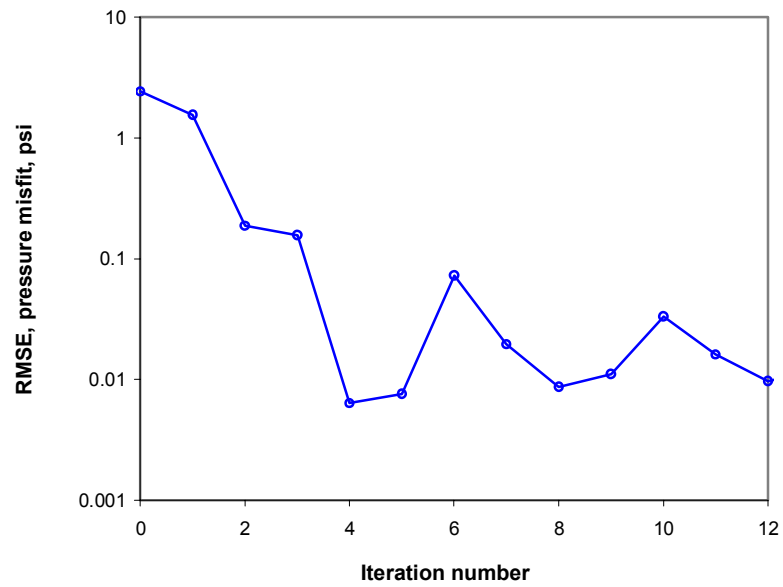


Fig. 5-8—Root-mean-square error with iteration for case 5-2.

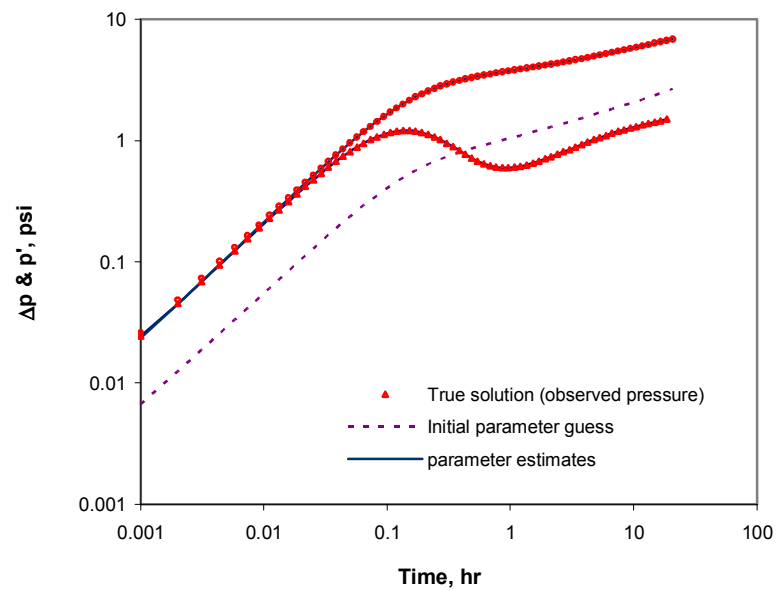


Fig. 5-9—Observed pressure response matched with parameter estimates at the fourth iteration for case 5-2.

Table 5-5 shows the covariance of the parameter estimates. The cross correlations between estimates are displayed in Table 5-6. Again, we see strong correlations between horizontal permeability and effective well length, and between vertical permeability and skin factor.

TABLE 5-5—COVARIANCE MATRIX FOR CASE 5-2

	<u>kh</u>	<u>kv</u>	<u>Lw</u>	<u>zw</u>	<u>s</u>
<u>kh</u>	2.03E+01	4.13E-01	-1.09E+02	-6.13E+00	-3.75E-02
<u>kv</u>	4.13E-01	9.81E-02	-2.26E+00	1.57E-01	8.98E-03
<u>Lw</u>	-1.09E+02	-2.26E+00	6.22E+02	4.08E+01	2.55E-01
<u>zw</u>	-6.13E+00	1.57E-01	4.08E+01	5.24E+00	5.33E-02
<u>s</u>	-3.75E-02	8.98E-03	2.55E-01	5.33E-02	1.23E-03

TABLE 5-6—CROSS CORRELATION MATRIX FOR CASE 5-2

	<u>kh</u>	<u>kv</u>	<u>Lw</u>	<u>zw</u>	<u>s</u>
<u>kh</u>	1.000	0.293	-0.974	-0.595	-0.238
<u>kv</u>	0.293	1.000	-0.289	0.219	0.816
<u>Lw</u>	-0.974	-0.289	1.000	0.714	0.291
<u>zw</u>	-0.595	0.219	0.714	1.000	0.664
<u>s</u>	-0.238	0.816	0.291	0.664	1.000

Comparing Case 5-2 with Case 5-1, we see that when we use the detected rates from the blind deconvolution technique, we can obtain reliable parameter estimates.

Case 5-3. This is a pseudo-synthetic case. We generated the measured pressure by referring to Kuchuk's procedure.⁸² We used the measured flow rate from an actual well to convolve the pressure responses calculated from a reservoir model with known parameters to produce wellbore pressures. The advantages of such a pseudo-synthetic case are that we can obtain a set

of wellbore pressures reflecting real wellbore storage effects. Moreover, since the measured rates contain measurement errors, we can also test our algorithm in presence of data errors.

The measured flow rates used in this pseudo-synthetic case were reported by Meunier, Wittmann, and Stewart.⁵¹ As synthesized with the actual flow rate data, the downhole pressures carry all the information from the rate measurement period, including noise. We call the synthetic pressures the “measured pressures” in the following presentation.

Because we have flow rate measurements, we can estimate parameters using both the measured pressures and measured flow rates. We take the well position as a known and estimate the other four parameters. Table 5-7 gives the initial guesses of the parameters, together with the estimates and 95% confidence intervals at the 30th iteration, and the true values of the parameters. At the 30th iteration, all parameter estimates are very close to the true values. The 95% confidence intervals of these estimates are very small, which indicate accurate estimation of the parameters.

TABLE 5-7—ESTIMATES AND TRUE VALUES OF WELL-RESERVOIR PARAMETERS FOR CASE 5-3

<u>Iteration No.</u>	<u>kh, md</u>	<u>kv, md</u>	<u>Lw, ft</u>	<u>s</u>
0	1000	100	3000	0
30	399.96	20.04	2500.40	0.006
95% confidence interval	± 0.08%	± 0.26%	± 0.08%	± 0.006
True value	400	20	2500	0

Fig. 5-10 indicates the changes of the estimates in the process of iterations. The nonlinear regression efficiently modifies all parameters to values close to their true values. Fig. 5-11 illustrates the root-mean-square error of the pressure misfit, which decreases very quickly in the first several iterations and reaches a terminal value on the order of 10^{-4} .

Fig. 5-12 is a log-log plot of pressure change and pressure derivative with respect to logarithmic time. The pressure response behaviors obtained from the true values of parameters and the estimates at the 30th iteration are presented, together with that at the initial guesses of the

parameters. Fig. 5-12 shows that the measured pressure response can be matched very well by using the measured flow rate in the nonlinear regression.

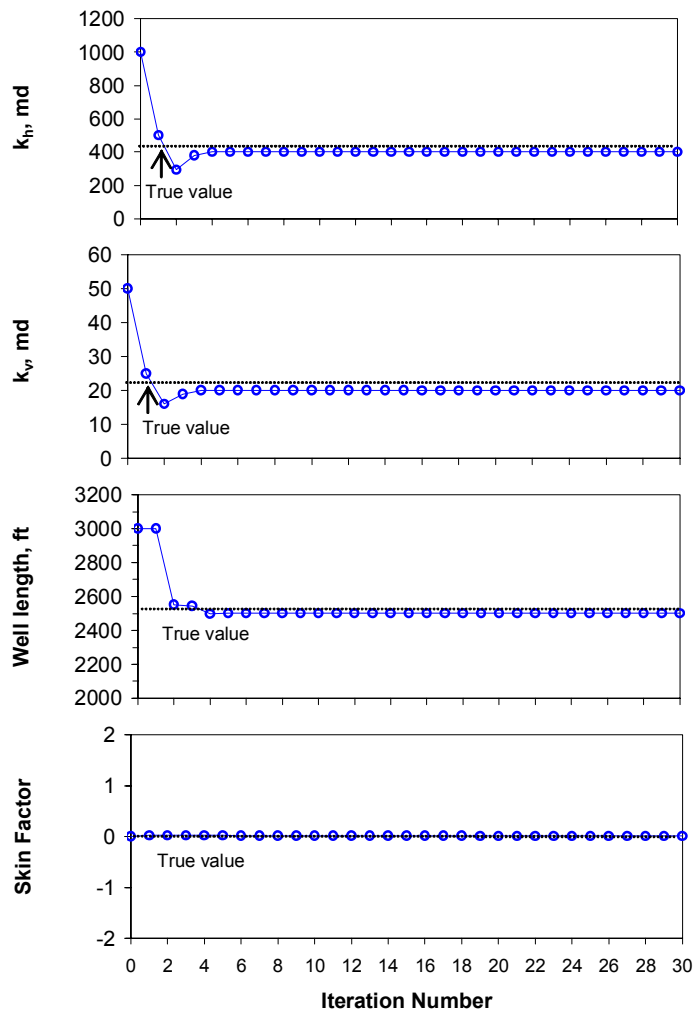


Fig. 5-10—Parameter estimates with iteration for case 5-3.

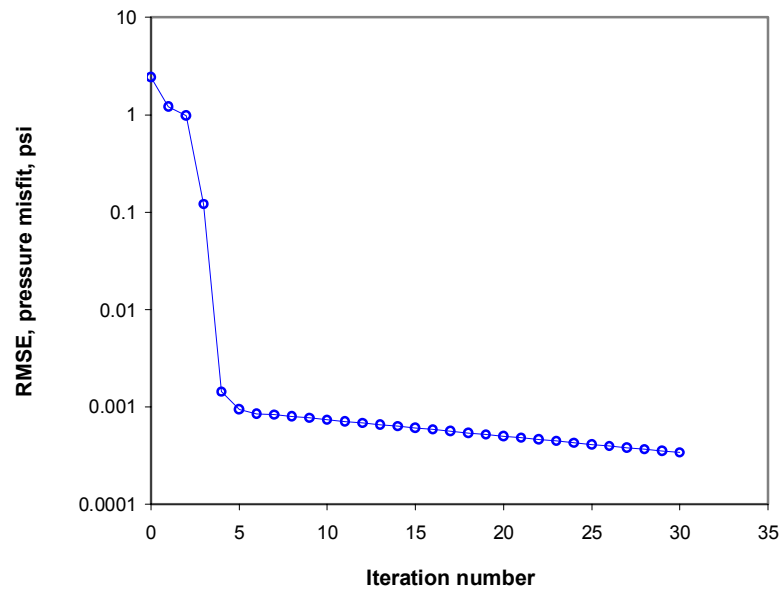


Fig. 5-11—Root-mean-square error with iteration for case 5-3.

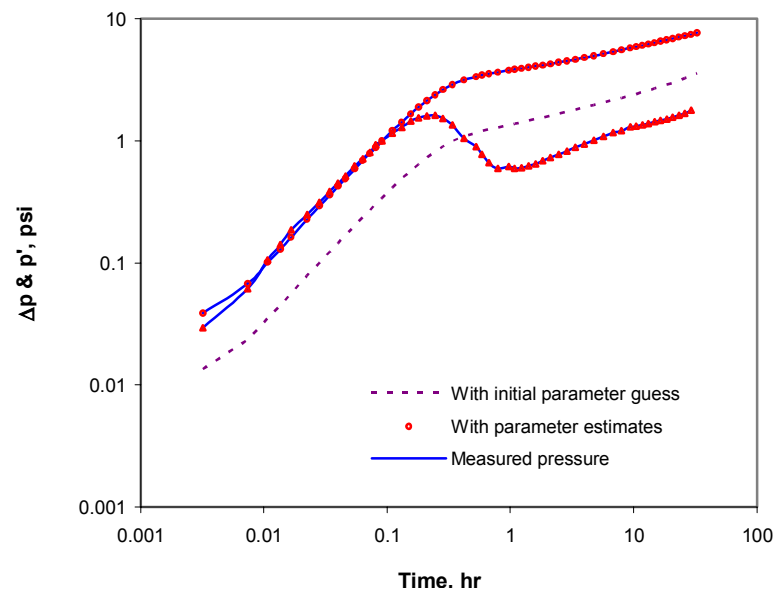


Fig. 5-12—Measured pressure response matched with parameter estimates at the 30th iteration for case 5-3.

Table 5-8 shows the covariance matrix of the parameter estimates. The cross correlations between estimates are displayed in Table 5-9.

TABLE 5-8—COVARIANCE MATRIX FOR CASE 5-3

	<u>kh</u>	<u>kv</u>	<u>Lw</u>	<u>s</u>
<u>kh</u>	2.42E-02	3.59E-04	-1.55E-01	-1.00E-04
<u>kv</u>	3.59E-04	6.78E-04	-1.35E-03	7.52E-05
<u>Lw</u>	-1.55E-01	-1.35E-03	1.08E+00	8.86E-04
<u>s</u>	-1.00E-04	7.52E-05	8.86E-04	9.44E-06

TABLE 5-9—CROSS CORRELATION MATRIX FOR CASE 5-3

	<u>kh</u>	<u>kv</u>	<u>Lw</u>	<u>s</u>
<u>kh</u>	1.000	0.089	-0.961	-0.209
<u>kv</u>	0.089	1.000	-0.050	0.940
<u>Lw</u>	-0.961	-0.050	1.000	0.278
<u>s</u>	-0.209	0.940	0.278	1.000

Case 5-4. In this case, we use the same wellbore pressure responses as those in Case 5-3. But we assume that we have only the measured pressure data without knowledge of the flow rates. Thus, we apply the blind deconvolution technique to detect the flow rates. From the minimum energy criterion, the detected rate corresponds to a step size of 0.22 (Fig. 5-13). The detected rates are shown in Fig. 5-14, which are approximate to the measured rates. The deviation of the detected rates from the measured rates is illustrated in Fig. 5-15.

Table 5-10 gives the initial guess of the parameters, together with the estimates and 95 % confidence intervals at the third iteration, and the true values of the parameters. From Table 5-10, we can see that after three iterations the nonlinear regression provides approximate parameter

estimates close to the true values from an engineering perspective. The estimates of horizontal permeability and effective wellbore length are reasonably reliable (the 95% confidence intervals are about 10% of the estimates), although the estimates of vertical permeability and skin factor contains larger uncertainties (relatively larger 95% confidence intervals).

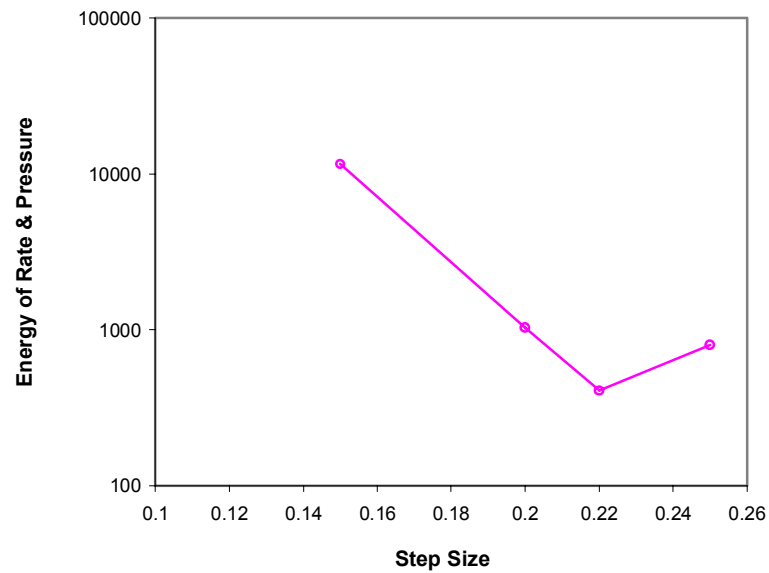


Fig. 5-13—Energy is minimum with step size of 0.22 for case 5-4.

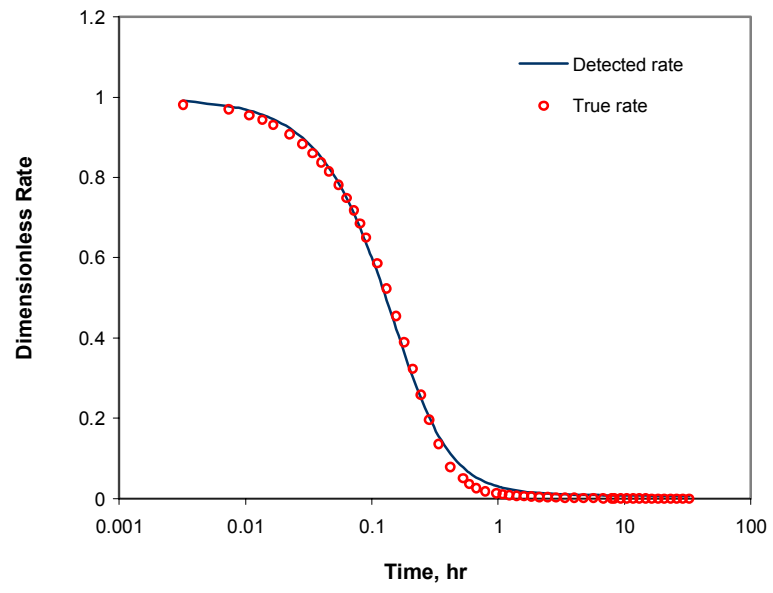


Fig. 5-14—Detected unloading rate using blind deconvolution for case 5-4.

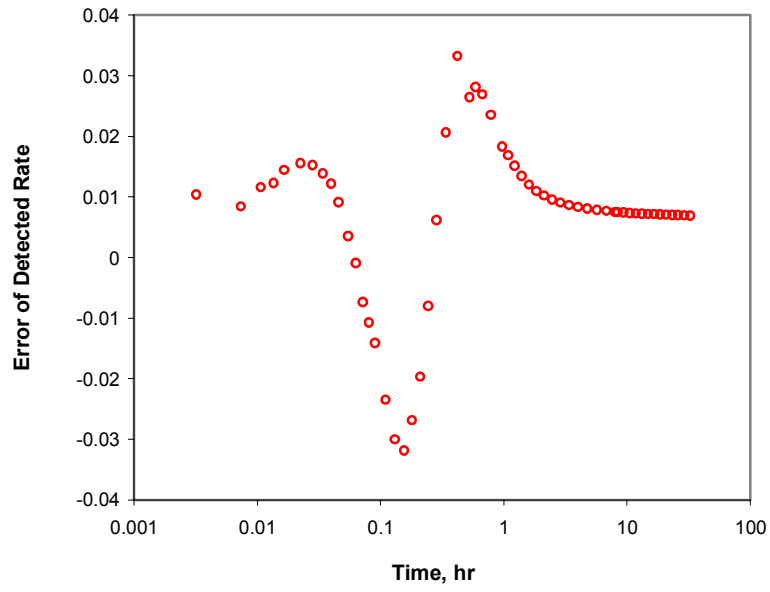


Fig. 5-15—Error of detected unloading rate using blind deconvolution for case 5-4.

TABLE 5-10—ESTIMATES AND TRUE VALUES OF WELL-RESERVOIR PARAMETERS FOR CASE 5-4

<u>Iteration No.</u>	<u>kh, md</u>	<u>kv, md</u>	<u>Lw, ft</u>	<u>s</u>
0	1000	100	3000	0
3	362.34	21.08	2707.72	0.421
95% confidence interval	± 10.65%	± 39.91%	± 10.33%	± 1.015
True value	400	20	2500	0

Fig. 5-16 indicates the changes of the parameter estimates with iterations in the process of nonlinear regression. Since there are certain differences between the detected rates and the measured rates, the estimates have some departure from the true values. But from an engineering perspective, they are reasonable and acceptable. The estimation of effective wellbore length is especially significant. This indicates that, through well testing, we can obtain a reasonably accurate estimate of effective wellbore length. In previous investigations,^{43,82} the parameter was often treated as a known, and was approximated as the drilled length or some other arbitrary value. However, using the drilled length usually results in a poor match between the model pressure and the measured pressure. Basically, the effective wellbore length should be treated as an unknown to be estimated. Since our blind deconvolution technique can provide the detected rate as a close approximation of true rate, we can obtain a reasonably reliable estimate of the effective wellbore length. Considering the effective wellbore length as an unknown is helpful for improving the quality of matching and parameter estimation.

Fig. 5-17 is the root-mean-square error of the pressure misfit which decreases to the order of 10^{-2} after several iterations. Fig. 5-18 is a log-log plot of pressure change and pressure derivative with respect to logarithmic time. Fig. 5-18 shows that the measured pressure responses can be well matched after the 30th iteration. Table 5-11 shows the covariance of parameter estimates. The cross correlations between estimates are displayed in Table 5-12.

With the detected rates, nonlinear regression can provide a reasonably reliable answer. This is because the detected rates can approximately capture the characteristics of the true flow rates resulting from changing wellbore storage. Using the detected flow rates, we can effectively

enhance the reliability of parameter estimation from nonlinear regression in the situation of no flow rate measurement while the changing wellbore storage is significant.

On the other hand, we should note that the accuracy of parameter estimates largely depends on the accuracy of detected rates. Comparing Case 5-4 with Case 5-3, we can see that the accuracy of flow rate data has a critical influence on the accuracy of the final estimates. Because the detected rate is an approximation of the true rate, the parameter estimates using the detected rate involve larger uncertainties than using the true rate. The parameter estimates are also affected by the cross correlations between parameters. From table 5-12, we see that vertical permeability and skin factor are strongly correlated (with a cross correlation coefficient of 0.966). This high positive cross correlation coefficient indicates that neither of them can be well determined independently, and if one of them is overestimated, the other one is also overestimated, and vice versa.

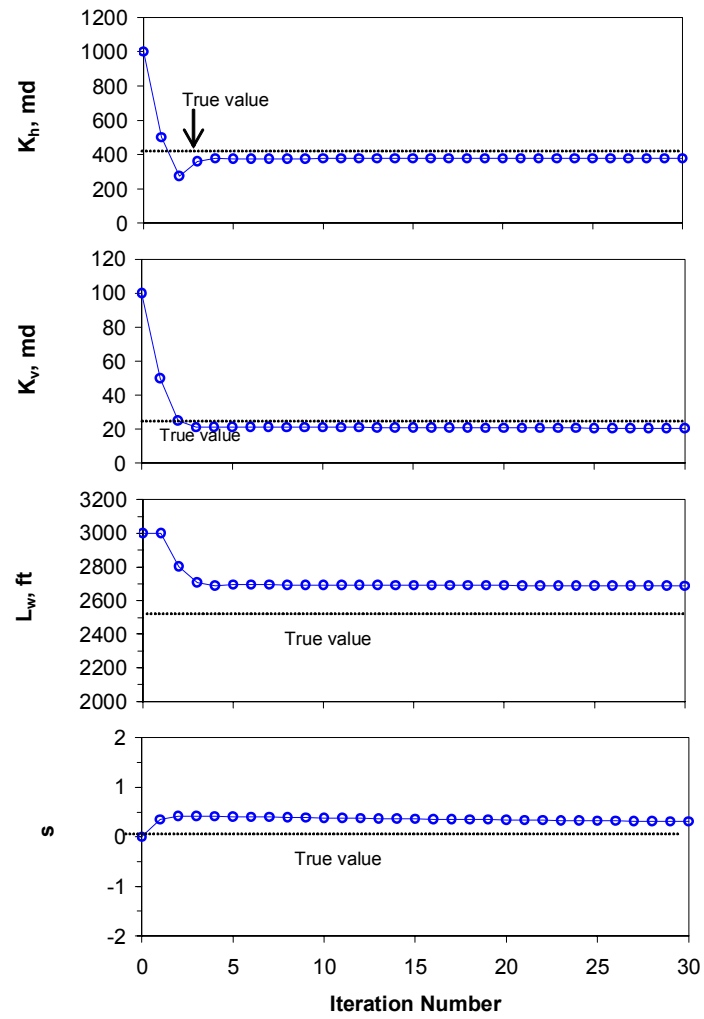


Fig. 5-16—Parameter estimates with iteration for case 5-4.

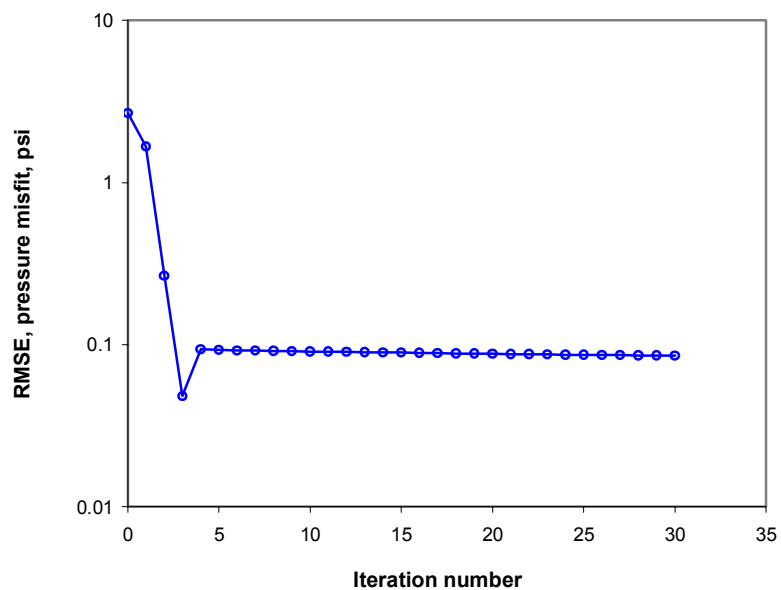


Fig. 5-17—Root-mean-square error with iteration for case 5-4.

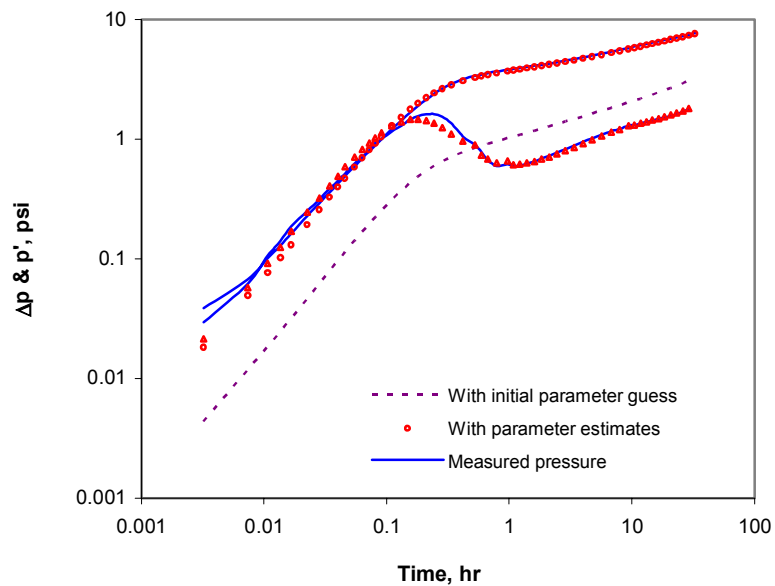


Fig. 5-18—Measured pressure response matched with parameter estimates at the third iteration for case 5-4.

TABLE 5-11—COVARIANCE MATRIX FOR CASE 5-4

	<u>kh</u>	<u>kv</u>	<u>Lw</u>	<u>s</u>
<u>kh</u>	3.72E+02	3.24E+00	-2.58E+03	-1.69E+00
<u>kv</u>	3.25E+00	1.77E+01	2.23E+00	2.06E+00
<u>Lw</u>	-2.58E+03	2.24E+00	1.95E+04	1.74E+01
<u>s</u>	-1.69E+00	2.06E+00	1.74E+01	2.58E-01

TABLE 5-12—CROSS CORRELATION MATRIX FOR CASE 5-4

	<u>kh</u>	<u>kv</u>	<u>Lw</u>	<u>s</u>
<u>kh</u>	1.000	0.040	-0.955	-0.173
<u>kv</u>	0.040	1.000	0.004	0.966
<u>Lw</u>	-0.955	0.004	1.000	0.245
<u>s</u>	-0.173	0.966	0.245	1.000

Case 5-5. This is a field buildup case, presented by Horne.⁴³ The reservoir and fluid properties are listed in Table 5-13. This case only had buildup wellbore pressure measurement without downhole rate measurement. Therefore, we first apply the blind deconvolution technique to detect the flow rate. From the minimum energy criterion, the rate is detected corresponding to a step size of 0.06 (Fig. 5-19). The detected rate is illustrated in Fig. 5-20.

TABLE 5-13—RESERVOIR AND FLUID PROPERTIES FOR CASE 5-5

Porosity, ϕ	= 0.25
Viscosity, μ	= 3 cp
Compressibility, c_t	= 7.0×10^{-5} psi ⁻¹
Formation volume factor, B	= 1.15 RB/STB
Formation thickness, h	= 45 ft
Wellbore radius, r_w	= 0.3 ft
Drilled wellbore length, L_w	= 1700 ft, centered
Initial reservoir pressure, p_i	= 3548 psi
Production rate, q	= 6186.6 STB/D
Production time, t	= 28.7 hrs

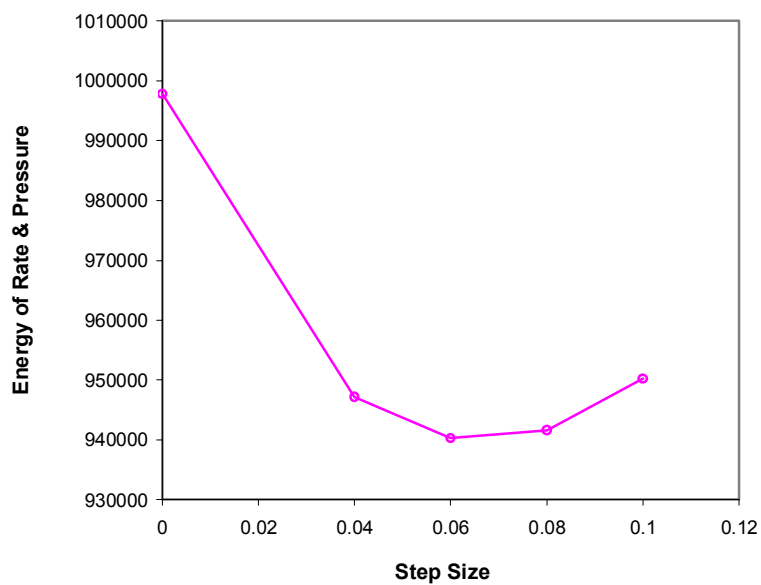


Fig. 5-19—Energy is minimum with step size of 0.06 for case 5-5.

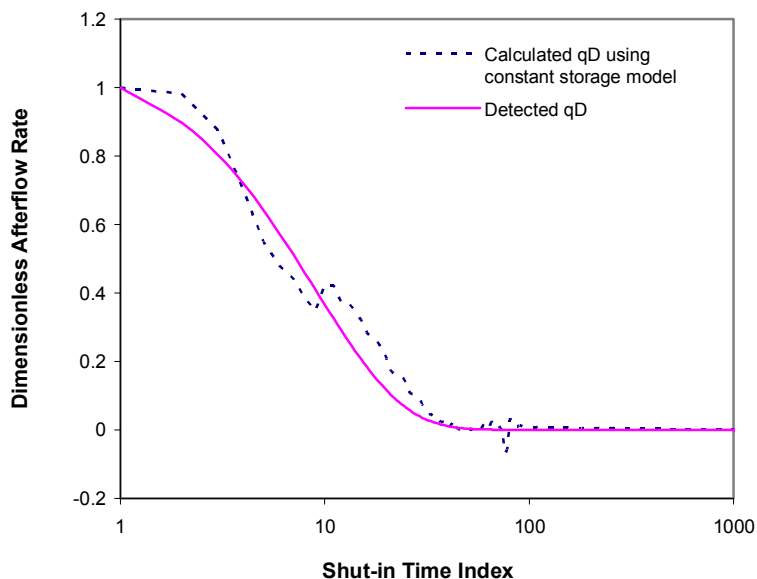


Fig. 5-20—Detected afterflow rate for case 5-5.

Table 5-14 gives the initial guess of the parameters, together with the estimates and 95% confidence intervals at the 30th iteration. The small 95% confidence intervals show that the parameter estimation is reliable from the viewpoint of engineering.

TABLE 5-14—INITIAL GUESSES AND ESTIMATES OF WELL-RESERVOIR PARAMETERS FOR CASE 5-5

<u>Iteration No.</u>	<u>kh, md</u>	<u>kv, md</u>	<u>L_w, ft</u>	<u>z_w, ft</u>	<u>s</u>
0	100	100	1700	22.5	0
30	3843.25	860.19	380.18	30.35	5.732
95% confidence interval	± 1.42%	± 20.49%	± 3.96%	± 7.26%	± 0.870

Figs. 5-21 to 5-23 are the parameter estimates with the iterations. The horizontal permeability, wellbore length and well vertical position rapidly become flat after the first several iterations. The vertical permeability and skin factor are basically stable after 30 iterations.

Similarly, the root-mean square error of pressure misfit quickly decreases to 0.5 (Fig. 5-24). Fig. 5-25 illustrates pressure change and pressure derivative with respect to logarithmic time in a log-log plot. The measured pressure behaviors can be matched quite well and the pressure derivatives of the model responses are basically consistent with the observed ones. Fig. 5-26 gives the wellbore storage coefficient and the detected afterflow rate. The afterflow rates were detected using blind deconvolution technique, while the wellbore storage coefficient was calculated from the detected rate data. Fig. 5-26 clearly indicates that there is a strong changing wellbore storage effect during the buildup test period. Table 5-15 shows the covariance matrix of parameter estimates. The correlations between estimates are displayed in Table 5-16. The skin factor is strongly correlated with vertical permeability. The effective wellbore length has a strong correlation with horizontal permeability.

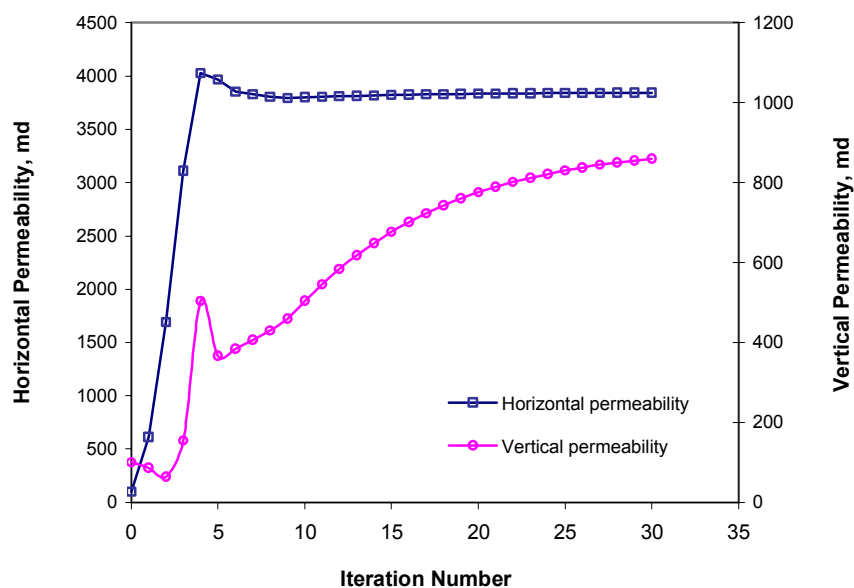


Fig. 5-21—Estimates of horizontal and vertical permeabilities with iteration for case 5-5.

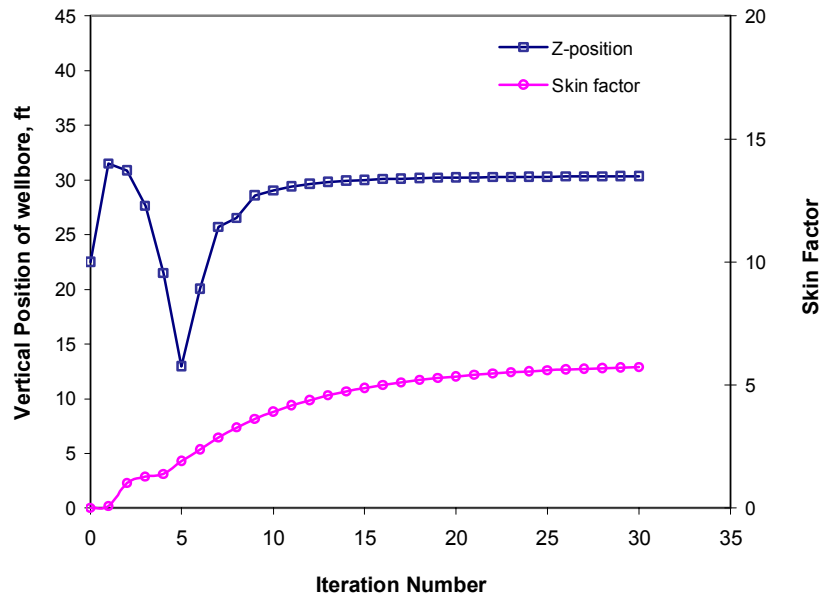


Fig. 5-22—Estimates of well vertical position and skin factor with iteration for case 5-5.

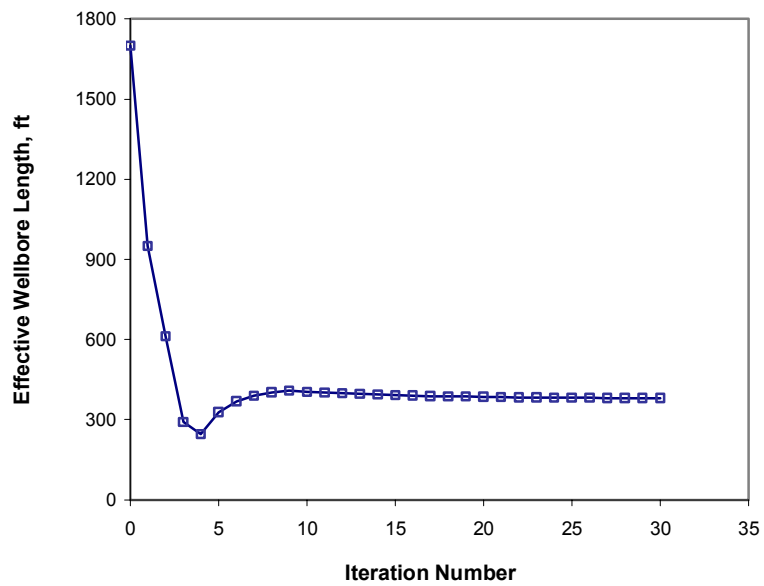


Fig. 5-23—Estimates of effective well length with iteration for case 5-5.

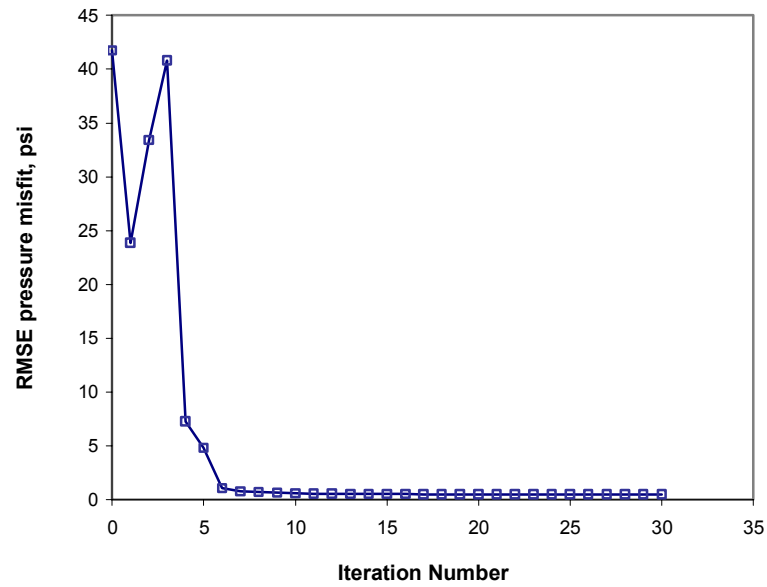


Fig. 5-24—Root-mean-square error with iteration for case 5-5.

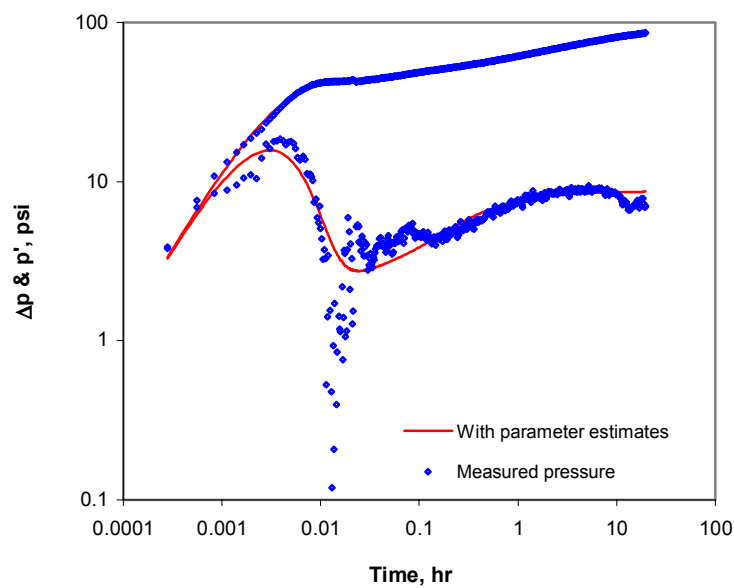


Fig. 5-25—Measured pressure response matched with parameter estimates at the 30th iteration for case 5-5.

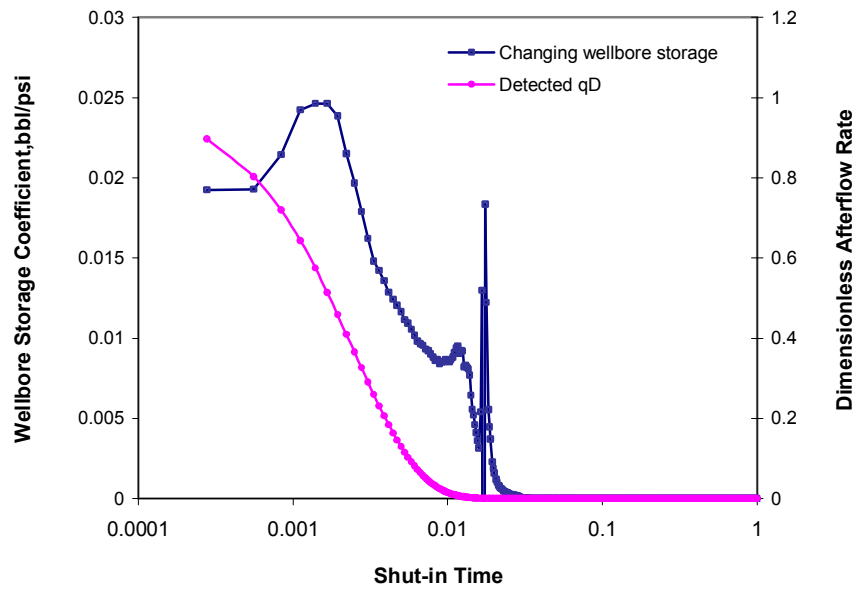


Fig. 5-26—Wellbore storage coefficient and detected afterflow rate for case 5-5.

TABLE 5-15—COVARIANCE MATRIX FOR CASE 5-5

	<u>kh</u>	<u>kv</u>	<u>Lw</u>	<u>zw</u>	<u>s</u>
<u>kh</u>	7.42E+02	4.49E+02	-1.80E+02	-1.08E+01	-9.29E-01
<u>kv</u>	4.49E+02	7.76E+03	-1.32E+02	6.18E+01	3.64E+01
<u>Lw</u>	-1.80E+02	-1.32E+02	5.66E+01	4.50E+00	3.87E-01
<u>zw</u>	-1.08E+01	6.18E+01	4.50E+00	1.21E+00	3.91E-01
<u>s</u>	-9.30E-01	3.64E+01	3.87E-01	3.91E-01	1.89E-01

TABLE 5-16—CROSS CORRELATION MATRIX FOR CASE 5-5

	<u>kh</u>	<u>kv</u>	<u>Lw</u>	<u>zw</u>	<u>s</u>
<u>kh</u>	1.000	0.187	-0.880	-0.360	-0.078
<u>kv</u>	0.187	1.000	-0.199	0.636	0.949
<u>Lw</u>	-0.880	-0.199	1.000	0.543	0.118
<u>zw</u>	-0.360	0.636	0.543	1.000	0.816
<u>s</u>	-0.078	0.949	0.118	0.816	1.000

5.5 Chapter Summary

This chapter presents a practical nonlinear regression technique for parameter estimation in horizontal well test analysis. The parameters include horizontal and vertical permeabilities, horizontal wellbore length, well vertical position and skin factor. Our studies indicate that the nonlinear regression technique can provide quite accurate and reliable well-reservoir information with both measured pressure and flow rate data. In the situations without flow rate measurement, using the detected flow rate obtained from blind deconvolution, the nonlinear regression can obtain a reasonably reliable estimation of parameters under the conditions of the changing wellbore storage. The effective wellbore length can be treated as an unknown to be estimated. It can be accurately estimated if the true rate information is available. With the approximate rate information, such as the detected rate from blind deconvolution, it can be reasonably well estimated from an engineering perspective.

CHAPTER VI

CONCLUSIONS AND RECOMMENDATIONS

Horizontal wells are widely applied in petroleum industry. Productivity evaluation and well test analysis are important components of horizontal well technology. However, it is well recognized that evaluation of productivity in horizontal wells is subject to more uncertainties and interpretation of well tests in horizontal wells is much more difficult, compared with counterparts in vertical wells. This study addressed important related issues, including a 3D coupled reservoir/wellbore model, productivity evaluation, a deconvolution technique and nonlinear regression of well tests. The 3D coupled reservoir/wellbore model accounts for the complex 3D flow geometry of horizontal wells and the strong reservoir/wellbore interaction that results from frictional pressure loss along the wellbore. Instead of considering the productivity index as a single value, the productivity index of horizontal well was treated as a random variable, and its uncertainty was then quantified. A novel deconvolution technique was developed to overcome the problem of wellbore storage, which constitutes a big challenge in horizontal well testing. The deconvolution technique is able to effectively remove the wellbore storage effect and recover the underlying reservoir behavior. Therefore, it can be very useful for reservoir system identification and parameter estimation. Since well-defined flow periods are often absent or not apparent in horizontal wells, and considerable wellbore storage effect is present, conventional techniques of horizontal well test analysis are often not effective. The nonlinear regression technique estimates parameters in a systematic manner. Combined with deconvolution, the nonlinear regression technique provides a practical way to improve the interpretation of horizontal well tests. The major conclusions and recommendations are summarized as follows.

The major conclusions:

1. Horizontal Well Performance Prediction Model

This horizontal well performance prediction model is able to reliably evaluate well productivity and rigorously simulate pressure transient testing. It was developed by

coupling a general 3D reservoir model, established by using the boundary element method, with a wellbore hydraulics model.

- This model can account for realistic reservoir and well conditions, such as arbitrary well configuration, permeability anisotropy, and variable rate production.
- This model has been demonstrated to be a powerful tool for accurately predicting the performance of horizontal wells. It is applicable for various inner boundary conditions such as uniform flux, infinite conductivity, and finite conductivity wellbores, and for various outer boundary conditions, such as no-flow, constant pressure, and mixed boundaries. It can be used to simulate various well tests, such as pressure drawdown, pressure buildup, and multi-rate tests.

2. Productivity Evaluation.

- Using the new performance prediction model, the transient, pseudo-steady state and steady state productivities can be reliably evaluated. A number of examples were presented to demonstrate such evaluations.
- Many parameters are required for the evaluation of well productivity in horizontal wells. However, estimates of these parameters are not likely to be accurate, resulting in uncertainty in productivity. The uncertainty in productivity estimates can be quantified based on the uncertainties of the parameters.

3. Deconvolution Technique.

A fast-Fourier-transform-based deconvolution method was presented for restoration of constant-rate pressure responses from measured pressure data with or without downhole rate measurements. It is characterized as follows:

- The deconvolution approach is computationally efficient and stable. Since the denoising technique developed can effectively remove or suppress the noise in measurement data, stable deconvolution results can be obtained even when the level of noise is quite high.
- For the situation where there is no downhole rate measurement, a blind deconvolution technique was developed, and the technique can simultaneously detect the rate function and recover reservoir pressure. This greatly enhances the application of the deconvolution technique.

- With this new technique, the early time behavior of a reservoir system masked by wellbore storage distortion can be unveiled. The wellbore storage coefficient can be variable in the general case. The new method thus provides a powerful tool to improve pressure transient test interpretation.
- The power and practical applicability of the approach were demonstrated with various synthetic and actual field cases, both with or without rate measurement.

4. Well Testing Nonlinear Regression Technique.

A nonlinear least square regression technique for analysis of horizontal well testing was presented, and the technique was proved to be effective and efficient in improvement of parameter estimation and interpretation of horizontal well tests.

- The nonlinear regression technique can provide quite accurate and reliable well-reservoir parameters, with both measured pressure and flow rate data. The estimated parameters include horizontal and vertical permeabilities, horizontal wellbore length, well vertical position and skin factor.
- In the situation without flow rate measurements, we can achieve a reasonably reliable estimation of parameters by using the detected flow rate from blind deconvolution. It is not necessary to estimate the wellbore storage coefficient because the detected flow rate already contains the characteristics of a changing storage coefficient.
- Taking the effective wellbore length as an unknown to be estimated proved helpful to improve the match of pressure responses and estimation of parameters. A reasonable estimation of the effective wellbore length can be obtained through nonlinear regression.
- The practical significance of this technique was demonstrated with synthetic and actual field cases.

The recommendations:

1. To quantify the uncertainty of productivity estimation, we first need to sample a certain distribution for parameter estimates. We used a simple sampling method by assuming each parameter independently followed a normal distribution. However, the parameters are correlated and thus follow a multi-variant normal distribution, which can be

determined by nonlinear regression analysis of well test data. It is necessary to develop more advanced sampling techniques to consider this factor to better quantify productivity uncertainty.

2. In our horizontal well performance prediction model, we considered a box-shaped reservoir. However, the BEM is applicable to reservoir boundaries of any shape. Since we used the BEM in building our model, the model can be conveniently extended to handle arbitrarily shaped reservoirs.

NOMENCLATURE

A	= sensitivity matrix
a	= constant, or drainage dimension along x -direction, ft [m]
B	= formation volume factor, rb/stb, [res m ³ /st m ³]
b	= constant, or drainage dimension along y -direction, ft [m]
C_D	= dimensionless wellbore storage coefficient
C_s	= wellbore storage coefficient, bbl/psi
c	= constant, or drainage dimension along z -direction, ft [m]
c_t	= total compressibility, 1/psi
$c_1 \sim c_4$	= constants
E	= residual (error) vector
F_w	= additional pressure loss due to friction in the wellbore
f	= Fanning friction factor, or function, or frequency, 1/sec
G	= Green's function
I	= unit matrix
J	= objective function, or productivity index, stb/day/psi
k	= permeability, md [m ²]
k_a	= geometric average permeability in the plane normal to wellbore direction, md [m ²]
L_{wD}	= dimensionless wellbore length
L_w	= effective wellbore length, ft [m]
M	= total number of nodes on wellbore
N	= total number of nodes on outer boundaries, or sample number
N_{Re}	= Reynolds number
p	= pressure, psi, [pa]
p_{av}	= average reservoir pressure, psi [pa]
p_D	= dimensionless pressure
p_e	= pressure at boundary, psi [pa]
p_i	= initial reservoir pressure, psi [pa]
p_w	= measured pressure response, psi [pa]

$p_{wf,h}$	= flowing pressure at the heel, psi [pa]
$p_{wf,r}$	= pressure response without considering pressure loss in wellbore, psi [pa]
p_{δ}	= constant-rate pressure response, psi [pa]
q	= surface rate, stb/day [m^3/s , or ft^3/hr]
q_D	= dimensionless afterflow rate
q_h	= flux (flow rate per unit length of wellbore), stb/day/ft [$m^3/s/m$]
q_{hD}	= dimensionless flux
q_r	= reference flow rate, stb/day [m^3/s , or ft^3/hr]
q_{sf}	= sandface flow rate, stb/day [m^3/s , or ft^3/hr]
q_t	= total flow rate from well, stb/day [m^3/s , or ft^3/hr]
q_v	= flow rate per unit volume, stb/day/ ft^3 [$m^3/s/m^3$]
R	= a point in 3D space located at $R(x, y, z)$
r	= radius, ft [m], or derivative of dimensionless sandface flow rate, 1/hr [1/s]
r_{eD}	= dimensionless drainage radius, ft [m]
r_w	= wellbore radius, ft [m]
r_{wD}	= dimensionless wellbore radius
S	= boundary surfaces of domain Ω
$S_1 \sim S_6$	= boundary surfaces of box-shaped domain
s	= Laplace domain variable, or skin factor
s_f	= skin factor
t	= time, hr [s]
t_D	= dimensionless time
u	= temperature, $^{\circ}C$
V	= reservoir volume, ft^3 [m^3]
X	= frequency-domain function
x	= time-domain function, or coordinate in x -direction
x_e	= length of drainage volume, ft [m]
x'	= x -coordinate of well axis
y	= coordinate in y -direction, or observed set of data
y'	= y -coordinate of well axis
z	= coordinate in z -direction

z'	= z -coordinate of well axis
α	= diffusivity, m^2/s
β	= estimated parameter vector
δ	= Dirac delta function
Δ	= difference
ε	= infinitesimal, absolute roughness
η	= diffusivity, ft^2/hr [m^2/s]
φ	= porosity, or basis function
λ	= transmissivity ratio
μ	= viscosity, cp [$\text{pa}\cdot\text{s}$]
θ, θ'	= polar angle
ρ	= fluid density, lb_m/ft^3 [kg/m^3], correlation coefficient
σ	= standard deviation
ω	= storativity ratio
Ω	= 3D domain
Ω_1	= source domain
ψ	= basis function
ξ	= basis function
ζ	= basis function
∇	= gradient
∇^2	= Laplace operator

Subscripts

cal	= calculated
d	= discrete
e	= element
f	= frequency domain
$integ$	= numerical integral
m	= measured

mod = afterflow rate model defined by Eq. 4-22
x = *x*-direction
y = *y*-direction
z = *z*-direction

Superscripts

\sim = Fourier transform
-1 = inverse Fourier transform
T = transpose

REFERENCES

1. Gringarten, A.C. and Ramey, H.J.: "The Use of Source and Green's Functions in Solving Unsteady Flow Problems in Reservoirs," *SPEJ* (Oct. 1973) 285.
2. Clonts, M.D. and Ramey, H.J., Jr.: "Pressure Transient Analysis for Wells with Horizontal Drainholes," paper SPE 15116 presented at the 1986 California Regional Meeting, Oakland, CA, 2-4 April.
3. Babu, D.K. and Odeh, A.S.: "Productivity of a Horizontal Well," *SPEE* (Nov. 1989) 417.
4. Babu, D.K. and Odeh, A.S.: "Productivity of a Horizontal Well: Appendix A and B," paper SPE18334 available from SPE Book Order Dept., Richardson, TX.
5. Carslaw, H.S., and Jaeger, J.C.: *Conduction of Heat in Solids*, Oxford Clarendon Press, Oxford (1959).
6. Numbere, D.T. and Tiab, D.: "An Improved Streamline Generating Technique Using the Boundary (Integral) Element Method," paper SPE 15135 presented at the 1986 California Regional Meeting, Oakland, CA, 2-4 April.
7. Masukawa, J. and Horne, R.N.: "The Application of the Boundary Integral Method to Immiscible Displacement Problems," paper SPE 15136 presented at the 1986 California Regional Meeting, Oakland, CA, 2-4 April.
8. Kikani, J. and Horne, R.N.: "Pressure-Transient Analysis of Arbitrarily Shaped Reservoir with the Boundary Element Method," *SPEFE* (Mar. 1992) 53.
9. Kikani, J. and Horne, R.N.: "Modeling Pressure-Transient Behavior of Sectionally Homogeneous Reservoirs by the Boundary-Element Method," *SPEFE* (June 1993) 145.
10. Sung, W., Lee, W. and Kim, I.: "Development and Validation of Interference Testing Analysis Model Using Boundary Element Method for Geometrically Complex Reservoirs," paper SPE 54272 presented at the 1999 SPE Asia Pacific Oil and Gas Conference and Exhibition, Jakarta, Indonesia, 20-22 April.
11. Sato, K. and Horne, R.N.: "Perturbation Boundary Element Method for Heterogeneous Reservoirs: Part 1-Steady-State Flow Problems," *SPEFE* (Dec. 1993) 306.
12. Sato, K. and Horne, R.N.: "Perturbation Boundary Element Method for Heterogeneous Reservoirs: Part 2-Transient Flow Problems," *SPEFE* (Dec. 1993) 315.
13. Sato, K. and Abbaszadeh, M.: "Tracer Flow and Pressure Performance of Reservoirs Containing Distributed Thin Bodies," *SPEFE* (Sept. 1996) 315.

14. Lough, M.F., Lee, S.H., and Kamath, J.: "An Efficient Boundary Integral Formulation for Flow through Fractured Porous Media," *Journal of Computational Physics* (July 1998), 143, 1-22.
15. Lough, M.F., Lee, S.H., and Kamath, J.: "A New Method to Calculate the Effective Permeability of Grid Blocks Used in the Simulation of Naturally Fractured Reservoirs," *SPE* (Aug. 1997) 219.
16. Koh, L.S. and Tiab, D.: "A Boundary-Element Algorithm for Modeling 3D Horizontal Well Problems Using 2D Grids," paper SPE 26228 presented at the 1993 SPE Petroleum Computer Conference, New Orleans, 11-14 July.
17. Stehfest, H.: "Algorithm 368, Numerical Inversion of Laplace Transforms," D-5, *Communications of the ACM* (Jan. 1970) **13**, No. 1, 47.
18. Borisov, J.P.: *Oil Production Using Horizontal and Multiple Deviation Wells*, Nedra, Moscow (1964). Translated by J. Strauss, S.D. Joshi (ed.), Phillips Petroleum Co., R&D Library Translation, Bartlesville, OK (1984).
19. Giger, F.M., Reiss, L.H., and Jourdan, A.P.: "Reservoir Engineering Aspects of Horizontal Drilling," paper SPE 13024 presented at the 1984 SPE Annual Technical Conference and Exhibition, Houston, 16-19 Sept.
20. Giger, F.M., Reiss, L.H., and Jourdan, A.P.: "Low Permeability Reservoir Development Using Horizontal Well," paper SPE 16406 presented at the 1987 SPE Joint Low-Permeability Reservoir Symposium/Rocky Mountain Regional Meeting, Denver, 18-19 May.
21. Joshi, S.D.: "Augmentation of Well Productivity Using Slant and Horizontal Wells," paper SPE 15375 presented at the 1986 SPE Annual Technical Conference and Exhibition, New Orleans, 5-8 Oct.
22. Karcher, B.J., Giger, F.M. and Combe, F.M.: "Some Practical Formulas to Predict Horizontal Well Behavior," paper SPE 15430 presented at the 1986 SPE Annual Technical Conference and Exhibition, New Orleans, 5-8 Oct.
23. Renard, G. and Dupuy, J.G.: "Influence of Flow on the Efficiency of Horizontal Wells," *JPT* (July 1991) 786.
24. Goode, P. A., and Kuchuk, F. J.: "Inflow Performance of Horizontal wells," *SPE* (Aug. 1991) 319-323.

25. Economides, M. J., Brand, C. W. and Frick, T.P.: "Well Configurations in Anisotropic Reservoirs," *SPEFE* (Dec. 1996) 257.
26. Helmy M. W., and Wattenbarger R. A.: "Simplified Productivity Equations for Horizontal Wells Producing at Constant Rate and Constant Pressure," paper SPE 49090 presented at the 1998 SPE Annual Technical Conference and Exhibition, New Orleans, 27-30 Sept.
27. Dikken, B. J.: "Pressure Drop in Horizontal Wells and its Effect on Production Performance," *JPT* (Nov.1990) 1426.
28. Thompson, L.G., Marique, J.L., and Jelmet, T.A.: "Efficient Algorithms for Computing the Bounded Reservoir Horizontal Well Pressure Response," paper SPE 21827 presented at the 1991 SPE Rocky Mountain Regional Meeting and Low-Permeability Reservoir Symposium, Denver, 15-17 April.
29. Besson, J.: "Performance of Slanted and Horizontal Wells on an Anisotropic Medium," paper SPE 20965 presented at Europe 1990, Hague, Netherlands, 22-24 Oct.
30. Spivey, J.P. and Lee, W.J.: "New Solutions for Pressure Transient Response for a Horizontal or Hydraulically Fractured Well at an Arbitrary Orientation in an Anisotropic Reservoir," paper SPE 49236 presented at the 1998 SPE Annual Technical Conference and Exhibition, New Orleans, 27-30 Sept.
31. Ozkan, E., Sarica, C., and Haci, M.: "Influence of Pressure Drop along the Wellbore on Horizontal-Well Productivity," *SPEJ* (Sept. 1999) 288.
32. Ouyang, L. B. and Aziz, K.: "A Simplified Approach to Couple Wellbore Flow and Reservoir Inflow for Arbitrary Well Configurations," paper SPE 48936 presented at the 1998 SPE Annual Technical Conference and Exhibition, New Orleans, 27-30 Sept.
33. Ding, Y.: "Using Boundary Integral Methods to Couple a Semi-analytical Reservoir Flow Model and a Wellbore Flow Model," paper SPE 51898 presented at 1999 SPE Reservoir Simulation Symposium, Houston, 14-17 Feb.
34. Davlau, F., Mouronval, G., Bourdarot, G., and Curutchet, P.: "Pressure Analysis for Horizontal Wells," paper SPE 14251 presented at the 1985 SPE Annual Technical Conference and Exhibition, Las Vegas, 22-25 Sept.
35. Cinco-ley, H. and Samaniego, F.: "Effect of Wellbore Storage and Damage on the Transient Pressure Behavior of Vertically Fractured Wells," paper SPE 6752 presented at the 1977 SPE Annual Technical Conference and Exhibition, Denver, 9-12 Oct.

36. Goode, P. A. and Thambynayagam, R. K. M.: "Pressure Drawdown and Buildup Analysis of Horizontal Wells in Anisotropic Media," *SPEFE* (Dec. 1987) 683.
37. Ozkan, E., Raghavan, R., and Joshi, S. D.: "Horizontal Well Pressure Analysis," *SPEFE* (Dec. 1989) 567.
38. Ozkan, E.: *Performance of Horizontal Wells*, PhD Dissertation, University of Tulsa, Tulsa, OK, 1987.
39. Kuchuk, F. J., Goode, P. A., Wilkinson, D. J., and Thambynayagam, R. K. M.: "Pressure-Transient Behavior of Horizontal Wells with and without Gas Cap or Aquifer," *SPEFE* (March 1991) 86.
40. Odeh, A.S. and Babu, D.K.: "Transient Flow Behavior of Horizontal Well: Pressure Drawdown and Buildup Analysis," *SPEFE* (Mar. 1990) 7.
41. Rosa, A.J.: "A Mathematical Model for Pressure Evaluation in An Infinite Conductivity Horizontal Well," manuscript of SPE 15967, Unsolicited.
42. Kuchuk, F. J.: "Well Testing and Interpretation for Horizontal Wells," *JPT* (January 1995) 36.
43. Horne, R.N.: *Modern Well Test Analysis*, Petroway, Inc., Palo Alto (1995).
44. Ozkan, E.: "Analysis of Horizontal-Well Responses: Contemporary vs. Conventional," paper SPE 52199 presented at the 1999 SPE Mid-Continent Operations Symposium, Oklahoma City, 28-31 Mar.
45. Kuchuk, F. J.: "Pressure-Transient Testing and Interpretation for Horizontal Wells," paper SPE 37796 presented at the 1997 SPE Middle East Oil Show & Conference, Bahrain, 15-18 Mar.
46. Van Everdingen, A.F. and Hurst, W.: "Application of the Laplace Transform to Flow Problems in Reservoirs," *Trans, AIME* (1949) 186, 305.
47. Gladfelter, R.E., Tracy, G.W., and Wilsey, L.E.: "Selecting Wells Which Will Response to Production-Stimulation Treatment," *Drill. and Prod. Prac.*, API (1955) 117.
48. Odeh, A.S. and Jones, L.G.: "Pressure Drawdown Analysis, Variable-Rate Case," *JPT* (Aug. 1965) 960.
49. Stewart, G., Wittmann, M.J., and Meunier, D.: "Afterflow Measurement and Deconvolution in Well Test Analysis," paper SPE 12174 presented at the 1983 SPE Annual Technical Conference and Exhibition, San Francisco, 5-8 October.

50. Fetkovitch, M.J. and Vienot, M.E: "Rate Normalization of Buildup by Using Afterflow Data," *JPT* (Dec. 1984) 2211.
51. Meunier, D., Wittmann, M.J., and Stewart, G.: "Interpretation of Pressure Buildup Tests Using In-Situ Measurement of Afterflow," *JPT* (Jan. 1985) 143.
52. Bostic, J.N., Agarwal, R.G., and Carter, R.D.: "Combined Analysis of Post Fracturing Performance and Pressure Buildup Data for Evaluating an MHF Gas Well," *JPT* (Oct. 1980) 1711.
53. Kuchuk, F. J. and Ayestaran, L.: "Analysis of Simultaneously Measured Pressure and Sandface Flow Rate in Transient Well Testing," *JPT* (Feb. 1985) 323.
54. Thompson, L.G., Jones, J.R., and Reynolds, A.C.: "Analysis of Pressure Buildup Data Influenced by Wellbore Phase Redistribution," *SPEFE* (Oct. 1986) 435.
55. Thompson, L.G. and Reynolds, A.C.: "Analysis of Variable-Rate Well-Test Pressure Data Using Duhamel's Principle," *SPEFE* (Oct. 1986) 453.
56. Coats, K.H. et al.: "Determination of Aquifer Influence Functions from Field Data," *JPT* (Dec. 1964) 1417; *Trans.*, AIME, 231.
57. Kuchuk, F. J., Carter, R.G., and Ayestaran, L.: "Deconvolution of Wellbore Pressure and Flow Rate," *SPEFE* (March 1990) 375.
58. Baygun, B., Kuchuk, F. J., and Arikan, O.: "Deconvolution under Normalized Autocorrelation Constraints," *SPEJ* (Feb. 1997) 246.
59. Rouboutsos, A. and Stewart, G.: "A Direct Deconvolution or Convolution Algorithm for Well Test Analysis," paper SPE 18157 presented at the 1988 SPE Annual Technical Conference and Exhibition, Houston, 5-8 October.
60. Fair, P.S. and Simmons, J.F.: "Novel Well Testing Applications of Laplace Transform Deconvolution," paper SPE 24716 presented at the 1992 Annual Technical Conference and Exhibition, Washington, DC, 4-7 October.
61. Fair, W.B.: "Pressure Buildup Analysis with Wellbore Phase Redistribution," paper SPE 8206 presented at the 1979 Annual Technical Conference and Exhibition, Las Vegas, 23-26 September.
62. Fair, W.B.: "Generalization of Wellbore Effects in Pressure-Transient Analysis," *SPEFE* (June 1996) 114.
63. Molina, R., Katsaggelos, A.K., Abad, J. and Mateos, J.: "A Bayesian Approach to Blind Deconvolution Based on Dirichlet Distributions", Proc. Of the IEEE 1997 International

- Conference on Acoustics, Speech and Signal Processing, Vol. 4, 2809~2812, Munich, Alemania.
64. Carasso, A.S.: "Direct Blind Deconvolution", *SIAM J. APPL. MATH.* (April 2001) **61**, No. 6, 1980.
 65. Sacchi, M.D., Velis, D.R., and Cominguez, A.H.: "Minimum Entropy Deconvolution with Frequency-Domain Constraints", *Geophysics* (June 1994) **59**, No. 6, 938.
 66. Erdogmus, D., Principe, J.C. and Vielva, L.: "Blind Deconvolution with Minimum Renyi's Entropy," Proc. Of EUSIPCO'02, Vol. 1, 557, Toulouse, France, Sept. 2002.
 67. Lee, W.J.: *Well Testing*, SPE, AIME, New York (1982).
 68. Ozisik, M.N.: *Heat Conduction*, John Wiley & Sons Inc., New York (1980).
 69. Katsikadelis, J.T.: *Boundary Element: Theory and Applications*, Elsevier Science Ltd. UK, (2002).
 70. Kytbe, P.K.: *An Introduction to Boundary Element Methods*, CRC Press, Boca Raton (1995).
 71. Paris, F., and Canas, J.: *Boundary Element Method: Fundamentals and Applications*, Oxford University Press, Oxford (1997).
 72. Brill, J.P.: "Multiphase Flow in Wells," SPE Monograph, Dallas (1999).
 73. Gringarten, A.C. and Ramey, H.J.: "Unsteady State Pressure Distributions Created by a Well with a Single Infinite Conductivity Vertical Fracture," *SPEJ* (Aug. 1974) 347.
 74. Ramirez, R.W.: *The FFT, Fundamentals and Concepts*, Tektronix, Inc., Englewood Cliffs, New Jersey (1985).
 75. Bracewell, R.N.: *The Fourier Transform and its Applications*, McGraw-Hill Book Co., Inc., New York (1986).
 76. Hegeman, P.S., Hallford, D.L., and Joseph, J.A.: "Well Test Analysis with Changing Wellbore Storage," paper SPE 21829 presented at the 1991 Rocky Mountain Regional Meeting and Low Permeability Reservoir Symposium, Denver, 15-17 April.
 77. Sabet, M.A.: *Well Test Analysis*, Gulf Publishing Company, Houston (1991).
 78. Lee, W.J. and Wattenbarger, R.A.: *Gas Reservoir Engineering*, SPE Inc., Richardson (1996).
 79. Lee, W.J., and Holditch, S.A.: "Application of Pseudotime to Buildup Test Analysis of Low Permeability Gas Wells with Long Duration Wellbore Storage Distortion", *JPT* (Dec. 1982) 2877.

80. Bourdet, D., Whittle, T.M., Douglas, A.A. and Pirard, Y-M.: "A New Set of Type Curves Simplifies Well Test Analysis", *World Oil* (May 1983) 95.
81. Kuchuk, F. J.: "New Methods for Estimating Parameters of Low Permeability Reservoirs," paper SPE 16394 presented at the 1987 SPE/DOE Low Permeability Reservoir Symposium, Denver, Colorado, 18-19 May.
82. Kuchuk, F. J., Goode, P. A., Brice, B. W., Sherard, D. W., and Thambynayagam, R. K. M.: "Pressure-Transient Analysis for Horizontal Wells," *JPT* (Aug. 1990) 974.

APPENDIX A

COEFFICIENTS OF DISCRETIZED LINEAR EQUATIONS

Coefficient H

The time interval $0 \sim t_D$ is discretized into K elements with $t_{D0}, t_{D1}, t_{D2}, \dots, t_{DK-1}, t_{DK}$. When we use constant time element, Eq. 2-49 may be written on time element e_k from t_{Dk-1} to t_{Dk} as

$$\begin{aligned}
 H\nabla p_D &= \iint_{C1} dS'_D \int_0^{t_D} G_D \nabla p_D d\tau_D \\
 &= \sum_{e_k} \iint_{C1} \nabla p_D^k dS'_D \int_{t_{Dk-1}}^{t_{Dk}} \frac{\exp\left[-\frac{|R_D - R'_D|^2}{4(t_D - \tau_D)}\right]}{8[\pi(t_D - \tau_D)]^{\frac{3}{2}}} d\tau_D
 \end{aligned} \tag{A-1}$$

Let

$$\sigma = \frac{|R_D - R'_D|}{2\sqrt{(t_D - \tau_D)}} \tag{A-2}$$

Then

$$\begin{aligned}
 H\nabla p_D &= \sum_{e_k} \iint_{C1} \nabla p_D^k dS'_D \int_{\frac{|R_D - R'_D|}{2\sqrt{(t_D - t_{Dk-1})}}}{\frac{|R_D - R'_D|}{2\sqrt{(t_D - t_{Dk})}}} \frac{\exp(-\sigma^2)}{2\pi^{\frac{3}{2}} |R_D - R'_D|} d\sigma \\
 &= \sum_{e_k} \iint_{C1} \nabla p_D^k \left\{ \frac{1}{2\pi^{\frac{3}{2}} |R_D - R'_D|} \left[\int_{\frac{|R_D - R'_D|}{2\sqrt{(t_D - t_{Dk-1})}}}^0 \exp(-\sigma^2) d\sigma + \int_0^{\frac{|R_D - R'_D|}{2\sqrt{(t_D - t_{Dk})}} \exp(-\sigma^2) d\sigma \right] \right\} dS'_D
 \end{aligned}$$

$$= \sum_{e_k} \iint_{C1} \nabla p_D^k \left[\frac{\operatorname{erf}\left(\frac{|R_D - R'_D|}{2\sqrt{(t_D - t_{Dk})}}\right) - \operatorname{erf}\left(\frac{|R_D - R'_D|}{2\sqrt{(t_D - t_{Dk-1})}}\right)}{4\pi|R_D - R'_D|} \right] dS'_D \quad (\text{A-3})$$

Therefore, for $H^{mn}\nabla p_D^n$

$$H^{mn}\nabla p_D^n = \iint_{C1} \nabla p_D^n \frac{\operatorname{erfc}\left(\frac{|R_D - R'_D|}{2\sqrt{(t_{Dn} - t_{Dn-1})}}\right)}{4\pi|R_D - R'_D|} dS'_D \quad (\text{A-4})$$

for $H^{nk}\nabla p_D^k$

$$H^{nk}\nabla p_D^k = \iint_{C1} \nabla p_D^k \left[\frac{\operatorname{erf}\left(\frac{|R_D - R'_D|}{2\sqrt{(t_{Dn} - t_{Dk})}}\right) - \operatorname{erf}\left(\frac{|R_D - R'_D|}{2\sqrt{(t_{Dn} - t_{Dk-1})}}\right)}{4\pi|R_D - R'_D|} \right] dS'_D \quad (\text{A-5})$$

When the space discretization is considered at a boundary surface such as $x = x_{bl}$ (if we assume constant pressure at boundary x_{bl}), the grid system of plane yz is shown in Fig. A-1. The dimensions along the y and z directions are divided into I elements and J elements, respectively, with $I+1$ and $J+1$ nodes.

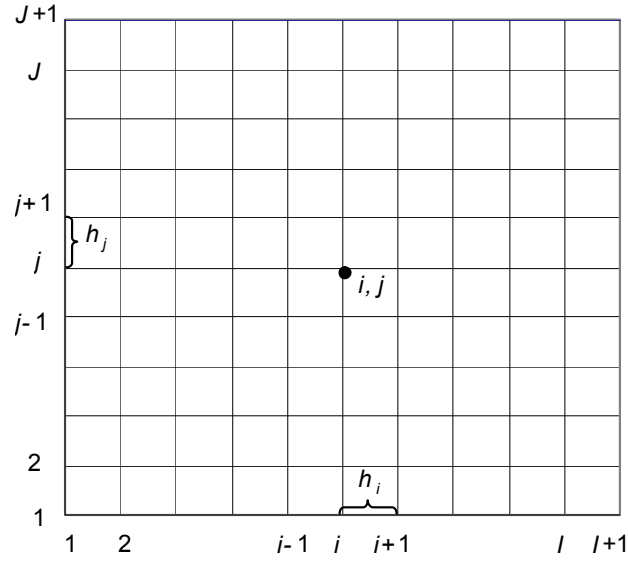


Fig. A-1 Grid system at boundary surface $x = x_{bl}$

The discretization of $H^{nk} \nabla p_D^k$ on plane yz can be expressed as Eq. A-6 using the basis function given in Eq. 2-64.

$$H^{nk} \nabla p_D^k = \sum_{j=1}^{J+1} \sum_{i=1}^{l+1} (\nabla p_D^k)_{ij} \int_0^1 \int_0^1 \sum_{m_2=0}^1 \sum_{m_1=0}^1 \varphi_{e,1+m_1}(v) \varphi_{e,1+m_2}(w) h_{i-m_1} h_{j-m_2} (\alpha_{m_1 m_2} f_{m_1 m_2}^H) dv dw \quad (\text{A-6})$$

where we express the bilinear basis function as the combination of two sets of linear basis functions (Eq. 2-62); i.e.

$$\begin{aligned} \psi_{e_1}(x, y) &= \varphi_{e_1}(x) \varphi_{e_1}(y) \\ \psi_{e_2}(x, y) &= \varphi_{e_2}(x) \varphi_{e_1}(y) \\ \psi_{e_3}(x, y) &= \varphi_{e_1}(x) \varphi_{e_2}(y) \\ \psi_{e_4}(x, y) &= \varphi_{e_2}(x) \varphi_{e_2}(y) \end{aligned} \quad (\text{A-7})$$

h stands for the size of a grid, and

$$f_{m_1 m_2}^H = \frac{\operatorname{erf}\left(\frac{|R_D - R'_D|}{2\sqrt{(t_{Dn} - t_{Dk})}}\right) - \operatorname{erf}\left(\frac{|R_D - R'_D|}{2\sqrt{(t_{Dn} - t_{Dk-1})}}\right)}{4\pi |R_D - R'_D|} \quad (\text{A-8})$$

$$m_1 = 0,1 \quad m_2 = 0,1$$

For $f_{m_1 m_2}^H$, the local coordinate transformations are, respectively,

$$\text{in } f_{0,0}^H \quad \begin{aligned} y' &= y_i + v h_i \\ z' &= z_j + w h_j \end{aligned} \quad (\text{A-9})$$

$$\text{in } f_{1,0}^H \quad \begin{aligned} y' &= y_{i-1} + v h_{i-1} \\ z' &= z_j + w h_j \end{aligned} \quad (\text{A-10})$$

$$\text{in } f_{0,1}^H \quad \begin{aligned} y' &= y_i + v h_i \\ z' &= z_{j-1} + w h_{j-1} \end{aligned} \quad (\text{A-11})$$

$$\text{in } f_{1,1}^H \quad \begin{aligned} y' &= y_{i-1} + v h_{i-1} \\ z' &= z_{j-1} + w h_{j-1} \end{aligned} \quad (\text{A-12})$$

Value of α depend on the location of the node, for example, for corner points

$$\alpha_{0,0} = 1, \quad \alpha_{1,0} = \alpha_{0,1} = \alpha_{1,1} = 0 \quad \text{at } i = 1, j = 1$$

$$\alpha_{1,0} = 1, \quad \alpha_{0,0} = \alpha_{0,1} = \alpha_{1,1} = 0 \quad \text{at } i = I + 1, j = 1$$

$$\alpha_{0,1} = 1, \quad \alpha_{0,0} = \alpha_{1,0} = \alpha_{1,1} = 0 \quad \text{at } i = 1, j = J + 1$$

$$\alpha_{1,1} = 1, \quad \alpha_{0,0} = \alpha_{1,0} = \alpha_{0,1} = 0 \quad \text{at } i = I + 1, j = J + 1$$

for edge points,

$$\alpha_{0,0} = \alpha_{1,0} = 1, \quad \alpha_{0,1} = \alpha_{1,1} = 0 \quad \text{at } j = 1$$

$$\alpha_{0,0} = \alpha_{0,1} = 1, \quad \alpha_{1,0} = \alpha_{1,1} = 0 \quad \text{at } i = 1$$

$$\alpha_{0,0} = \alpha_{1,0} = 1, \quad \alpha_{0,1} = \alpha_{1,1} = 0 \quad \text{at } j = J + 1$$

$$\alpha_{1,0} = \alpha_{1,1} = 1, \quad \alpha_{0,0} = \alpha_{0,1} = 0 \quad \text{at } i = I + 1$$

for inner points,

$$\alpha_{0,0} = \alpha_{1,0} = \alpha_{0,1} = \alpha_{1,1} = 1 \quad \text{at } 1 < i < I + 1, 1 < j < J + 1$$

Coefficient E

Similarly, Eq. 2-50 may be expressed as follows with discretization on the constant time element e_k from t_{Dk-1} to t_{Dk} . Here, we assume a no-flow boundary at $y = y_{b1}$.

$$\begin{aligned}
 Ep_D &= -\iint_{C2} dS'_D \int_0^{t_D} p_D \nabla G_D d\tau_D \\
 &= \sum_{e_k} \iint_{C2} p_D^k dS'_D \int_{t_{Dk-1}}^{t_{Dk}} \frac{(y-y')}{16\pi^{\frac{3}{2}} [(t_D - \tau_D)]^{\frac{5}{2}}} \exp\left[-\frac{|R_D - R'_D|^2}{4(t_D - \tau_D)}\right] d\tau_D \quad (A-13)
 \end{aligned}$$

Integrating by parts, we have

$$Ep_D = \sum_{e_k} \iint_{C2} p_D^k \frac{(y-y')}{16\pi^{\frac{3}{2}}} \left\{ -\frac{4 \exp\left[-\frac{|R_D - R'_D|^2}{4(t_D - \tau_D)}\right]}{\sqrt{t_D - \tau_D} |R_D - R'_D|^2} \right\}_{t_{Dk-1}}^{t_{Dk}} + \int_{t_{Dk-1}}^{t_{Dk}} \frac{2 \exp\left[-\frac{|R_D - R'_D|^2}{4(t_D - \tau_D)}\right]}{|R_D - R'_D|^2 [(t_D - \tau_D)]^{\frac{3}{2}}} d\tau_D \left\} dS'_D \quad (A-14)$$

The second term of the right hand side of Eq. A-14 is similar to the integrand with respect to time in Eq. A-1, so we obtain

$$Ep_D = \sum_{e_k} \iint_{C2} p_D^k \frac{(y-y')}{4\pi^{\frac{3}{2}} |R_D - R'_D|^2} \left\{ \frac{\exp\left[-\frac{|R_D - R'_D|^2}{4(t_D - t_{Dk-1})}\right]}{\sqrt{t_D - t_{Dk-1}}} - \frac{\exp\left[-\frac{|R_D - R'_D|^2}{4(t_D - t_{Dk})}\right]}{\sqrt{t_D - t_{Dk}}} \right. \\
 \left. + \frac{\sqrt{\pi}}{|R_D - R'_D|} \left[\operatorname{erf}\left(\frac{|R_D - R'_D|}{2\sqrt{t_D - t_{Dk}}}\right) - \operatorname{erf}\left(\frac{|R_D - R'_D|}{2\sqrt{t_D - t_{Dk-1}}}\right) \right] \right\} dS'_D \quad (A-15)$$

Hence, for $E^{nn} \nabla p_D^n$,

$$E^{nn} p_D^n = \iint_{C2} p_D^n \frac{(y-y')}{4\pi^{\frac{3}{2}} |R_D - R'_D|^2} \left\{ \frac{\exp\left[-\frac{|R_D - R'_D|^2}{4(t_{Dn} - t_{Dn-1})}\right]}{\sqrt{t_{Dn} - t_{Dn-1}}} - \frac{\sqrt{\pi}}{|R_D - R'_D|} \left[\operatorname{erf}\left(\frac{|R_D - R'_D|}{2\sqrt{t_{Dn} - t_{Dn-1}}}\right) \right] \right\} dS'_D \quad (\text{A-16})$$

For $E^{nk} \nabla p_D^k$,

$$E^{nk} p_D^k = \iint_{C2} p_D^k \frac{(y-y')}{4\pi^{\frac{3}{2}} |R_D - R'_D|^2} \left\{ \frac{\exp\left[-\frac{|R_D - R'_D|^2}{4(t_{Dn} - t_{Dk-1})}\right]}{\sqrt{t_{Dn} - t_{Dk-1}}} - \frac{\exp\left[-\frac{|R_D - R'_D|^2}{4(t_{Dn} - t_{Dk})}\right]}{\sqrt{t_{Dn} - t_{Dk}}} \right. \\ \left. + \frac{\sqrt{\pi}}{|R_D - R'_D|} \left[\operatorname{erf}\left(\frac{|R_D - R'_D|}{2\sqrt{t_{Dn} - t_{Dk}}}\right) - \operatorname{erf}\left(\frac{|R_D - R'_D|}{2\sqrt{t_{Dn} - t_{Dk-1}}}\right) \right] \right\} dS'_D \quad (\text{A-17})$$

The treatment of space discretization of Eq. A-16 and Eq. A-17 is similar to that of the coefficient H . Since we consider the space discretization on plane xz at $y = y_{b1}$ which is assumed to be a no-flow boundary, the dimensions along the x and z directions are divided into I elements and J elements, respectively, with $I+1$ and $J+1$ nodes. So we have

$$E^{nk} p_D^k = \sum_{j=1}^{J+1} \sum_{i=1}^{I+1} (p_D^k)_{ij} \int_0^1 \int_0^1 \sum_{m_2=0}^1 \sum_{m_1=0}^1 \varphi_{e,1+m_1}(v) \varphi_{e,1+m_2}(w) h_{i-m_1} h_{j-m_2} (\alpha_{m_1 m_2} f_{m_1 m_2}^E) dv dw \quad (\text{A-18})$$

where

$$f_{m_1 m_2}^E = \frac{(y-y')}{4\pi^{\frac{3}{2}} |R_D - R'_D|^2} \left\{ \frac{\exp\left[-\frac{|R_D - R'_D|^2}{4(t_{Dn} - t_{Dk-1})}\right]}{\sqrt{t_{Dn} - t_{Dk-1}}} - \frac{\exp\left[-\frac{|R_D - R'_D|^2}{4(t_{Dn} - t_{Dk})}\right]}{\sqrt{t_{Dn} - t_{Dk}}} \right. \\ \left. + \frac{\sqrt{\pi}}{|R_D - R'_D|} \left[\operatorname{erf}\left(\frac{|R_D - R'_D|}{2\sqrt{t_{Dn} - t_{Dk}}}\right) - \operatorname{erf}\left(\frac{|R_D - R'_D|}{2\sqrt{t_{Dn} - t_{Dk-1}}}\right) \right] \right\} \quad (\text{A-19})$$

If $R_D \in C_1$, we have

$$E^{*mn} p_D^n = E^{mn} p_D^n \quad (\text{A-20})$$

If $R_D \in C_2$, we have

$$E^{*mn} p_D^n = E^{mn} p_D^n - \beta p_D^n \quad (\text{A-21})$$

Coefficient Q

The treatment of coefficient Q is similar to that of coefficient H . In the derivation of Q , we use cylindrical coordinates. After discretization on time, we obtain Eq. A-22 from Eq. 2-48 (for details, see Ref. 33).

$$\begin{aligned} Qq_D &= \int_0^{t_D} d\tau_D \int_0^{2\pi} d\theta \int_0^{L_{wD}} q_{hD} G_D dl'_D \\ &= \sum_{e_k} \frac{1}{4\pi} \int_0^{2\pi} d\theta \int_0^{L_{wD}} \frac{q_{hD}^k}{|R_D - R'_D|} \left[\operatorname{erf}\left(\frac{|R_D - R'_D|}{2\sqrt{(t_D - t_{Dk})}}\right) - \operatorname{erf}\left(\frac{|R_D - R'_D|}{2\sqrt{(t_D - t_{Dk-1})}}\right) \right] dl'_D \\ &= \sum_{e_k} \frac{1}{\pi} \int_0^{L_{wD}} q_{hD}^k dl'_D \int_0^{\frac{\pi}{2}} \frac{1}{\sqrt{(x-x')^2 + (2r_w \sin \theta)^2}} \left[\operatorname{erf}\left(\frac{\sqrt{(x-x')^2 + (2r_w \sin \theta)^2}}{2\sqrt{t_D - t_{Dk}}}\right) - \operatorname{erf}\left(\frac{\sqrt{(x-x')^2 + (2r_w \sin \theta)^2}}{2\sqrt{t_D - t_{Dk-1}}}\right) \right] d\theta \end{aligned} \quad (\text{A-22})$$

For $Q^{mn} q_D^n$,

$$Q^{mn} q_D^n = \frac{1}{\pi} \int_0^{L_{wD}} q_{hD}^n dl'_D \int_0^{\frac{\pi}{2}} \frac{1}{\sqrt{(x-x')^2 + (2r_w \sin \theta)^2}} \left[\operatorname{erfc}\left(\frac{\sqrt{(x-x')^2 + (2r_w \sin \theta)^2}}{2\sqrt{t_{Dn} - t_{Dn-1}}}\right) \right] d\theta \quad (\text{A-23})$$

For $Q^{nk} q_D^k$,

$$Q^{nk} q_D^k = \frac{1}{\pi} \int_0^{L_{wD}} q_{hD}^k dl'_D \int_0^{\frac{\pi}{2}} \frac{1}{\sqrt{(x-x')^2 + (2r_w \sin \theta)^2}} \left[\begin{array}{c} \operatorname{erf}\left(\frac{\sqrt{(x-x')^2 + (2r_w \sin \theta)^2}}{2\sqrt{t_{Dn} - t_{Dk}}}\right) \\ - \operatorname{erf}\left(\frac{\sqrt{(x-x')^2 + (2r_w \sin \theta)^2}}{2\sqrt{t_{Dn} - t_{Dk-1}}}\right) \end{array} \right] d\theta \quad (\text{A-24})$$

Since q_{hD} is considered as a function of only time and position along the wellbore length (assumed to be the x -direction), the linear basis function is used for well discretization. The well length is divided into I elements with $I+1$ nodes. So, we have

$$Q^{nk} q_{hD}^k = \sum_{i=1}^{I+1} (q_{hD}^k)_i \int_0^{\frac{\pi}{2}} d\theta \int_0^1 \sum_{m=0}^1 \varphi_{e,1+m}(v) h_{i-m} \alpha_m f_m^Q dv \quad (\text{A-25})$$

where

$$f_m^Q = \frac{1}{\pi} \frac{1}{\sqrt{(x-x')^2 + (2r_w \sin \theta)^2}} \left[\begin{array}{c} \operatorname{erf}\left(\frac{\sqrt{(x-x')^2 + (2r_w \sin \theta)^2}}{2\sqrt{t_{Dn} - t_{Dk}}}\right) \\ - \operatorname{erf}\left(\frac{\sqrt{(x-x')^2 + (2r_w \sin \theta)^2}}{2\sqrt{t_{Dn} - t_{Dk-1}}}\right) \end{array} \right] \quad (\text{A-26})$$

and

$$\alpha_0 = 1, \quad \alpha_1 = 0 \quad \text{at } i = 1$$

$$\alpha_1 = 1, \quad \alpha_0 = 0 \quad \text{at } i = I + 1$$

$$\alpha_0 = \alpha_1 = 1 \quad \text{at } 1 < i < I + 1$$

APPENDIX B

FLUX DISCONTINUITY AT CORNER/CROSS POINTS

When a completed wellbore is not straight but curved, corner points must be formed, as shown in Fig. B-1. At a corner point, the flux is not continuous since the normals to the adjacent elements may be different. The same problems exist at cross points formed when boundary planes meet. To solve this type of problem, discontinuous elements need to be used.

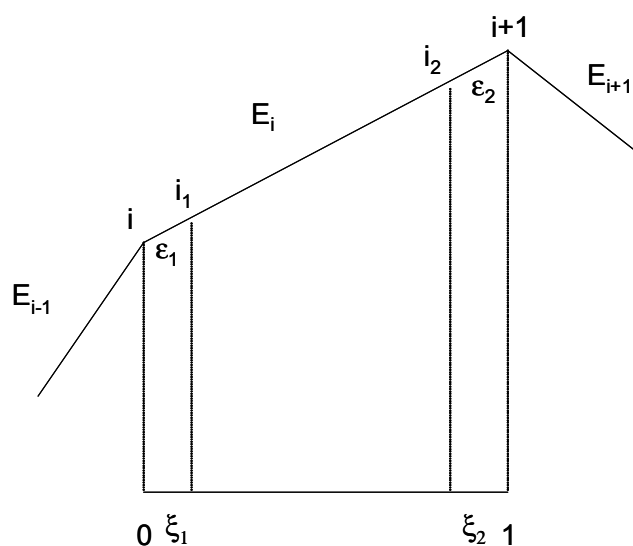


Fig. B-1 Discontinuous linear elements

1-D Discontinuous Element

At corner nodes i and $i+1$ shown in Fig. B-1, the fluxes are not continuous. By converting the two adjacent elements at a corner into two discontinuous elements and by replacing the corner node with two nodes arbitrarily close to it, the flux can be assigned to the two nodes⁷⁰. For example, on element E_i , i_1 and i_2 are two new nodes. ϵ_1 and ϵ_2 are the distance between new nodes and original nodes; i.e.,

$$\begin{aligned} \epsilon_1 &= |i - i_1| \\ \epsilon_2 &= |(i+1) - i_2| \end{aligned} \tag{B-1}$$

In the local coordinator system rescaled to $[0,1]$, the coordinators of nodes i_1 and i_2 are, respectively,

$$\begin{aligned}\xi_1 &= \frac{\varepsilon_1}{h_i} \\ \xi_2 &= 1 - \frac{\varepsilon_2}{h_i}\end{aligned}\tag{B-2}$$

where h_i is the length of element E_i . q_{i1} and q_{i2} , at i_1 and i_2 respectively, can be expressed as follows:

$$\begin{bmatrix} q_{i1} \\ q_{i2} \end{bmatrix} = \begin{bmatrix} \varphi_1(\xi_1) & \varphi_2(\xi_1) \\ \varphi_1(\xi_2) & \varphi_2(\xi_2) \end{bmatrix} \begin{bmatrix} q_1 \\ q_2 \end{bmatrix}\tag{B-3}$$

From the linear basis function, we can obtain q_1 and q_2 in terms of q_{i1} and q_{i2} .

$$\begin{bmatrix} q_1 \\ q_2 \end{bmatrix} = \frac{1}{h_i - \varepsilon_1 - \varepsilon_2} \begin{bmatrix} h_i - \varepsilon_2 & -\varepsilon_1 \\ -\varepsilon_2 & h_i - \varepsilon_1 \end{bmatrix} \begin{bmatrix} q_{i1} \\ q_{i2} \end{bmatrix}\tag{B-4}$$

Let

$$Q = \frac{1}{h_i - \varepsilon_1 - \varepsilon_2} \begin{bmatrix} h_i - \varepsilon_2 & -\varepsilon_1 \\ -\varepsilon_2 & h_i - \varepsilon_1 \end{bmatrix}\tag{B-5}$$

Hence, for an arbitrary point on element E_i , we have

$$\begin{aligned}q(\xi) &= [\varphi_1(\xi) \quad \varphi_2(\xi)] \begin{bmatrix} q_1 \\ q_2 \end{bmatrix} \\ &= [\varphi_1(\xi) \quad \varphi_2(\xi)] Q \begin{bmatrix} q_{i1} \\ q_{i2} \end{bmatrix}\end{aligned}\tag{B-6}$$

2D Discontinuous Element

The cross nodes, points on edges of intersecting two boundary surfaces, have discontinuous fluxes. We take the element E_{1j} in Fig. B-2 as an example to indicate the treatment method for the discontinuous element problem. In the element E_{1j} , only points 1 and 3 need to be treated. Similarly, we take ε_1 and ε_3 to denote the deviation from points 1 and 3 in the horizontal direction, respectively. The local coordinates for points j_1 and j_3 are $(\xi_1, 0)$ and $(\xi_3, 1)$, respectively, and ξ_1 and ξ_3 may be expressed as follows.

$$\begin{aligned}\xi_1 &= \frac{\varepsilon_1}{h_1} \\ \xi_3 &= \frac{\varepsilon_3}{h_1}\end{aligned}\tag{B-7}$$

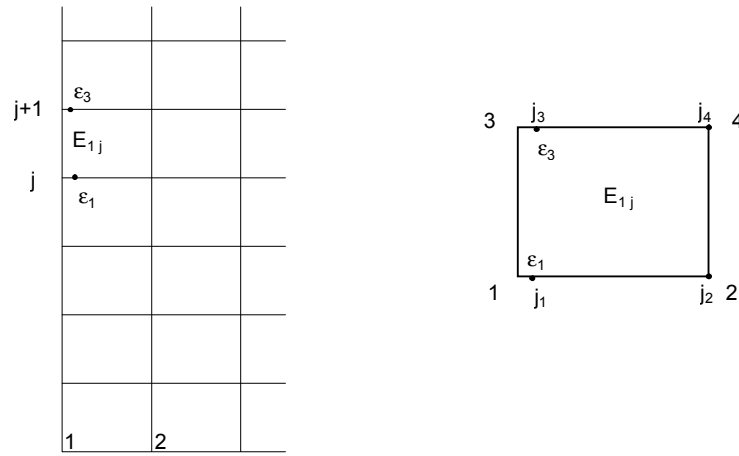


Fig. B-2 Discontinuous bilinear element

where h_1 is the length of element E_{1j} in horizontal direction. $q_{j1} \sim q_{j4}$, corresponding to $j_1 \sim j_2$ respectively, can be expressed as follows:

$$\begin{bmatrix} q_{j1} \\ q_{j2} \\ q_{j3} \\ q_{j4} \end{bmatrix} = \begin{bmatrix} \varphi_1(\xi_1, 0) & \varphi_2(\xi_1, 0) & \varphi_3(\xi_1, 0) & \varphi_4(\xi_1, 0) \\ 0 & 1 & 0 & 0 \\ \varphi_1(\xi_3, 1) & \varphi_2(\xi_3, 1) & \varphi_3(\xi_3, 1) & \varphi_4(\xi_3, 1) \\ 0 & 0 & 0 & 1 \end{bmatrix} \begin{bmatrix} q_1 \\ q_2 \\ q_3 \\ q_4 \end{bmatrix}\tag{B-8}$$

From the bilinear basis function, Eq. 2-63, we can obtain $q_1 \sim q_4$ in terms of $q_{i1} \sim q_{i4}$.

$$\begin{bmatrix} q_1 \\ q_2 \\ q_3 \\ q_4 \end{bmatrix} = Q \begin{bmatrix} q_{j1} \\ q_{j2} \\ q_{j3} \\ q_{j4} \end{bmatrix}\tag{B-9}$$

where

$$Q = \frac{1}{(h_1 - \varepsilon_1)(h_1 - \varepsilon_3)} \begin{bmatrix} h_1(h_1 - \varepsilon_3) & -\varepsilon_1(h_1 - \varepsilon_3) & 0 & 0 \\ 0 & (h_1 - \varepsilon_1)(h_1 - \varepsilon_3) & 0 & 0 \\ 0 & 0 & h_1(h_1 - \varepsilon_1) & -\varepsilon_3(h_1 - \varepsilon_1) \\ 0 & 0 & 0 & (h_1 - \varepsilon_1)(h_1 - \varepsilon_3) \end{bmatrix} \quad (\text{B-10})$$

Therefore, for an arbitrary point (ξ, η) in element E_{1j} , we have

$$\begin{aligned} q(\xi, \eta) &= [\varphi_1(\xi, \eta) \quad \varphi_2(\xi, \eta) \quad \varphi_3(\xi, \eta) \quad \varphi_4(\xi, \eta)] \begin{bmatrix} q_1 \\ q_2 \\ q_3 \\ q_4 \end{bmatrix} \\ &= [\varphi_1(\xi, \eta) \quad \varphi_2(\xi, \eta) \quad \varphi_3(\xi, \eta) \quad \varphi_4(\xi, \eta)] Q \begin{bmatrix} q_1 \\ q_2 \\ q_3 \\ q_4 \end{bmatrix} \quad (\text{B-11}) \end{aligned}$$

APPENDIX C

FFT ALGORITHM

In this appendix, we provide a description of an FFT algorithm, based on *The FFT, Fundamentals and Concepts* by Robert W. Ramirez.⁷⁴

The FFT is a fast algorithm for computing the discrete Fourier transform. The direct evaluation of the DFT requires N^2 operations, where N is the number of samples. In fact, all algorithms faster than the N^2 approach, are lumped under the heading of FFT. Here, we discuss an FFT approach that is based on the Sande-Tukey algorithm. This algorithm operates on N samples, where N is equal to 2 raised to an integer power, $N = 2^M$ (M is an integer). This algorithm requires $N \times M$ operations.

The expression for the DFT is:

$$X_d(k) = \sum_{n=0}^{N-1} x_d(n) e^{-i2\pi kn/N} \quad (\text{C-1})$$

For notational convenience, Eq. C-1 is expressed as:

$$A(n) = \sum_{t=0}^{N-1} x_0(t) W^{-nt} \quad (\text{C-2})$$

$$n = 0, 1, \dots, N-1$$

where $W = e^{i2\pi/N}$, $x_0(t)$ represents the set of data in the time domain. The computation of the FFT of $x_0(t)$ consists of $\log_2 N = M$ stages. Each stage requires pairs of computations of the following form:

$$x_{m+1}(r) = x_m(r) + x_m(s) \quad (\text{C-3})$$

and

$$x_{m+1}(s) = [x_m(r) - x_m(s)] W^{-p} \quad (\text{C-4})$$

where r, s, p are all integers between 0 and $N-1$, and m is between 0 and $M-1$.

A 16-point FFT example is illustrated in Fig. C-1 to indicate how the computations take place. The data are gathered into groups at each stage, and the groups are broken into smaller groups until per group has one datum.

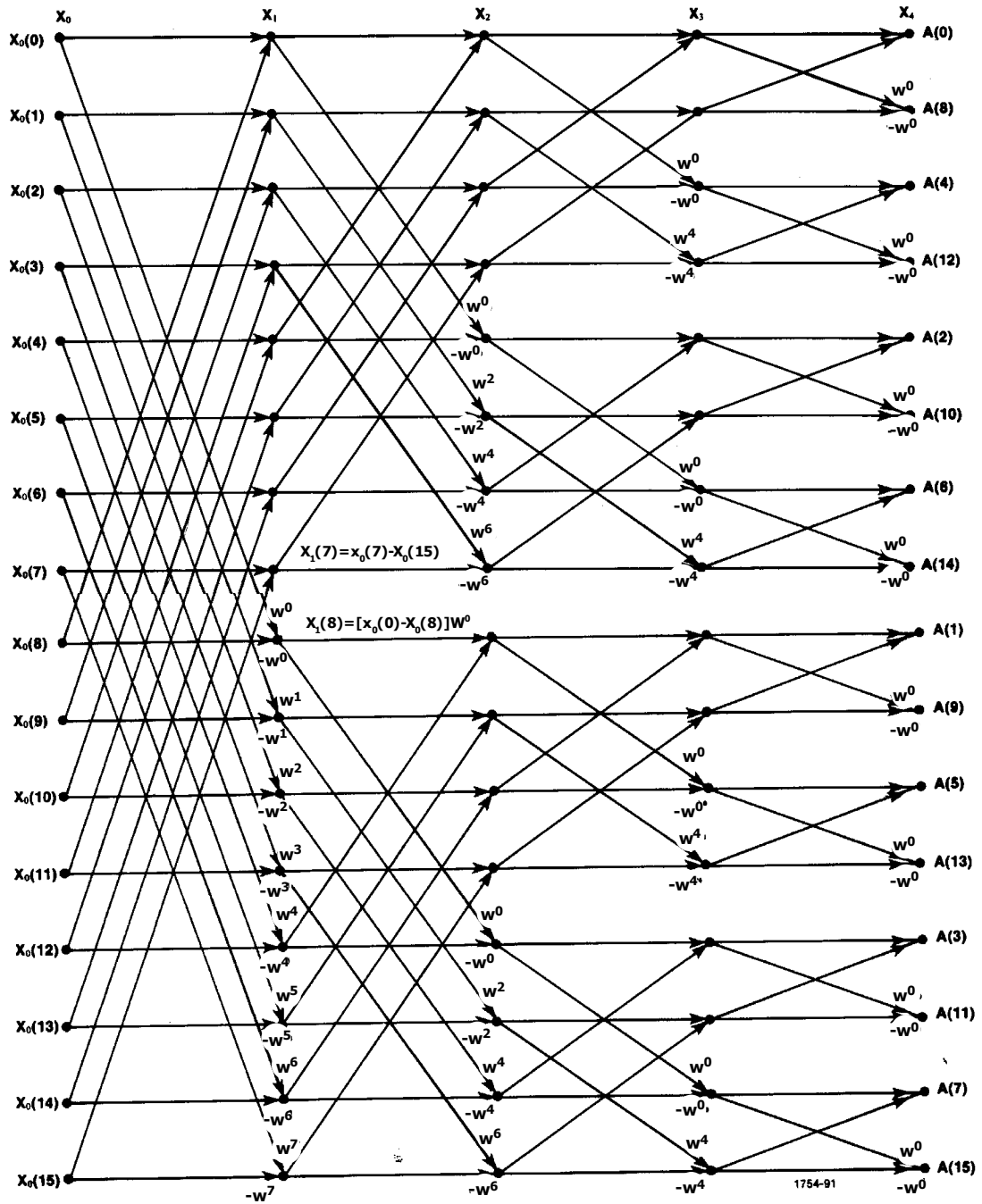


Fig. C-1—Flow diagram for a 16-point, decimation-in-frequency FFT algorithm (after Ramirez⁷⁴).

The data elements within each group are computed from pairs of corresponding elements from the preceding groups. Each of the heavy dots in Fig. C-1 represents a point of computation. After the final stage is completed, the $x_0(t)$ are transformed to $A(n)$; i.e., data in the time-domain are transformed to those in the frequency-domain. The order of the Fourier coefficients is scrambled, and can be unscrambled by bit reversal, which re-expresses the subscripts of $A(n)$ in binary code.

A FFT algorithm in Fortran77 was used in this work and can be found in the public domain (www.netlib.org), where it is listed as misc/fft.f.

VITA

Yueming Cheng was born in Karamayi, Xingjiang, China on August 29, 1964. She received her Bachelor of Science in Petroleum Engineering from Southwestern Petroleum Institute, Sichuan, China, in July 1985 and Master of Science in Petroleum Engineering from Graduate School, Research Institute of Petroleum Exploration and Development (RIPED), Beijing, China, in July 1991. She was an assistant engineer in Fracturing and Acidizing Technology Research Center, RIPED's Branch Institute after receiving her BS degree. During graduate study for the MS degree, she was a research associate in the Department of Oil and Gas Fields Development, RIPED. Then as a reservoir engineer, she worked in the Department of Oil Production Engineering, RIPED until starting her doctoral program in the United States in September 1998. She has worked on well test analysis, hydraulic fracture design and performance evaluation, reservoir simulation studies, and oil/gas well design. During her graduate years in the U.S., she had a working experience as a summer intern with Schlumberger Oilfield Services working on reservoir temperature estimation. Her permanent address is 20 University Road, Beijing 100083, People's Republic of China.